INFORMATION TO USERS

The most advanced technology has been used to photograph and reproduce this manuscript from the microfilm master. UMI films the text directly from the original or copy submitted. Thus, some thesis and dissertation copies are in typewriter face, while others may be from any type of computer printer.

The quality of this reproduction is dependent upon the quality of the copy submitted. Broken or indistinct print, colored or poor quality illustrations and photographs, print bleedthrough, substandard margins, and improper alignment can adversely affect reproduction.

In the unlikely event that the author did not send UMI a complete manuscript and there are missing pages, these will be noted. Also, if unauthorized copyright material had to be removed, a note will indicate the deletion.

Oversize materials (e.g., maps, drawings, charts) are reproduced by sectioning the original, beginning at the upper left-hand corner and continuing from left to right in equal sections with small overlaps. Each original is also photographed in one exposure and is included in reduced form at the back of the book. These are also available as one exposure on a standard 35mm slide or as a 17″ x 23″ black and white photographic print for an additional charge.

Photographs included in the original manuscript have been reproduced xerographically in this copy. Higher quality 6″ x 9″ black and white photographic prints are available for any photographs or illustrations appearing in this copy for an additional charge. Contact UMI directly to order.

Multiply-charged ion emission from a cyclotron-resonance-heated plasma ion source

Whaley, David Riley, Ph.D.

The University of Michigan, 1989

MULTIPLY-CHARGED ION EMISSION FROM A
CYCLOTRON-RESONANCE-HEATED PLASMA ION SOURCE

by

David Riley Whaley

A dissertation submitted in partial fulfillment
of the requirements for the degree of
Doctor of Philosophy
(Nuclear Engineering)
in The University of Michigan
1989

Doctoral Committee:

Professor Ward D. Getty, Co-Chairman
Professor Ronald M. Gilgenbach, Co-Chairman
Assistant Professor Mary L. Brake
Professor Terry Kammash

RULES REGARDING THE USE OF

MICROFILMED DISSERTATIONS

For My Parents, Mom and Dad

ACKNOWLEDGEMENTS

I find myself, at the end of my graduate career, indebted to a great many people who have made my years at Michigan enjoyable ones. Above all, highest regards go to Dr. Ward D. Getty, whose intellect and insight into physical problems are surpassed only by his character and concern for his students. I have never seen him unwilling to take whatever time is necessary to work through a problem with a confused student (usually myself) or help where needed in any way possible, no matter how trivial or how involved the task happened to be. His wealth of knowledge has been an invaluable resource for myself and all students involved in the day-to-day problems that arise in the lab. He has truly been an instrumental part of my graduate program and I am sure that all of his past students would agree that they were extremely fortunate to have had Ward as an advisor.

I have worked with Tim Goodman, a fellow graduate student, for several years and still find that I learn from him. His "let's-get-down-to-the-basics" approach to science has many times made me rethink a problem only to realize that I had overlooked some important factor. Whether he is demonstrating how to thread a hole without breaking the 2-56 tap or explaining the intricacies of the plasma WECE instability, Tim has a patience and enthusiasm that I find rare. He has been an excellent co-worker and a valued friend.

I would like to thank Professor Ron Gilgenbach for always showing interest when I came to him with a question or for discussion. He has a great enthusiasm for research and instinctive experimental insights. It was also a nice change of pace to be taught most of my plasma physics courses by someone who knows what it is _really_ like

to work in a laboratory. Thanks goes to Professor Mary Brake for serving on my committee and reading these *220+* not-so-exciting pages in one weekend. She is one person that I don't think I have ever seen without a smile. And Professor Terry Kammash deserves thanks for all of his help with special requests that I have made - from needing time on his MFECC computer account to wanting a post-doc in Europe.

On a less academic note, I could not begin to think of the fun times I've had in my graduate years - the football games, the barbecues, the trips to Florida, the nights at Fraser's Pub - without thinking of Dale Alexander who has truly been a party to some crazy antics. No details will be included here. And where Dale left off, Pete Ventzek picked up. Pete's refreshing outlook on what really makes grad school worthwhile was an inspiration which forced me to enjoy even the last few months of thesis writing.

My parents have always been a source of support throughout my fleeting brush with academia - during the decade of the eighties. They have always showed interest in anything I was doing even though I knew they understood very little of what I was rambling on about. Friends from outside the department have provided alot of good times. Tom Treusdell, Mike Sills, Steve Malina, Pete Santinga, and Cal Klein will always be good friends. In addition, all of the guys of the Plasma Experimental Bay have provided a nice diversion from the work which was always at hand. Many thanks go to Bob Lucey, Marc Herniter, Mike Cuneo, Steve Bidwell, Craig Outten, Jian-guang Wang, Joel Miller, Jin Choi, Kevin Junck, Tom Repetti, Mike Passow, and Tom Spencer.

Finally, the Department of Energy deserves thanks for funding my past $4\frac{1}{2}$ years of graduate school. Craig Williamson, in particular, has been invaluable in helping with and approving special requests made of him by myself and other DOE fellows. The opportunity afforded me by the program to work at Lawrence Livermore National Laboratory has proven very useful to me in my work at Michigan. National Science Foundation also deserves mention for providing financial support for the experiment described in this dissertation. And with that let me just say, "GO BLUE" and I'm outta here.

TABLE OF CONTENTS

LIST OF TABLES

LIST OF FIGURES

LIST OF APPENDICES

CHAPTER 1

INTRODUCTION

1.1. Motivation for Study

Over the last two decades, interest has developed in sources of multiply-charged ions. These ions result from one of several processes which strip electrons from the shells of neutral atoms. These ions can then be extracted from these electron-stripping devices and used in a wide variety of applications.[1-10]

Nuclear physicists have specific interest in multiply-charged ion beams for several reasons. The existing experimental data for atomic collision processes for other than singly-ionized ions is very limited. With a reliable source of multiply-charged ions, careful studies of high-Z ion atomic structures can be performed as well as tests of fundamental atomic behavior, which becomes more marked at high ion charge states.[11] Also, experiments are being conducted requiring fully-stripped medium mass ions to investigate compound nuclei formation occurring when highly-charged projectile ions strike a target nucleus.[12]

High-Z ion injection into cyclotrons allow scientists to achieve much higher energy beams practically "for free". These high-energy, high-Z beams are being used to study many varied phenomenon. For example, a combination high-Z ion source and 88-inch cyclotron allows for the testing of computer microprocessor chips for susceptibility to "single-event upset" or "bit-flip". In space, cosmic rays continuously bombard space

1

vehicles and the computers they contain. These cosmic rays can deposit large quanta of energy in the computer boards causing information-containing bits to flip. These uncontrollable errors are a major concern for space vehicles and satellites. High-Z ion bombardment of microchips simulate this cosmic-ray bombardment and yields information on susceptibility of specific systems to this phenomenon.[12]

Fusion researchers also have interest in the study of multiply-charged ions. Impurities are a major problem in fusion devices. Ideally, fusion plasmas consist only of light ions, however, high-mass impurities are also always present and become highly stripped in the hot-electron environment. These impurities then radiate and lead to power losses which cool the plasma. Understanding of high-Z ion collisions and therefore, high-Z ion sources, have justifiably become a priority for fusion scientists.

1.2. Multiply-Charged Ion Generation Schemes

Several methods exist for creating beams of multiply-charged ions. The first method is one which has not become widely used due to difficulty inherent with the scheme.[13] This scheme involves injecting very energetic (several MeV / nucleon), low-charge-state ions through a thin foil whose thickness is only a few micrometers. The thin foil contains in its crystalline structure, atoms and high-density, cold electrons ($n_e \sim 10^{24}$ cm^{-3}). Since the electrons are cold, the relative interaction velocity and ion velocity are approximately equal at $\sim 10^9$ cm/s. The transit time for the ions is then $\sim 10^{-13}$ s during which time the stripping of the low-Z ions take place. There are two types of collisions in competition during the interaction: the step-by-step collisional ionization of the incident ions and the recombination of the multiply-charged ions through electron capture. At high relative interaction velocity, the ionization process predominates and the ion beam

emerges from the foil highly charged. This, however, requires an ion acceleration step prior to injection into the foil which is difficult and expensive.

Another, more wide-spread method for creating multiply-charged ions involves use of the Penning Ionization Gauge (PIG).[12] The PIG source consists of an anode chamber with cathodes at either end and an externally applied axial magnetic field whose field lines run perpendicular to the face of each cathode. Atoms of the desired element are introduced into the chamber and an arc discharge is generated creating a plasma which fills the chamber. Positive ions striking the surface of the cathode cause cathode secondary electron emission. These emitted electrons then follow the magnetic field lines into the plasma volume and collisionally ionize the ions present. The ions become multiply-charged and are extracted from the source chamber.

PIG sources pose many problems as a source of heavy, high-Z ions because they are unable to heat the electrons to high enough energies so they may strip the ions of their inner electrons and they are also unable to confine ions for a sufficiently long time to build up high charge states. Reliability causes many problems also. The steady bombardment of the cathodes in the PIG source causes the secondary electron emission coefficient of the cathodes to drop precipitously until the cathodes cannot supply a sufficient number of electrons for the ionizing collisions. The source must then be shut down and the cathodes replaced. This results in a *20 - 30%* decrease in the availability of the source which can be a major frustration to anyone using such a source.

Electron Beam Ion Sources (EBIS) have been proven to yield fully-stripped light ions up to charge *18*. The EBIS requires a dense, hot electron beam travelling along the axis of a solenoid of $B_{\parallel} \sim 1.0\ T$. This beam passes through a series of insulated cylindrical electrodes to which a large positive potential is applied to facilitate the

confinement of newly created ions. The space charge of the electron beam produces a potential well which radially traps the ions. High-Z ions are produced primarily by successive collisional ionization. The energy of the electron beam can be adjusted such that a given charge state, Z, is most probable after the beam has traversed the EBIS chamber. The ions are then extracted by lowering the potential of a "blocking" electrode at the end of the source.

Ion exposure time in an EBIS, and therefore degree of ionization, is limited by the space charge neutralization time, τ_n. This is the time necessary to build up a charge density of ions equal to the electron density of the electron beam. When this occurs, the ion-confining potential well levels off. The time necessary to remove Z electrons, τ_Z, is given by:[14]

$$\tau_Z \ (sec) = \frac{1.6 \ x \ 10^{-19}}{J \ (A \ / \ cm^2)} \sum_{n=0}^{Z} \frac{1}{\sigma_{n \to (n+1)} \ (cm^2)} . \qquad (1.1)$$

The highest yield of Z-times ionized ions from an EBIS source is attained when the initial number of neutral atoms in the chamber is adjusted such that $\tau_Z \sim \tau_n$. For common beams, this requires a very low background ($\sim 10^{-8}$ Torr) of the desired element. Since the residual background gas must be at least an order of magnitude below this, ultra high vacuum is required for these devices.

Problems arise due to the stringent cathode heat dissipation requirements and current density limitations of the electron gun needed to produce these high-density, high-energy electron beams. Also the pulsed nature of these machines allows only for very short bursts of highly charged ions as opposed to steady state operation in PIG

sources and electron cyclotron resonant sources. The EBIS sources do, however, produce the highest-Z ions available, though in comparatively small quantities.

The electron cyclotron resonant (ECR) ion source has emerged as the most promising source of highly-charged ions. Since it is a cathodeless device, it overcomes the problem of availability inherent in the PIG source. By virtue of the electron-heating scheme, the ECR ion source creates a high-energy electron population which, unlike the PIG source, is capable of stripping even the inner electrons of heavy elements. It also requires no "ion preparation" stage, as with the foil stripping method, which necessitates the use of a pre-ionizer and accelerator prior to the stripping process. It is a steady-state device and can deliver continuous beams of highly-charged ions. Many years experience with these sources have proven them to be nearly *100%* reliable.

An ECR ion source uses microwaves to heat the electrons in a magnetically confined plasma. The heating frequency is chosen such that it matches the electron cyclotron resonant (ECR) frequency at some location in the plasma region. The magnetic configuration is usually a minimum-B mirror but can be a simple mirror also. With the ECR heating, a population of electrons, stochastically heated to several keV, are created. These electrons undergo collisions with ions present in the plasma, stripping them of their bound electrons. The processes which yield many-times ionized ions involve successive, step-by-step, collisional ionization and single-step Auger ionization. Therefore, there are two requirements for production of highly-charged ions from an ECR ion source via these two processes. These requirements are high electron density to insure many electron-ion collisions and long ion confinement times so that successive collisional ionizations have sufficient time to occur. Typically, the criteria are summarized as $n_e \tau_i >$

10^8 s/cm^3 for multiply-charged light species, $n_e \tau_i > 10^{10}$ s/cm^3 for totally stripped light species, and $n_e \tau_i > 10^{13}$ s/cm^3 for totally stripped heavy species.[10]

The chart below summarizes the different schemes which have been described in this section for generating multiply-charged ions.

Table 1.1. Properties of Competing Highly-Charged Ion Sources

Source Types	Comments
Foil Stripping Sources	• high energy ion beam passing through thin foil • requires preionizer and accelerator prior to ion stripping
PIG Sources	• cathode device • low availability • produces low-Z beams
EBIS	• high energy electron beam required • pulsed device • high heat dissipation • produces high-Z beams
ECR Sources	• cathodeless device • continuous • high availability • produces med/high-Z beams

There are advantages and disadvantages to each scheme, however the ECR ion source method has generally been accepted as the preferred method for reasons discussed above.

1.3. MIMI as an ECR Ion Source

ECR ion sources have been used successfully as sources of highly-charged ions in several laboratories around the world. Pioneering research on these sources was first performed by R. Geller at the Department de la Physique du Plasma et de la Fusion Controlee in Grenoble, France.[15] There, Geller used a simple magnetic mirror to confine a high-pressure (10^{-4} Torr), ECR-heated, plasma discharge from which he extracted multiply-charged light ions. Since that time, ECR ion source systems have become much larger and more complex but have increased in performance significantly. Beams of fully stripped heavy ions such as Ar^{18+} have been extracted from some sources.[16] Design of most of these ion sources has been based on experimental results of previous machines and these sources are "tuned" empirically for the best running conditions. Very little diagnostic information is available and an understanding of the processes involved in the build up of these highly-charged ions is needed. This is a partial motivation for the work presented here.

The Michigan Mirror Machine is presently used as an ECR ion source. It has all the attributes of a standard source: magnetic mirror configuration, ECRH employed to start up and heat the plasma, high mass gases leaked into the system from low base pressure. It differs from most ECR ion sources in its extensive diagnostic capabilities. Diagnostics have been implemented to measure electron density, electron temperature, plasma potential, x-ray emission, and time-resolved charge state distributions. Also, ion cyclotron resonant heating (ICRH) has been implemented to directly heat the ions and alter their charge state distributions. The effects of this near-midplane ion heating is monitored by the diagnostic systems.

An understanding of these high-Z ion sources has been gained through this investigation and a method to affect the distribution of ionization levels among the possible states has been explored. The research that follows is a small part of the efforts of a growing group of scientists interested in these promising sources.

CHAPTER 2

HISTORICAL DEVELOPMENT OF ECR ION SOURCES

The development of ECR ion sources arose from a need for heavy, highly-stripped ions which are not available from standard PIG sources. The first ECR ion source appeared in the late 1960's and consisted of a system with a standard magnetic bottle geometry containing a plasma heated with *1-2 kW* of *10 GHz* microwaves. Since that time, ECR ions sources have developed into complex machines of several stages with permanent magnets supplying the minimum-B stabilizing field. Following is a brief review of the development of these sources and the corresponding increase in production of the much needed high-Z ions.

2.1. Early Stages of ECR Ion Sources

The earliest and most simple of ECR ion sources was Machine For Ion Stripping (MAFIOS) designed and built at the Departement de la Physique du Plasma et de la Fusion Controlee.[17] A magnetic mirror was created with electromagnets which produced a field of *2 kG < B < 4 kG*. This created an electron resonant zone in the plasma for *10 GHz* microwaves which were admitted to the plasma region through a BeO_2 window which lay on the magnetic axis. As these waves propagated through the chamber, they became resonant with the plasma electrons where the microwave frequency matched the electron cyclotron resonant (ECR) frequency. In this resonant region, electrons can either

9

absorb energy from the wave or transfer energy to the wave. On average, though, there is a net energy transfer from the wave to the electrons. This stochastic heating causes strong damping of the microwaves and efficient energy transfer occurs. This is the process by which hot electron populations are created by ECR heating in all ECR ion sources. Multiply-charged ions are then created due to several electron-ion interactions to be discussed later.

The principle underlying the construction of MAFIOS was the violation of the Child-Langmuir law limiting the possible current extracted from a plasma volume, allowing for extraction of high-intensity ion beams. This law states that the possible extracted current is:

$$i = \kappa V_{extr}^{\frac{3}{2}} \tag{2.1}$$

where V_{extr} is the voltage applied to the extraction electrode and κ is the perveance of the beam. Generally high extraction voltages are used to increase the extracted current followed by a deceleration stage which produces only a modest-intensity slow ion beam. This law however does not hold when the ions impinging on a floating extraction electrode (behind which is the extraction gap of high electric field created by a series of biased electrodes) already have some directed energy, eV_o. In this case, the ion current is limited to:[18]

$$i = \kappa \left(V_0^{\frac{1}{2}} + V_{extr}^{\frac{1}{2}} \right)^3 . \tag{2.2}$$

These conditions are satisfied for a floating electrode placed just beyond the mirror peak of an ECR ion source. The hot electron plasma confined in a magnetic bottle builds up a positive ambipolar plasma potential. Between the hot electron plasma and the floating electrode, a sheath (covering the hole in the electrode) is formed in which there exists a potential drop of:[19]

$$\Delta V \sim V_0 = \frac{kT^-}{e \log \left\{ \dfrac{M^+ T^-}{M^- T^+} \right\}} .$$

(2.3)

The cold ions of the plasma are accelerated as they fall through this plasma sheath and acquire an energy eV_O before penetrating into the extraction gap with the accelerating, high electric field. The electrode is placed just slightly beyond the mirror position so that most of the energetic electrons are reflected before reaching the floating electrode. This facilitates the ion-electron separation near the extraction gap and has been shown to be necessary for the extraction of high-intensity, multiply-ionized ion beams. It is this acquired energy that allows for increased ion beam intensity for relatively low extraction voltages.

Using this type of source and extraction system, it was found that extraction voltages of only ~100 V was sufficient to obtain slow ion beams of *tens of mA/cm²*. This current density is much larger than would be expected using standard Child-Langmuir calculations. These high current densities are necessary since the fraction of high charge state ions in the ion beam is quite small. For example, to extract *1 μA/cm²* of N^{7+} ions, it is necessary to extract a total nitrogen current of *100 mA/cm²*. The charge state distributions measured on MAFIOS always peaked at the lowest charge state and

populations of higher charge states decreased rapidly with Z. A typical charge state distribution is shown in Table 2.1. These distributions are similar to those distributions achieved with the PIG sources though the current densities measured were much higher than the PIG sources.

Table 2.1. Charge State Distribution for Nitrogen in MAFIOS

Species	Relative Concentration
N^+	44. %
N^{2+}	36. %
N^{3+}	13.5 %
N^{4+}	4.5 %
$N^{5+} + N^{6+} + N^{7+}$	2.0 %

A source similar to MAFIOS in all respects was built at Oak Ridge National Laboratory in parallel with MAFIOS.[20] It too used a simple magnetic bottle to confine a population of hot, ECR-heated electrons. This source, ELMO, produced similar charge state distributions to that of MAFIOS, though the current densities were somewhat lower due to the different ion extraction system used.

2.2. Next Generation - Minimum-B Stabilization

MAFIOS led the way for development of the next generation ECR ion source. The charge state distributions achieved by the MAFIOS source appeared promising,

however, there were several problems inherent in its design. The machine did not allow for large $n_e\tau_i$ products ($n_e\tau_{iMAFIOS} \sim 10^7\ s/cm^2$) which are necessary for production of highly-stripped, high-mass ions. The need to increase the ion lifetime and maintain a large, hot electron density necessitated the use of an MHD-stabilizing, minimum-B magnetic field structure. INTEREM[21] was such a source, built at Oak Ridge National Laboratory for production of high-Z ions in 1974-1976. This source, very similar to the MAFIOS and ELMO sources, utilized Ioffe coils which create a magnetic field which, as seen from the magnetic axis at midplane, is increasing in all directions.[22] This "minimum-B" geometry stabilizes the ion-and-electron-lifetime-limiting MHD instability and creates closed ECR resonant surfaces in the plasma device which do not intersect any wall. These conditions can increase ion and electron lifetimes orders of magnitude over that of a simple mirror device.

INTEREM was such a minimum-B device and did show that high-Z ion charge state distributions could be produced. It was similar to MAFIOS in heating frequency, magnetic field strength and physical size, though the minimum-B magnetic field structure allowed a larger $n_e\tau_i$ product and consequently, high average-Z charge state distributions. For comparison, Table 2.2 shows a spectrum for nitrogen from INTEREM for operating conditions similar to the MAFIOS source. In Table 2.2, N^{7+} was not reported because it is degenerate (i.e. possesses identical m/q) with H^{2+} which was abundant in the spectra. The reason that abundances of N^+ are not reported is unknown. By comparing Table 2.1 and 2.2, a distinct shift toward higher charge states is evident. In MAFIOS, the most abundant charge state was the singly-ionized state and the relative concentration of higher charge states decreased quickly with Z. The concentration of any state higher than N^{4+} is negligible. In contrast, for the minumum-B stabilized INTEREM ion source, the charge

Table 2.2. **Charge State Distribution for Nitrogen in INTEREM**

Species	Relative Concentration
N^{2+}	15. %
N^{3+}	30. %
N^{4+}	36. %
N^{5+}	16. %
N^{6+}	3.0 %
N^{7+}	?

state distributions peak at N^{4+} and significant quantities are measured up to N^{6+} and possibly N^{7+}, the fully-stripped charge state. Indeed, the addition of the Ioffe coils strongly affects the source's ability to strip the ions of their electrons.

Very little additional information is available for the INTEREM source (e.g. parameter dependences of CSD's, results for various gases, etc.) since it was dismantled in early 1976, shortly after the initial runs with N_2.

2.3. Multiple Stage Sources

INTEREM showed that minimum-B magnetic geometry successfully increases the average ionization state for multiply-charged ions. This magnetic configuration increases the $n_e \tau_i$ product to a range where fully-stripped light ions can be produced in measurable quantities. Another major problem exists, however, which limits the ultimate charge state

obtainable. Charge exchange becomes non-negligible as a loss mechanism with high-Z ions in a high pressure neutral background. This neutral background is required for initial breakdown of the gas by the ECR-heating microwaves. To solve this problem, a first stage preionizer was added to the ion source system. Plasma is created in the high pressure region in the preionizer with either a dc or rf discharge, typically at a pressure of 10^{-4} - 10^{-3} Torr. This stage is connected to the main ECR-heated plasma region by field lines which pass through a small aperture in the preionizer and extend to the mirror midplane. A low pressure is maintained in the main plasma region by differential pumping. Ions and electrons created in the preionizer, diffuse along a decreasing magnetic field into the ECR-heated region. There, the electrons are heated by ECRH and, since the base pressure outside the preionizer is kept at a minimum, the ions become multiply charged without loss due to charge exchange.

The first of these multiple stage sources was the Super Machine For Ion Stripping (SUPERMAFIOS) built in 1975 in the MAFIOS laboratory in Grenoble, France. This source contained a preionizer and also a minimum-B stabilizing hexapole magnet. Its heating powers were limited to 20 kW but it was found that charge state distributions were not significantly altered for microwave heating powers above 1 kW. Unfortunately, published charge state distribution data from SUPERMAFIOS do not exist for nitrogen for comparison to MAFIOS and INTEREM. Comparative xenon charge state distributions have been published and are shown in Table 2.3.[23] Observe that, as with INTEREM, the average charge state in SUPERMAFIOS is much higher than with MAFIOS. However, different from both MAFIOS and INTEREM, the lowest charge states are almost completely depopulated and there is a smooth tail toward the highest charge states. These characteristics are owed to low charge exchange rates made possible

Table 2.3. Charge State Distribution for Xenon in MAFIOS and SUPERMAFIOS

Species	Relative Concentration MAFIOS	Relative Concentration SUPERMAFIOS
Xe^{2+}	11. %	0.9 %
Xe^{4+}	13. %	4.0 %
Xe^{6+}	11. %	13. %
Xe^{8+}	9.0 %	16. %
Xe^{10+}	1.0 %	10. %
Xe^{12+}	0.2 %	5.0 %
Xe^{14+}	0.0 %	3.0 %
Xe^{16+}	0.0 %	1.5 %
Xe^{18+}	0.0 %	0.9 %

by use of the first stage preionizer. Higher base pressures increase charge exchange rates which preferentially depopulate the high ionization states and "fill in" the low ionization states. These characteristics are not exhibited by SUPERMAFIOS. Also, the $n_e \tau_i$ product for SUPERMAFIOS is estimated at 10^9 s/cm^3 compared to 10^7 s/cm^3 for MAFIOS. As discussed earlier, this brings the SUPERMAFIOS machine into the parameter regime where fully-stripped light ions and highly-stripped heavy ions can be obtained.

The ability of SUPERMAFIOS to create and extract Xe^{18+} ions was a significant breakthrough. Next, Geller suggested that the $n_e \tau_i$ product could be increased further by adding another magnetic mirror in tandem with the existing one. This resulted in the addition of a third stage to SUPERMAFIOS and TRIPLEMAFIOS was born. The only change was the addition of one more set of mirror coils, opposite the preionizer, which did not include a set of minimum-B stabilizing coils. Charge state distributions similar to those of Table 2.3 (SUPERMAFIOS) with a slightly higher average Z were observed. The major difference was that the current density of the extracted beam had increased ~10x from ~ 30 µA in SUPERMAFIOS to ~ 300 µA in TRIPLEMAFIOS.

2.4. Contemporary Sources

Since the experimentally-verified feasibility of high-charge, ion-beam extraction from ECR ion sources, many laboratories have built their own sources following the design of SUPERMAFIOS and TRIPLEMAFIOS. Design parameters change slightly from source to source but are all essentially the same. However, some innovations have been added to increase either performance or ease of operation. For example, the energy consumption of the magnetic coils of SUPERMAFIOS was prohibitive for many laboratories and design changes were effected to rectify this problem. In 1979-1980, ECREVIS was designed and built in Louvain-la-Neuve, Belgium utilizing superconducting instead of room temperature magnets.[24] This brought the energy requirements down from *3 MW* of SUPERMAFIOS to less than *1 kW*. In 1979, MICROMAFIOS was built whose hexapole field was produced by permanent magnets made of samarium cobalt (*SmCo5*).[25] This source, as its name implies, is a much scaled down version of SUPERMAFIOS, which, as a surprise to many, produced similar

charge state distributions (CSD) to SUPERMAFIOS. Since that time, MICROMAFIOS has been the standard for all ECR ion sources. Many have been built for use as injectors for already existing cyclotrons and others have been built for atomic physics research.

The chart below shows the evolution of ECR ion sources from the large, single-stage, non-stabilized, electromagnet sources to the smaller, MHD-stabilized, permanent or superconducting magnet sources. The reader is reminded that this is only a partial list and apologies are made for any omissions.

Electron cyclotron resonance ion sources have improved markedly since the early 1970's in both performance and ease of construction and operation. They have become the most dependable sources available, often operating continuously over many months. They yield the most reliable high-Z ion beams of any source and are in use on tens of cyclotrons around the world. They also yield high-Z beams for atomic physics and ion beam applications research. As the number of ECR ion sources grows, optimal designs will be developed through experience and understanding gained through research. ECR ion sources will continue to be the simplest, most reliable, most versatile, high-Z ion sources available and as understanding of these sources increases, the performance characteristics will continue to improve.
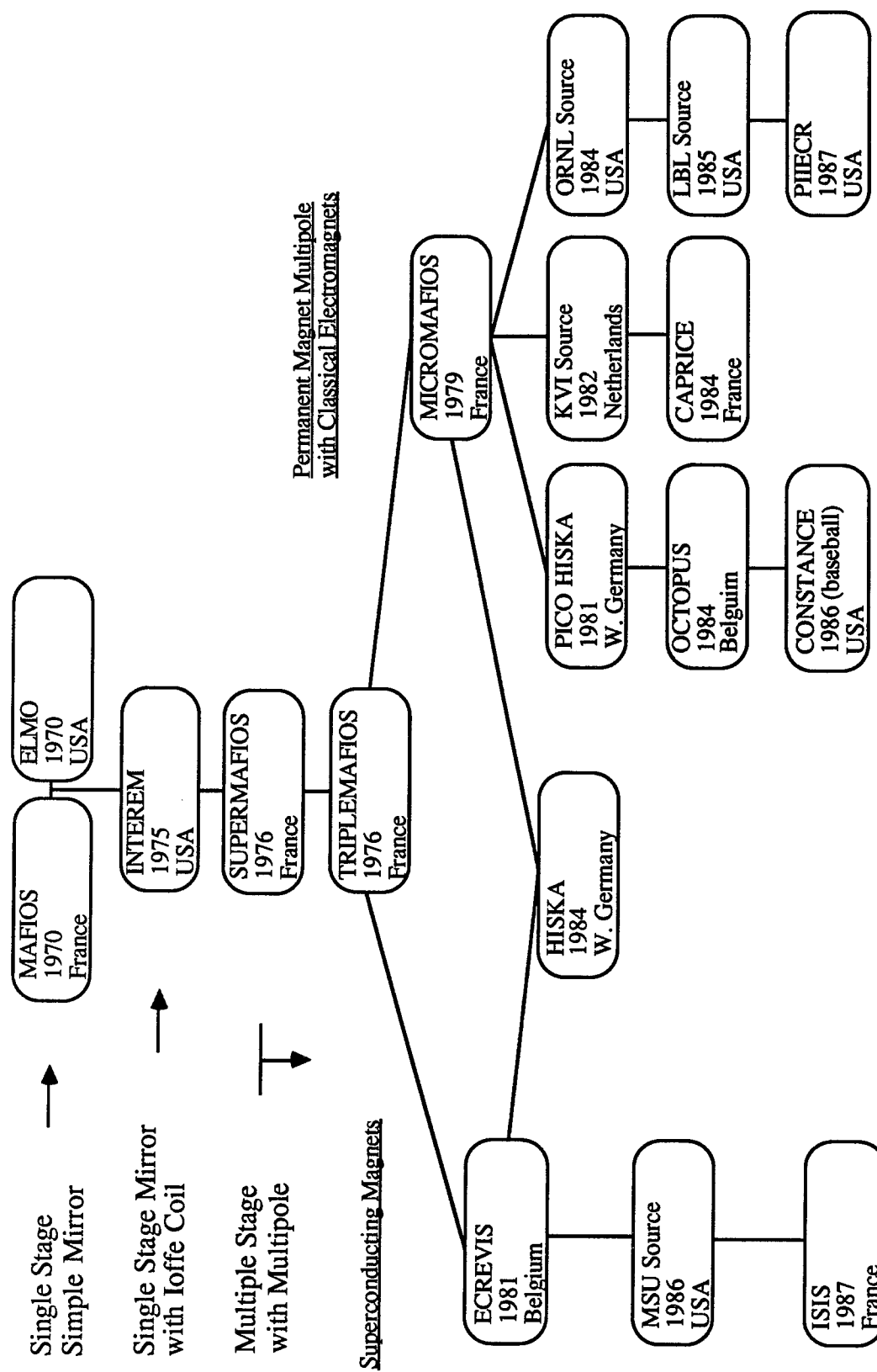
Figure 2.1. Development of ECR ion sources.

CHAPTER 3

EXPERIMENTAL CONFIGURATION

The Michigan Mirror Machine (MIMI) is a minimum-B stabilized magnetic mirror operated in the Plasma Experimental Bay at The University of Michigan. It has been used to study whistler-mode ECR heating and soft x-ray emission of mirror plasmas.[26-27] With the decline of interest in the mirror configuration as a viable fusion reactor design, emphasis for research on MIMI has shifted to more practical avenues. The inherent lossy nature of the mirror lends itself quite easily to the investigation presented here and the linear nature of the experiment allows for easy access of diagnostics to the midplane region along magnetic field lines. A description of the physical layout of the experiment is presented in this chapter as well as a description of the ECR heating and diagnostic systems. The computer-controlled timing system which triggers all of the scopes and diagnostics is also described.

3.1. Vacuum System and Magnetic Field Configuration

The standard magnetic mirror/quadrupole configuration for MIMI is shown in Fig. 3.1. The midplane region is composed of a *15 cm* diameter, *150 cm* long stainless-steel tube around which the mirror coils and quadrupole are placed. Two large tanks are located at either end of the tube and used for pumping, and diagnostic and ECR-heating access to the midplane. Pumping is performed by two turbomolecular pumps (Balzer's Model TPU 510 and Sargent-Welch Model 3106S), one located on each end tank. These

20
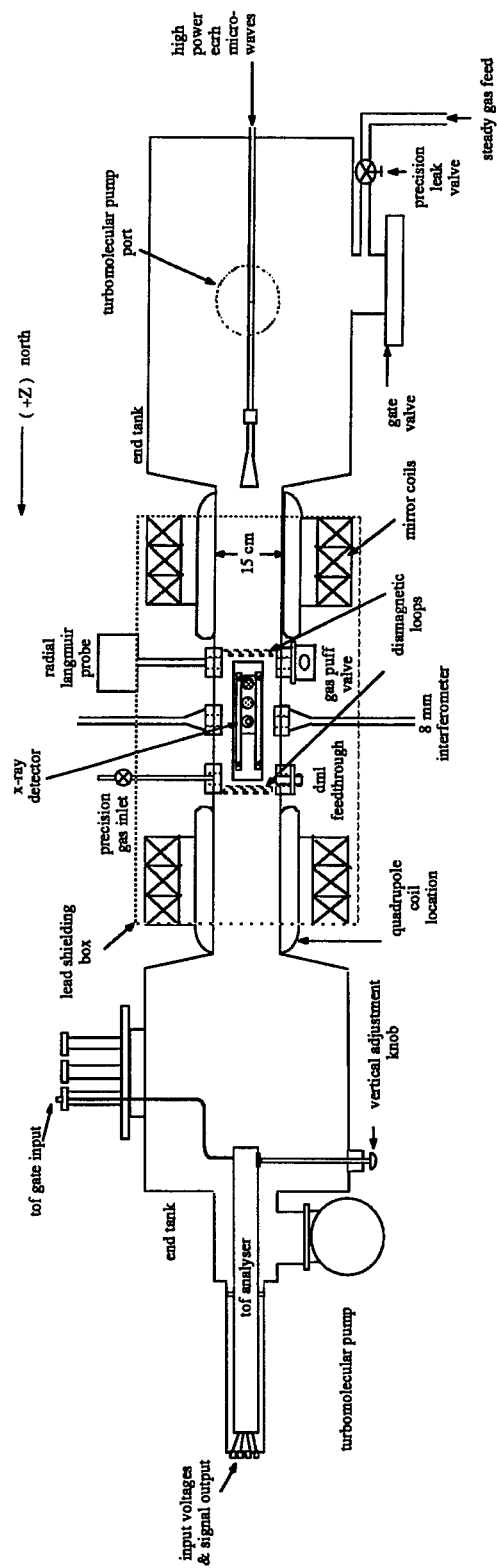
Figure 3.1. MIMI schematic including vacuum system, magnetic coils, ECRH feed, diagnostics, and shielding.

pumps are chosen to provide an oil-free, high-vacuum environment. They are exhausted to standard roughing pumps, fitted with foreline traps to prevent backstreaming. The combined pumping speed of the turbo pumps is *900 l/s*. Typical base pressures for the system after baking and discharge cleaning is *1 x 10^-7 T*.

The charged-particle confining magnetic field is created by two sets of solenoidal coils shown on either side of the midplane in Fig. 3.1. These are water-cooled electromagnets which create a midplane magnetic field of *2.94 G/A* with typical currents of *800 A* and therefore typical midplane magnetic fields of *2.4 kG*. These magnets have a mirror ratio, R_m, of *2:1*. Figure 3.2 shows the calculated, on-axis axial magnetic field as a function of mirror coil current. These values correspond, to within *5%*, to the fields measured using a standard Gauss meter. The magnetic field for which the plasma electrons are resonant with the microwave field is shown as a horizontal line at *2.66 kG*. The intersection of this line with the magnetic field curve for a particular coil current is the location of resonance on axis for that current. The figure illustrates that possible operating currents exist between *~500 A* and *~850 A* which allows for resonance locations between the mirror peak and midplane, respectively. Figure 3.3 represents a cross section of the midplane, in *z* and *r*, showing the magnetic field surfaces corresponding to the electron resonance zones for various mirror currents. The location of these zones on axis corresponds to the resonance locations shown in Fig. 3.2.

The quadrupole supplies the MHD-stabilizing, minimum-B magnetic field structure necessary for plasma stability. With the proper ratio of mirror-coil current to quadrupole current, resonant surfaces (such as the one shown in Fig. 3.3) can be created which close on themselves and do not intersect any wall or limiter. Such a surface is shown in Fig. 3.4. These closed mod-B surfaces are important to increase the available
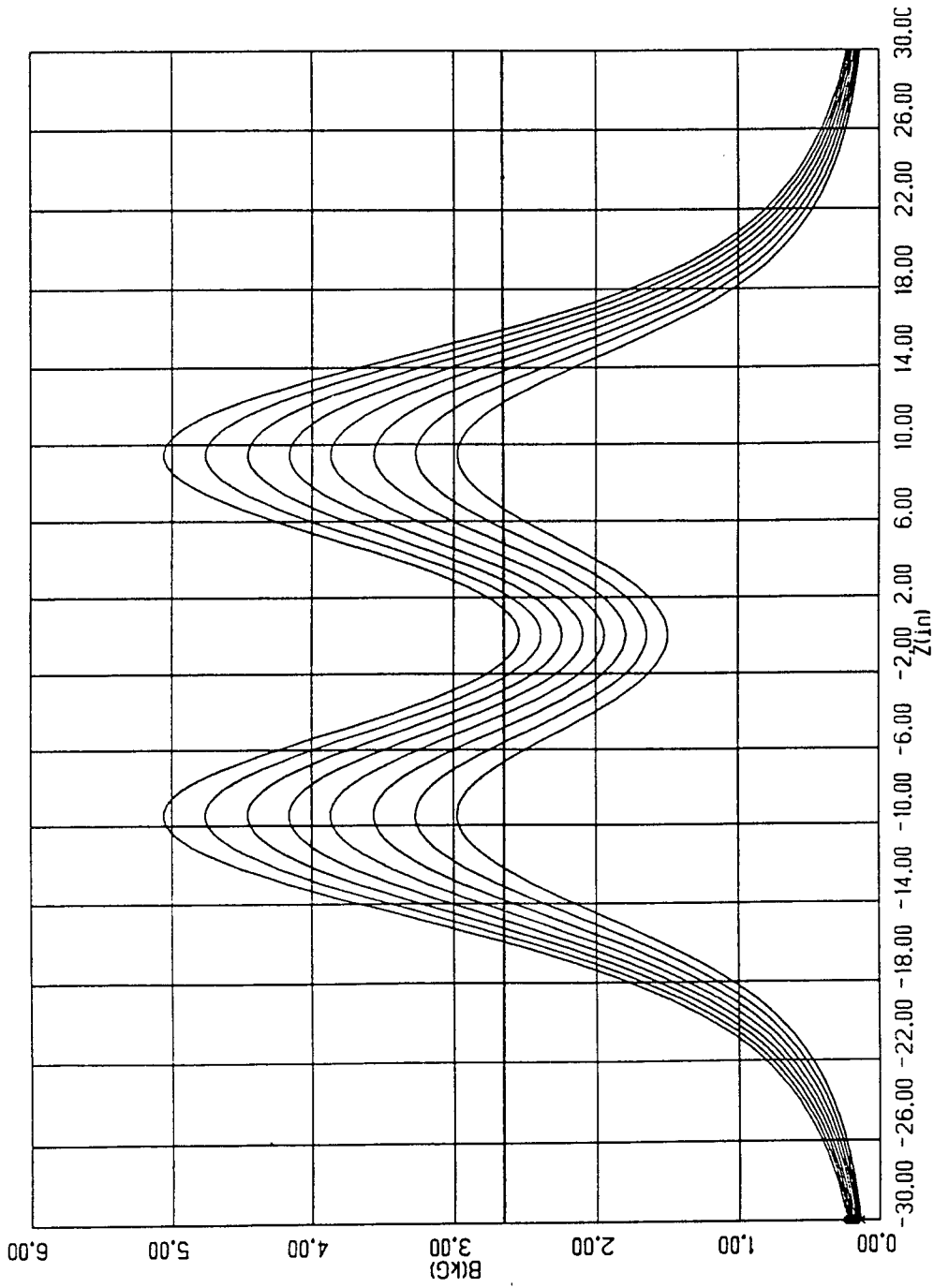
Figure 3.2. Calculated MIMI on-axis axial magnetic field. The magnetic field corresponding to the electron cyclotron resonance at the klystron heating frequency of 7.43 GHz is drawn at 2.66 kG. The intersection of this line and the magnetic field profile for a given coil current determines the location of the ECR resonance zones. The profiles shown correspond to coil currents, starting at the lowest field value, of 500, 550, 600, 650, 700, 750, 800 , 850 A.
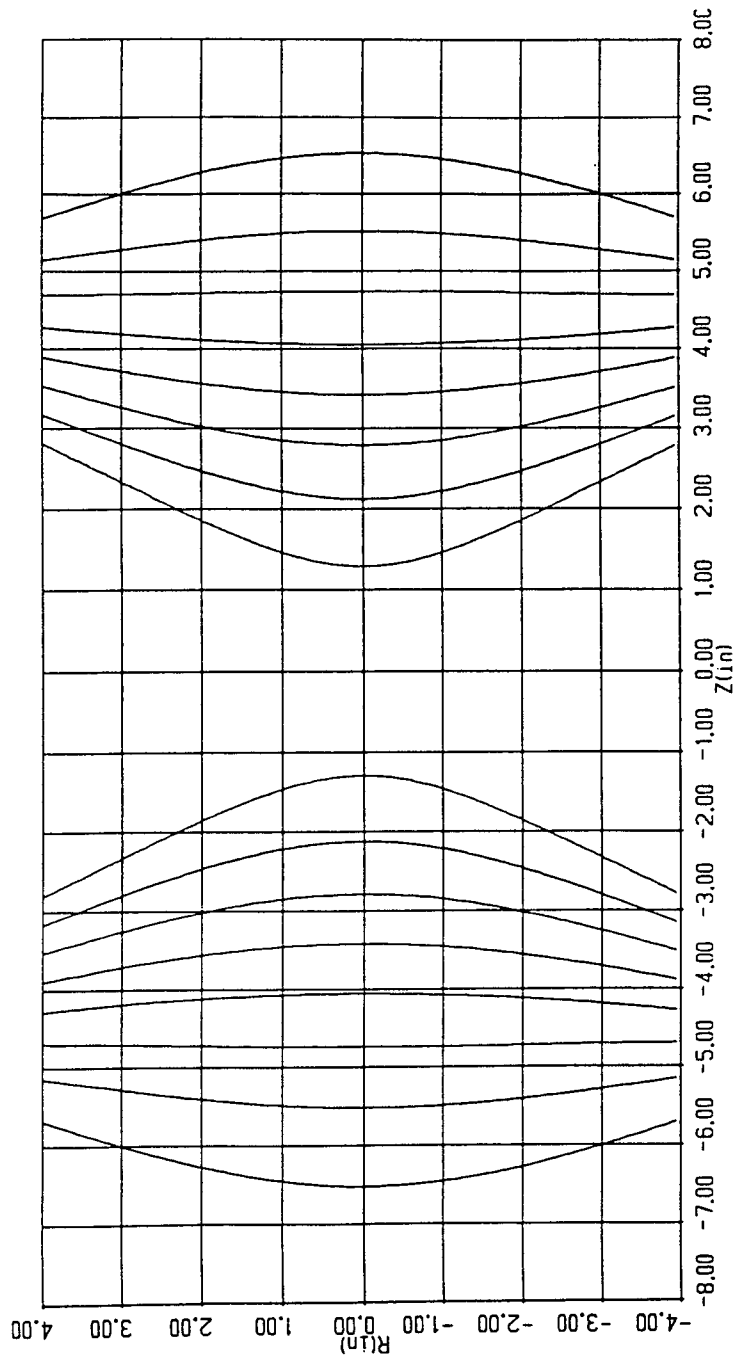
Figure 3.3. Resonant heating surfaces for MIMI operated as a simple mirror. The resonant surfaces correspond to a magnetic field of 2.66 kG. The surfaces shown exist for mirror coil currents, starting with the exterior profiles, of 500, 550, 600, 650, 700, 750, 800, 850 A. The vacuum vessel wall is located at a radius of 3 in.
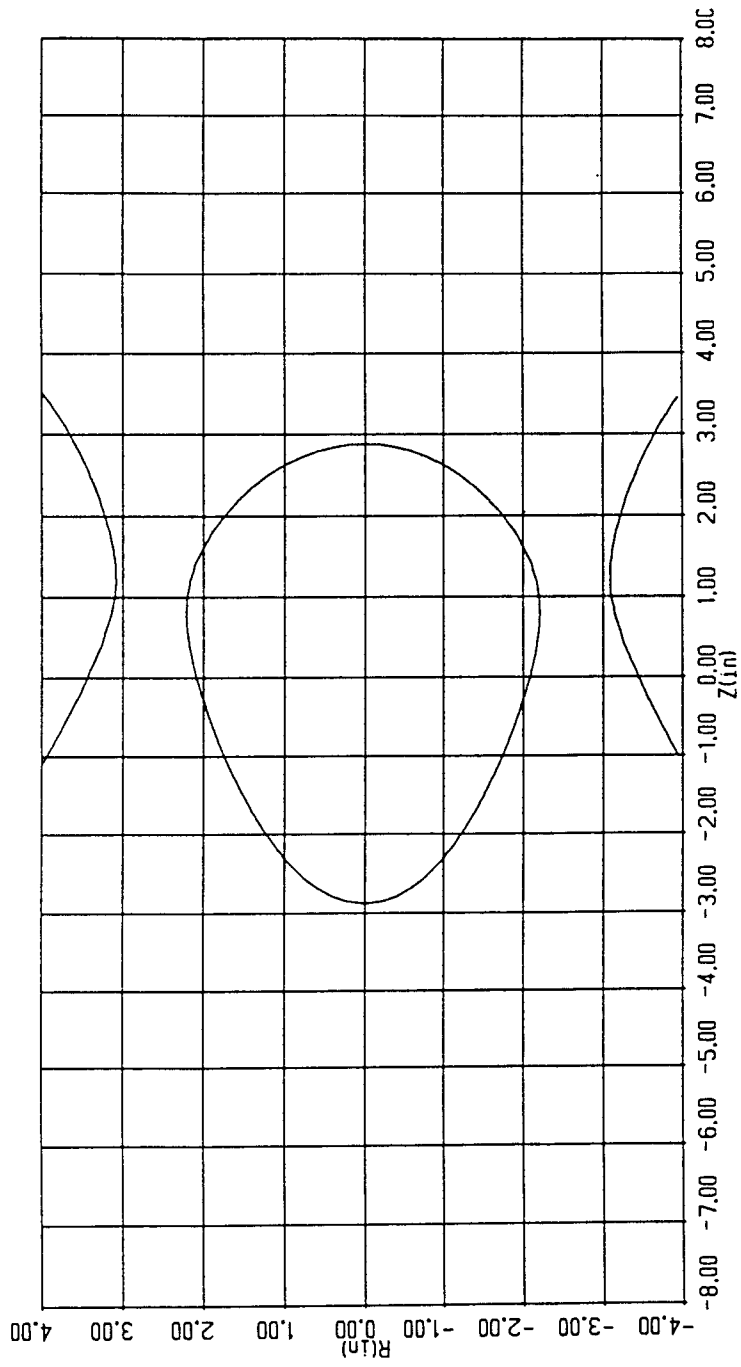
Figure 3.4. Resonant heating surface for MIMI operated as a minimum-B mirror. In this case, the heating surface is contained completely within the vacuum system, not intersecting any walls or limiters. This particular case corresponds to a mirror-to-quadrupole ratio of 750A/950A.

area where electron heating can occur and to keep heating zones away from the walls. Again, calculated and measured quadrupole magnetic field values agree to within five percent.

3.2. ECR Heating System

The electrons in the MIMI plasma are heated through electron cyclotron resonance heating (ECRH) with ~1 kW of 7.43 GHz microwave power. These high power microwaves are generated by a series of microwave oscillators and amplifiers. The entire heating system, including forward and reflected power detectors, is shown in Fig. 3.5.

The microwaves are generated by a Hewlett-Packard signal generator that outputs ~1 mW of microwave power at 7.43 GHz. This oscillator is run CW and its output is fed into the input of a Hewlett-Packard traveling-wave-tube (TWT) microwave amplifier. The microwaves are modulated at this stage. When the modulation input receives an "ON" signal (+3V), the amplifier outputs ~1 W for the mW input from the oscillator. When the modulation input switches to "OFF" (0 V), the output is attenuated by 20 dB. The width of the modulation "ON" pulse, generated at the controlling CAMAC crate, determines the length of the plasma. The output of the TWT amplifier is fed into a Varian klystron amplifier which has a gain of 30 dB, yielding 1 kW of output power. This power is carried by H-band waveguide, through a vacuum teflon window into the vacuum system and launched down-axis, ~25 cm from the midplane.

A bi-directional coupler is mounted on the high-power side of the klystron to monitor forward and reflected power. Calibrated crystal detectors on the forward and reflected power legs allows for monitoring of the power incident on the plasma and for assuring that the klystron reflected power limit of 100 W is not exceeded. A frequency
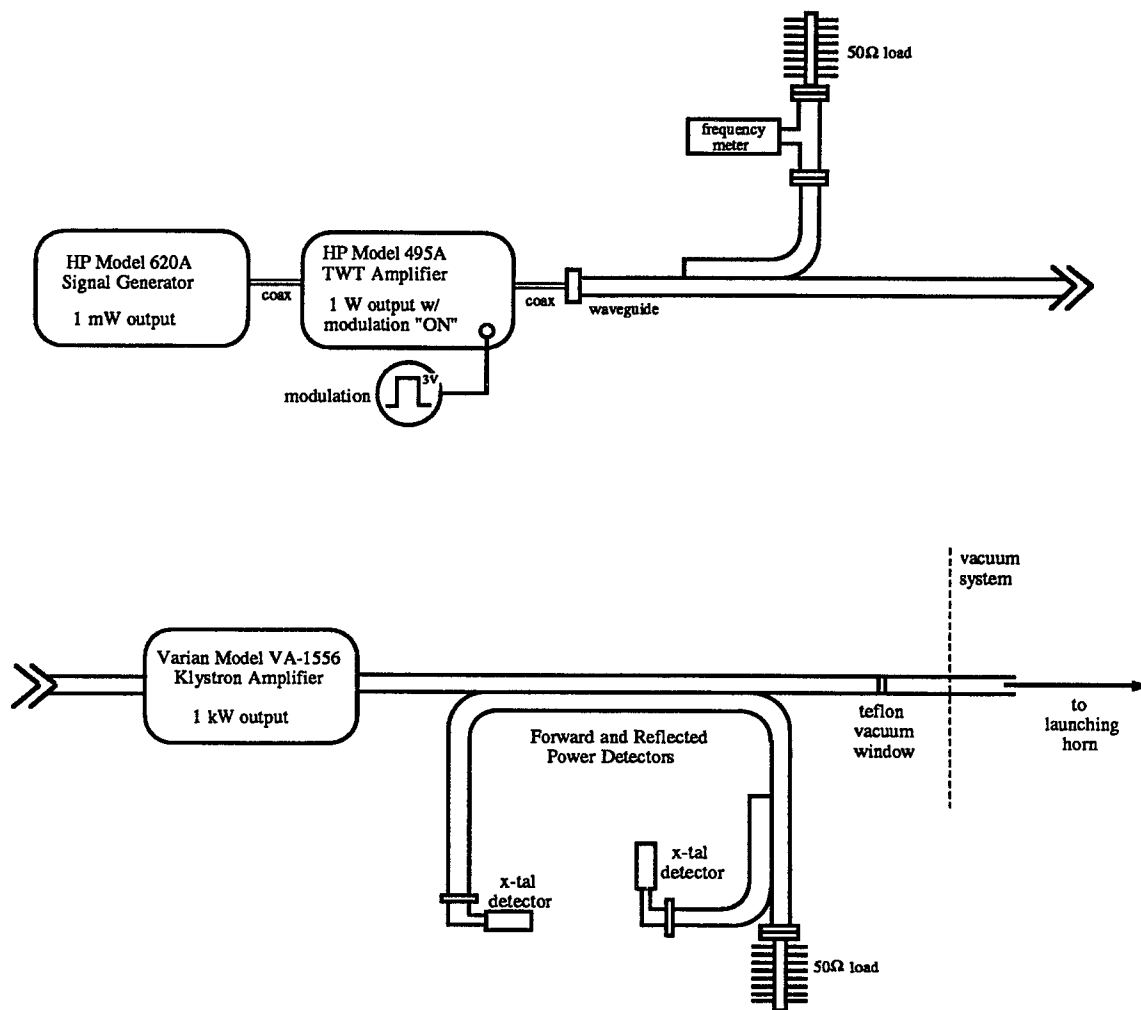
Figure 3.5. Microwave power system. The signal is generated by a Hewlett-Packard traveling wave tube amplifier with a gain of *30 dB* and a Varian klystron amplifier with a gain of *30 dB*. Final output power is typically *1 kW*. The signal is modulated at the TWT amplifier.

meter, located on the low power side of the klystron amplifier and terminated in a *50 Ω* load, enables exact measurement of microwave frequency. This is measured, rather precisely, to be *7.43 GHz*, determined by the frequency for which maximum power is achieved from the klystron.

The klystron is designed to be operated in CW mode with a supply voltage of *9.5 kV* at *0.7 A*. If it is operated as such, *6.7 kW* must be dissipated by the klystron cooling system. Since MIMI is a pulsed experiment, instead of operating the klystron in *CW* mode and modulating the input (from the HP TWT amplifier), the klystron is also pulsed, the beginning of the klystron pulse starting prior to the beginning of the TWT modulating pulse and the end of the klystron pulse occurring after the end of the TWT pulse. With this method, a low klystron duty cycle reduces cooling system requirements and increases tube life. A duty cycle as low as *3%* is achievable for pulse lengths of *50 ms*.

To switch the *9.5 kV* klystron supply voltage, a high voltage switch and high voltage switching circuit are required. The switch chosen is a *10 kV* Jennings vacuum relay and is shown in the circuits of Fig. 3.6. The switch is normally open and requires a *26 V* bias across the *290 Ω* relay coil resistance to close the switch. When the switch closes, the *9.5 kV* klystron supply voltage is applied to the klystron. The circuit of Fig. 3.6 (a) provides this *26 V* pulse, to the switch coil, for an input pulse of *3 V* supplied by the CAMAC controller. This *3 V* CAMAC controller pulse is of variable length and the klystron will receive the supply voltage for the entire width of the CAMAC pulse. The high voltage switching circuit is shown in Fig. 3.6 (b). Terminals 1 and 2 in Figs. (a) and (b) correspond to the two high voltage terminals of the vacuum relay. The *13.6 kΩ* resistance represents the klystron which draws *0.7 A* at *9.5 kV*. The *RC* series combination connected across the switch is included to reduce arcing while the switch is

(a)

(b)
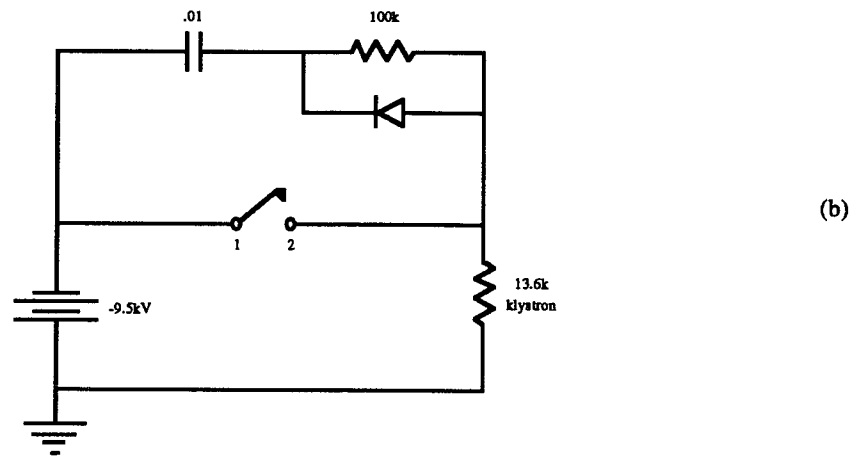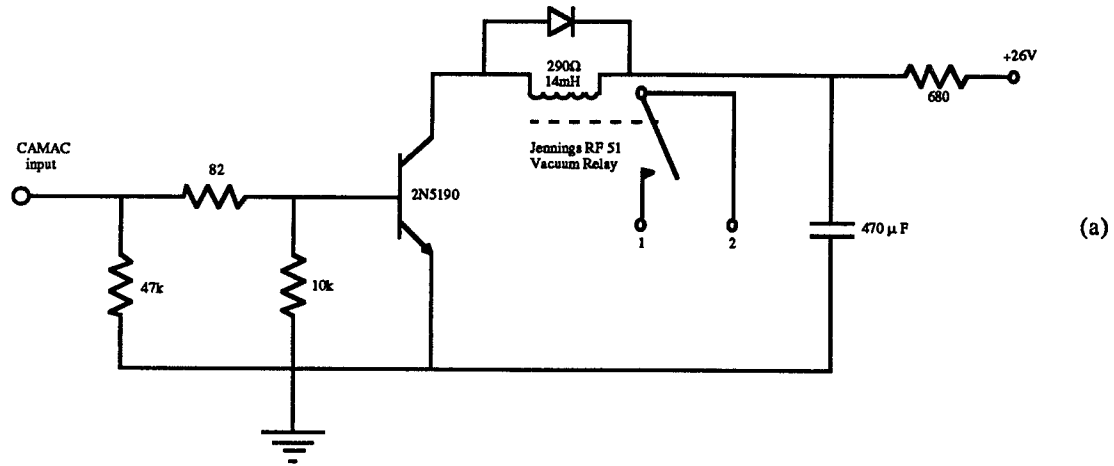
Figure 3.6. (a) Pulsing circuit for vacuum relay. This circuit requires a +3V input pulse to close the high voltage klystron relay. (b) High voltage klystron pulsing circuit. The klystron is simulated by the 13.6 kΩ resistance which draws .7 A at 9.5 kV. The RC series combination connected across the switch reduces arcing as the switch opens and the diode allows for fast charging of the capacitor after the switch has opened.

opening. This holds the voltage across the contacts of the switch low until the contacts

have had sufficient time to physically separate. The diode across the *100 kΩ* resistor

allows fast charging of capacitor C_1 after the switch has opened. This circuit has worked

quite well in switching the high klystron supply voltage allowing for a low klystron duty

cycle and low average klystron dissipated power.

A table of typical MIMI operating parameters is shown below in Table 3.1.

Table 3.1. Typical MIMI Operating Parameters

Parameter	Value
Pulse Length	10 - 100 ms
Max. Microwave Power	1.5 kW
Microwave Frequency	7.43 GHz
Electron Density	.7 - 2.0 x 10^{11} cm^{-3}
Electron Temperature	1-5 keV
Midplane Magnetic Field	
Mirror Coils	1.5 - 2.5 kG
Quadrupole Coils	0.0 - 1.1 kG
Mirror Ratio	2:1
Mirror Length	49 cm
Vessel Diameter	15 cm
Plasma Diameter	10 cm
Base Pressure	1.0 x 10^{-7} Torr
Pulse Rate	40/min

3.3. Standard Diagnostics

Several standard diagnostics have been constructed for use on MIMI. Since most

of these diagnostics are well known and widely used, only a brief description of each will

be presented here. The reader is referred to standard plasma diagnostic texts, such as

Ref. 28, for more detailed information about any specific diagnostic.

3.3.1. Diamagnetic Loop

Over the past three years, several diamagnetic loops (DML's) have been used on

MIMI. They all have different designs and different response characteristics but all

operate with the same principle. In a plasma, there is a balance of forces between plasma

pressure and the Lorentz force. This is described by the MHD fluid eqn.:

$$\nabla p = \nabla(nkT_e + nkT_i) = j \ x \ B \ , \tag{3.1}$$

assuming $n_i = n_e$. To determine the azimuthal current which must flow to counteract the

outward pressure force, the cross product of Eqn. 3.1 is taken with $\underline{B}$ and factored to:

$$j_\phi \ \hat{\phi} = \frac{B \ x \ j \ x \ B}{B^2} = \frac{B \ x \ \nabla p}{B^2} = (kT_e + kT_i) \frac{B \ x \ \nabla_r n}{B^2} \ . \tag{3.2}$$

This current is known as diamagnetic current and it is the time changing azimuthal

diamagnetic current to which the diamagnetic loops respond. As the plasma density

increases at the beginning of the plasma pulse, the diamagnetic current, j_ϕ, increases.

This decreases the magnetic field in the plasma which decreases the magnetic flux through

the diamagnetic loop which surrounds the plasma. An emf is thereby induced in the loop

proportional to dj_ϕ/dt. Integrating this signal will therefore yield a measure of the diamagnetic current at any time during the plasma pulse and given a model for the radial density distribution, a value of n_okT_e can be obtained (no ion heating).

The actual processing of the raw DML signal is somewhat more complex than that described above since the plasma and DML's are coupled to the vacuum vessel, through which eddy currents can flow. The effects of these eddy currents are compensated for using a method described in Ref. 29. The loops are calibrated using a test coil, placed inside the loops in the vacuum vessel, whose current paths are wrapped in the shape of the expected diamagnetic current. A known current is pulsed into the test coil and the output from the integrating/compensation circuit is measured. This measurement is then converted to n_okT_e/V, after Ref. 29, and used to measure the density-temperature product for the plasma. One of the several loops used in MIMI is shown in Fig. 3.7. Total turns number 1500 and the final calibration is 1.0×10^{14} eV/cm^3-V with typical 1 V signals.

3.3.2. Microwave Interferometer

A plasma, as a dispersive medium, allows for easy measurement of electron density utilizing its variation of the index of refraction with density. The index of refraction for a plasma is defined as:

$$\eta = \frac{c\ k}{\omega} \ ,$$

(3.3)

where ω and k obey the dispersion relation:

Figure 3.7. Diamagnetic loop design. 750 turns of twenty-eight guage wire is wrapped in the circular groove shown in each of the two loops. The cross bars are included in the design for support. The entire structure is placed inside the vacuum vessel, centered on the midplane.

$$\omega^2 = \omega_p^2 + c^2 k^2 \qquad\qquad (3.4)$$

where $\qquad \omega_p^2 = \dfrac{ne^2}{\varepsilon_o m}$.

If a beam of microwaves propagates through a plasma of sufficient density, its wavelength will necessarily increase. This change in wavelength during the time that the microwaves are propagating through the plasma, manifests itself in a phase shift relative to its phase if the plasma had not been present. This measure of phase shift can be used to calculate ω_p and, therefore, n_e.

The MIMI microwave interferometer density measurement system is shown in Fig. 3.8. The microwaves are generated by a *35 GHz* Gunn diode and split into a reference and plasma leg. The microwaves in the plasma leg, after passing through a phase shifter, propagate across the MIMI vacuum vessel with the series of horns and Fresnel lenses shown. This is "mixed" with the signal from the reference leg with a "magic tee". The outputs of the magic tee are proportional to the square of the sum and difference of the inputs. These outputs are fed into a differential amplifier which yields the final signal:[29]

$$V_{diff\,amp} = V_{magic\,tee\,1} - V_{magic\,tee\,2} = V_{offset} + \Delta V \sin(\Delta\Theta) \qquad (3.5)$$

where $\quad V_{offset} = \dfrac{V_{ref}^2 + V_{plasma}^2}{2} \left(\alpha_1^2 - \alpha_2^2 \right) \quad$ and

$$\Delta V = 2V_{ref}^2 V_{plasma}^2 \left(\alpha_1^2 + \alpha_2^2 \right) .$$
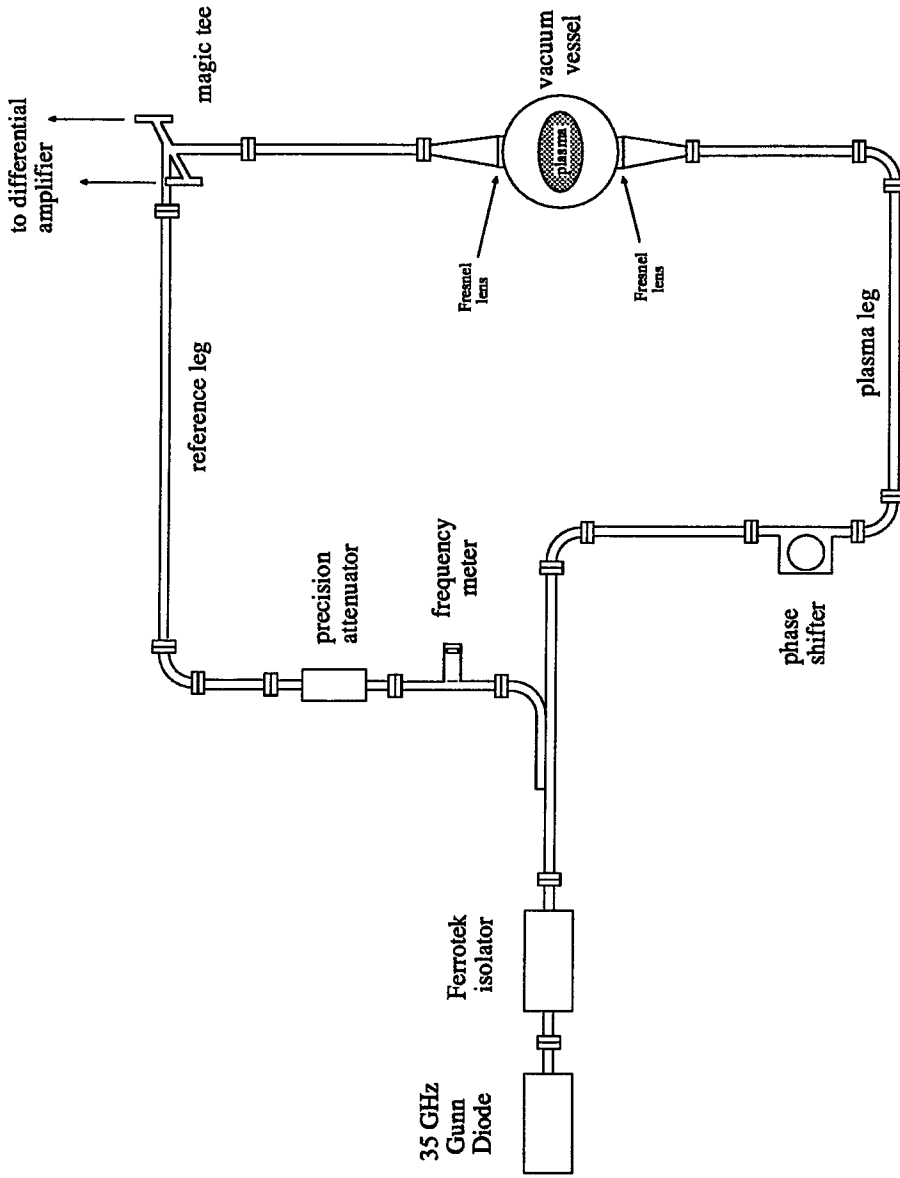
Figure 3.8. Microwave interferometer system. Change in plasma microwave wavelength allows for measurement of electron density.

Here, V_{ref} and V_{plasma} are the magic tee input microwave amplitudes for the reference and plasma leg respectively, and α_1 and α_2 are proportionality constants relating to the diode sensitivities in each of the two inputs to the magic tee.

Equation 3.5 shows the output of the differential amplifier is proportional to the sine of the phase difference between the plasma and reference leg, $sin(\Delta\Theta)$. The phase shifter in the plasma leg is adjusted so that $sin(\Delta\Theta) = 0$ in the absence of plasma. $\Delta\Theta$, with the plasma present, can then be calculated from measurement after Eqn. 3.5. This can then be used to calculate line integrated electron density as:[29]

$$\frac{1}{L}\int_0^L n(x)\,dx = 118\frac{(\Delta\Theta)(f)}{L}\quad cm^{-3}$$

(3.6)

with $\Delta\Theta$ in radians and f in Hertz. Usually the microwave frequency is chosen sufficiently high so that $sin(\Delta\Theta) \sim \Delta\Theta$ and the signal is proportional to line integrated density.

3.3.3. X-Ray Detectors

Several types of x-ray detectors have been implemented on MIMI. These include an NE102 scintillator-light pipe-PMT x-ray detector, P-I-N diode x-ray detector (shown in Fig. 3.1), and Schotky diode x-ray detector. Each detector has sensitivity in a different visible light – x-ray range and is used to measure Bremsstrahlung x-ray emission in MIMI. X-ray emission measurements are not closely related to the topic of this dissertation and therefore will not be discussed further here. A complete description of these diagnostics can be found in Ref. 30.

3.3.4. Langmuir Probe

Electrostatic probes have been used extensively to measure a wide variety of plasma parameters in many plasma devices. Their simplicity and ease of construction make them the ideal choice for a diagnostic on a simple plasma system. Such parameters as electron and ion temperatures, electron and ion densities, plasma and floating potentials can be determined from a single set of i-v measurements. Analysis becomes much more complex and quantitative results much more unreliable when the probe is inserted into an anisotropic electron velocity distribution and a moderate magnetic field, such as found in MIMI. Theoretical analysis of probe response under these conditions is quite involved and will not be dealt with here. Instead, the reader is referred to Refs. 29, 31, and 32 and references contained therein.

The Langmuir probe shown in Fig. 3.1 consists of a tungsten wire shielded with two stainless steel shields and insulated from each other and the plasma with thin ceramic tubing. A detailed schematic of the probe is shown in Fig. 3.9. The stainless steel shields serve both to increase the bandwidth of the probe and to act as an rf shield to shield the tungsten center conductor from plasma noise and oscillations. The center conductor extends into the plasma *1 cm* from the probe tip and is oriented parallel to the magnetic axis. This *1 cm* section is the particle collecting portion of the probe. All other parts visible to the plasma are covered with insulating ceramic. The probe is inserted radially from one of the top circular ports near the midplane of MIMI.

Since little reliable theory exists for Langmuir probe signals for the conditions present in MIMI, the radial Langmuir probe (RLP) is used to obtain qualitative measurements of floating potentials, and therefore space potentials given large magnetic fields[29]. As discussed in chapter 6, the Langmuir probe is used to indicate increasing ion

to oscilloscope

radial position control

radial position control

vacuum O-ring seal

stainless steel shield ————
ceramic insulator ▬▬▬▬
tungsten center conductor ══════

Torr-Seal
vacuum seal

1-cm probe tip
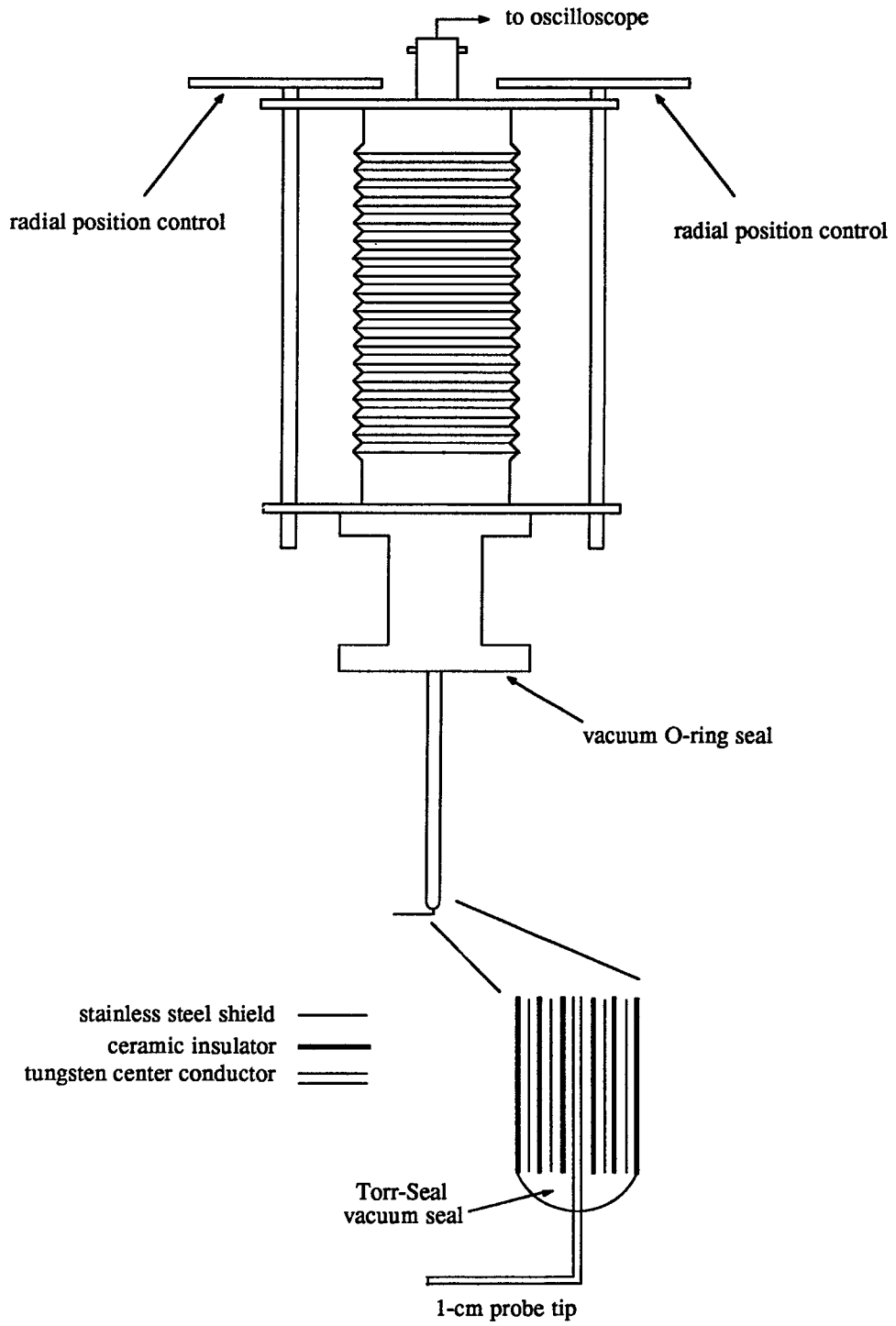
Figure 3.9. Langmuir probe schematic. The probe is inserted radially from a circular port near the midplane.

temperature with ICRH by monitoring the RLP ion saturation current as ICRH is implemented. Also, MHD unstable behavior will be reflected in the RLP signals, due to rapid variations in the plasma potential, and is therefore a good diagnostic to qualitatively determine plasma conditions and operating parameters for MHD stability.

3.4. Time-of-Flight Spectrometer

3.4.1. Options

It became necessary to design and construct a diagnostic which is capable of measuring the distribution of ion species flowing from the midplane region. There are several options available. The first is a standard magnetic spectrometer. In this type of spectrometer, a beam of ions composed of several m/q species enters a region of constant magnetic field with $B \perp v$. The particles undergo a Lorentz acceleration inversely proportional to their m/q ratios, $a = q/m \, (v \, x \, B)$. This acceleration forces the particles to bend in the arc of a circle. The radius of curvature of high m/q ions is larger than that of low m/q ions. This has the effect of separating ions with differing m/q values which can then be detected using conventional ion detectors. Figure 3.10 illustrates the principles of this spectrometer.

Though this detector type is frequently used, there are several drawbacks. To detect all ion species in a beam, either a series of detectors must be placed at the exit aperture or the magnetic field must be swept so all ions eventually find their way into a single detector. Either method is difficult to use. One would need an array of at least several hundred detectors to achieve acceptable spectrum resolution. Such a

ion beam

electromagnet

$\odot$

$\underline{B}$

path 1

path 2

path 3

$\odot$

$\underline{B}$

$(m/q)_1 < (m/q)_2 < (m/q)_3$

ion detectors
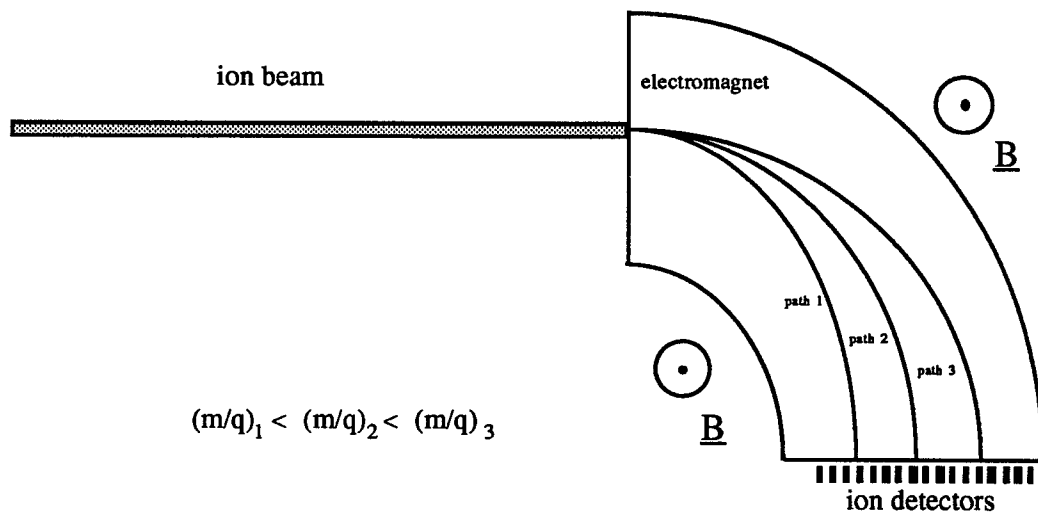
Figure 3.10. M/Q separation in a magnetic spectrometer.

multi-component system would be expensive and difficult to implement. If the magnetic field were swept, electromagnets would be required as well as high-current, vacuum feedthroughs and a fast sweeping circuit. Another difficulty lies in the fact that the magnetic field of the mirror coils extends a large distance from the midplane. A field of ~100 G exists in the pumping tanks of MIMI. This is a sufficiently large field to significantly perturb the orbits of the ions in the spectrometer. Therefore, magnetic shielding must be included in the design of such a spectrometer. This increases the physical size and complexity of the device.

Another, more viable option for an m/q-sensitive spectrometer is a Wein spectrometer. In this device, ions are accelerated through a large potential, V_O, before they enter a region with crossed electric and magnetic fields. The ions experience forces in this region from both the electric and magnetic fields. The fields are oriented so that the force from the electric field,

$$F_E = m_i a = qE , \qquad (3.7)$$

and the force from the magnetic field,

$$F_B = m_i a = qv \times B = q\sqrt{\frac{2qV_0}{m_i}} \; \hat{z} \times B , \qquad (3.8)$$

oppose each other. Note that the magnetic field force is m/q dependent. If an ion possesses an m/q such that the two forces are equal in magnitude, it feels zero net force and passes through the spectrometer undeflected. An ion detector placed at the exit aperture of the spectrometer would then detect that specific m/q species. All others would

be deflected to one side of the exit aperture or the other. See Fig. 3.11. To measure a spectrum, the electric or magnetic field must be swept. This is easier than in the case of the magnetic spectrometer since the magnetic field can remain constant and the electric field, created by biased parallel plates, can be swept. However, the spectrometer must also be shielded from the external mirror magnetic field so as not to perturb the necessarily constant magnetic field of the Wein spectrometer. A perturbing of the magnetic field would result in a loss of resolution. This need for a constant unperturbed magnetic field again makes this type of spectrometer difficult to construct and implement.

The third design, and the one which ultimately was chosen, utilizes the time-of-flight principle. In this case, a packet of ions, comprised of different m/q species, impinges on the acceleration region of the linear spectrometer. When the packet enters this region, it is accelerated due to the high electric field in the region. This acceleration occurs over a very short distance and is different for different mass-to-charge ratio ions. Ions with high m/q experience lower acceleration than do ions with low m/q. See Eqn. 3.7. After the ions have passed through the acceleration region, they pass into a field-free region. Here, high m/q ions will have a lower velocity than low m/q ions. The ions drift ballistically down this field-free region, separating axially according to their velocity, the faster ions arriving at the ion detector at the far end first. See Fig. 3.12. The output of the ion detector is then displayed on an oscilloscope and if the drifting distance is long enough to separate the species in space, the scope trace will then yield a time-resolved "picture" of the subpackets of each separate m/q species. The area under each peak will reflect the current density of each species in the original ion packet. Time-of-flight spectrometers have been used successfully to measure ion species present in various

$(m/q)_1$ < $(m/q)_2$ < $(m/q)_3$

B ⊙   E   ⊙   E   ⊙

accelerated ion

path 3

beam

⊙   ⊙   ⊙ B

path 2

ion detector

path 1
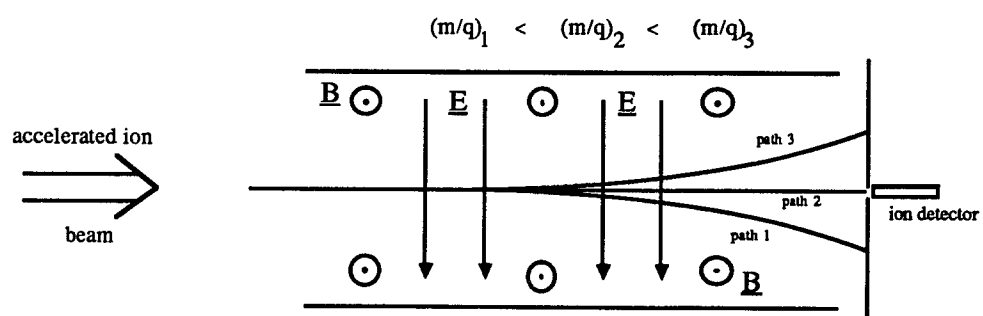
Figure 3.11. M/Q separation in a Wein spectrometer.
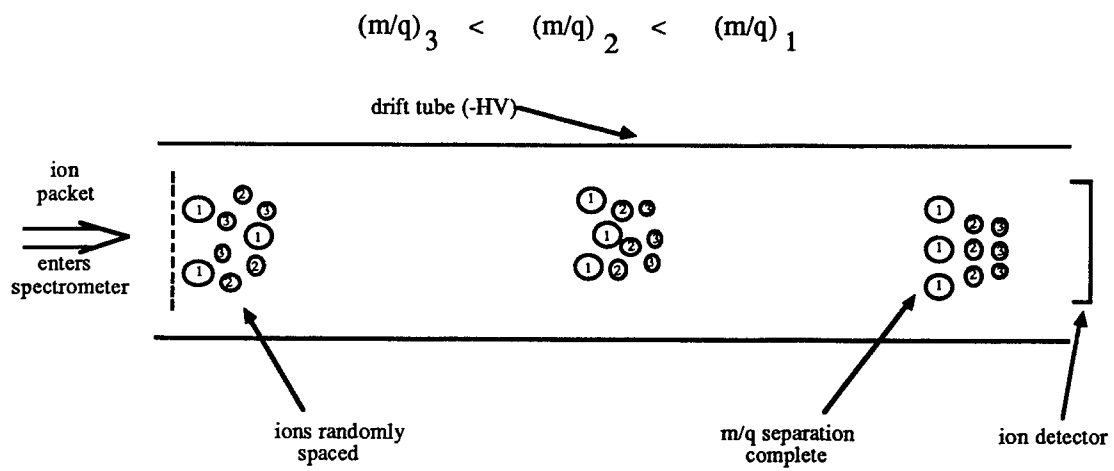
Figure 3.12. M/Q separation in a time-of-flight spectrometer.

plasma devices.[33-37]

There are several advantages to this type of spectrometer. First is the electrostatic nature of the device. No external magnetic field is required and the spectrometer is insensitive to fringing fields from the mirror electromagnets. All ion motion is parallel to the fringing magnetic field and is therefore unaffected. Also, an entire spectrum requires only tens of microseconds to collect which allows for temporal measurements of ion charge state distributions. It is a linear device, unlike either the magnetic or Wein spectrometers, and fits into a *10 cm* diameter, *1.5 m* long extension of the vacuum system. Only one ion detector is required and an entire spectrum can be obtained without sweeping any fields. No high-current, vacuum feedthroughs are necessary since all parts of the spectrometer are merely biased at correct dc bias values. Other advantages of a TOF spectrometer include ease of construction and ability to use vacuum-compatible materials for all components. These are the reasons for which a time-of-flight spectrometer is chosen to measure the distribution of ion species present in MIMI plasmas.

3.4.2. Initial Design

The initial design of the spectrometer is shown in Fig. 3.13. Three major areas of interest are the entrance region, the focusing region, and the collecting region. The entrance region serves to collimate and gate the beam of ions. As mentioned earlier, the TOF spectrometer accelerates a small packet of ions of varying m/q species. This small packet of ions is selected from the continuous stream of ions and electrons, originating in the midplane region, by the gating and acceleration grids. Figure 3.13 shows the potential on axis of the spectrometer. The gating grid is biased at a positive dc voltage, and the high voltage drift tube and acceleration grid are biased at a large negative voltage.
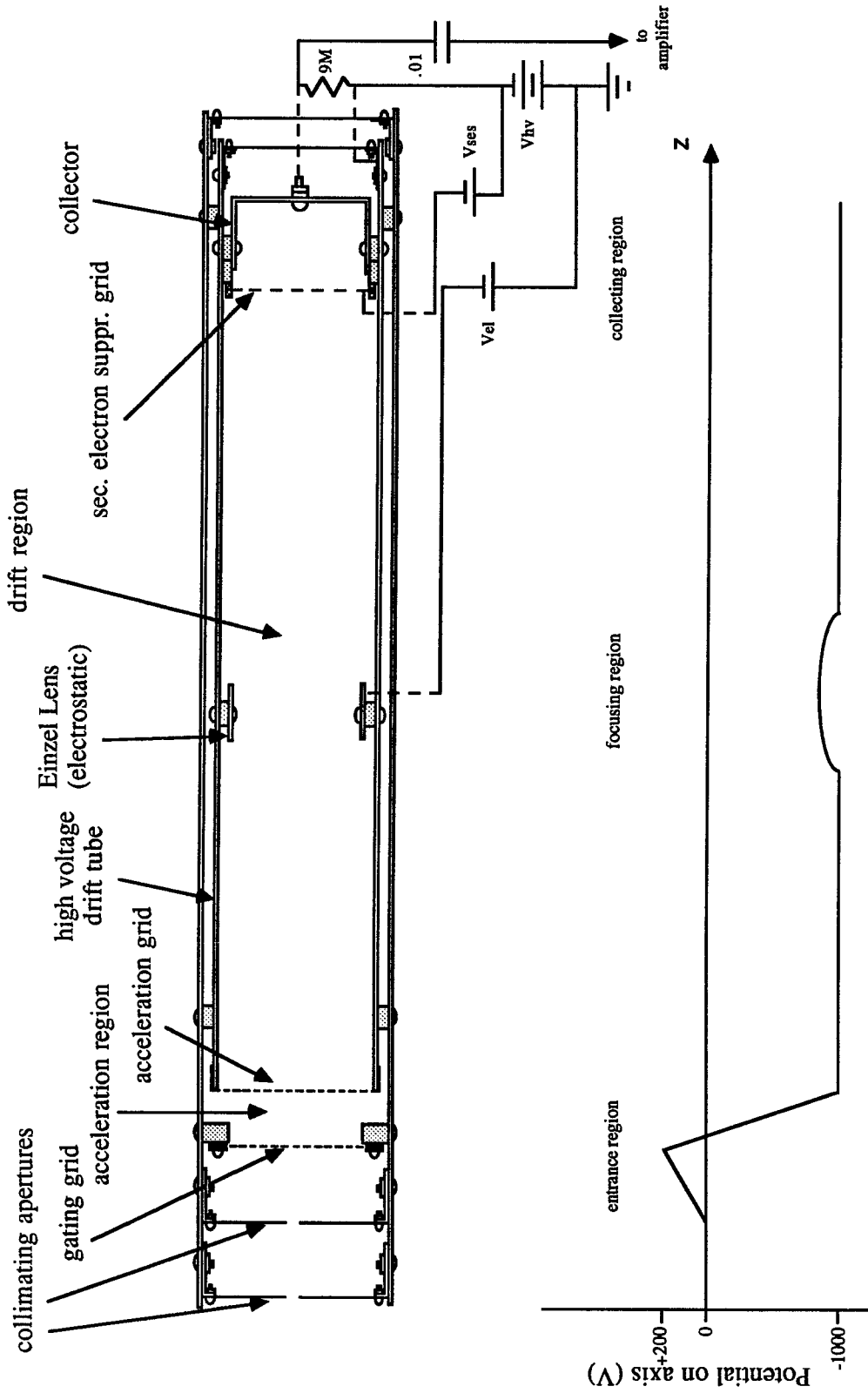
Figure 3.13. Time-of-flight spectrometer initial design.

As the plasma impinges on the spectrometer aperture, ions are repelled by the gating grid since they arrive only with energy $E_{ion} = E_p + E_t$ where $E_p = qV_{plasma}$ and $E_t = ion$ *thermal energy*. This energy seldom exceeds $200q_{ion}$ eV. Low-energy electrons are repelled by the acceleration grid, though high-energy electrons with $E_{//} > q_e V_{acc}$ eV can penetrate the high voltage drift tube. The spectrometer is not magnetically shielded and as a result a non-zero magnetic field exists in the drift tube. The spectrometer is tilted sightly with respect to the magnetic axis and this magnetic field is used to guide these high-energy electrons away from the collector at the far end of the drift tube.

If these were the only biases placed on the spectrometer components, no signal would be measured at the collector. When a charge state distribution is desired, a fast, negative pulse typically of *200 V* height, *50 - 400 ns* width and *20 ns* rise time is applied to the gating grid, superimposed on the *+200 V* dc bias. This pulse drives the gating grid voltage to zero and thus provides a brief window in time during which the ions can pass into the spectrometer unimpeded. As described earlier, this short burst of ions is then accelerated as it passes through the acceleration region, and as it drifts the length of the drift tube separates axially since $v \propto (q/m)^{1/2}$. The bias and pulse circuit for the gating grid is shown in Fig. 3.14.

Concern arose as to the problem of space charge expansion of the beam. The ion packet, after acceleration can be considered a beam of ions of length:

$$L = \Delta t \sqrt{\frac{2q_i}{m_i} (V_p + V_{acc})} \tag{3.9}$$

where Δt = *width of gating pulse*
V_p = *plasma potential*
V_{acc} = *acceleration voltage*
m/q = *constant (i.e. single species beam)*.

to gating grid

.08 μF

Velonex
pulser

50 Ω

100kΩ

1kΩ

V_g
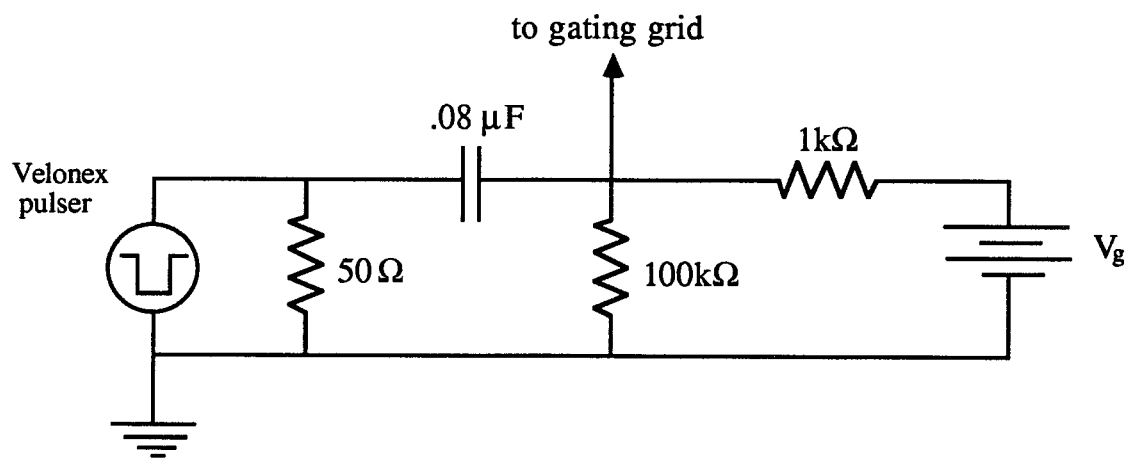
Figure 3.14. Bias and pulse circuit for gating grid.

Sufficient current densities are expected to cause expansion of the beam. If the beam, whose diameter is originally limited to the diameter of the small entrance aperture, expands to a diameter larger than the detector at the opposite end, a portion of the beam will be lost.

The radial expansion of the beam is calculated using a method developed by J. Osher.[38] Universal beam envelope curves are shown in Fig. 3.15 plotted as a function of $K_1(z/r_o)$ for cylindrical beams, $(1/2K_1)(dr/dz)$ for cylindrical beam slopes and $K_2(z/r_o)$ for a sheet beam. Here,

$$K_1 = 570 \cdot \sqrt{\left(\frac{M}{Q}\right)^{1/2} \frac{I(A)}{V_{acc}^{3/2}(V)}} \,, \tag{3.10}$$

$$K_2 = 717 \cdot \sqrt{\left(\frac{M}{Q}\right)^{1/2} \frac{I(A)}{V_{acc}^{3/2}(V)}} \,. \tag{3.11}$$

Using typical parameters for the spectrometer and assuming a pure beam of Ar^{1+} ions, the required values are: $z = 1.\, m$, $r_o = .159\ cm.$, $M/Q = 40$, $V_{acc} = 1000\ V$. Also currents measured directly behind the entrance aperture using a Faraday cup show currents can reach as high as *200 nA* for argon. Therefore, using the cylindrical beam model, $K_1 z/r_o = 2.27$. From Fig. 3.15 we see that this corresponds to a radial expansion of the beam of ~6x. This would result in unacceptable losses and therefore a focusing lens is included in the TOF design.

An electrostatic Einzel lens is chosen for simplicity. It consists merely of a *3.8 cm* long tube fitted inside and one-half the distance down the length of the high voltage drift tube. See Fig. 3.13. The lens is an approximation to a standard Einzel lens which
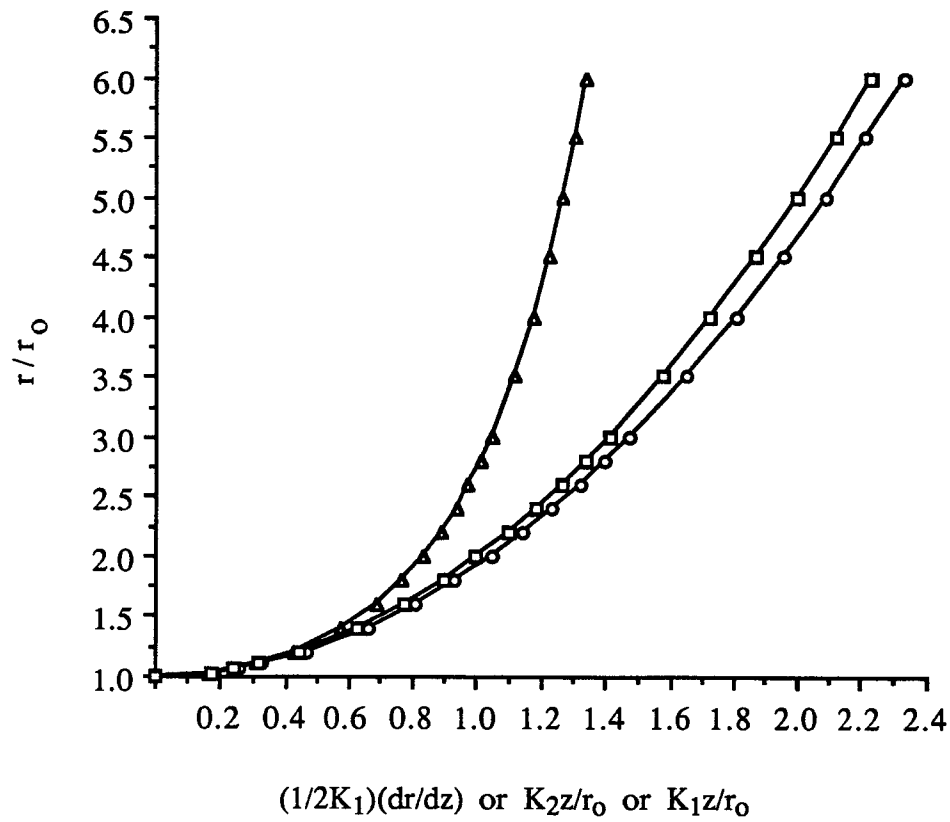
Figure 3.15. Universal beam envelope curves for r/r_o vs. $(1/2K_1)(dr/dz)$ for (Δ) cylindrical beam slope, K_2z/r_o for ($\Box$) sheet beam, and K_1z/r_o for (o) cylindrical beam.

consists of three parallel planar electrodes with apertures which lie on the beam axis. The center electrode is biased positive with respect to the outer two electrodes for ion focusing and typically has non-negligible thickness. The outer electrodes usually are thin. However, experiments have shown that the influence of the thickness of the outer electrodes on the distribution of potentials on axis is negligible.[39] Therefore, the high voltage tube is used to approximate the outer electrodes and the central electrode is biased positive with respect to it. The lens creates a potential structure inside the normally field-free region which focuses the ion beam to the axis of the spectrometer. If the bias voltage is chosen correctly, the focal length of the lens equals the distance to the ion detector and all of the beam is collected. This configuration requires only one additional power supply. The axial position of the lens is chosen to decrease the voltage requirements for the lens. If the lens were located near the entrance aperture, a small $\Delta V = V_{acc} - V_{lens}$ would be required for focusing. This would necessitate a large V_{lens}. As the lens is moved down the drift tube, a greater potential difference between the drift tube and the lens is required for focusing thereby decreasing the required lens voltage. At $z_{lens} = (1/2)L_{tube}$, the beam will not have excessively defocused and the voltage requirements for the lens power supply will be acceptable.

To assure that the lens will be effective in focusing an ion beam, the spectrometer is modeled using a particle trajectory code developed by W. Herrmannsfeldt.[40] Important results are shown in Fig. 3.16. In these figures, single ion trajectories are calculated from the point at which they enter the drift tube to the opposite end of the spectrometer. The cylindrical axis of symmetry lies along the z axis and the ion detector is located in the bottom, right corner of the boundary. The magnetic field is also included in the calculation and is plotted as the curved line on the figure. The ions
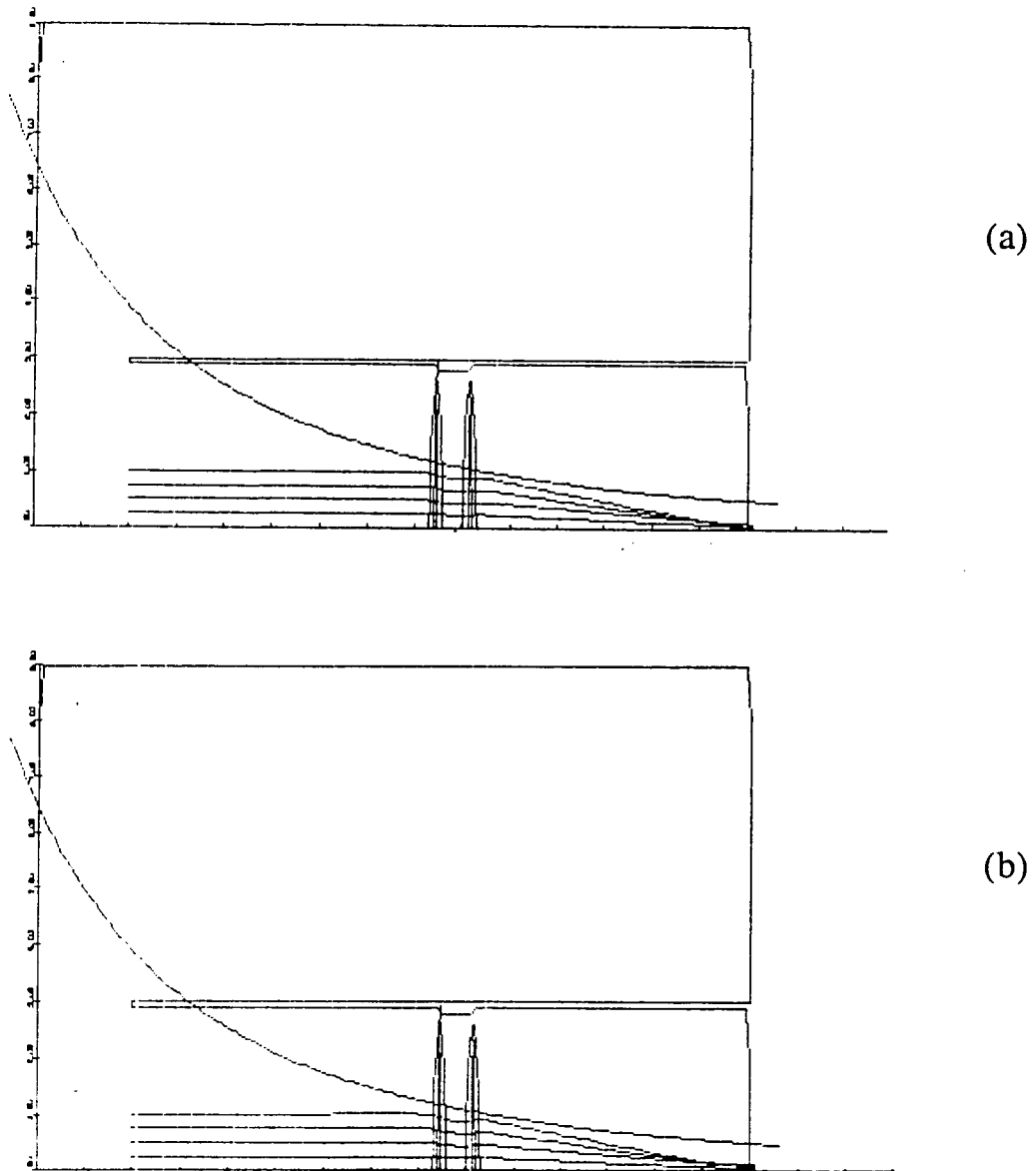
Figure 3.16. Particle trajectories in TOF spectrometer showing focusing capabilities of Einzel lens. The problem is cylindrically symmetric with the spectrometer axis lying on the horizontal axis of the figure. Ions are given initial energies of *1000 eV* to simulate the effect of the acceleration region. The lens is biased *570 V* above the drift tube. The magnetic field curve represents the magnetic field in the drift tube. The ion detector is located in the lower right corner of the boundary. Horizontal and vertical axes are not drawn to scale. (a) trajectories for particles with $m/q = 40$ at radii $r_o = 2.1, 4.2, 6.4, 8.5$ mm and (b) trajectories with $m/q = 4$ at radii $r_o = 2.1, 4.2, 6.4, 8.5$ mm.

are given initial energy of *1000 eV* to simulate the effect of the acceleration region. Therefore the drift tube is biased at ground and the lens positive with respect to it. Potential profile lines are shown at *100 V* increments and the paths for different initial conditions are plotted. Figure 3.16 (a) shows that particles entering the focusing region at different radii are all focused onto the ion detector at the opposite end of the spectrometer. Comparison of Fig. 3.16 (a) and 3.16 (b) shows that the focusing is m/q independent, as it must be.

This is also seen experimentally. A segmented collector, shown in Fig. 3.17, is placed at the location of the ion detector with a diameter equal to the ID of the drift tube. The lens voltage is varied from a $\Delta V = V_{acc} - V_{lens}$ of *0.0* to a ΔV where the current on the center electrode is maximized. Figure 3.18 shows the effect of ion focusing with the lens. The collected currents have been normalized to the area of the center electrode. As shown in Fig. 3.18, for $V_{lens}/V_{acc} = 1$ (i.e. no focusing), the beam has expanded to the diameter of the outer ring of electrodes. This is an expansion of at least *7.4x* which was expected from the beam expansion calculations and represents loss of the ion beam and degradation of performance. Figure 3.18 also shows the same situation with $V_{lens}/V_{acc} =$ *.48*. The current is now all focused to the central four electrodes with no signal seen on the outer ring of electrodes. It is also highly peaked in the center as predicted by the particle trajectory code. This will become particularly important when the large area Faraday cup is replaced with a much smaller area electron multiplier.

After focusing, the ions impinge on an ion detector at the far end of the drift tube. By this time, the ions are spatially resolved, the low m/q ions reaching the detector before the high m/q ions. Table 3.2 lists flight times for argon ions as a function of charge state
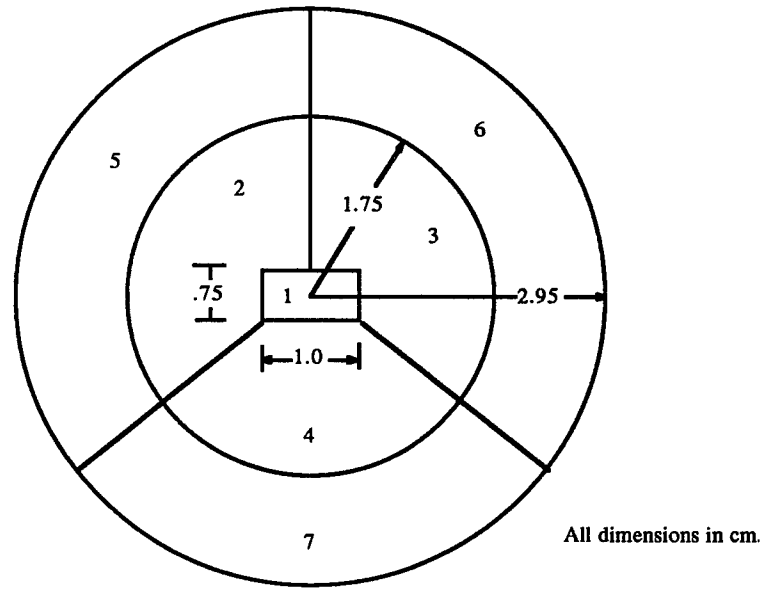
Figure 3.17. Segmented collector used to measure effect of Einzel lens on divergence of ion beam. Each section is electrically isolated and used to measure current density over each respective area.
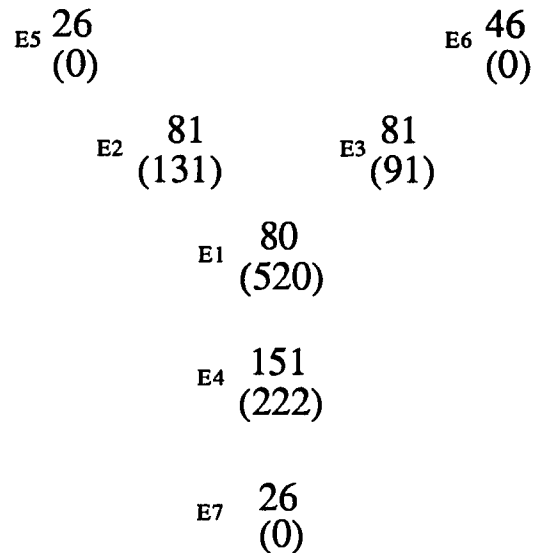
Figure 3.18. Current distribution of segmented collector. Top values are for $V_{lens} = V_{acc}$ (i.e. no focusing). Bottom values are for $V_{lens} = .48 \, V_{acc}$. Values are collected current in nA/cm^2. Shows strong focusing properties of Einzel lens. Current is distributed among possible charge states showing that, with focusing, typical currents collected on central electrode for each charge state is $\sim 10\text{-}100 \, nA/cm^2$.

Table 3.2. Argon Flight Times for 1000V Acceleration Voltage

Species	Flight Time
Ar^{1+}	14.72 μs
Ar^{2+}	10.41 μs
Ar^{3+}	8.50 μs
Ar^{4+}	7.36 μs
Ar^{5+}	6.58 μs
Ar^{6+}	6.01 μs
Ar^{7+}	5.56 μs
Ar^{8+}	5.21 μs
Ar^{9+}	4.91 μs
Ar^{10+}	4.66 μs

for typical operating parameters. As seen in the table, to resolve highly-charged ions of $\Delta Q = 1$, sub-microsecond time scales are involved. Initially, the ion detector is composed of a Faraday cup and a fast amplifier/line driver. The Faraday cup is shown in the collecting region of Fig. 3.13. A secondary electron suppressor grid is attached to the entrance of the cup since the highly energetic ions striking the cup have a high probability of causing secondary electron emission which would lead to misleading signal sizes. The Faraday cup is biased at the same potential as the flight tube, and the suppressor grid is typically biased *300 V* below this voltage. A large resistor is placed between the high voltage drift tube and the Faraday cup (see Fig. 3.13) to isolate the tube from the Faraday

cup for the fast current pulses. A blocking capacitor is placed in the current line to block the high voltage of the Faraday cup from the amplifier.

Realizing that the currents collected will typically be fractions of microamperes, an amplifier was designed which will convert these small current signals to non-negligible voltage signals. The requirements for this amplifier are:

- high transresistance -- typically $1V/\mu A$ since currents as small as $10 - 50\ nA$ are expected,

- large bandwidth -- $2\ MHz$ for $t_{rise} = 200\ ns$,

- low input impedance to provide a low Z path to ground for the current pulses from the collector,

- $50\ \Omega$ drive capability.

The circuit used initially which meets these requirements, is shown in Fig. 3.19. The $LH0032$ is a high speed operational amplifier and the $LH0033$ is a high speed line driver/current amplifier. The input impedance is controlled by a $1K$ pot and set at $500\ \Omega$. The total impedance to ground as seen from the Faraday cup is:

$$|Z| = \left[R_{amp}^2 + \frac{1}{\left(\omega C_{block} \right)^2} \right]^{1/2} = 501\ \Omega \tag{3.12}$$

for $R_{amp} = 500\ \Omega$, $C_{block} = .01\ \mu F$, and $500\ ns$ wide pulses. As required, this is significantly below the isolation resistance between the drift tube and collector. Diodes are also placed at the input of the $LH0032$ to protect it from high voltage transients. The signal from the amplifier output is fed directly into an oscilloscope where the time
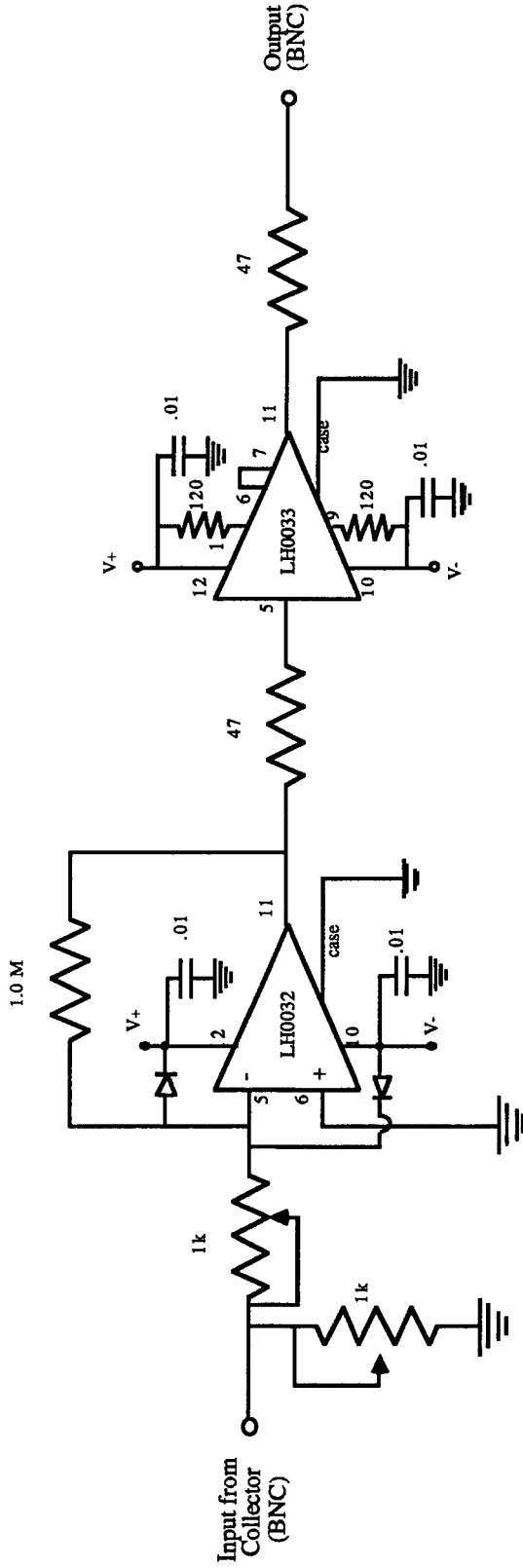
Figure 3.19. Circuit diagram for initial amplifier/line driver used to amplify current pulses from Faraday cup of time-of-flight spectrometer. This amplifier has a transresistance of 880 mV/μA and a bandwidth of 1.5 MHz.

resolved current pulses can be seen. A typical spectrum is shown in Fig. 3.20. For this spectrum, the spectrometer entrance is located directly under the mirror peak. Operating parameters are shown in the figure. Several peaks are visible, from both the leak gas, krypton, and from impurities such as carbon, nitrogen, and oxygen. Charge states as high as Kr^{8+} are seen as well as impurities up to C^{4+}. Low charge states of krypton are not seen for reasons discussed later.

Figure 3.20 shows that the initial design of the time-of-flight spectrometer yields reasonably good spectra with acceptable resolution capable of resolving peaks of highly-charged, heavy-mass ions. Temporal data was taken with the spectrometer in this configuration. Results will be shown in Sec. 6.2.
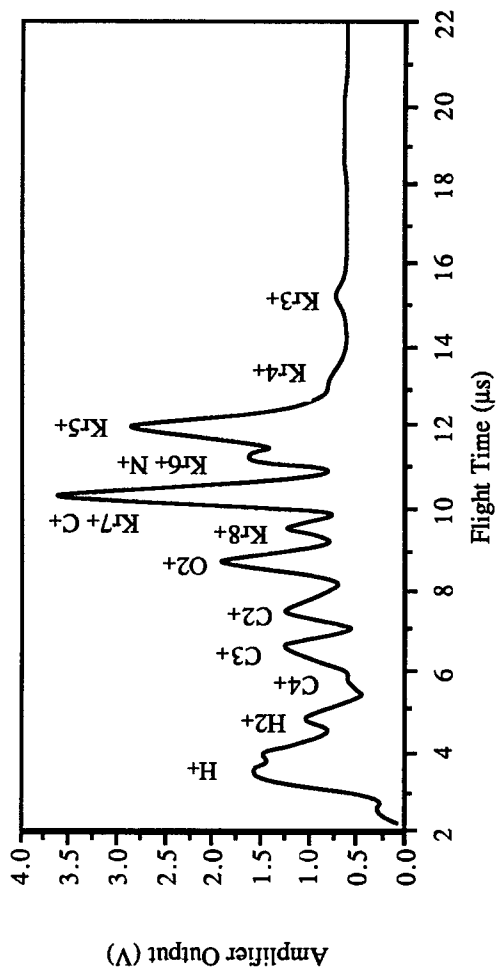
Figure 3.20. Typical time-of-flight spectrum for krypton for in itial spectrometer configuratio n. Operating parameters are: Vg = +200 V, Vtube = -800 V, Vlens = -400 V, Δt = 800 ns, Vpulse = - 180 V.

3.4.3 Modifications - Final Design

It became apparent that some modifications of the spectrometer were necessary because of several problems inherent in its original design. These problems include attenuation of high m/q signals, low collected currents, and low resolution.

Effects of the first problem, attenuation of high m/q signals, are apparent in Fig. 3.20. Only signals for $m/q < 28$ are seen. There are two possible causes for this effect. The first deals with transit-time effects of the ions as they pass through the gating region of the spectrometer. Referring to Fig. 3.13, consider an ion which passes through the second grounded aperture into the gating region of the spectrometer. This ion possesses energy $E_i = q_i V_p$ where $V_p = $ plasma potential. When the gating grid is not being pulsed, it has a voltage V_g applied to it. As the ion approaches this grid, it is reflected when it reaches a potential equal to V_p. It has penetrated into the gating grid region a distance:

$$d_{penetration} = \{ \frac{V(z)}{V_g} \} \ d = \eta \ d \qquad (3.13)$$

where $d = $ distance between the entrance aperture and gating grid. At this point its velocity has slowed to:

$$v_1 = \sqrt{\frac{2 q_i (V_p - \eta V_g)}{m_i}} \ . \qquad (3.14)$$

Therefore, when the gating grid pulses to $V_g = 0$, the ion must traverse a distance $z = d (1 - \eta)$ to enter the acceleration region. If the grid pulses back to V_g before the ion has traversed this entire distance, it will feel a deceleration and may be

stopped before it reaches the acceleration region. The distance traveled during a gating

pulse of width Δt is $v_1\Delta t$ and the distance required to reflect an ion at initial velocity v_1

undergoing an acceleration $-a$, is $v_1^2/2a$. Transmission requires:

$$z_{tot} = v_1 \, \Delta t + \frac{v_1^2}{2a} > d(1 - \eta) \tag{3.15}$$

Equation 3.15 can be written in terms of plasma and spectrometer parameters and

reduced to:

$$\frac{M}{Q} < 1.92 \, \frac{\Delta t^2 \, (\mu s)}{d^2 \, (cm)} \left[\frac{V_g}{(V_g - V_p)} \right]^2 (V_p - \eta V_g) \tag{3.16}$$

$$for \quad 0 < \eta < \left(\frac{V_p}{V_g} \right)$$

where M/Q has the units amu/esu. This limiting value of M/Q is a maximum for $\eta = 0$,

or an ion is most likely to pass through the gating grid if it impinges on the gating region

just as the gating pulse starts. For the spectrum of Fig. 3.20, the parameters are

$\Delta t = .8 \, \mu s$, $d = 1.2 \, cm$, $V_g = 200 \, V$. For $\eta = 0$, attenuation of the high m/q

signals occur for $V_p \leq 60 \, V$ This is a typical value of the plasma potential for the MIMI

ECR-heated plasmas and therefore, this effect can become quite marked.

The second possible cause of attenuation of high m/q ion signals relates to

magnetic field effects on ion trajectories inside the collimating region of the spectrometer.

For the spectrum of Fig. 3.20, the entrance aperture of the spectrometer is located at the

mirror peak. To pass into the gating region of the spectrometer, ions must first pass

through two collimated apertures whose diameters, d, are *.32 cm* and whose separation,

L, is *5.1 cm*. See Fig. 3.13. If an ion Larmor radius is larger than the radius of the

apertures, to pass through both apertures it must possess sufficient parallel energy so that

it undergoes only a small fraction of a Larmor orbit as it traverses the distance between

the apertures. If it does not, it will be collected by the second aperture and not reach the

gating region. The time necessary for the ion to traverse the distance between the two

apertures, L, is:

$$t_L = \frac{L}{v_{//}} = .723 \ L \ (\ cm \ ) \ \frac{M_i^{1/2} \ (\ amu \ )}{T_{//}^{1/2} \ (\ eV \ )} \ \mu s \ . \tag{3.17}$$

The time necessary for an ion to traverse an angle, Θ, so that if it passes through the first

aperture it will just pass through the second aperture, is:

$$t_\Theta = \frac{d}{\omega_{ci} \ \rho_L} = 1.02 \ d \ (\ cm \ ) \ \frac{M_i^{1/2} \ (\ amu \ )}{T_\perp^{1/2} \ (\ eV \ )} \ \mu s \ . \tag{3.18}$$

Transmission requires $t_L < t_\Theta$. Therefore,

$$\frac{T_{//}}{T_\perp} > .499 \left(\frac{L}{d} \right)^2 = 128 \ . \tag{3.19}$$

Since $T_{//} \sim T_\perp$, Eqn. 3.19 is not satisfied and ions with $\rho_L > d/2$ will be attenuated.

For a krypton spectrum, only ions with $\rho_L < .16 \ cm$ can be measured, For

$B_0 = 4 \ kG$ and assuming $T_\perp \sim 10 \ eV$, only ions with $Q > 4$ have $\rho_L < d/2$. This

effect is apparent in Fig. 3.20. The Kr^{5+} peak is quite large while the Kr^{4+} and Kr^{3+} peaks are quite small with no signal visible whatever from Kr^{2+} and Kr^{1+}.

The two effects causing high m/q attenuation are eliminated by withdrawing the spectrometer from the region of high magnetic field, removing the second collimator, and reducing the aperture-to-gating-grid distance by ~$10x$. The spectrometer is presently placed on axis, ~2 m from the midplane. See Fig. 3.1. The magnetic field at the aperture is 45 G and drops to 5 G at the opposite end of the flight tube. With the spectrometer withdrawn from the magnetic field, the ions impinging on the aperture have wholly parallel energy. There are, therefore, no Larmor orbit effects. The gating grid setup is changed and a schematic of the present configuration is shown in Fig. 3.21. The aperture-to-gating-grid distance is decreased from 1.2 cm to $.13$ cm, thereby eliminating the attenuation effects described by Eqn. 3.16.

The problem of low collected currents is rectified by replacing the Faraday cup with an electron multiplier. This multiplier is a Vacumetrics AEM-1000 multiplier which has a gain of ~10^5 at 1.5 kV. Two 5000 pF capacitors are connected across the last two dynodes of the multiplier to increase its pulsed current capabilities. This multiplier is chosen since it uses a dynode material which does not degrade upon exposure to atmosphere. This is important since the spectrometer is frequently removed from the system. Unlike the Faraday cup, the multiplier requires a separate voltage supply and can therefore be operated at a different voltage that the high voltage drift tube. To isolate the multiplier from the drift tube so as not to introduce electric fields into the necessarily field-free region, an isolation grid is placed directly in front of the multiplier. This grid has a direct electrical connection to the drift tube. The isolation grid also allows the operator to change the gain of the multiplier without affecting the ion flight times or lens focusing

plasma endloss

↓

————————————————— Cu faceplate .050
——————————————————— SS aperture .0001   d = .32
→| |← d

——————————   ——————————— TFE shim .025

—————————————————————— SS mount .005
Ni gating grid (apply pulse here)

——————————   ——————————— TFE shim .025

▬   ▬ Cu ring held to faceplate
with 4-40 SS screws

acceleration region

————————————————————— acceleration grid

↓

fast ions to electron multiplier
97.8 cm away
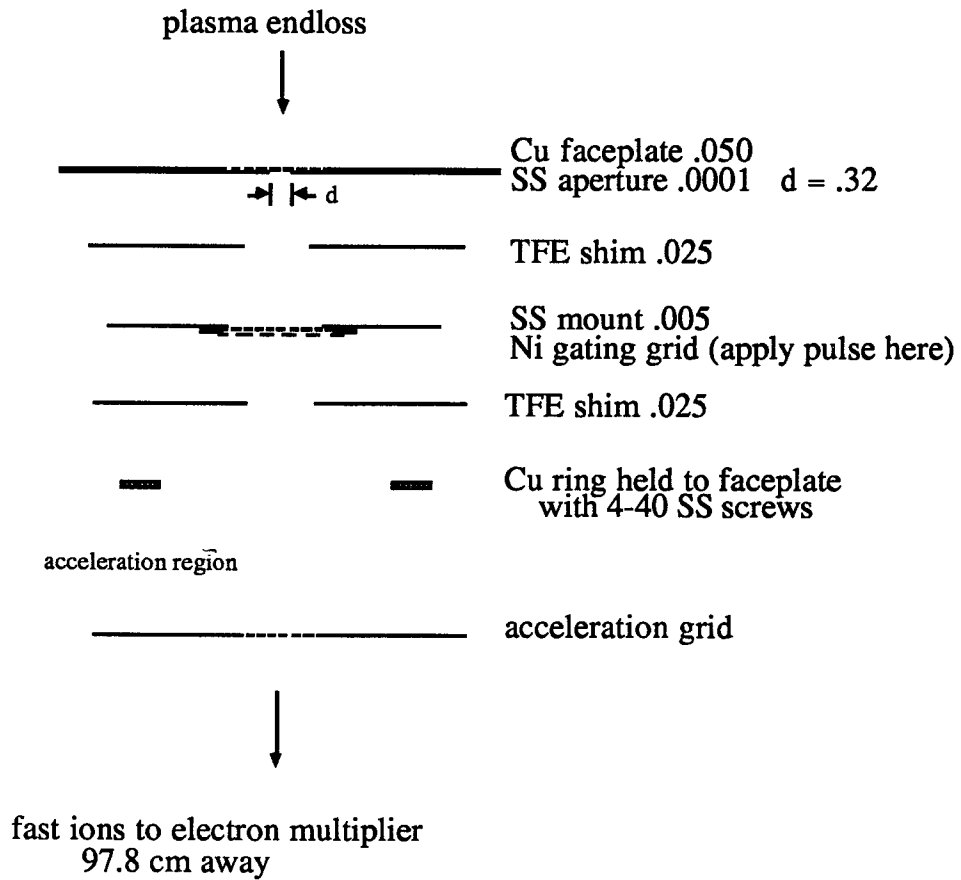
Figure 3.21.   Modified gating grid used to eliminate gating-region, transit-time effects which cause attenuation of high m/q ion signals. All dimensions are in cm.

properties. The aforementioned modifications of the spectrometer can be seen in Fig. 3.22.[41]

The resolution of the signal is increased by use of the electron multiplier which has a response time of *3 ns* and by use of a faster amplifier than the one shown in Fig. 3.19. Since the multiplier delivers high currents, the gain requirements of the amplifier are less demanding. To achieve the largest bandwidth possible, it was decided to build an amplifier with two amplification stages so the voltage gain requirements of each stage would be lowered to *~20 dB*. For a compensated amplifier, this allows for a bandwidth of *7 MHz* which corresponds to a rise time of *50 ns*. This is still slower than the multiplier but sufficiently fast for the application for which it was designed. A line driver is included in the design allowing the amplifier to drive a *50 Ω* load at the scope or digitizer. The circuit diagram for this amplifier is shown in Fig. 3.23. The total transresistance is *4.7 mV/μA*.
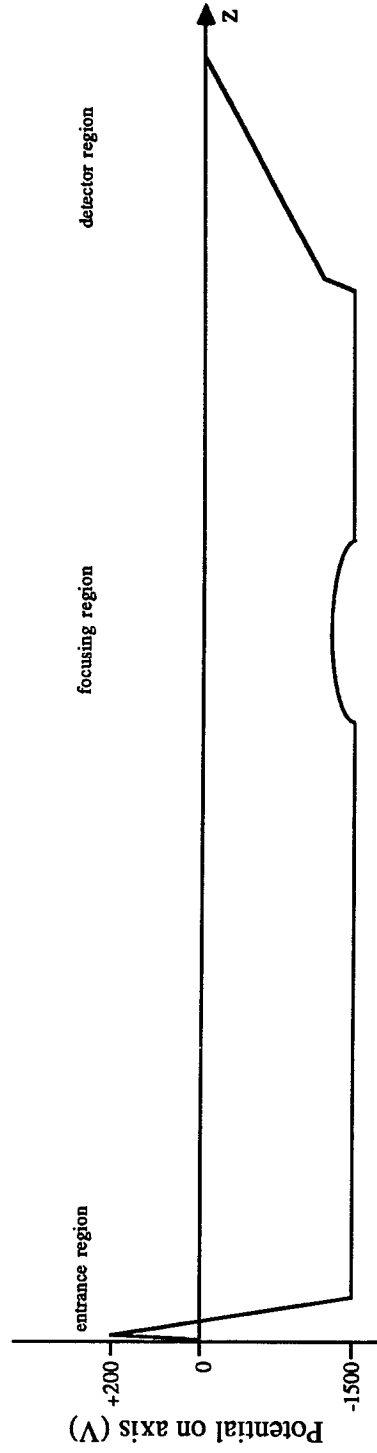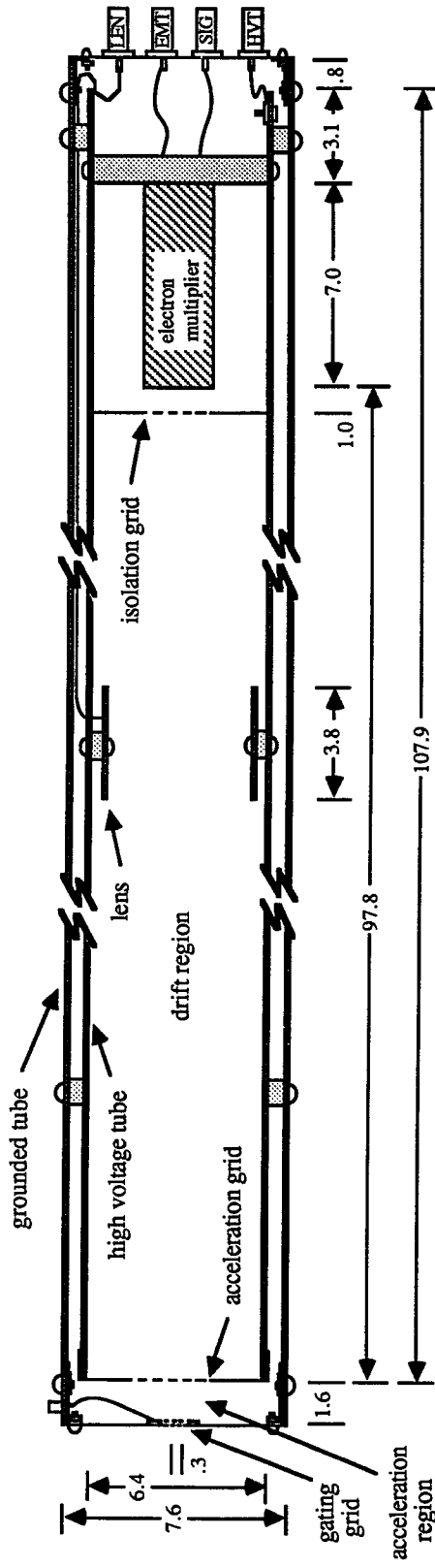
Figure 3.22. Time-of-flight spectrometer final design. See Fig. 3.21 for blowup of gating grid.
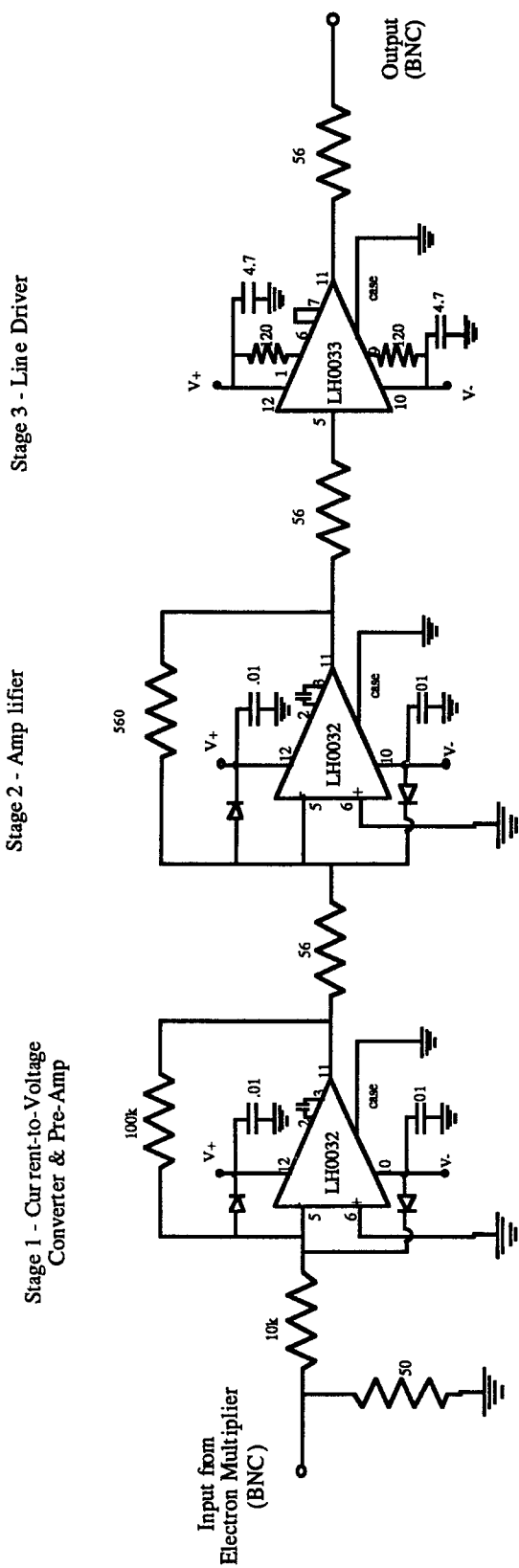
Figure 3.23. Circuit diagram for final amplifier/line driver used to amplify current pulses from electron multiplier of time-of-flight spectrometer. This amplifier has a transresistance of 4.7 mV/μA and a bandwidth of 7 MHz.

3.4.4 Data Processing and Sample Results

The data processing chain is shown in Fig. 3.24. The output of the amplifier is digitized using a LeCroy TR8818A, *100 MHz* transient digitizer. A clock speed of at least *100 MHz* is required to achieve the desired resolution. Since each spectrum requires *10μs* at *10 ns/point*, and the digitizer maximum total storage is *128(1024)* points/trace, about *130* spectra can be stored per shot, covering *1.25* ms of plasma time. The raw data points are stored in binary on a hard disk for processing at a later time, each shot requiring over *128K* memory.

Each individual spectrum (one of *130* spectra stored per shot) is subject to random signal fluctuations due to amplifier noise, secondary electron and x-ray bombardment of the multiplier, plasma fluctuations, and statistical spreads. These random fluctuations obscure small peaks of highly-charged, working-gas ions. To eliminate this effect, the *130* digitized spectra are averaged together which averages to zero these fluctuations and makes possible the identification of small peaks which would otherwise be obscured. The averaging process also makes possible shot-to-shot reproducibility. This is important when measurements involving more than one plasma shot are made.

The averaging is performed by the FORTRAN program listed in Appendix A. All of the digitized data points for each of the *130* spectra are contained in a single array SPECTRUM containing over *130,000* data points. Each set of *~1000* points contains the information for a single digitized spectrum, sequential data points separated by *10 ns* of real time (*100 MHz* clock). The program flow chart is shown in Fig. 3.25. To perform the averaging, the program moves through the array of raw data SPECTRUM, in steps of *1000*, each step fixing on the peak of a particular species determined by the user. This peak must be well resolved so "peak jumping" from spectrum to spectrum does not

Current
Pulses In
→

Electron Multiplier

Preamp &
Line Driver

LeCroy
Amplifier

LeCroy
Digitizer

Spectra
Averaging
Performed
Here

Averaged Spectrum
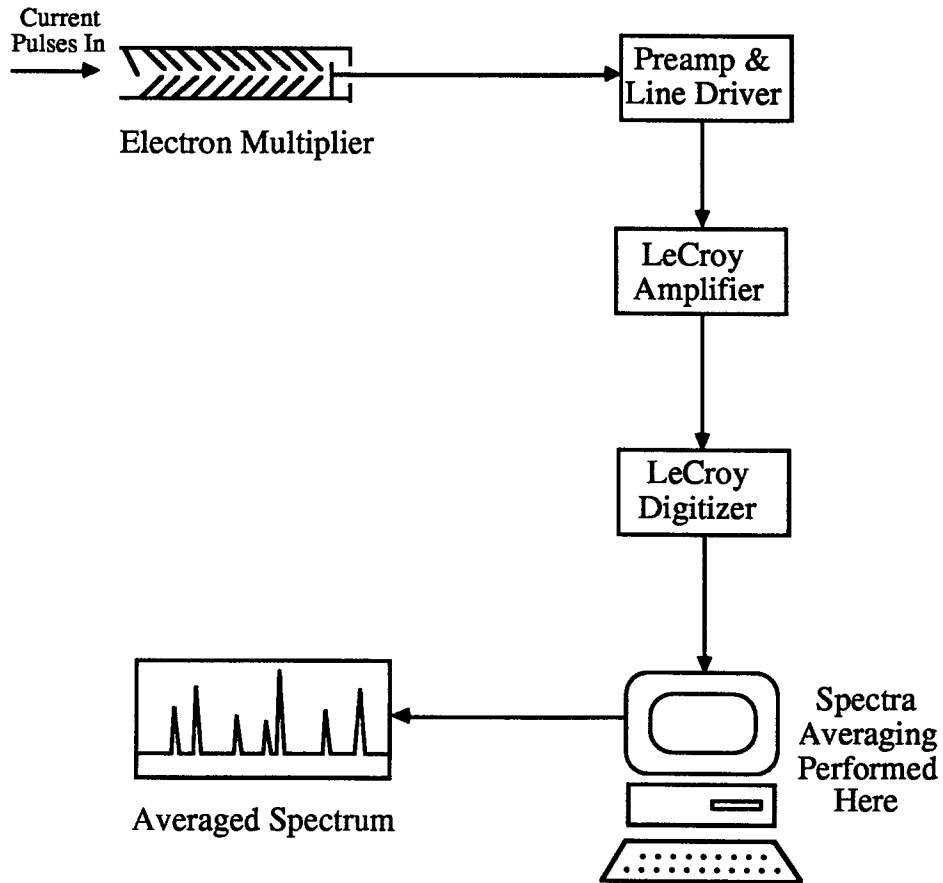
Figure 3.24. Data acquisition and processing system. Ion packets are detected by a Vacumetrics AEM-1000 electron multiplier. The output of the EM is amplified by the amplifier of Fig. 3.23 and this output is again amplified and digitized by a LeCroy TR8818A transient digitizer. The digitized spectra are averaged to give the final output.
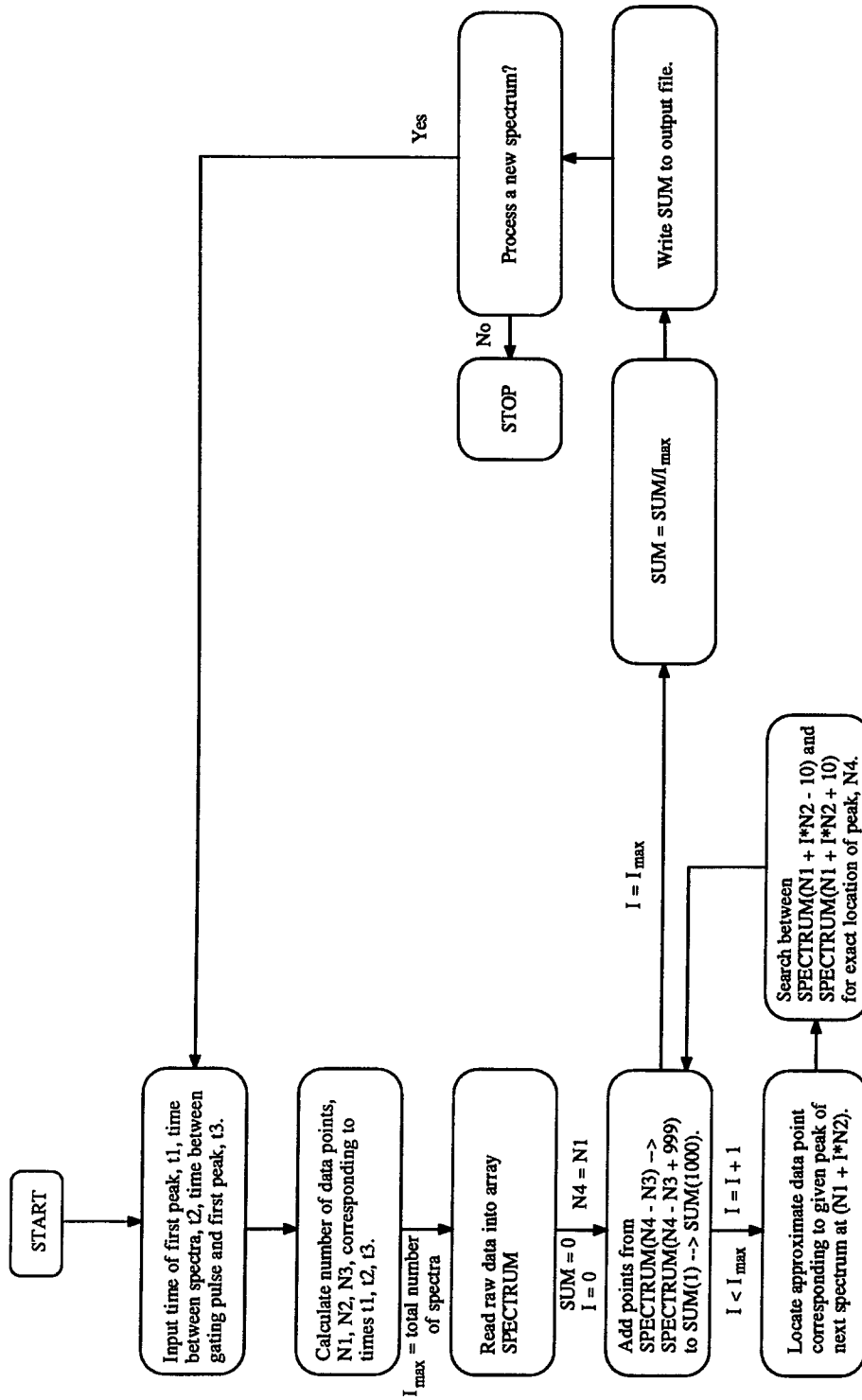
Figure 3.25. Flow chart for program SPECTRUM_AVERAGER

START

Input time of first peak, t1, time between spectra, t2, time between gating pulse and first peak, t3.

Calculate number of data points, N1, N2, N3, corresponding to times t1, t2, t3.

I_{max} = total number of spectra

Read raw data into array SPECTRUM

SUM = 0
I = 0   N4 = N1

Add points from
SPECTRUM(N4 - N3) ->
SPECTRUM(N4 - N3 + 999)
to SUM(1) --> SUM(1000).

I < I_{max} I = I + 1

Locate approximate data point corresponding to given peak of next spectrum at (N1 + I*N2).

Search between
SPECTRUM(N1 + I*N2 - 10) and
SPECTRUM(N1 + I*N2 + 10)
for exact location of peak, N4.

I = I_{max}

SUM = SUM/I_{max}

Write SUM to output file.

Process a new spectrum?

Yes

No

STOP

occur. After having found the array location, SPECTRUM(N_4), which corresponds to the peak for the given species for that particular spectrum, the program adds to another array, SUM, *1000* data points surrounding SPECTRUM(N_4) which covers the *10 μs* of real time required for the spectrum. The data points added to SUM are SPECTRUM(N_4-N_3) to SPECTRUM(N_4-N_3+*999*) where N_3 is the number of points from the beginning of the spectrum to the fixing peak. N_3 remains the same for all spectra. The program then moves forward *1000* data points to the next spectrum and locates the N_4 of the fixing peak. This continues until all spectra gave been located and added to SUM. The values in SUM are then divided by the total number of spectra added to it and SUM then contains a single spectrum of the average of the *130* spectra contained in the original raw data array SPECTRUM.

The process of acquiring many TOF spectra over a short time period and then averaging them has proven quite effective in increasing the signal-to-noise ratio to acceptable levels and in reducing random signal fluctuations so that shot-to-shot reproducibility is assured. Figures 3.26 and 3.27 illustrate these improvements, which are quite marked.

The inception of this data processing technique is the final modification to the time-of-flight spectrometer system described in section 3.4.2. The problem of attenuation of high m/q ion signals is solved by changing the gating grid system and withdrawing the spectrometer from the high magnetic field region. The use of a fast response time electron multiplier as an ion detector in place of a Faraday cup allows for the detection of small ion currents. This also decreases the gain requirements of the amplifier used to amplify the current pulses before reaching the scope or digitizer. With the gain requirements reduced, an amplifier is designed with a much larger bandwidth than
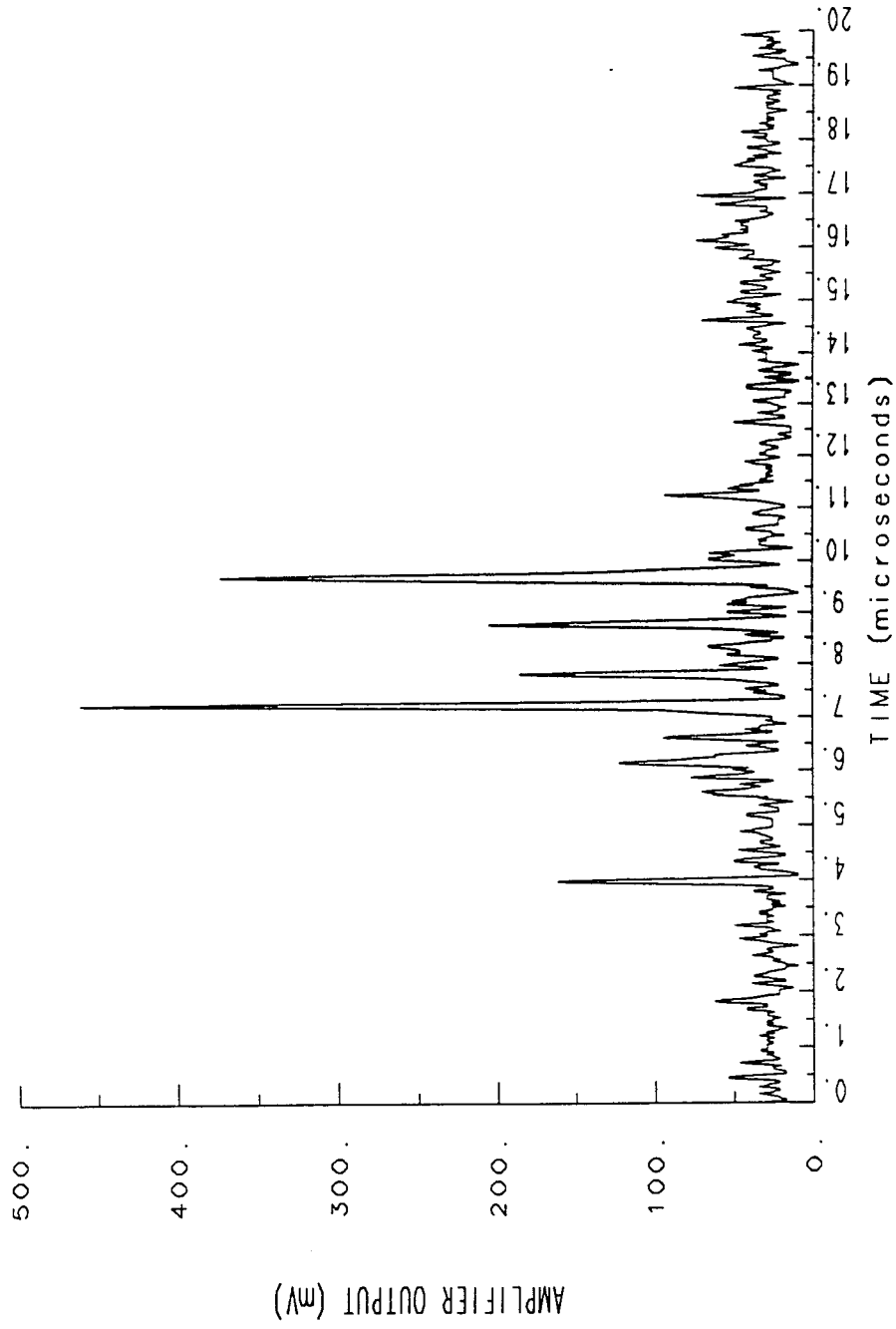
Figure 3.26. Single digitized neon TOF spectrum. The final processed spectrum is comprised of the average of 130 such spectra. Large amounts of noise and random signal fluctuations are evident in this spectrum which average to zero during the averaging process. An example of a processed spectrum is shown in Fig. 3.27.
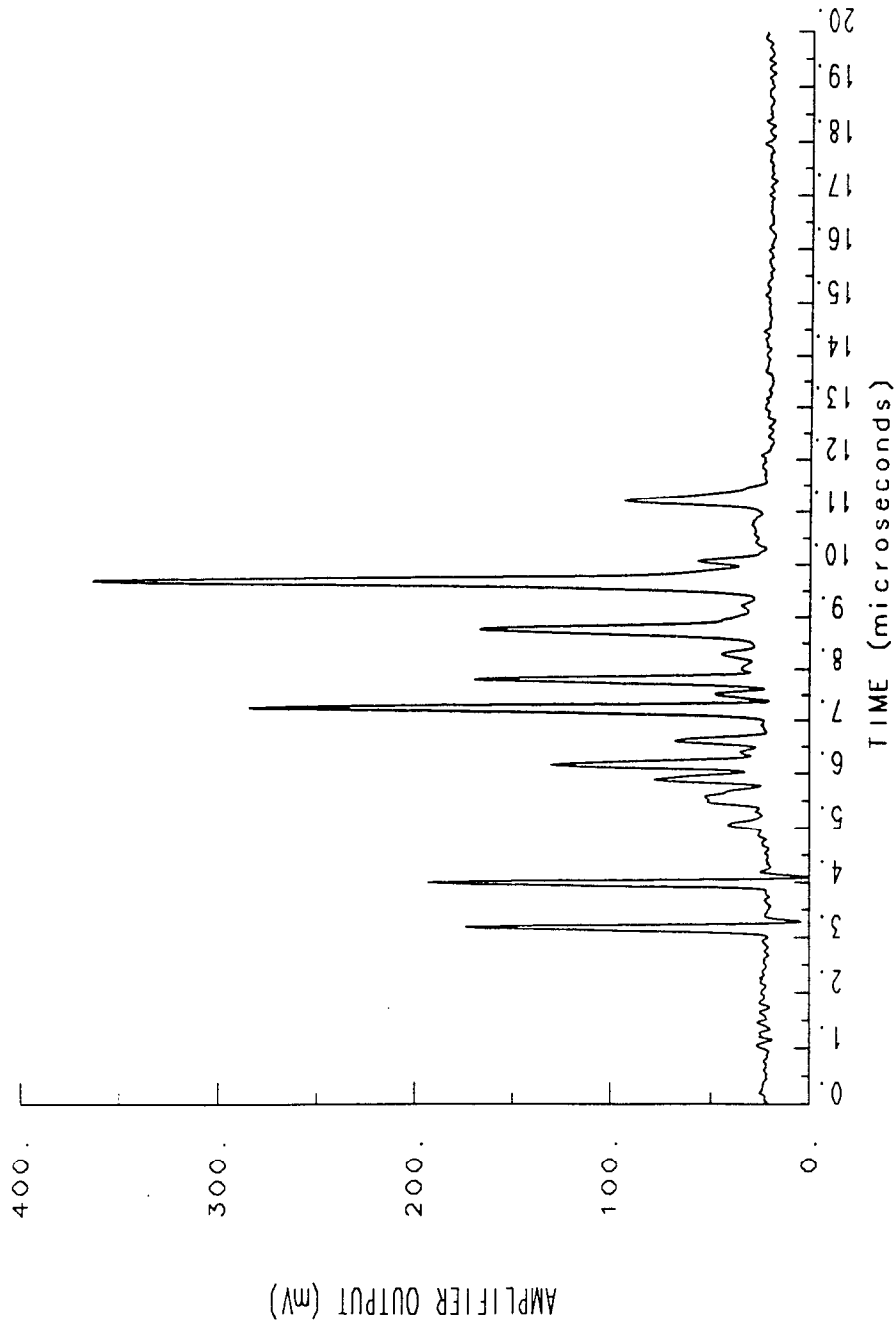
Figure 3.27. Averaged neon TOF spectrum. Many small peaks emerge which are obscured by noise in the individual spectra. The peak area from these processed plots determine the relative endloss current densities.

was originally possible. The signal-to-noise ratio is increased significantly by digitizing the output of the amplifier for many spectra and averaging to zero random signal fluctuations. This process allows for measurement of small signals of highly-charged, working-gas ions which would otherwise be obscured by noise. The modifications of the spectrometer and data acquisition and processing system results in significant improvement in the overall operation of the diagnostic. It is now capable of reliable measurements of small quantities of highly-charged ions created in the midplane region of the plasma.

3.5. Timing

Due to the pulsed nature of the experiment, many scopes, diagnostics, and pieces of equipment require timing pulses. MIMI is pulsed once every ~1.5 s and the timing of all the equipment is controlled by a Jorway Model 463 controller crate and CAMAC timing modules Model 221 and 3989. The CAMAC system outputs twelve timing channels, each carrying a +$3V$ timing pulse of varying start time and width. A PASCAL program run on an Apollo computer workstation, allows for user input of pulse start times and widths relative to an input pulse from a $1/90$ - 60 cycle pulser. The output of the CAMAC controller is isolated from the system by an optical coupler circuit assuring no feedback effects from any cables which may contain noise or other spurious signals.

A timing schematic is shown in Fig. 3.28. Considerations for the set points of the timing pulses are as follows.

- All scopes are triggered at $t = 0$ (time of the CAMAC trigger pulse from the $1/90$ - 60 cycle pulser).
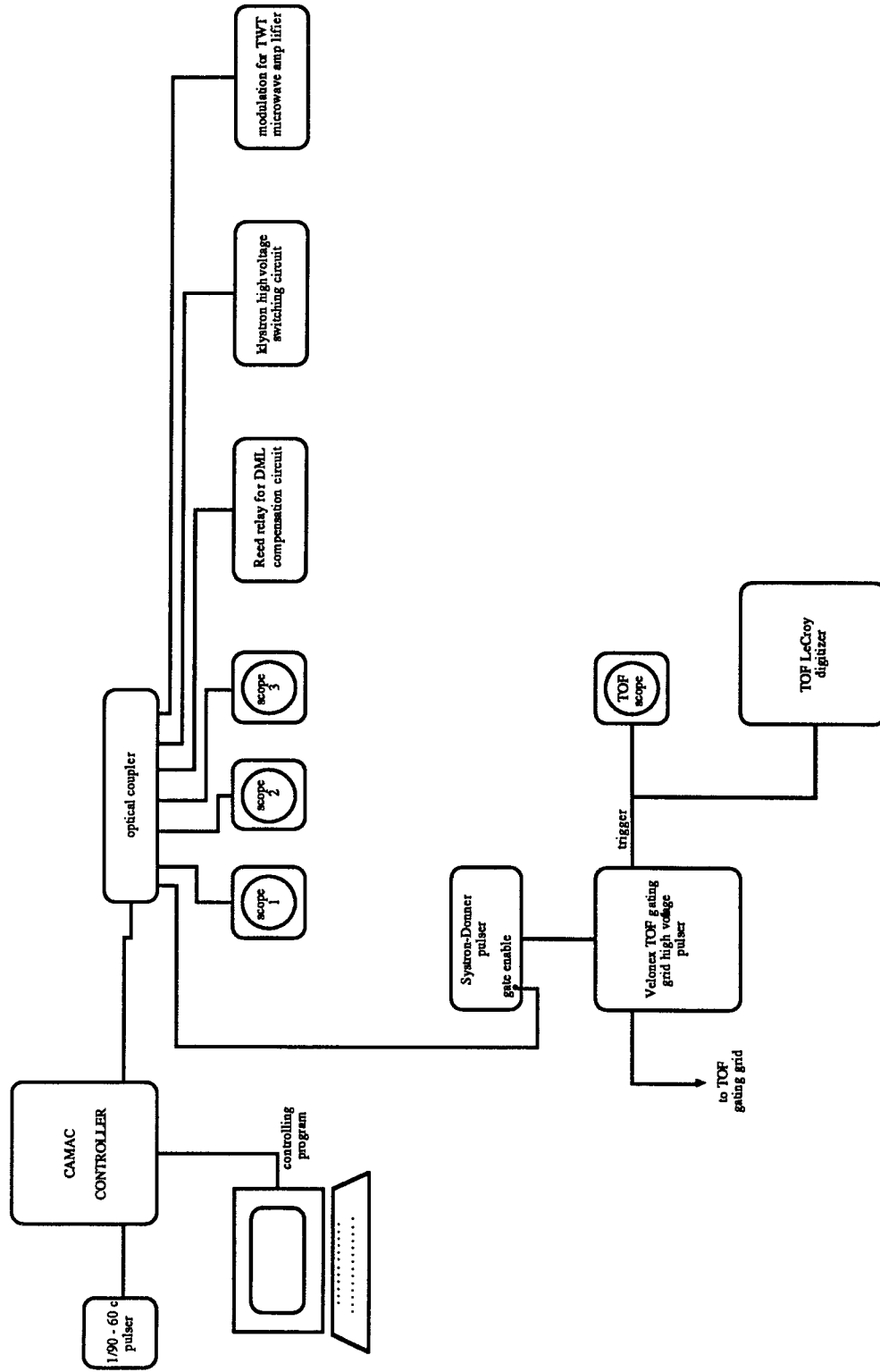
Figure 3.28. MIMI timing schematic. The timing for all equipment is controlled by a CAMAC crate controller which is triggered every 1.5 s by a 1/90 - 60 cycle pulser. All equipment controlled by the CAMAC is shown above.

- The klystron switching circuit timing pulse applies high voltage to the klystron amplifier when the pulse is "ON" and removes the high voltage when the pulse is "OFF". The "ON" time of this pulse must span the time during which the TWT microwave amplifier is "ON" since the klystron amplifies the output of this amplifier. Pulse widths of this pulse are typically *50 ms* for a *30 ms* TWT pulse.

- The TWT modulation pulse determines the length of the plasma since microwaves are amplified by the klystron and launched into the midplane only when the TWT modulation pulse is "ON". This pulse must lie between the start and stop times of the klystron pulse. It is typically delayed *10 ms* from the beginning of the klystron pulse due to a klystron high voltage spike which occurs when the klystron switch closes. TWT pulse widths and therefore plasma times are typically *30 ms*.

- The diamagnetic loop compensation circuit includes a Reed relay which, in effect, shorts the input when the relay is in a closed position. It requires a *+3 V dc* bias to open the relay and allow a DML measurement to be taken. Therefore, a pulse from the CAMAC is supplied which just spans the width of the TWT pulse and allows a DML measurement over the entire width of the plasma "ON" time.

- The time-of-flight spectrometer triggering is somewhat more complex. Since the TOF requires a gating grid pulse every *10 µs* for *~1.25 ms* (*~125* successive pulses), a Systron-Donner Model 100C pulser is used in tandem with the CAMAC controller. Gating grid pulsing requirements for the time-of-flight spectrometer are discussed in Sec. 3.4.4. The CAMAC pulse is input to the "gate enable" of the Systron-Donner pulser. During the "ON" time of this CAMAC pulse, the Systron-Donner pulser outputs *1 µs* wide pulses at a rate of *100 kHz*. These are the pulses which trigger the gating grid Velonex pulser, one TOF spectrum collected per pulse, which then triggers the TOF

scope and LeCroy digitizer. The CAMAC, therefore, controls the time over which the

TOF spectra are collected and the Systron-Donner pulser controls the frequency at which

the spectra are collected. A typical set of timing pulses is shown in Fig. 3.29.

Klystron switch pulse
from CAMAC

t = 0   t = 50 ms

TWT amplifier modulation
pulse from CAMAC

t = 10 ms   t = 40 ms

DML Reed relay pulse
from CAMAC

t = 5 ms   t = 45 ms

Systron-Donner 'gate enable'
pulse from CAMAC

t = 30 ms   t = 32.5 ms

Velonex trigger pulses
from Systron-Donner

t = 30 ms   t = 32.5 ms

Velonex trigger pulses
from Systron-Donner
expanded

t = 30 ms
t = 30.010 ms
t = 30.020 ms
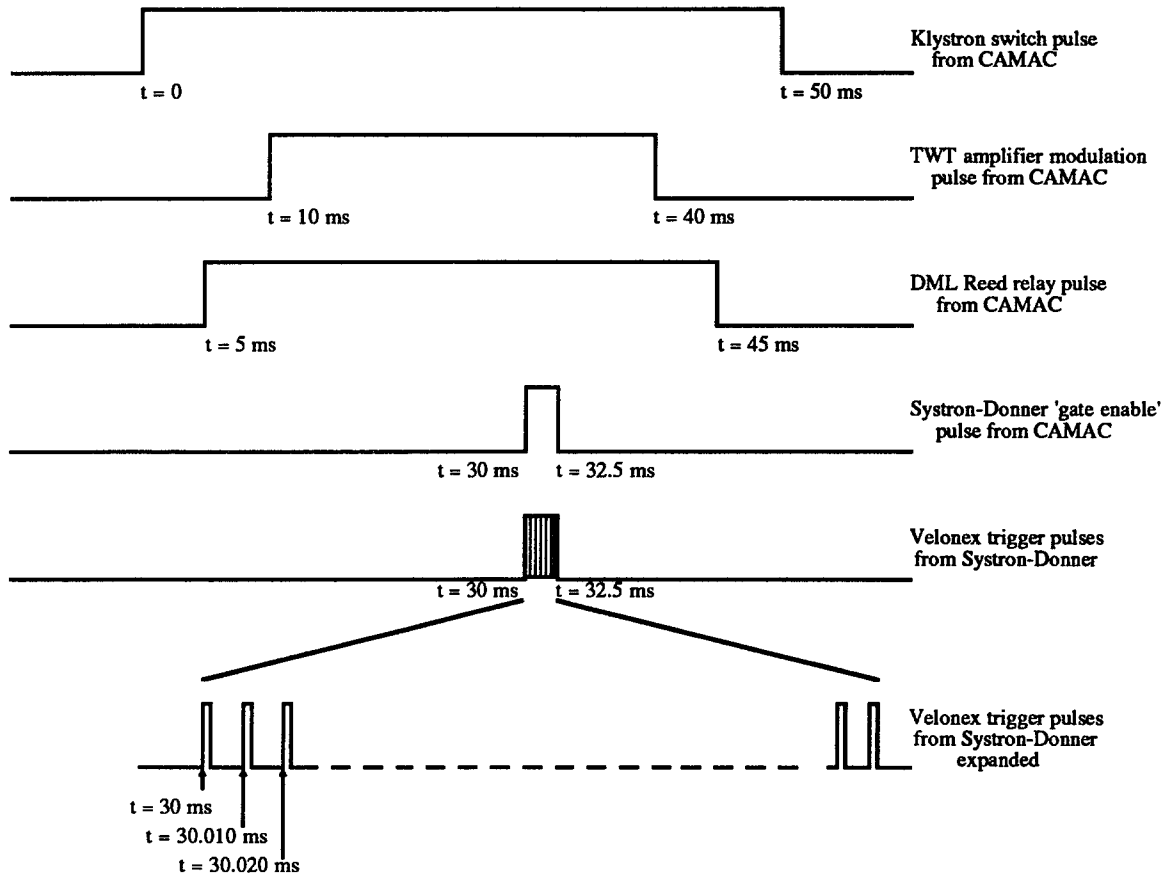
Figure. 3.29. Typical MIMI timing sequence.

CHAPTER 4

ION CYCLOTRON RESONANCE FREQUENCY HEATING

One of the major goals of this experiment is to determine whether changes in the MIMI ion charge state distributions can be attained by direct heating of the plasma ions through ion cyclotron resonant heating (ICRH). With this in mind, an ICRH heating system has been designed and built for the MIMI vacuum system. The following chapter addresses ICRH antenna modeling considerations, circuit designs, and antenna electromagnetic fields. The computer code ANTENA[42,43] is used extensively to compute vacuum inductive fields and model the antenna-plasma interaction to determine such quantities as antenna loading, power deposition profiles, and plasma spectral response (e.g. $P_{abs} = f(k_z)$). A description of the code is followed by results used to determine the best antenna configuration for typical MIMI parameters. Measurements of the actual EM fields are included as well as a discussion of the mechanism of energy transfer from these fields to the resonant plasma ions. Design and operating characteristics of the antenna rf drive system are also presented.

4.1. The Antenna-Plasma Coupling Code -- ANTENA

The antenna types modeled by the code ANTENA are shown in Fig. 4.1. Filamentary current paths are shown for clarity, however the code provides for defined, non-zero current path widths. The geometries chosen are a reflection of ICRH antennas which have been used successfully in past or existing plasma devices. The full-turn loop

(a) full turn loop

(b) half Nagoya

(c) Nagoya type III

(d) saddle coil

(e) line current

(f) partial turn loop

(g) array composed of superposition of above coils
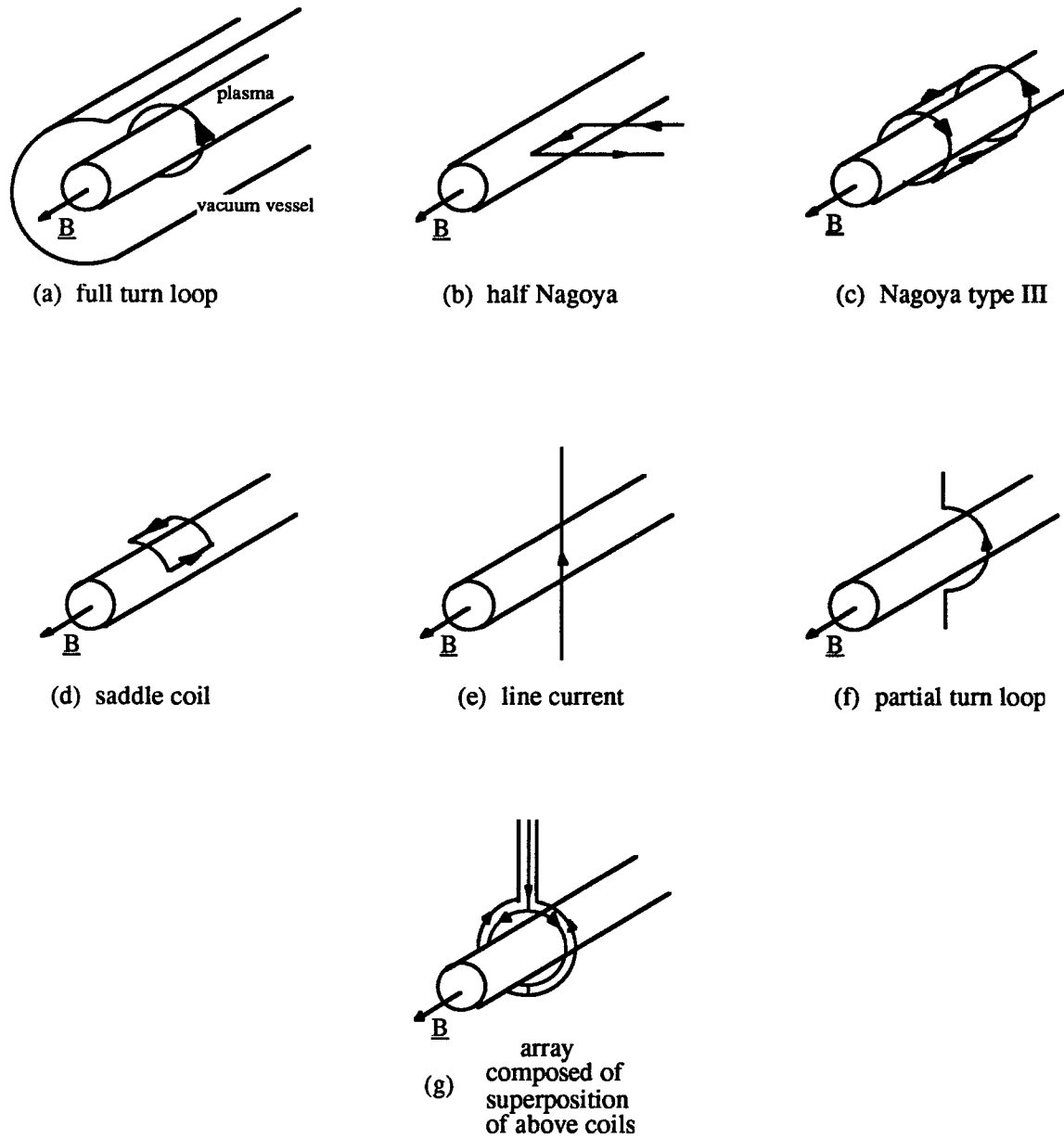
Figure 4.1. Antenna configurations modeled by the antenna-plasma coupling code ANTENA. Antennas not shown in this figure can be modeled by the superposition of the above geometries, such as that shown as the array antenna (g) above.

is one element in a Stix coil used on the *B-65* and *B-66* experiments at Princeton University. The half Nagoya, Nagoya III, and saddle coils have been used extensively on the *RFC-XX* experiment at Nagoya University, Japan. The line-current antenna models the rod antennas used in the Phaedrus end plugs. The most widely used antenna, however, is the partial-turn loop antenna used in many mirror and tokamak experiments. Antenna configurations other than those shown can be modeled by superimposing the fields of more than one of the antennas of Fig. 4.1. For instance, the double-half-turn loops used on TMX-U can be modeled by two partial turn loops separated 180° azimuthally and operated 180° out of phase.

A sample antenna-plasma geometry is shown in Fig. 4.2. The plasma is modeled as an infinitely long cylinder of radius a, surrounded by an infinitely long conducting vacuum wall of radius c. All antennas of Fig. 4.1 have a characteristic radius b, which must lie between a and c. Electromagnetic fields are calculated for the entire region, $r < c$, with which appropriate derived quantities can then be computed. The electromagnetic fields are calculated by solving Maxwell's equation for waves propagating in a plasma with variation $e^{i\omega t}$. These equations take the form:

$$\nabla \times E(r) = \mu_o \frac{\partial H}{\partial t} = i\omega\mu_o H(r) \tag{4.1}$$

and

$$\nabla \times H(r) = \varepsilon_o \underline{\underline{\varepsilon}}(r) \cdot \frac{\partial E(r)}{\partial t} + J_{ext}(r)$$
$$= -i\omega\varepsilon_o \underline{\underline{\varepsilon}}(r) \cdot E(r) + J_{ext}(r) . \tag{4.2}$$

Here, $\underline{\underline{\varepsilon}}(r)$ is the local dielectric tensor assumed only to be a function of r. J_{ext} represents the antenna currents. The above equations are solved for each of the regions
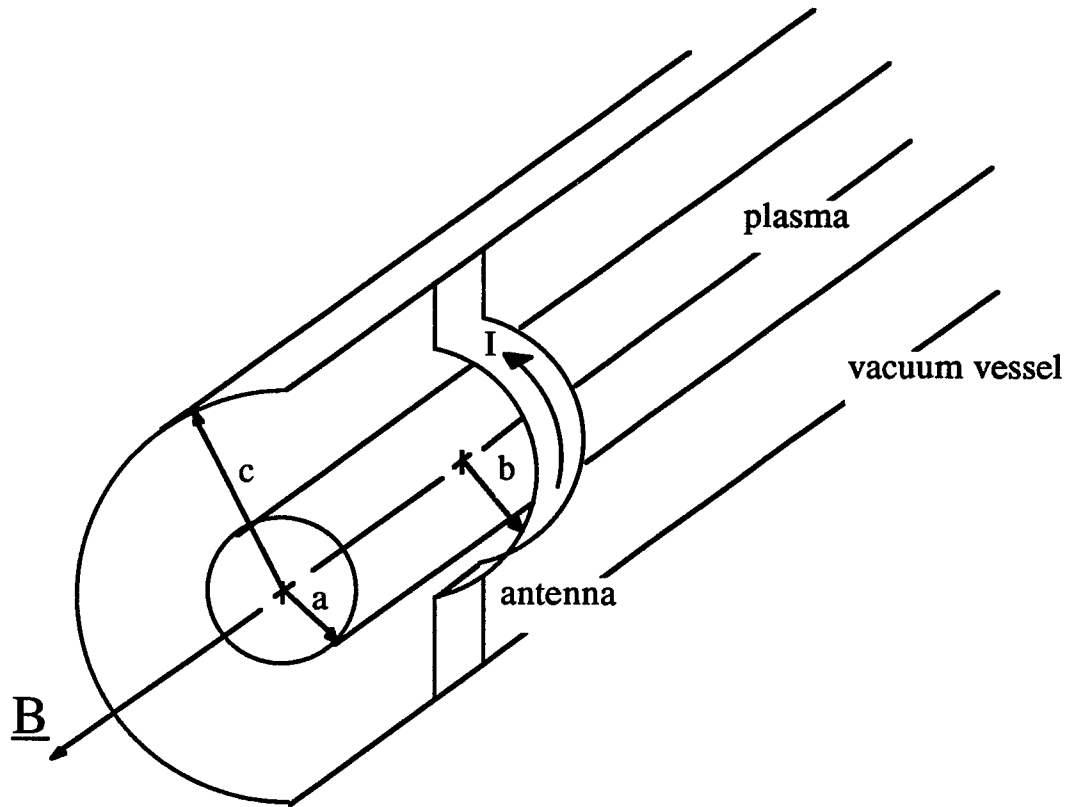
Figure 4.2. Antenna-plasma geometry for ANTENA code for the half turn loop. The plasma, antenna, and vacuum vessel wall have radii a, b, and c, respectively. The code requires $a < b < c$.

$r < a$, $a < r < b$, and $b < r < c$ with appropriate boundary conditions imposed at $r = a, b$, and c.

The above is a difficult three-dimensional problem in (r,ϕ,z) which can be reduced to a one-dimensional problem in (r,n,k_z) by realizing that if the antenna is removed from Fig. 4.2, the geometry is uniform in ϕ and z. The spatial variation of field quantities can then be represented by the inverse Fourier transform:

$$F(r,\phi,z) = \frac{1}{2\pi} \int\limits_{-\infty}^{\infty} dk_z \sum_{n=-\infty}^{\infty} F(r,n,k_z) \, e^{in\phi + ik_z z} . \tag{4.3}$$

The Fourier sum in n is used since the problem is periodic in ϕ while the Fourier integral is used in k_z since the problem is infinite in axial extent. Complex exponentials are used for convenience.

Associated with the inverse transform of Eqn. 4.3, is the transform into n-k_z space. This transform is defined as:

$$F(r,n,k_z) = \frac{1}{2\pi} \int\limits_{-\infty}^{\infty} dz \int\limits_{0}^{2\pi} d\phi \, F(r,\phi,z) \, e^{-in\phi - ik_z z} . \tag{4.4}$$

The next step now becomes obvious. The field-defining equations, Eqns. 4.1 and 4.2, are Fourier transformed using Eqn. 4.4. The three-dimensional boundary value problem in (r,ϕ,z) is now reduced to a one-dimensional boundary value problem in r – for a specified azimuthal (n) and axial (k_z) mode number. The k_z spectrum is continuous, however the azimuthal modes take on the values $0, \pm 1, \pm 2, \dots.$ In n-k_z space, all quantities in Eqns. 4.1 and 4.2 become functions of only r. $E(r,n,k_z)$ and $H(r,n,k_z)$ are the variables to be computed. $J_{ext}(r,n,k_z)$ is derived analytically from Eqn. 4.4 for each

antenna configuration and $\underline{\varepsilon}(r)$ remains unchanged since it is assumed to be only a function of r.

$J_{ext}(r,\phi,z)$ can be modeled using a current sheet to represent the antenna currents. A current sheet is an infinitesimally thin current flowing on the surface of a tube of radius b. The Fourier transform of these currents yields an infinite set of current sheets of the form $J \propto J(r,n,k_z) e^{in\phi + ik_z z}$. It is the superposition of this infinite set of current sheets, with the weighting of Eqn. 4.4, which yields the desired current distribution for each antenna configuration. See Fig. 4.3. A derivation of $J_{ext}(r,n,k_z)$ for the full turn loop is shown in Appendix C.

The calculation of $\underline{\varepsilon}(r)$ proceeds as follows. The conductivity tensor is found by determining the plasma perturbed distribution function from the linearized Vlasov equation. The velocity moments of the perturbed distribution function yield the conductivity tensor, $\underline{\sigma}$, necessary for the calculation of $\underline{\varepsilon}$.[44] The linear, collisionless, Vlasov equation takes the form:

$$\frac{\partial f_1}{\partial t} + v \cdot \frac{\partial f_1}{\partial r} + \frac{q}{m}(v \times B_o) \cdot \frac{\partial f_1}{\partial v} = -\frac{q}{m}(E_1 + v \times B_1) \cdot \frac{\partial f_0}{\partial v} , \quad (4.5)$$

where $\quad f = f_0 + f_1$

$$E = E_0 + E_1$$

$$B = B_0 + B_1.$$

The solution of Eqn. 4.5 may be written as:

$$f_1(r, v, t) = -\frac{q}{m} \int_0^t E_1(r, t') \cdot \frac{\partial f_0(r, v)}{\partial v} dt' . \quad (4.6)$$

$$J_\phi (b,n,k_z) \, e^{in\phi + ik_z z} \, e^{i\omega t}$$

vacuum vessel

plasma

c

b

a

B
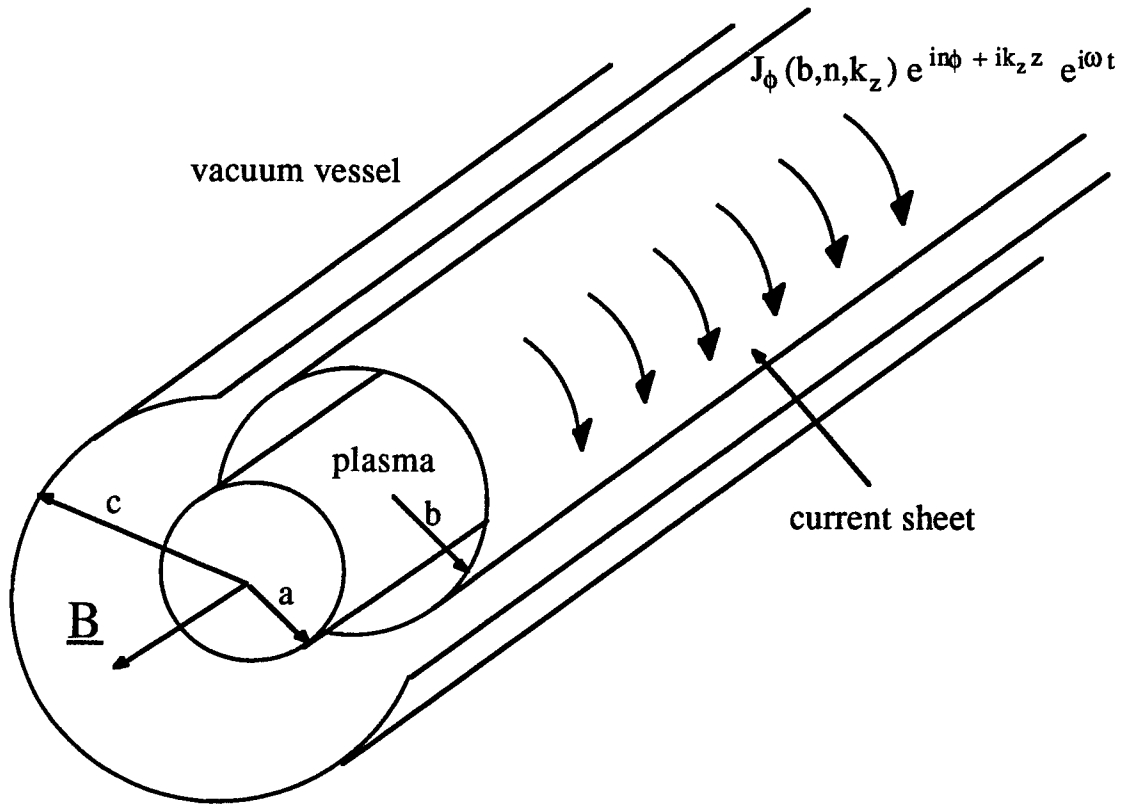
current sheet

Figure 4.3. ANTENA current sheet model for azimuthal antenna current. Actual current is formed by the superposition of an infinite set of the above sheets for $n = 0, \pm 1, \pm 2, \ldots$ and $-\infty < k_z < +\infty$.

The above integration is performed along the trajectories of the unperturbed particles – sinusoidal in x and y but constant in z along B. To evaluate f_1, an unperturbed distribution, f_o, is required. A local Maxwellian is assumed,

$$f_0(r,v) = n(r) \, \pi^{-3/2} \, v_\alpha^{-3} \, e^{-v^2/v_\alpha^2} \qquad (4.7)$$

$$\text{where} \qquad v_\alpha^2(r) = \frac{2 \, kT(r)}{m_i} \, .$$

Also, the electric field is approximated by a Taylor series expansion in r and an assumed $e^{ik_z z}$ dependence in z. The expression for $E(r)$ can be shown to take the form:[42]

$$E(r) = E(r,\phi) \, e^{ik_z z} \, . \qquad (4.8)$$

The above expression assumes $\rho_i/L_E \ll 1$ where L_E is the scale length of the wave electric field.

Using Eqns. 4.7 and 4.8, the perturbed distribution function can be determined using Eqn. 4.6. The velocity moments of the perturbed distribution function then defines the conductivity tensor which is related to the dielectric tensor as:

$$\underline{\underline{\varepsilon}} = \underline{\underline{I}} + \frac{i \underline{\underline{\sigma}}}{\omega \, \varepsilon_o} \, . \qquad (4.9)$$

The actual analytical form of this dielectric tensor is given in Ref. 42. For the plasma model developed in the ANTENA code, Eqn. 4.5 is modified by the addition of a

particle-conserving collision term to the right-hand side. This "Krook model" collision term,

$$- v f_1 + v \frac{n_1}{n_o} f_o \; ,$$

(4.10)

modifies slightly the form of $\underset{=}{\varepsilon}$ derived from the collisionless Vlasov equation.

All quantities required for field Eqns. 4.1 and 4.2 have now been calculated. The Fourier-transformed electric and magnetic fields are now solved in $n\text{-}k_z$ space and transformed back to $\phi\text{-}z$ space using Eqn. 4.3. The code can output either the non-transformed or transformed field quantities for any position $r < c$. The power absorbed by the plasma can be calculated by realizing that, locally, the plasma currents in phase with the local electric field determine the absorbed power, or

$$p(w \; / \; m^3 \;) = \tfrac{1}{2} \; Re \; (\; E \; \cdot \; J^* \;)$$

(4.11)

where $*$ indicates the complex conjugate. J is the current density defined as:

$$J \; = \underset{=}{\sigma} \, E$$

(4.12)

where $\underset{=}{\sigma}$ is calculated earlier from the velocity moments of the perturbed distribution function. Local power deposition is found using Eqn. 4.11 and total power deposition inside a cylinder of radius r_o is calculated by integrating Eqn. 4.11 for $-\infty < z < +\infty$ and $0 < r < r_o$.

The antenna loading is found by calculating the total power absorbed by the plasma (i.e. integrating Eqn 4.11 for $-\infty < z < \infty$ and $0 < r < a$) and using the relation

$$Z_{load} = \frac{2\,P_{tot}}{|\,I\,|^2}\,.$$

(4.13)

4.2. Antenna Types and Antenna Loading

The ANTENA code is used to determine the antenna type which will produce the greatest coupling to typical MIMI plasmas and subsequently the chosen antenna's loading parameters. Although, as described in Sec. 4.1, the code does not specifically account for an axially varying magnetic field, it is used to determine the scaling of antenna loading parameters as a function of antenna type, charge-to-mass ratio of the species present in the plasma, ion/electron density, plasma size, etc. The code is run on the e-machine CRAY II computer located at Lawrence Livermore National Laboratory in Livermore, California. The CRAY computers are part of the NMFECC network sponsored by the Department of Energy, United States government. The procedure to log on to the NMFECC system and run the ANTENA code is included in Appendix D as are typical input and output files for the ANTENA code.

The first concern when considering an ICR heating system for a plasma is which antenna type is most suitable. The decision must be based on availability of space in the vacuum system, location of current feedthroughs, natural antenna modes, and most importantly, how well the antenna couples to the plasma. The Nagoya III antenna, shown in Fig. 4.1 (c), is chosen for several of the above reasons. Due to good coupling characteristics, central cell ion heating in magnetic mirrors has been limited, almost

exclusively, to either single half-turn loop antennas, double half-turn loop antennas, and Nagoya III antennas. Since the double-half turn antenna has been shown to have superior coupling characteristics to the single half turn antenna, the range of antenna types is then narrowed to the Nagoya III antenna and the double half-turn loop. ANTENA code results are used to determine which of these will experience the greatest loading from the plasma and this is corroborated intuitively by considering the EM fields generated by both types of antennas. The physical model for the plasma and antenna is summarized in Table 4.1 below.

Figure 4.4 shows the important results of the runs used to determine which antenna type would best couple to the MIMI plasmas. Each data point represents antenna loading due to local power deposition integrated over the cross-section of the plasma from $0 < r < a$, for the frequency range and mass-to-charge ratios shown. The values of $m/q = 1, 3.5, 14,$ and 40 are chosen since they lie on or near ion mass-to-charge ratios found for typical MIMI running conditions. Resonant behavior is obvious for low m/q ions near $\omega = \omega_{ci}$, though it is somewhat masked by the nature of the logarithmic plot. As the mass-to-charge ratio increases, the ion Larmor radii become comparable to the radius of the plasma and a decrease in resonant coupling becomes evident as the ions are no longer tightly bound to the magnetic field lines. The major result, though, of the runs of Fig. 4.4 is the increased loading of the Nagoya III antenna. Specifically, for $\omega = \omega_{ci}$ and $m/q = 1$, the loading for the Nagoya III antenna is ~ 5 times greater than that of the double half-turn antenna. Again, these antenna loading computations are meant only for scaling purposes since the code does not completely model the experimental plasma - antenna - B field configuration. The values of Z_{ant} shown in Fig. 4.4, though, are typical of loading values found in other ICRH plasma experiments. These results showing

Table 4.1. Standard Plasma and Antenna Parameters Used in ANTENA

Input

Parameter	Variable	Value	Unit
plasma radius	a	5.08	cm
antenna radius	b	5.72	cm
vacuum vessel radius	c	7.35	cm
(r_o, ϕ_o, z_o) for calculations	rhocm	0.0	cm
	phicm	0.0	degrees
	zcm	0.0	cm
number of azimuthal modes summed	nazim	20	
antenna current	cur	100	A
magnetic field	bfld	3500	G
electron density	ntot	$5x10^{11}$	cm^{-3}
M/Q of plasma ions	mass	4	
radial density distribution	iprof	Gaussian	

significantly better loading of the Nagoya III antenna does suggest that this antenna would be the most efficient means to transfer energy to the plasma ions.

This is not an unexpected result which can be accounted for merely by considering the differences in geometry between the Nagoya III antenna and the double
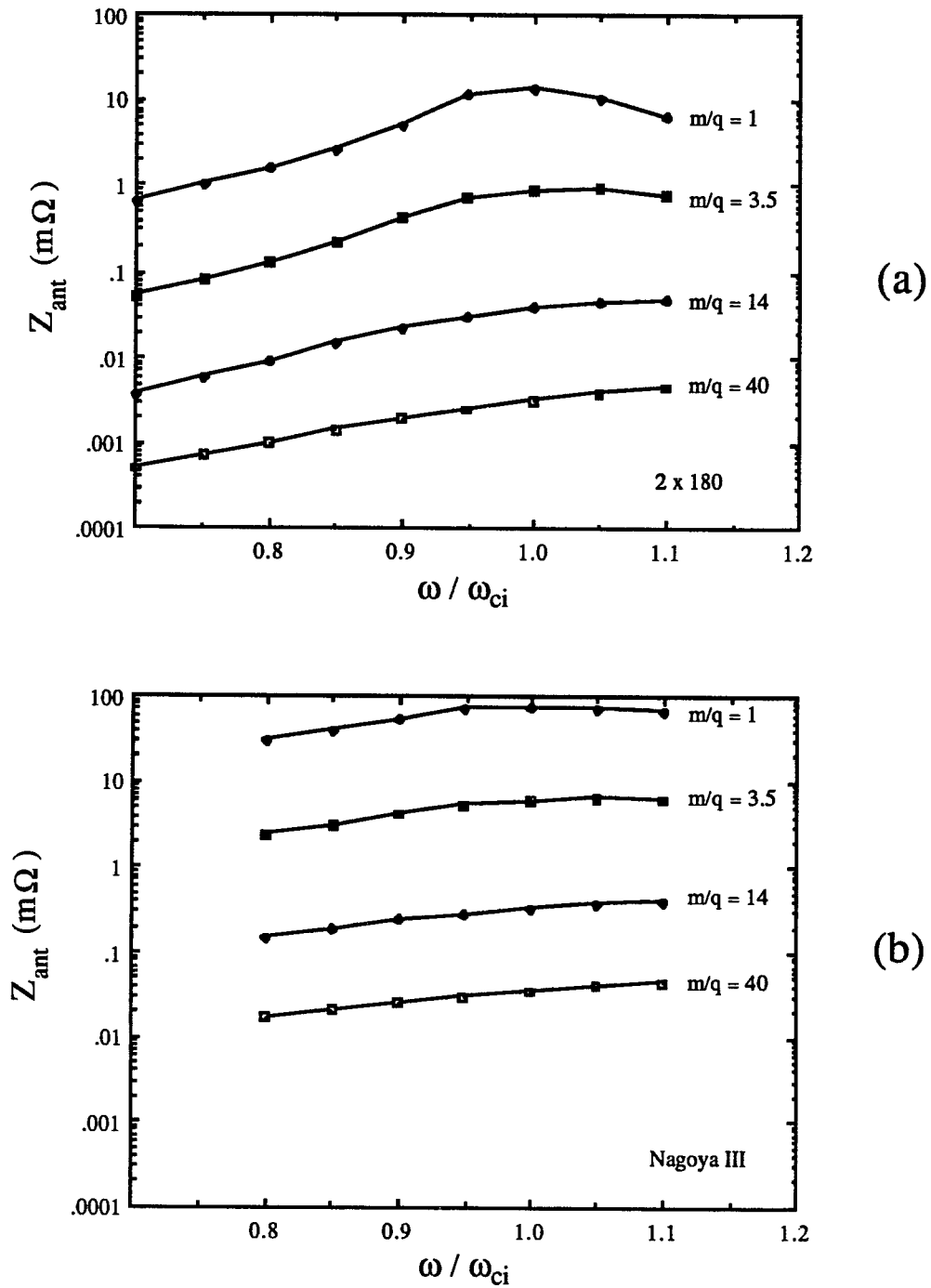
Figure 4.4. Antenna loading for the (a) *2 x 180°* loop antenna and the (b) Nagoya III antenna as a function of both frequency and mass-to-charge ratio. The Nagoya III antenna demonstrates superior coupling.

half-turn loop antenna. With the Nagoya III antenna, the axial straps serve to provide current paths between the ends of, what could be considered, two double half-turn loops (see Fig. 4.1 (c)). Between the loops, in the midplane region, the B_x fields of these two end turns add vectorially and thus provide twice the B_x field as one double half-turn loop for the same rf current. Also, both axial currents add to this same B_x field and further increases its magnitude. It is therefore evident that much higher magnetic field strengths can be attained by the Nagoya III antenna for the same input rf current.

The Nagoya III antenna also seems a good choice from the standpoint of both vacuum system availability and location of rf current feedthroughs. The geometry of the antenna is such that the copper straps, of which the antenna is made, can be positioned axially and azimuthally in the midplane region such that they do not interfere with any diagnostics. To make the rf current connection, one of the axial current paths is broken and the input is connected to one side of the break and the output to the other. Examination of Fig. 4.1 (c) shows that this will provide the proper current direction in all parts of the antenna. The fact that the antenna input and output are located at the same position allows the rf feedthroughs to be located on the same flange. This would not be true of the double half-turn antenna. This is important since long lead lengths are eliminated which would increase the inductance and resistance of the circuit used to resonate the antenna and thereby decrease the achievable antenna currents. (This will be further discussed in Sec. 4.4.) This antenna also only requires the use of one feedthrough flange, which makes available for use with another diagnostic, the extra flange required for the double half-turn antenna.

A Nagoya III antenna was built for MIMI. Its design, including characteristic dimensions is shown in Fig. 4.5. The rf current connections are made to the extended
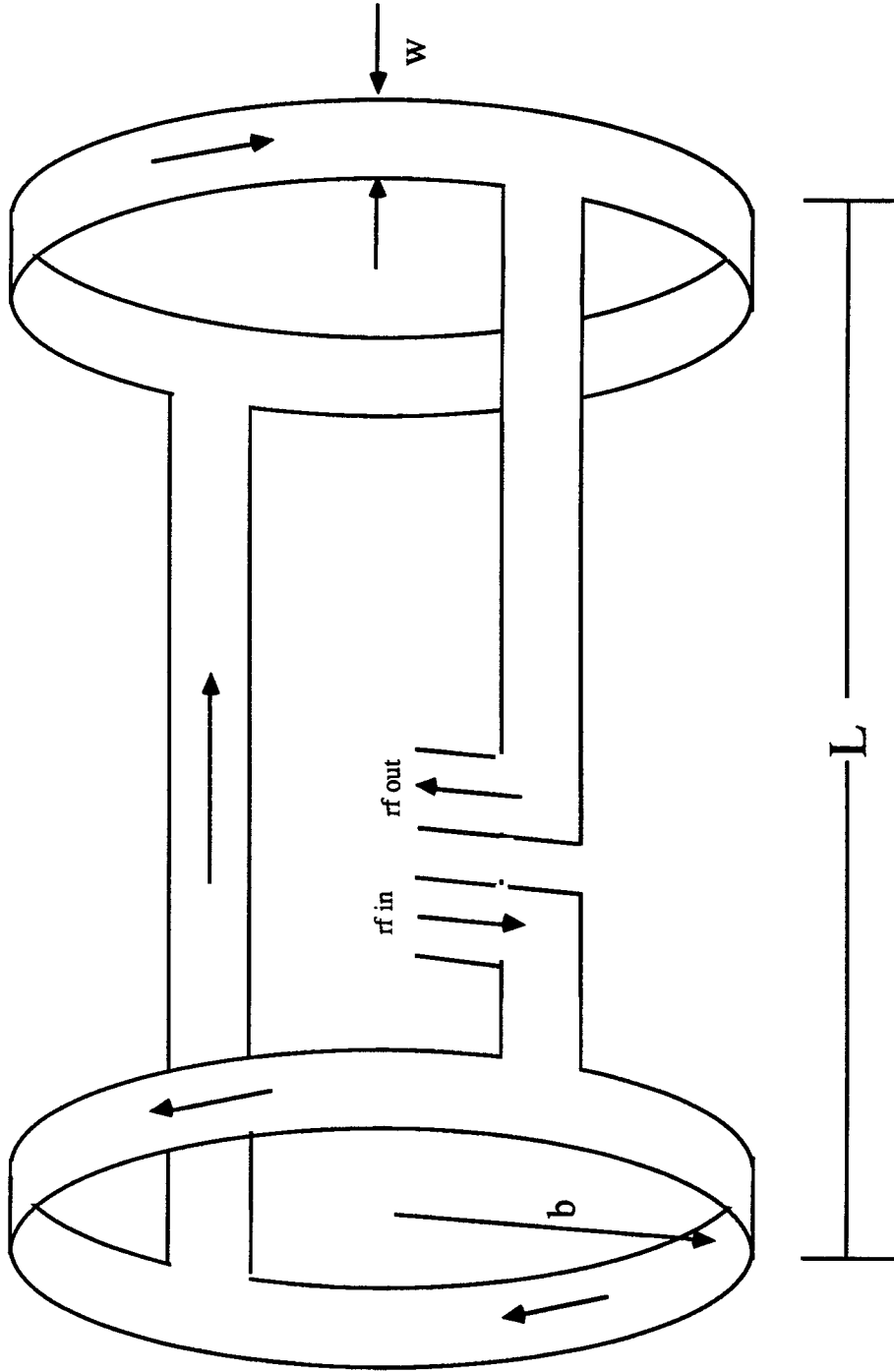
Figure 4.5. Nagoya III antenna used for ICRF heating on MIMI. The rf feeds shown are connected to high current vacuum feedthroughs. The resonant and matching circuit are located outside the vacuum system. The dimensions for the actual antenna are L = 30.5 cm, w = 1.91 cm, and b = 5.72 cm.

copper straps shown in the figure. Both input and output vacuum current feedthroughs are located on the north edge of the west rectangular port flange. See Fig. 3.1. The matching and resonant circuit will be discussed in Sec. 4.4.

To test the accuracy of the ANTENA code, the vacuum inductive magnetic field of the antenna is measured using a B-dot loop and compared with computed values. The fields computed using the ANTENA code are shown, in Fig. 4.6, to be in excellent agreement with the measured fields. Care must be taken, however, to assure that a sufficient number of azimuthal modes are summed in the B-field computation. Otherwise, fictitious currents will appear at $r = r_{antenna}$ and $\Theta = \pi/2$, π, and $3\pi/2$. Twenty azimuthal modes appear to be a sufficient number to achieve accurate computed magnetic field values.

The parallel-wave-number (k_z) spectrum is calculated for this specific antenna for the plasma detailed in Table 4.1. This k_z spectrum is reported as ion power absorption as a function of k_z, the Fourier-transformed axial position variable, z. These k_z values represent the wave numbers of the waves present in the plasma. Wave propagation in a medium implies that the dimensions of the medium are comparable to or larger than the wavelength of the propagating wave. Initially to assure this is true, the radii of the plasma, antenna, and vacuum vessel have been artificially increased to *50 cm, 55 cm,* and *60 cm* respectively from the actual values shown in Table 4.1. The antenna is then excited just below the cyclotron frequency for an *m/q = 4* ion. The waves propagating from the antenna, along the axis, produce a characteristic k_z spectrum.

The CMA[45] diagram for a cold plasma yields insight into the computed spectrum for this configuration. The parameter regime in which MIMI is operated is marked by an * on the CMA diagram of Fig. 4.7 (i.e. $\omega < \omega_p$ and $\omega < \omega_{ci}$). In this magnetic field and density regime, it is evident that two waves will propagate. Regardless of the
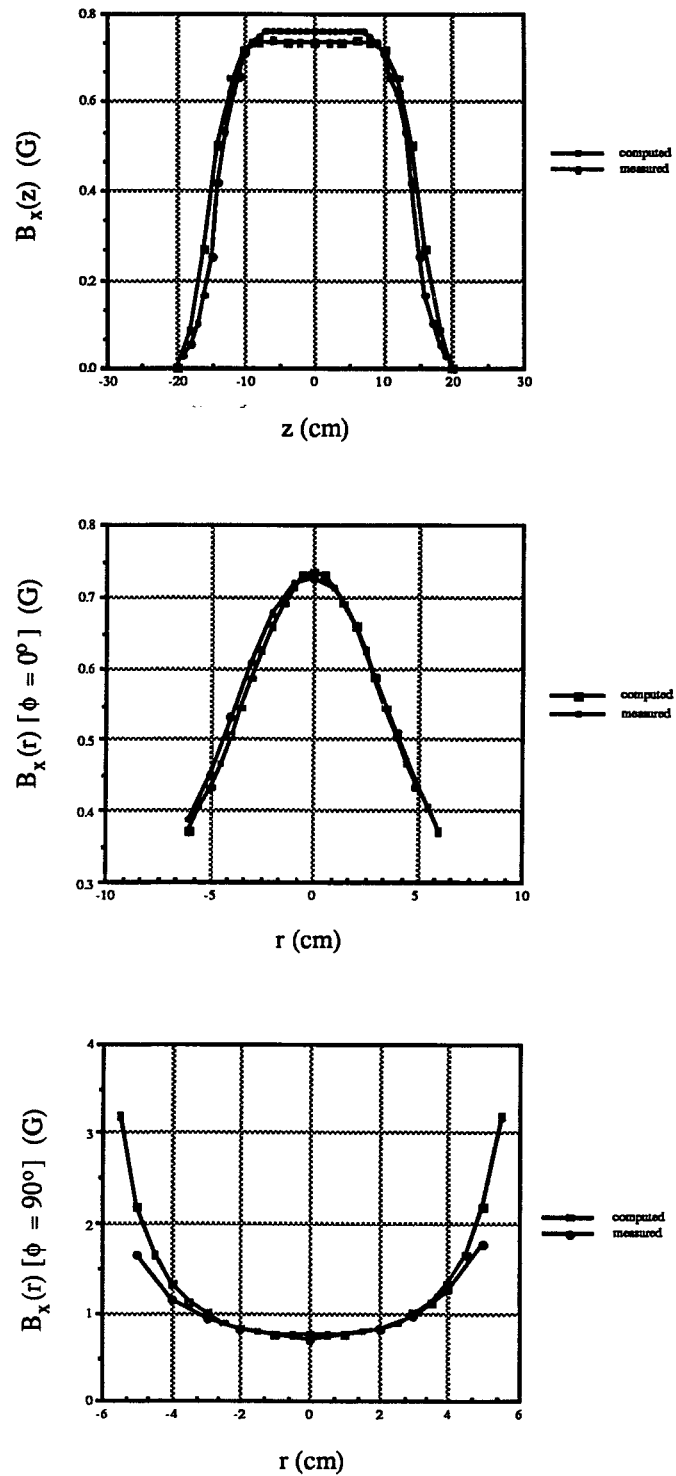
Figure 4.6. Comparison of measured and computed magnetic fields of ICRH antenna built for MIMI. The antenna is excited at *1.0 MHz* with a peak rf current of *10 A*.

Figure 4.7. CMA diagram for a two-component plasma. The magnetic field can be considered to be oriented along the y axis. The MIMI operating parameter regime is marked with a * showing that, for parallel propagation, right and left-hand circularly polarized waves will propagate.

direction of propagation, one wave always has a larger phase velocity than the other. The R-X wave will therefore be referred to as the fast wave and the L wave as the slow wave, as is commonly found in the literature. One can consider the magnetic field oriented along the positive y axis of the CMA diagram. For perpendicular propagation, the fast wave takes the form of a pure X wave while the slow wave does not propagate. Similarly for parallel propagation, the fast and slow waves become purely-right and purely-left-hand, circularly-polarized waves, respectively. Waves propagating at an oblique angle to the magnetic field are of mixed nature. Mirror machines are concerned with parallel propagation whose wave dispersion relation takes the form:

$$k_z {}^R_L = \frac{\omega}{c} \left[\frac{\omega^2 \mp \omega \, \omega_{ce} - \omega_{ce} \, \omega_{ci} - \omega_p^2}{\left(\omega \pm \omega_{ci} \right) \left(\omega \mp \omega_{ce} \right)} \right]^{1/2} . \tag{4.14}$$

Since the above equation is derived assuming a cold, collisionless plasma, it is singular at $\omega = \omega_{ci}$. To calculate a realistic value for the fast and slow wave numbers, a wave is excited slightly below the ion cyclotron frequency at $\omega = .95 \, \omega_{ci}$. The wave numbers calculated for the fast and slow wave are thus:

$$k_R \;\; = k_{fast} \;\; = \;\; .011 \; cm^{-1} \, ,$$

$$k_L \;\; = k_{slow} \;\; = \;\; .066 \; cm^{-1} .$$

ANTENA code runs for the above parameters show power to be coupled to only two azimuthal modes, $m = -1$ and $m = +1$. The computed k_z spectra for these modes are shown in Fig. 4.8. The k_z values associated with the $m = -1$ and $m = +1$ modes correspond to the predicted values for k_{slow} and k_{fast} quite closely. These computed k_z
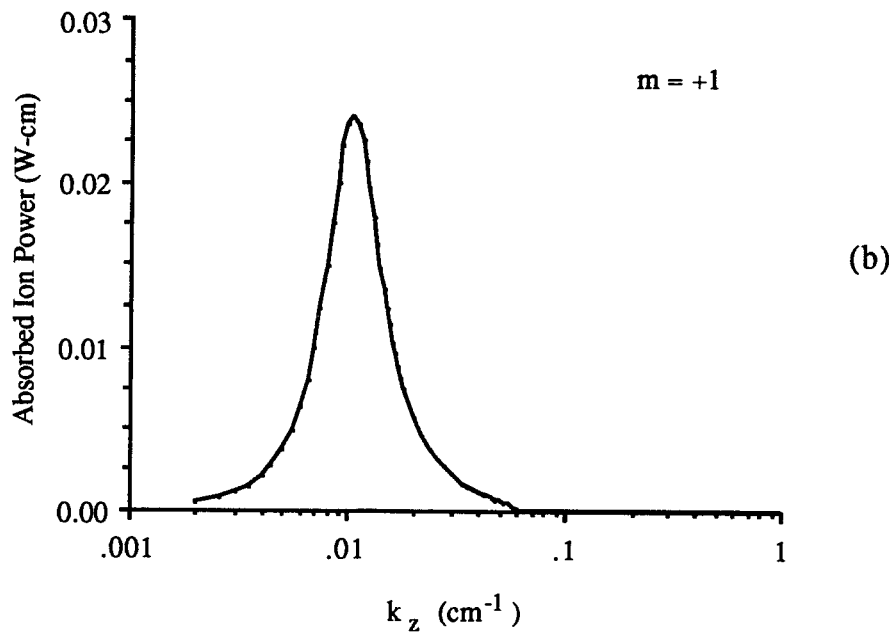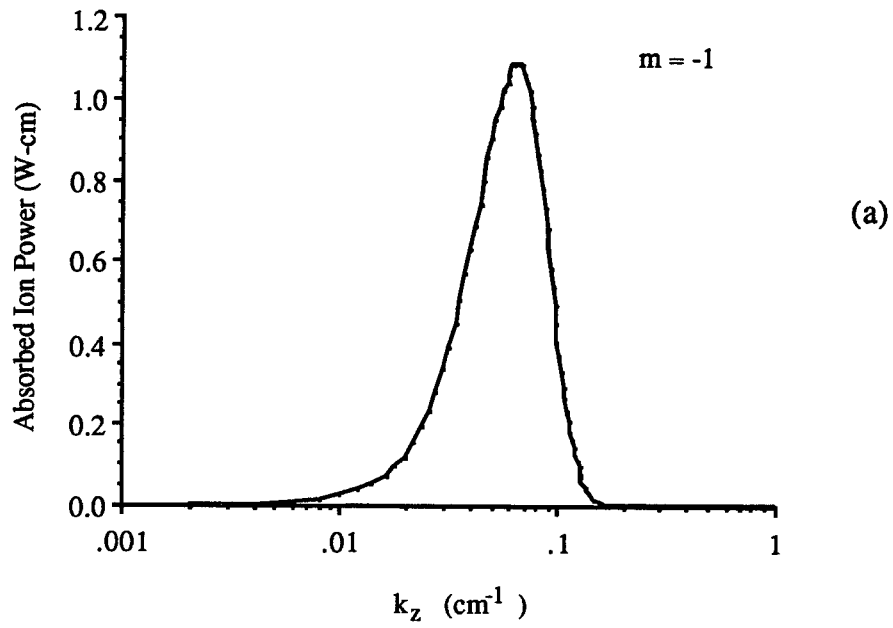
Figure 4.8. Parallel-wave-number spectrum on axis for large plasma for azimuthal modes (a) $m = -1$ and (b) $m = +1$.

spectra are indeed the spectra for the slow and fast waves, each wave possessing distinctly different coupling characteristics. As discussed earlier, the slow wave is a left-hand, circularly-polarized wave whose electric field rotates in the same sense as the ions. The fast wave is a right-hand, circularly-polarized wave whose electric field rotates in the same sense as the electrons but at a frequency much too low to be cyclotron damped. It would be expected, therefore, that the slow wave would couple much more strongly to the plasma than the fast wave. This is indeed the case as evidenced by the antenna loading computations of Fig. 4.8.

The case for the actual conditions of Table 4.1 is now considered. For this case, the plasma has become considerably smaller than the wavelength of the slow wave. This will distort the k_z spectrum of Fig. 4.8. The spectrum of a MIMI-sized plasma, shown in Fig. 4.9, has picked up an extra lobe on the upper end of the spectrum and widened due to the decrease in plasma size. For this case, the travelling, left-hand circularly-polarized wave is not the dominant mechanism for power transfer to the ions. This is discussed in the section following.

4.3. ICRH Coupling to MIMI-Sized Plasmas

Since ICRH wavelengths are typically much larger than the characteristic dimensions of small mirror systems, the entire concept of resonant interaction between a plasma wave and energy absorbing ions must be rethought. Central to the idea of wave propagation in a plasma is the existence of a plasma medium which is comparable to or larger than the wavelength of the wave. For slow wave heating, the wave is thought to propagate from a high magnetic field region to a magnetic beach where $k_z \to 0$ as $\omega \to \omega_{ci}$. At this time, plasma ions are resonant with the electric field of the wave and a
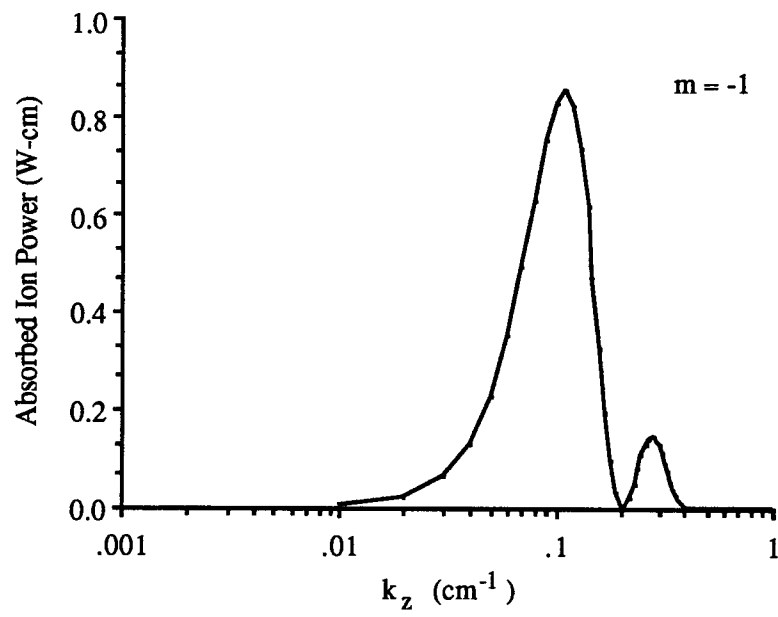
Figure 4.9. Parallel-wave-number spectrum for MIMI-sized plasma. Note the change from the larger plasma of Fig. 4.8.

net energy transfer occurs.

This scheme, however, is not applicable to MIMI-sized plasmas. Figure 4.9 shows slow wave heating wavelengths for MIMI to be:

$$\lambda_{slow} = \frac{2\pi}{k} = \frac{2\pi}{.1\ cm^{-1}} = 63\ cm\ . \qquad (4.15)$$

MIMI plasma are less than *5 cm* in radius and less than *20 cm* in length. This traveling, slow-wave-heating scheme does not then apply. A more realistic view of the absorption mechanism involves antenna near fields and large resonance widths.

The near field of an antenna is a large oscillating electromagnetic field which attenuates very quickly with increased distance from the antenna. It is evanescent in the plasma and will penetrate a plasma column a distance of:

$$d_{penetration} = \frac{V_A}{\omega} \qquad (4.16)$$

where V_A = *Alfven velocity*

ω = *excitation frequency.*

This distance is typically *1 m* for MIMI plasmas and full penetration of the near field is expected. Since the antenna surrounds the plasma to be heated, no significant attenuation of the near fields due to spatial separation of the plasma and antenna occurs.

Another indication that near field absorption is the mechanism for power transfer to the plasma ions is the density dependence of the antenna loading. Near field loading is predicted to be linear with density while slow wave loading is expected to be independent

of density for $.8\ \omega_{ci} < \omega < \omega_{ci}$. Figure 4.10 shows the ANTENA computed density dependence of the antenna loading to be consistent with a near-field absorption model.

Since it appears that the antenna near field is responsible for the majority of the energy transfer to the ions, the concept of resonance must now be investigated. An ion will absorb energy through a resonant interaction if, in its frame of reference, it sees a constant accelerating electric field. Since, in a mirror machine, ions are constantly spiraling around magnetic field lines, the wave electric field must cycle at a frequency equal to the ion cyclotron frequency for the ion species of interest. This is the frequency then, at which the antenna that surrounds the plasma is excited. The near field of the antenna creates an oscillating electric field throughout the entire plasma, provided $r_p < L_{antenna}$ (true for MIMI). The question then arises over how much of its path an ion is resonant, or equivalently, during what part of its bounce time does the particle remain in phase with the exciting field. If $v_{\perp\ ion} = v_{\perp}$ is the perpendicular ion velocity and E_+ is the right-hand, circularly-polarized component of the excited field, then the condition of "remaining in phase" requires that $v_{\perp}$ does not slip in phase with respect to E_+ by more than 90° during one pass through resonance. This phase slip can be expressed as:[47]

$$\phi(\ t\ ) = \int_0^t \Omega(\ t'\ )dt' + k_z z - \omega t \qquad (4.17)$$

where Ω is the local ion cyclotron frequency. If the mirror magnetic field is considered parabolic, $\Omega(t)$ can be written as:

$$\Omega(\ t\ ) = \Omega_o\ (\ 1 + \frac{\Lambda^2}{L^2}\ sin^2\ \Omega_b t\ ) \qquad (4.18)$$
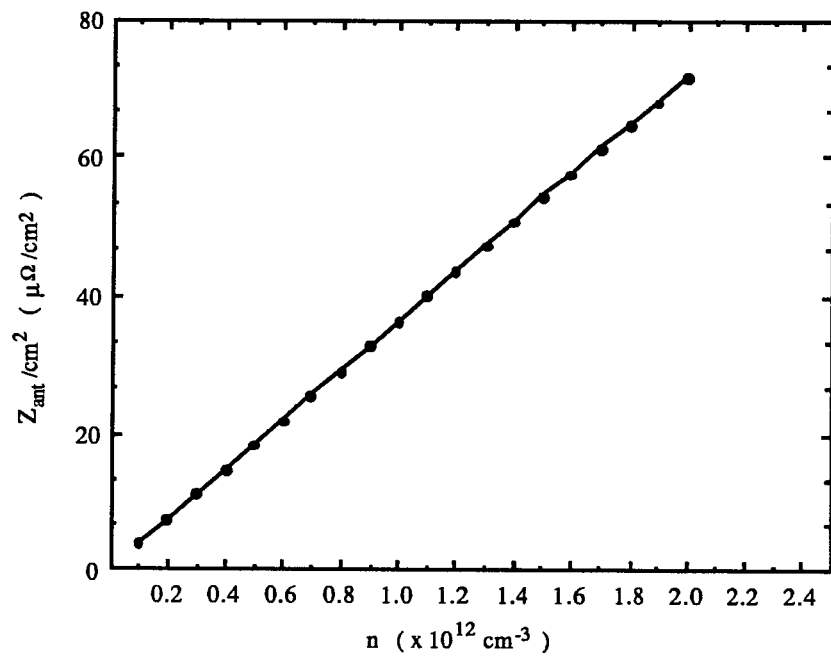
Figure 4.10. Antenna loading per unit cross section area computed at center of MIMI-sized plasma as a function of density. Linear scaling suggests near-field absorption.

assuming,

$$B = B_o \left(1 + \frac{z^2}{L^2} \right) .$$

(4.19)

In this well, an ion's gyrocenter mirrors with the axial variation:

$$z = \Lambda \sin \Theta$$

(4.20)

where $\quad \Lambda = \left(\frac{v_{z_o}}{v_{\perp_o}} \right) L \quad$ and $\quad \Theta = \Omega_b t = \left(\frac{v_{\perp_o}}{L} \right) t .$

All "o" subscripted variables refer to midplane quantities. The following expression for $\phi(t)$, the phase slip experienced between $v_\perp$ and E_+ in time t, is derived from Eqns. 4.17 - 4.20.

$$\phi(t) = \frac{\Omega_o t}{2} \left(\frac{v_{z_o}}{v_{\perp_o}} \right)^2 \cos 2\Theta_1$$
$$- \frac{\Omega_o}{4\Omega_b} \left(\frac{v_{z_o}}{v_{\perp_o}} \right)^2 \sin 2\Omega_b t + k_z \left(\frac{v_{z_o}}{v_{\perp_o}} \right) L \sin \Omega_b t$$

(4.21)

where Θ_1 is the resonance angle defined by the equation:

$$z_{res} = \Lambda \sin \Theta_1 .$$

(4.22)

Given the above expression for the particle phase slip, it is evident that resonance widths can become very large. Alternatively, this means that the particle may remain in phase with the field during a significant fraction of its transit through the mirror. The phase slip experienced by a particle in one-half bounce time, $t_b / 2$ ($= \pi / \Omega_b$), is:

$$\phi(t_b / 2) = \frac{\pi \, \Omega_o}{2 \, \Omega_b} \left(\frac{v_{z_o}}{v_{\perp_o}} \right)^2 \cos 2\Theta_1 \qquad radians \; . \qquad (4.23)$$

For midplane heating where $z_1 = 0 \rightarrow \Theta_1 = 0 \rightarrow \cos 2\Theta_1 = 1$, or turning point heating where $z_1 = \Lambda \rightarrow \Theta_1 = \pi/2 \rightarrow \cos 2\Theta_1 = -1$, the maximum phase slip experienced in one-half bounce time is:

$$\left| \phi(t_b / 2) \right|_{max} = \frac{\pi \, \Omega_o}{2 \, \Omega_b} \left(\frac{v_{z_o}}{v_{\perp_o}} \right)^2 \qquad radians \qquad (4.24)$$

which for MIMI reduces to:

$$\left| \phi(t_b / 2) \right|_{max} = 340 \, \frac{Q}{M^{\frac{1}{2}}} \left(\frac{T_{||o}(eV)}{T_{\perp o}^{\frac{3}{2}}(eV)} \right) \qquad radians \qquad (4.25)$$

with M in amu and Q in esu. Using the above expression, a singly-ionized argon ion with a 5 eV parallel temperature, need only be heated above 30 eV to experience resonance throughout its transit of the mirror. This is quite an unexpected result.

The concept of a particle experiencing resonance throughout a large fraction of its path in a mirror is far from the image of a wave propagating in a plasma to a well-defined location where the ions are resonant with the wave fields. This loss of sensitivity to spatial location of the resonance allows for ion energy absorption for a wide range of

ICRH frequencies, even frequencies which place the "resonance" location outside of the particle path. It also allows for energy absorption by more than one charge state in a plasma for the same excitation frequency. It should be remembered, however, that this type of coupling is generally much less efficient than coupling due to resonance with a standard right-hand, circularly-polarized traveling wave.

4.4. Matching and Resonant Circuit Design

Plasma ions in MIMI are heated by the presence of large electromagnetic fields, oscillating at the local ion cyclotron frequency. These oscillating fields are created by large rf currents flowing through the conducting bars of an antenna which surrounds the plasma. The antenna rf currents should be as large as possible to couple the greatest possible power to the resonant ions. The circuit which produces these large currents and also matches the complex antenna impedance to the source output impedance is discussed below.

The large rf currents are produced by resonating the antenna with its own inherent inductance. A parallel resonant circuit is used. The currents circulating in the resonant portion of the circuit become much larger than that supplied by the rf power source. This source is, invariably, a linear rf amplifier with a bandwidth large enough to cover the frequency range of interest. It too has requirements for efficient operation, the most limiting of which is the requirement that the load connected across the amplifier output be matched to the amplifier's output impedance, R_g (generally $50\ \Omega$ real). This "matching" assures the maximum power transfer to the connected load.

Figure 4.11 (a) illustrates the circuit which will both resonate the antenna and transform the complex load to *50 Ω* real. The capacitors, C_1 and C_2, in the figure are actual physical capacitors, however, the R_s is included to represent losses due to the non-ideal nature of the inductor. Ideally, an inductor is completely reactive but in practice this is never the case. This must be considered when designing a circuit with reactive components. The figure of merit for an inductor is its Q_o value. The Q_o of an inductor represents the degree of energy loss experienced by an rf signal as it passes through the inductive element. The loss mechanisms appear in the form of resistance in the inductor wires, large fringing fields, etc. Low losses are experienced in a high Q_o inductor. The Q_o value is related to the equivalent series resistance, R_s, by:

$$Q_o = \frac{\omega L_{inductor}}{R_s} .$$ (4.26)

With the frequency dependent R_s included in the model, the inductor representing the antenna in Fig. 4.11 (a), can be considered ideal. Q_o values for typical inductors range from *10* to over *300*. For ease of analysis, the series R_s is converted to a parallel R_p which is valid for $\omega L >> R_s$. These equivalent resistances are related by:

$$R_p = Q_o^2 R_s = Q_o \omega L .$$ (4.27)

The final circuit used in the analysis is shown in Fig. 4.11 (b).

The two conditions previously mentioned may now be imposed on the circuit of Fig. 4.11 (b). The resonance condition requires:
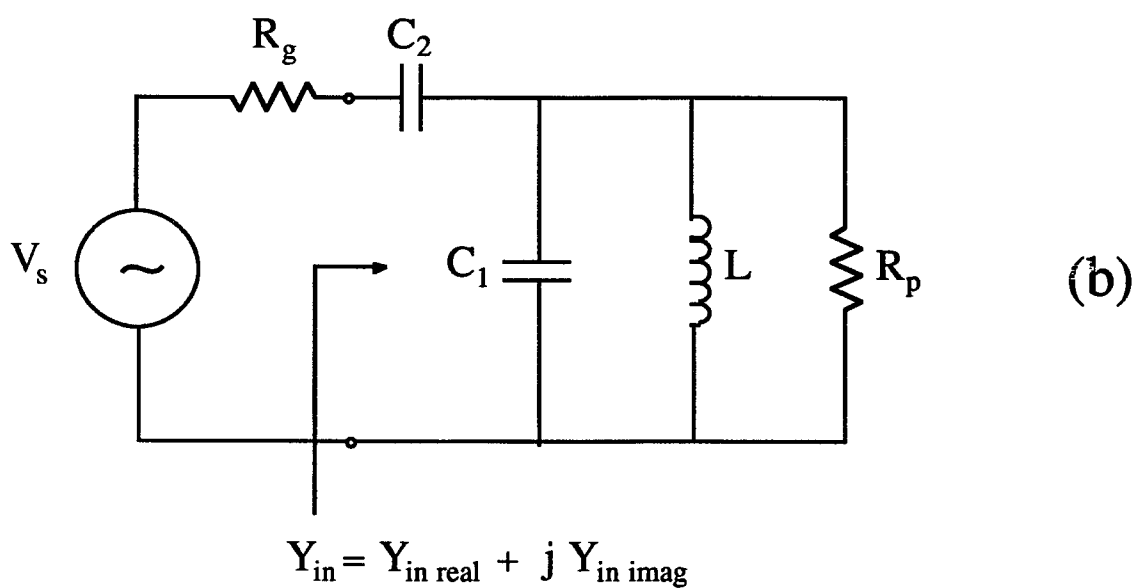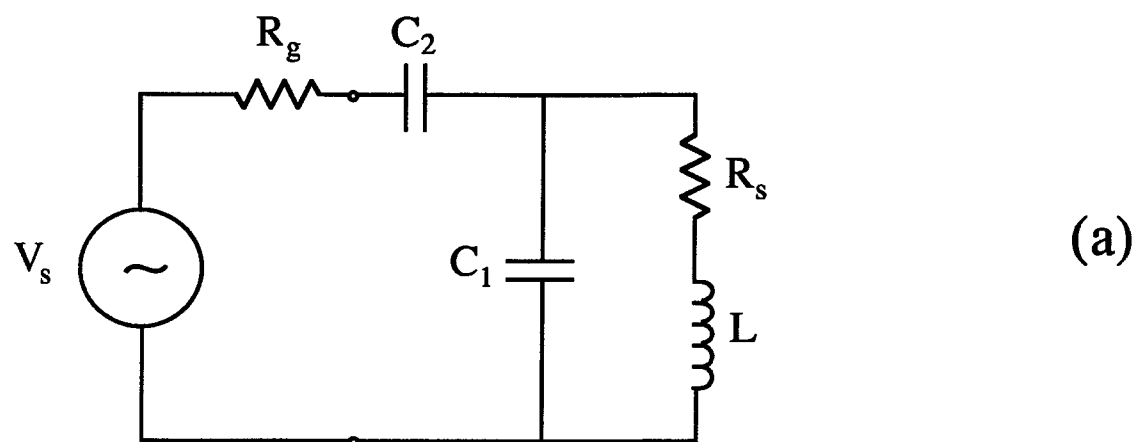
Figure 4.11. Resonant and matching circuit for ICR heating system. Losses in the antenna are modeled with (a) an equivalent series resistance and (b) with an equivalent parallel resistance. R_s and R_p are related as $R_p = Q_o^2 R_s$.

$$Y_{in \ imaginary} = 0 \ . \tag{4.28}$$

The matching condition requires:

$$Y_{in \ real} = \frac{1}{R_g} \tag{4.29}$$

where R_g is the output impedance of the source. Imposing Eqns. 4.28 and 4.29 on the circuit of Fig. 4.11 (b) yields requirements on C_1 and C_2 to assure resonance and matching. The requirements may be written in terms of known circuit parameters.

$$C_1 = \frac{1}{\omega_o L} - C_2$$

$$\tag{4.30}$$

$$C_2 = \frac{1}{\omega_o} \left(\frac{1}{Q_o \ \omega_o \ L \ R_g} \right)^{\frac{1}{2}}$$

The current which will flow through the inductor/resistor pair of Fig.4.11(b) at resonance may now be calculated for a given peak source voltage. This current may be shown to be:

$$\left| I_L \right| = \frac{V_s}{R_g} \left(\frac{1}{1 + R_p / R_g} \right)^{\frac{1}{2}} Q_L \tag{4.31}$$

where $\qquad Q_L = loaded \ Q \ of \ circuit$

$$= \frac{1}{\dfrac{1}{Q_o} + \dfrac{1}{Q_{ext}}}$$

$$Q_o = \frac{R_p}{\omega_o L}$$

$$Q_{ext} = \frac{\left(R_g \ / \ \omega_o^2 \ R_g^2 \ C_2^2 \right)}{\omega_o L} \ .$$

The above expression assumes $Q_o >> 1$. This represents a current increase over a non-resonant circuit of:

$$\frac{\left| I_L \right|_{resonant \ and \ matched}}{\left| I_L \right|_{non-resonant}} = \left(\frac{1}{1 + R_p / R_g} \right)^{\frac{1}{2}} Q_L \qquad (4.32)$$

Since, for the frequency range of interest, $R_p \sim R_g$, the resonant current increase is seen to be significant since $Q_L >> 1$. Comparing Eqn. 4.31 to a resonant but non-matched circuit (i.e. $C_2 \longrightarrow \infty$) yields:

$$\frac{\left| I_L \right|_{resonant \ and \ matched}}{\left| I_L \right|_{resonant \ and \ non-matched}} = \left(\frac{1}{1 + R_p / R_g} \right)^{\frac{1}{2}} \frac{Q_{L \ res \ \& \ matched}}{Q_{L \ res \ \& \ non-matched}} \qquad (4.33)$$

$$= \frac{1}{2} (1 + R_p / R_g)^{\frac{1}{2}} \ .$$

This is a somewhat surprising result. Equation 4.33 shows that the highest currents are not always attained with a matched load. Specifically, if the rf frequencies of interest are

low enough so that R_p ($=Q_o \omega_o L$) is small, then the highest currents are attained in the unmatched case. This condition occurs when

$$f \leq \frac{3 R_g}{2 \pi Q_o L} .$$

(4.34)

Therefore, if the inequality of Eqn. 4.34 is satisfied and the rf source is stable for any impedance load (reactive as well as resistive) then matching is not necessary or desirable. If the source requires a resistive load, then matching will be required, after the circuit of Fig. 4.11 (b), and the corresponding decrease of resonant current must be tolerated.

To calculate this threshold frequency for typical MIMI operating parameters, the following measured values are used: $Q_o = 50$, $L = .6 \, \mu H$, $R_g = 50 \Omega$. The threshold frequency below which matching is not required is:

$$f_{threshold} = 800 \ kHz .$$

(4.35)

This is a typical ICR heating frequency as it corresponds to the cyclotron frequency for $m/q = 6$ ions in a $3 \ kG$ magnetic field. Therefore, since the ENI rf amplifier used is stable for reactive loads, the resonating circuit is, at most times, not matched to the source.

The schematic for the RF antenna drive is shown in Fig. 4.12. The workhorse of the circuit is a $60 \ dB$ gain, ENI A500 rf amplifier. It is capable of driving a $50 \ \Omega$ load at $500 \ W \ CW$. Since the impedance of the source at resonance is 25-$75 \ \Omega$ real, the power dissipated in the antenna at full power would cause both the antenna to overheat and the soldered circuit elements to melt. For this reason, the $1 \ mW$ rf drive required for the ENI
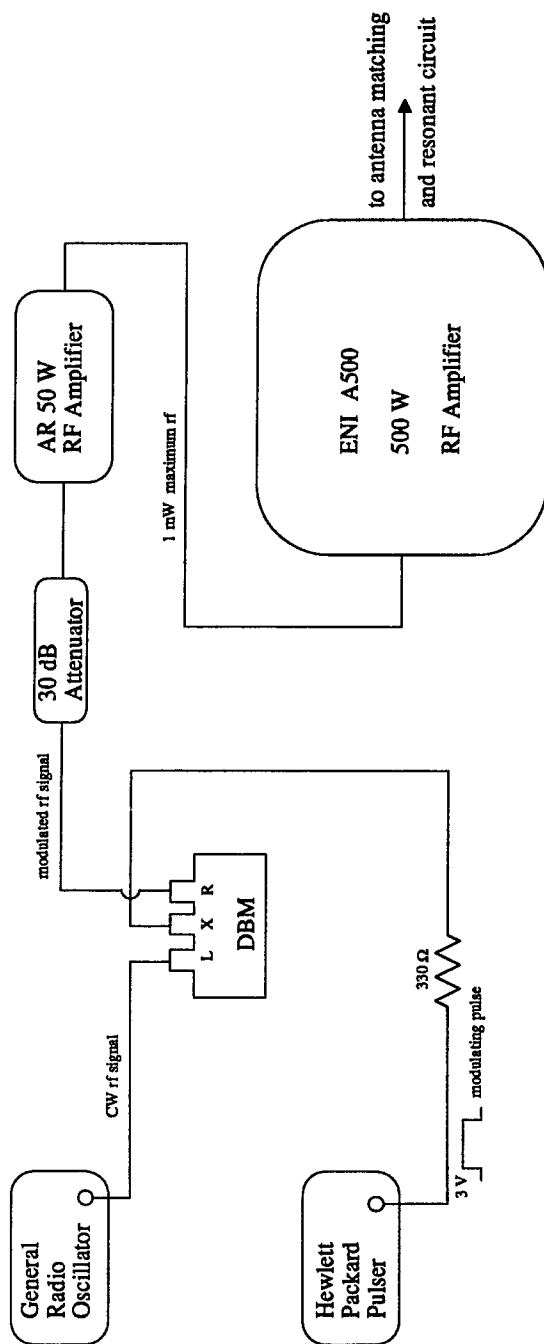
Figure 4.12. Resonant antenna RF drive schematic. The double-balanced mixer/HP pulser provides the modulated rf pulse. The 30 dB attenuator/AR amplifier is necessary since the minimum undistorted oscillator output is 2 mW. The 50 W amplifier is then used as the drive for the 60 dB gain ENI amplifier.

amplifier is modulated so that an instantaneous power of *500 W* is applied to the antenna resonant circuit but for pulse widths of only *45 ms*. This rf pulse is timed to bracket the plasma pulse. Using this method, *500 W* of instantaneous rf power is applied during the entire plasma shot but the average power is limited to *17 W*.

The modulation is performed with a double-balanced mixer. The two inputs are a *CW* rf signal and a gating pulse. When the gating pulse is "high", the rf signal passes to the output unattenuated but when the gating pulse is "low", the rf signal is attenuated *25 dB*. The *330 Ω* resistor at the output of the Hewlett-Packard pulser is required to limit the current into the DBM. Unfortunately, the oscillator outputs a distorted signal below *2 mW*, which is greater than the *1 mW* maximum input to the ENI amplifier. Therefore, after passing through the DBM, the modulated rf signal is attenuated *30 dB* and then amplified by an Applied Research *50 W* amplifier to levels of *0-1 mW*.

Antenna loading by the plasma during the rf pulse is usually a small, if not immeasureable effect. Assuming a typical loading of $R_p = .1\ \Omega$ and a reasonable antenna Q_o of *50*, the $\Delta\Theta_Z$ due to plasma loading can be calculated as:

$$\Delta\Theta_Z = tan^{-1}\frac{\omega_o L}{R_s + R_p} - tan^{-1}\frac{\omega_o L}{R_s} \qquad (4.36)$$

where $R_s = .075\ \Omega$ for $Q_o = 50$ and $\omega = 2\pi(1MHz)$. This yields a $\Delta\Theta_Z = 1.5^o$. This loading effect is too small to measure by standard rf loading detector techniques and therefore loading measurements will not be included in the work presented here.

CHAPTER 5

MODELING

Many processes occur in the plasma of an ECR ion source which affect the
ultimate achievable charge state distribution. These processes are strongly dependent on
plasma parameters such as electron and ion densities and temperatures, ion mass, neutral
density, average Z, etc. as well as reaction cross sections for single-impact ionization,
multiple-impact ionization, charge exchange, and radiative recombination. The processes
which dominate vary from source to source and depend upon individual operating
parameters. An attempt is made here to model the MIMI plasma and the dominant
processes which most strongly affect MIMI steady-state distributions. Two competing
collisional ionization processes are described. The modeling involved in a steady-state,
zero-dimensional computer code, ICSD, used to compute ion confinement times and
equilibrium charge state distributions is presented, as is a method to compute expected ion
endloss energy distributions. Sample results are presented in this chapter while
comparisons with experimental data are included in chapter 6.

5.1. The Ionization Process

The only significant process that occurs in MIMI plasmas which "bumps" up a
neutral atom or ion to a higher charge state is electron collisional ionization. This
collisional ionization can take the form of single-impact ionization, where one free
electron-neutral atom interaction results in the production of an i-times ionized ion, or

multiple-impact ionization, where a single electron is removed with every electron-ion collision to produce, after i collisions, an i-times ionized ion. Both the single and multiple impact ionization processes can be important.

Single-impact ionization, also known as Auger ionization, creates a multiply-charged ion from a neutral atom by the following process:

$$A^o + e^- \rightarrow A^{n+} + (n+1)e^-. \tag{5.1}$$
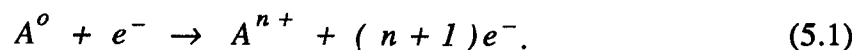
This occurs when a free electron removes an inner-shell electron from a neutral atom. The vacancy is filled by an electron from a higher shell and the difference in binding energy is either released in the form of a photon (radiative de-excitation) or transferred to another electron in the shell structure of the atom (non-radiative de-excitation). If this energy is larger than the binding energy of that electron, it is removed to the continuum. Radiative de-excitation effectively moves the original vacancy to a higher shell while while non-radiative de-excitation effectively creates two vacancies in a higher shell from the original vacancy. For low-Z ions, however, non-radiative de-excitation dominates as it does for outer-shell vacancies in all ions. Each of the two new vacancies from the Auger transition are then capable of creating two more vacancies and a cascade develops until the vacancies reach the outer-most shell. A multiply-charged ion has then been produced. The entire process requires less than 10^{-15} s and, on the time scale of any experiment, occurs instantaneously. Figure 5.1 shows the production of a Kr^{18+} ion due to one original vacancy in the $1s$ subshell of a neutral krypton atom.

A process known as "electron shake-off" can supplement Auger ionization. If the ejection of the inner-shell electron from the Auger ionization is rapid enough, the
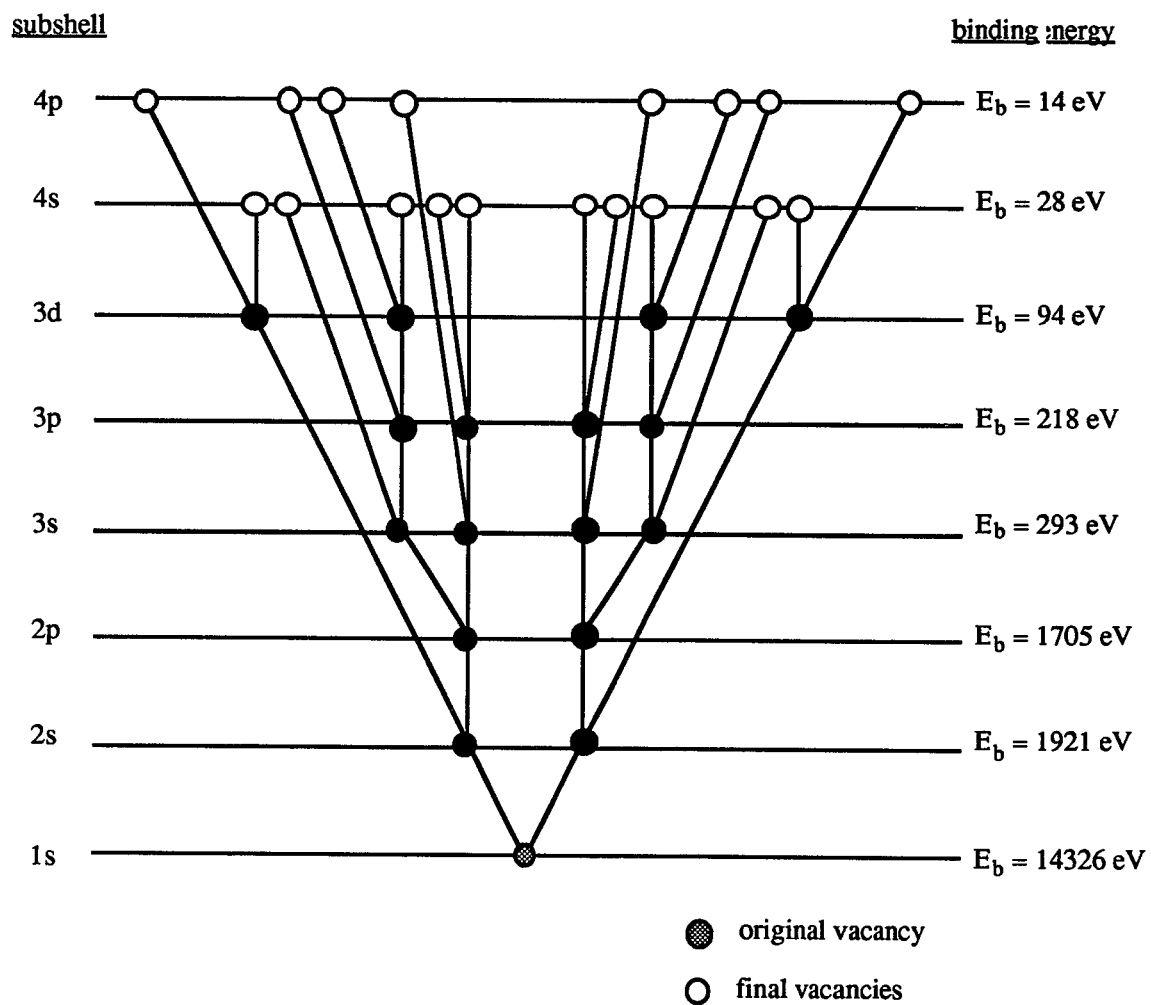
Figure 5.1. Auger ionization in krypton. Production of a Kr^{18+} ion from the single ionization of an inner shell electron.

remaining bound electrons, which have orbital velocities small compared to the ejected electron's, experience a sudden perturbation due to the sudden change in the central potential and screening constants. They may undergo a transition to an excited state or to the continuum as a result of this perturbation. Electron shake-off is required to account for some observed ionization states which are forbidden by Auger ionization alone. Calculations have shown that significant fractions of the higher charge states of specifically, neon, can be accounted for by electron shake-off.[48]

Unfortunately, cross sections for the Auger and electron shake-off ionization processes are not well known. Commonly, the cross section is modeled using the Bethe-Born approximation:[49]

$$\sigma_o^i (E) = \sigma_o^{i*} \frac{E_{ai}}{E} \ln\left(\frac{E}{E_{ai}}\right) .$$

(5.2)

Here, E_{ai} is the threshold energy for the process (i.e. the binding energy for the subshell where one vacancy is capable of creating i vacancies). σ_o^{i*} is a difficult value to determine. Some experimental work has been performed to determine σ_o^{i*} for the noble gases.[50-52]

In contrast to the single-step process, multiple-step ionization creates multiply-charged ions by successive collisional ionizations, each of which removes one electron per impact.

$$A^{(i-1)+} + e^- \rightarrow A^{i+} + 2e^-$$

(5.3)
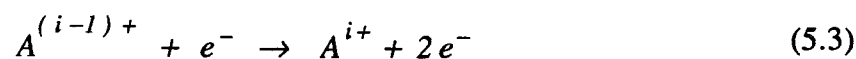
This is also modeled with the Bethe-Born approximation as:[53]

$$\sigma_i^I(E) = \sigma_i^{I*}\left(\frac{E_o}{E_{bi}}\right)^2\left(\frac{E_{bi}}{E}\right)\,ln\left(\frac{E}{E_{bi}}\right) \tag{5.4}$$

where E_O = *ionization potential of*
             neutral atom

         E_{bi} = *ionization potential of*
             i^{th} *charge state*

         σ_i^{I*} = *proportionality constant to*
             be determined by experiment.

Much more cross section data is available for this process for the determination of σ_i^{I*}.

Data for noble gases with $2 < Z < 18$ can be found in Refs. 50 and 52. These cross sections are also modeled empirically, often using the Lotz formulation.[54-55] The two approximations are in agreement for $kT_e >> E_{bi}$ with the Lotz formulation more accurate for lower electron energies.

The relative strengths of each of these two processes are dependent on plasma conditions. For example, in a cold xenon plasma, charge states have been reported up to Xe^{10+} for an electron population of only $250\ eV$.[14] This is energetically possible for the multiple-step process but forbidden by the single-step process. However, in a hot xenon plasma $(T_e > 10\ keV)$, Xe^{18+} appears almost instantaneously at the beginning of the pulse but then continues to slowly increase in density during the plasma shot.[23] The initial rise is mostly due to the single-step process, while the subsequent increase is due to a relatively slow build-up of the lower charge states by the multiple-step process. In general, single-step ionization will dominate in hot, dense plasmas with large relative neutral densities. Single-step ionization from other than neutral atoms is not considered in this treatment.

5.2. ICSD Equilibrium Model and Computer Code

The Ion Charge State Distribution (ICSD) computer code is the embodiment of a steady-state plasma model utilizing a rate equation approach to compute equilibrium charge state distributions and charge-state-specific ion confinement times.

5.2.1. Development

The ICSD model and computer code attempt to model the following pertinent plasma processes:

- single-step ionization to high charge states,
- multiple-step ionization to high charge states,
- radiative recombination,
- charge exchange,
- diffusion,
- charge neutrality.

The steady-state rate equations, including quasi-neutrality, can be written as:

$$\frac{dn_i}{dt} = 0 = n_e n_{i-1} < \sigma v >^{ms}_{i-1 \to i} - n_e n_i < \sigma v >^{ms}_{i \to i+1} \qquad \text{multiple-step}$$

$$+ n_e n_o < \sigma v >^{ss}_{o \to i} \qquad \text{single-step}$$

$$+ n_e n_{i+1} < \sigma v >^{rr}_{i+1 \to i} - n_e n_i < \sigma v >^{rr}_{i \to i-1} \qquad \text{rad. recombination}$$

$$+ n_o n_{i+1} < \sigma v >^{cx}_{i+1 \to i} - n_o n_i < \sigma v >^{cx}_{i \to i-1} \qquad \text{charge exchange}$$

$$- \frac{n_i}{\tau_i} \qquad for \ 1 \le i \le Z_{max} \qquad \text{diffusion}$$

and $$\sum_{i=1}^{Z_{max}} n_i \, Z_i \;=\; n_e \; . \qquad\qquad\qquad\qquad \text{charge neutrality}$$

$$(5.5)$$

Note that the system described by Eqns. 5.5 allows for multiple impact of ions created through the single-step process. It does not include, however, further Auger ionization of ions created by either the single or multiple-impact process.

The above system of equations can be simplified by considering relative magnitudes of loss terms for typical MIMI plasmas. These plasmas produce moderately-stripped ions but never approach highly-stripped or fully-stripped. Therefore, the above processes need only be considered for low-Z ions.

The loss processes include diffusion, radiative recombination, and charge exchange. Diffusion is generally the largest of these processes with a typical limiting maximum value of $\tau_{c\ diff} \sim 10^{-2}$ s. Radiative recombination losses can be calculated using the model of Ref. 56. Here, the radiative recombination loss for an argon plasma is considered for the worst case which would be found in a MIMI plasma. From Ref. 56:

$$<\sigma v>^{rr}_{i\to i-1} \;=\; 5.20 \; x \; 10^{-14} \; q_i \; X_i \; e^{X_i} \, \Psi(\, X_i \,) \quad cm^3 \; s^{-1} \qquad (5.6)$$

where $$X_i = \frac{ionization\ potential\ of\ i^{th}\ electron}{electron\ temperature}$$

$$\Psi(\, x \,) \;=\; \int_x^\infty \frac{e^{-t}}{t} \, dt \; .$$

Assuming $q_i = 5$ and $T_e = 5\ keV$, then $X_i = 1.82x10^{-2}$, $\Psi(X_i) = 3.4$ and

$$<\sigma v >^{rr}_{Ar\ 5 \to 4} = 1.6 \times 10^{-14}\ cm^3\ s^{-1}\ .$$ (5.7)

The relative losses then become:

$$\frac{loss\ due\ to\ radiative\ recomb\ .}{loss\ due\ to\ diffusion} = \frac{n_e\ <\sigma v >^{rr}_{Ar\ 5 \to 4}}{1 / \tau_{c\ diff}} \sim 1.6 \times 10^{-4}$$ (5.8)

It is therefore evident that for charge states of interest, radiative recombination can be neglected relative to diffusion.

Next consider charge exchange losses for the same ions and plasma conditions. An empirical charge exchange cross section fit from Mueller and Salzborn can be expressed as:[57]

$$\sigma^{cx}_{i \to i-1} = A_k\ i^{\alpha_k}\ I_p^{\beta_k}\ cm^2$$ (5.9)

where $k = number\ of\ captured\ electrons = 1$
$A_1 = 1.43 \times 10^{-12}$
$\alpha_1 = 1.17$
$\beta_1 = -2.76$
$i = charge\ state = 5$
$I_p = ionization\ potential = 91\ eV.$

Using the above expression for $\sigma_{5 \to 4}$, assuming $10\ eV$ ions, and assuming a neutral density of:

$$n_o = 3.6 \times 10^{16}\ P(T)\ cm^{-3}\ ,$$ (5.10)

the relative losses for Ar^{5+} are found to be:

$$\frac{loss\ due\ to\ charge\ exchange}{loss\ due\ to\ diffusion} = \frac{n_o\ \sigma^{cx}_{Ar\ 5\rightarrow 4}\ v}{1/\tau_{c\ diff}} = .027\ . \qquad (5.11)$$

Although charge exchange losses are much larger than radiative recombination losses, they still are relatively small compared to typical diffusion losses. Since charge exchange becomes more prevalent for higher charge states, losses for charge states much higher than five, then, would become an appreciable fraction of $1/\tau_{c\ diff}$ and would then need be included in the model. Equations 5.8 and 5.11 show that MIMI plasmas are diffusion dominated and therefore the diffusion term will be the only loss term remaining in Eqns. 5.5.

The ionization terms of Eqns. 5.5 must now be considered. Defining:

$$\beta_{i,1} = <\sigma_o^i(\ E\ )v>^{ss}_{o\rightarrow i} = \int_o^\infty \sigma_o^i(\ E\ )v\ f(\ E\ )\ dE \qquad (5.12)$$

and

$$\beta_{i,2} = <\sigma_i^1(\ E\ )v>^{ms}_{i\rightarrow i+1} = \int_o^\infty \sigma_i^1(\ E\ )v\ f(\ E\ )\ dE \qquad (5.13)$$

and using Eqns. 5.2 and 5.4 for $\sigma_o^i(\ E\ )$ and $\sigma_i^1(\ E\ )$, the ionization coefficients $\beta_{i,1}$ and $\beta_{i,2}$ become

$$\beta_{i,1} = \sigma_o^{i*}\ \sqrt{\frac{8}{\pi\ m_e\ kT_e}}\ E_{ai}\ \Psi(\frac{E_{ai}}{kT_e}) \qquad (5.14)$$

$$\beta_{i,2} = \sigma_i^{1*} \sqrt{\frac{8}{\pi \, m_e \, kT_e}} \; (\frac{E_o}{E_{bi}})^2 \, E_{bi} \; \Psi(\frac{E_{bi}}{kT_e}) \; . \tag{5.15}$$

$\Psi(x)$ is defined in Eqns. 5.6. Equations 5.14 and 5.15 assume $f(E)$ is Maxwellian and $kT_e >> E_{ai}, E_{bi}$. E_{ai} is the threshold energy for the Auger process to remove i electrons, or equivalently, the binding energy of the subshell where one vacancy is capable of creating i vacancies via Auger transitions. E_{bi} is the threshold energy for removing the outer-most electron from an i-times ionized ion (i.e. the ionization potential). E_o is the ionization potential of the neutral atom. The proportionality constants σ_o^{i*} and σ_i^{1*} are determined by experiment. These values are not well known, particularly for high charge states and discrepancies of factors of two are not uncommon. Cross section data for the noble gases can be found in Refs. 50-52, from which σ_o^{i*} and σ_i^{1*} can be computed.

The only term remaining from Eqns. 5.5 which has not been addressed is the diffusion term which is governed by ion confinement. This is the subject of the following section.

5.2.2. Ion Confinement

In an ECR-heated mirror plasma, high electron densities evolve at the ECR resonance zone. These electrons create a negative potential dip at the resonance zone which is superimposed on the otherwise positive plasma potential. This potential dip serves to electrostatically confine ions, the greater confining effect existing for the more highly-charged ions. The magnitude of this effect also depends on the degree of collisionality of the ions. Ions in an ECR ion source are much more collisional than in fusion devices due to the lower ion temperatures and higher ion charges involved

$(v_{coll} \propto Z^2 / T^{3/2})$. The degree of collisionality is determined by the ratio, η_{coll}, of the bounce time of a specific ion in the mirror to its scatter time, or equivalently, the number of scatters that an ion will experience during each bounce. Both the bounce time and scatter time are a function of the charge state of the ion.

The scatter time chosen is the Spitzer 90° scatter time which is the time for a particle of charge state i, to undergo a series of small angle scatterings off field particles of charge state j, which will change the test particle's velocity vector by 90°. This scatter time can be written as:[58]

$$\frac{1}{\tau_{ij}} = \frac{8\pi\, n_j\, Z_i^2\, Z_j^2\, e^4\, \ln\Lambda\ \varepsilon(v_i/v_j)}{m_i^2\, v_i^3} \tag{5.16}$$

$$= \frac{.276\ N_j\, Z_i^2\, Z_j^2\, \varepsilon(v_i/v_j)}{M_i^{1/2}\, T_i^{3/2}}\quad \mu s^{-1}$$

where
- i denotes scattered particle quantities
- j denotes scattering particle quantities
- $\varepsilon = .63$ for $v_i = v_j$
- T_i in eV
- $q_i = Z_i e$
- $m_i = M_i m_p$
- $n_j = N_j \times 10^{11}\ cm^{-3}$.

Since a plasma contains ions of many charge states j, the reciprocal of the collision time must be summed over all possible scattering charge states. The final result is:

$$\frac{1}{\tau_{i\,tot}} = \frac{1}{\tau_{ii}} = \sum_j \frac{1}{\tau_{ij}} = \frac{.174\ Z_i^2}{M_i^{1/2}\, T_i^{3/2}}\ \sum_j N_j\, Z_j^2\quad \mu s^{-1}\ . \tag{5.17}$$

Ion confinement is divided into three distinct confinement regimes dependent on the collisionality of the specific charge state in the plasma. These regimes are non-collisional confinement (Pastukhov) for which $\eta_{coll} << 1$, moderately-collisional confinement (flow) for which $\eta_{coll} \sim 1$, and highly collisional confinement (spatial diffusion) for which $\eta_{coll} >> 1$. Confinement times of mirror trapped ions in a potential well of depth ϕ may be written as:[59,60]

- Pastukhov confinement, $\eta_{coll} << 1$,

$$\tau_P = \tau_{ii} \; g(R) \left(\frac{Z_i q\phi}{kT_i} \right) e^{\frac{Z_i q\phi}{kT_i}} \tag{5.18}$$

- Flow confinement, $\eta_{coll} \sim 1$,

$$\tau_f = RL \left(\frac{m_i}{kT_i} \right)^{1/2} e^{\frac{Z_i q\phi}{kT_i}} \tag{5.19}$$

- Collisional confinement, $\eta_{coll} >> 1$,

$$\tau_{coll} = \frac{L^2}{D} = \frac{L^2}{\frac{kT_i}{m_i} \tau_{ii}} \tag{5.20}$$

where
R = mirror ratio
$g(R) = [(R + 1)/R] \; ln(2R+2)$
ϕ = potential dip
τ_{ii} = 90° scatter time
L = characteristic length of plasma.

It should be noted that Eqn. 5.20 includes only effects of free diffusion. Ambipolar potential effects are not included but can easily be incorporated into the diffusion coefficient shown in the previous equation. Rognlien and Cutler[61] have shown that the flow and Pastukhov confinement times may be combined in a single expression valid for $\eta_{coll} \leq 1$. The final confinement times and their regimes of validity are:

- Flow and Pastukhov confinement, $\eta_{coll} \leq 1$,

$$\tau_{fP} = RL(\frac{m_i}{kT_i})^{1/2} \{ 1 + \tau_{ii}\frac{g(R)}{R}\frac{1}{L}(\frac{Z_i q\phi}{kT_i})(\frac{kT_i}{m_i})^{1/2} \} e^{\frac{Z_i q\phi}{kT_i}}$$

(5.21)

- Collisional confinement, $\eta_{coll} >> 1$,

$$\tau_{coll} = \frac{L^2}{(\frac{kT_i}{m_i})} (\frac{1}{\tau_{ii}}) .$$

(5.22)

Note that some ions in the distribution will be governed by τ_{fP} and some will be governed by τ_{coll}. Also note that for collisional plasmas, confinement times vary as Z_i^2 and the higher charge states become very well confined. For moderately-collisional and non-collisional plasmas, confinement times vary as $(1 + \beta\frac{1}{Z_i}) e^{\frac{Z_i q\phi}{kT_i}}$. Therefore, if $q\phi/kT_i << 1$ then an increase in Z_i will result in a drop in τ_{conf} and if the ion temperature is not significantly greater than the potential dip, the confinement time will begin to increase again for larger Z_i. A low ion temperature will result in an increase in τ_{fP} with Z_i for all Z_i.

5.2.3. Method of Solution and Sample Results

All terms for the set of equations describing the build-up of a steady-state charge state distribution in a typical MIMI plasma have been discussed in some detail. The solution of Eqns. 5.5 may now be approached. Again, the most difficult part of the solution is dealing with the diffusion term, n_i/τ_i.

Explicit forms for τ_i are given by Eqns. 5.21 and 5.22. There are some problems with using these expressions precisely as they appear. First, the confinement times will be discontinuous as Z_i moves from one collision regime to the next. This is an unphysical result. Second, there is ambiguity in the constants preceding each of the expressions for τ_{conf}. For example, the form of the characteristic distance, L, used in the expressions is uncertain. For collisional diffusion, L should be near r_p, the distance to the walls along the direction of steepest density gradient. For collisionless diffusion, L should be much closer to the mirroring length since radial particle diffusion is limited by the magnetic field. Also typically, discrepancies of factors of at least two are found in the constants published in the literature since these expressions are merely approximations for more exact forms. For these reasons, all dependence on n_i, T_i, R, m_i, Z_i, τ_{ii} is retained in the expressions of Eqns. 5.21 and 5.22, however the constants $RL \left(\dfrac{m_i}{kT_i} \right)^{1/2}$ of τ_{fP} and $\dfrac{L^2}{(kT_i / m_i)}$ of τ_{coll}, which are not functions of charge state, are assigned arbitrary values, and computed self-consistently with Eqns 5.5.

An additional requirement of continuity is imposed at the boundary of the collisional and flow-Pastukhov regimes which relates the arbitrary constants assigned to each of the two collisional regimes mentioned above. This condition takes the form:

$$\frac{1}{\tau_{coll}(Z = Z_c)} = \frac{1}{\tau_{fP} (Z = Z_c)} \tag{5.23}$$

$$\text{where} \qquad Z_c = \tfrac{1}{2} \left(Z_{i\ coll\ min} + Z_{i\ fP\ max} \right) . \qquad (5.24)$$

Defined in this way, Z_c is a fictitious charge state lying half-way between the highest charge state in the flow-Pastukhov regime and the lowest charge state in the collisional regime. The regime for each charge state is assigned on the following basis:

$$\eta_{coll} = \frac{t_{bi}}{\tau_{ii}} \le 10 \qquad \Rightarrow \qquad flow - Pastukhov \qquad (5.25)$$

$$\eta_{coll} = \frac{t_{bi}}{\tau_{ii}} > 10 \qquad \Rightarrow \qquad collisional \qquad (5.26)$$

where τ_{ii} is given in Eqn. 5.17, and

$$t_{bi} = t_{bounce} = \frac{\pi\, L}{v_{\perp o}} , \qquad (5.27)$$

assuming a parabolic magnetic field profile $B = B_o(1+z^2/L^2)$.

With the above definitions, confinement times for the entire distribution may be derived:

$$\frac{1}{\tau_i} = \alpha_o\, X_i \qquad (5.28)$$

$$\text{where} \qquad X_i = \begin{cases} \tau_{ii}(\, Z_i\,) & Z_i > Z_c \\[2ex] \tau_{ii}(\, Z_c\,)\, \dfrac{h(\, Z_c\,)}{h(\, Z_i\,)}\, e^{(\, Z_c - Z_i\,)\frac{q\phi}{kT}} & Z_i < Z_c \end{cases}$$

with $$h(Z_i) = \{ 1 + \tau_{ii}(Z_i) \frac{g(R)}{R} \frac{1}{L} (\frac{Z_i q\phi}{kT_i})(\frac{kT_i}{m_i})^{1/2} \} \ .$$

The number of unknowns for the system of $(Z_{max}+1)$ coupled equations, Eqns. 5.5, is now reduced to $(Z_{max}+1)$. The unknowns are $\{n_i\}$ for $1 \le i \le Z_{max}$ and α_o. The symbol $\{\ \}$ represents a vector quantity. The form of the confinement times precludes an analytical solution since τ_i is a complicated function of $\{n_i\}$, Z_i. It can be shown, though, that the system of equations is unconditionally convergent for all physical values of densities, temperatures, masses, etc. The system is solved using the computational iterative scheme described below.

1. Input values for $\{ \sigma_o^{i*} \}$, $\{ \sigma_i^{1*} \}$, $\{E_{ai}\}$, $\{E_{bi}\}$, Z_{max}, M_{ion}, L_{mirror}, R_{mirror}, $\Delta\phi$, T_e, T_i, n_e, n_o.

2. Compute $\beta_{i,1}$, $\beta_{i,2}$ for input T_e (separate code).

3. Assign initial estimate for $\{n_i\}$ for $1 \le i \le Z_{max}$. Since the system is so strongly convergent, this estimate does not change for varying input parameters.

4. Assign confinement regimes for each charge state based on $\{n_i\}$.

5. Solve system of equations for α_o given $\{n_i\}$ and Z_c.

6. Compute new $\{n_i\}$ given new α_o and Z_c.

7. Compute new Z_c for $\{n_i\}$, α_o.

8. If $Z_{c\ new} \ne Z_{c\ old}$ then repeat steps 4-8 until Z_c does not change. When Z_c remains the same for two consecutive iterations, the solutions for $\{n_i\}$, α_o, and Z_c are self-consistent.

9. Compute $\{\tau_i\} = f(\{n_i\}, \alpha_o, Z_c)$.

10. Output results: $\{n_i\}, \{\tau_i\}$.

The source codes and sample input and output decks for the programs which perform the steps above are listed in Appendix E.

A set of sample results is shown in Fig. 5.2. The figure shows the computed normalized ion densities and confinement times as a function of charge state for several neutral background densities. Figure 5.2 (a) shows that, as the neutral background pressure is decreased, a gradual shift to higher charge states occurs. This is a result of large $n_o<\sigma v>_{0\to1}$ reaction rates for large neutral pressures. The ionization coefficient for ionization from neutrals to singly-ionized ions, $<\sigma v>_{0\to1}$, is an order of magnitude larger than any other coefficient. If n_o is large, the reaction rate, $n_o<\sigma v>_{0\to1}$, will dominate and a large Ar^{1+} population will develop. As n_o is decreased, reaction rates of other processes become comparable to the $n_o<\sigma v>_{0\to1}$ rate and, since charge neutrality must be maintained, higher charge states gradually become populated.

The computed confinement times shown in Fig. 5.2 (b) reflect this increased $<Z>$ with decreased neutral density. First note that only the first two or three charge states are not governed by collisional confinement (i.e. $Z_c = 2.5, 3.5$). Therefore, for higher charge states, from Eqn. 5.28, $\tau_{coll} \propto (1/\tau_{ii}) \propto Z_i^2$. That is, as the charge state of an ion increases, it becomes more collisional which increases the time necessary to diffuse a given distance in the plasma. The quadratic nature of the Z_i dependence is quite apparent. Now consider the behavior for a given ionization state. The confinement time varies as $\tau_{coll} \propto \dfrac{1}{\tau_{ii}} \propto \sum_j N_j Z_j^2$. As the neutral density is decreased, the higher
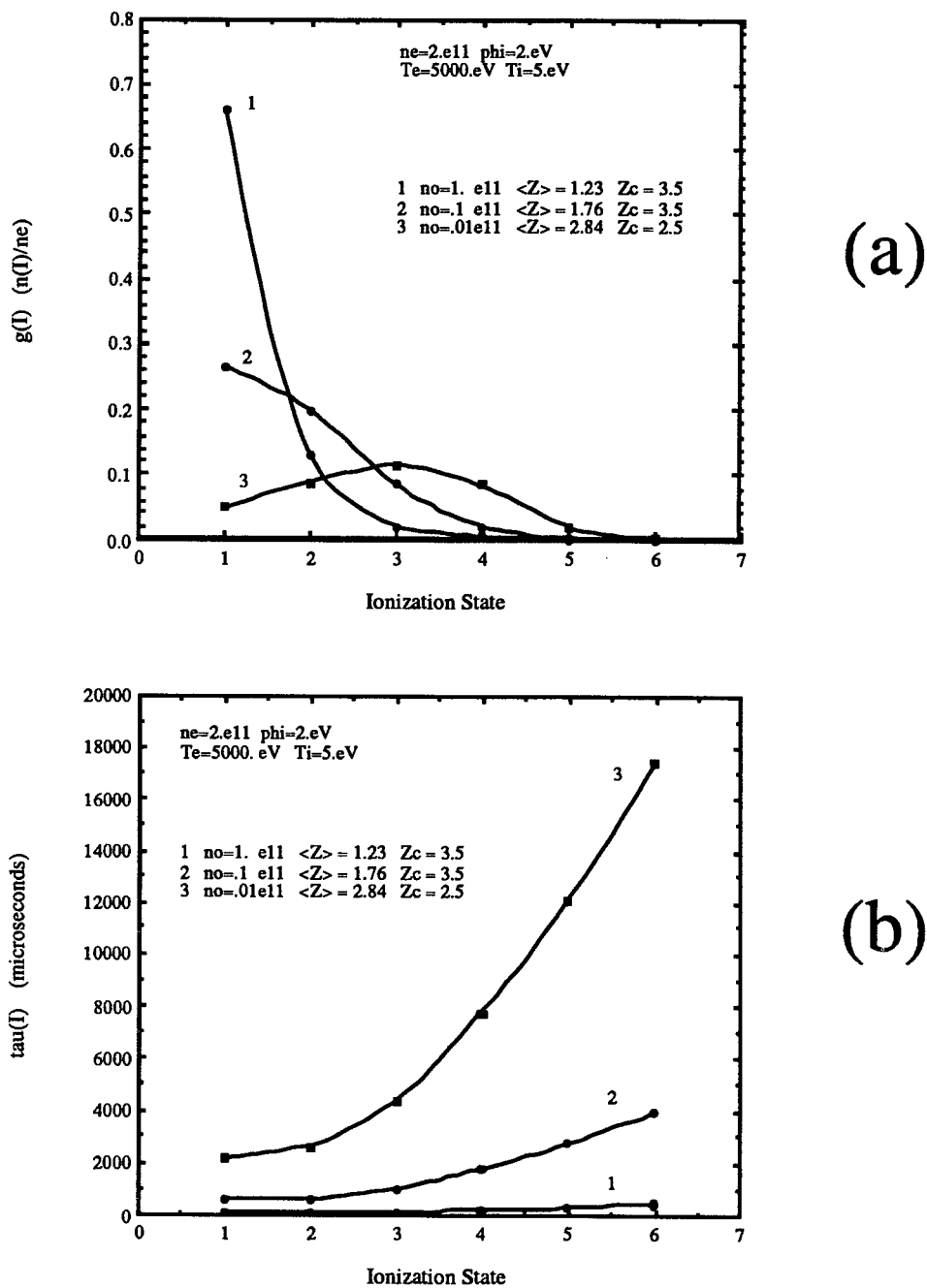
Figure 5.2. Sample output from ICSD code. (a) Computed normalized ion densities and (b) confinement times for Ar^{i+} for $1 < i < 6$. Several solutions for varying neutral background pressures are shown.

charge states become populated and since the weighting of N_j is with Z_i^2, τ_{coll} must necessarily increase with $<Z>$. This behavior is again evident in Fig 5.2 (b).

Figure 5.2 is merely a sample result from the ICSD code. Modeling of the actual system using this code, and comparison to experimental data will be presented in chapter 6.

5.3. Monte Carlo Simulations

The time-of-flight spectrometer, described in Sec. 3.4, allows for the measurement of charge-state-specific ion energy distributions, $f_i(E)$. This measurement technique is described in Sec. 6.3. These energy distributions, measured at the entrance to the spectrometer $\sim 2m$ from the plasma, are markedly different than the distributions that exist in the plasma. There are several reasons for this which deal with midplane plasma potential spread and magnetic field perpendicular-to-parallel energy transformations.

Consider the plasma potential profile shown in Fig. 5.3 (a). An ion born at a midplane location of non-zero plasma potential, ϕ_p, possesses zero energy relative to that potential. When the ion leaves the plasma and falls to system ground, it gains energy $E_{ion} = q_i \phi_p$. If there exists a spread in plasma potential in the ionizing region of the plasma, this spread will be reflected in a spread in the endloss ion energy directly attributed to the plasma potential. If this were the only mechanism by which endloss ions gain energy, the energy distribution of these ions would be dependent only on the axial profile of the plasma potential. Figs. 5.3 (b) and (c) illustrate two possible analytical models approximating the actual potential profile. The resulting ion endloss energy distributions are shown in Figs. 5.3 (d) and (e). These distributions assume that ions are
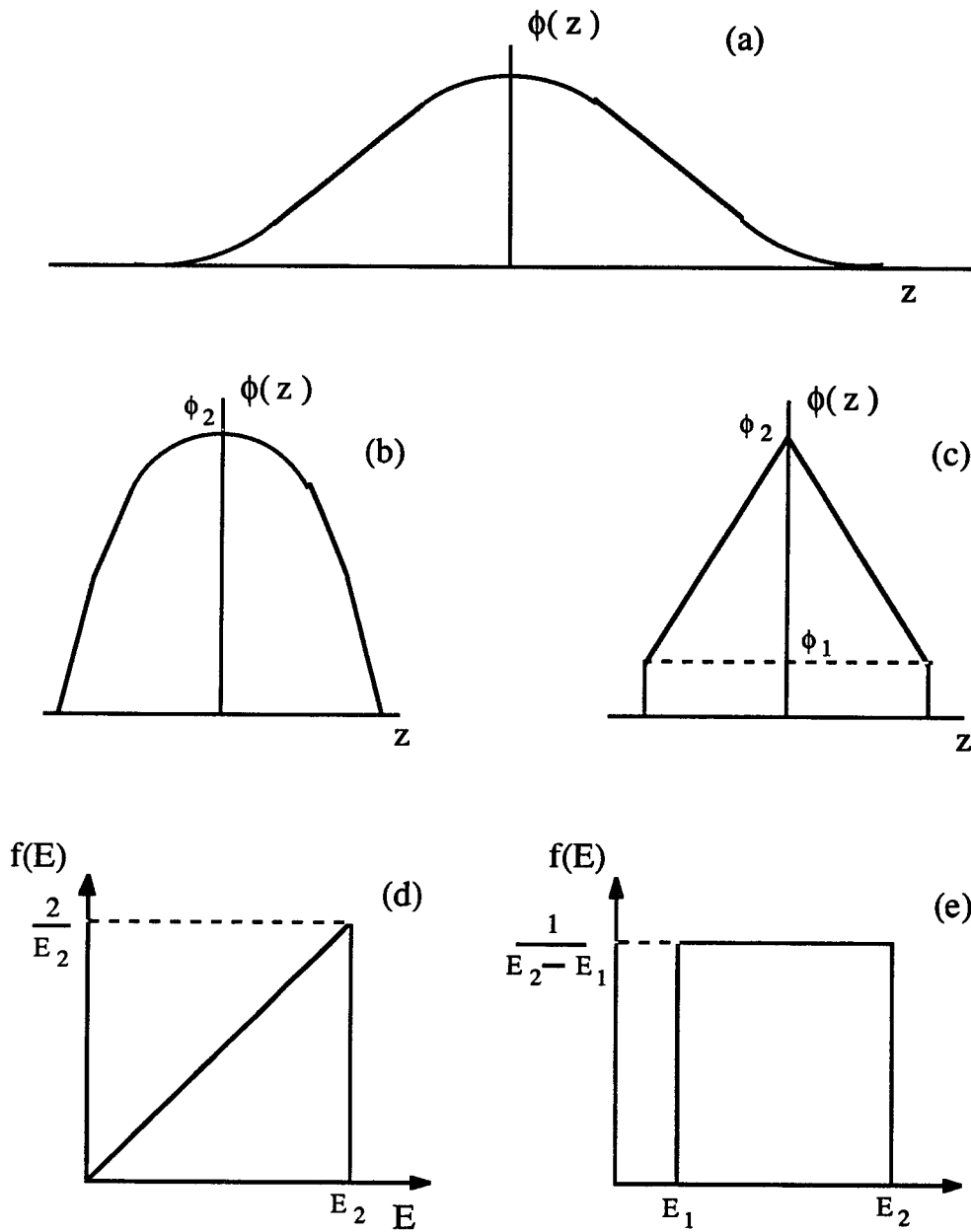
Figure 5.3. Plasma potential profiles. (a) Typical actual mirror plasma potential profile, (b), (d) parabolic approximation and associated energy distribution, (c), (e) linear approximation and associated energy distribution. In (b) - (d), $E_1 = q\phi_1$ and $E_2 = q\phi_2$.

born randomly throughout the midplane region. This spread in plasma potential, which exists in all mirror devices, therefore contributes to the total ion energy distribution.

Consider also a bi-Maxwellian ion distribution, of temperatures $T_\perp, T_{//}$. An ion leaving the midplane region in the endloss will take with it a parallel energy from the parallel Maxwellian distribution and a perpendicular energy from the perpendicular Maxwellian distribution. The parallel energy is unaffected by the magnetic field and the ion will carry that energy, which remains wholly parallel, until it strikes a wall or undergoes a collision. The perpendicular energy is different however. The magnetic moment, μ, of the particle must be conserved. As the particle in the endloss moves through a continuously decreasing magnetic field, its perpendicular energy must decrease proportionally to conserve magnetic moment

$$\mu = \frac{E_\perp}{B} .$$

(5.29)

This lost perpendicular energy is converted into parallel energy. By the time the ion reaches one of the endtanks in MIMI, over 98 percent of its perpendicular energy has been converted to parallel energy. This energy is superimposed on the original parallel energy distribution and both are superimposed on the distribution due to the non-zero plasma potential. It is the total distribution that is measured by the spectrometer, which makes each of the individual contributions difficult to identify.

The problem then becomes, given the distributions of Fig. 5.4, how do these three distributions combine to yield the distribution measured by the TOF? A Monte Carlo approach is employed to solve this problem. Each of the distribution functions can be considered a probability distribution function (PDF). The probability that a particle

(a)

(b)

(c)
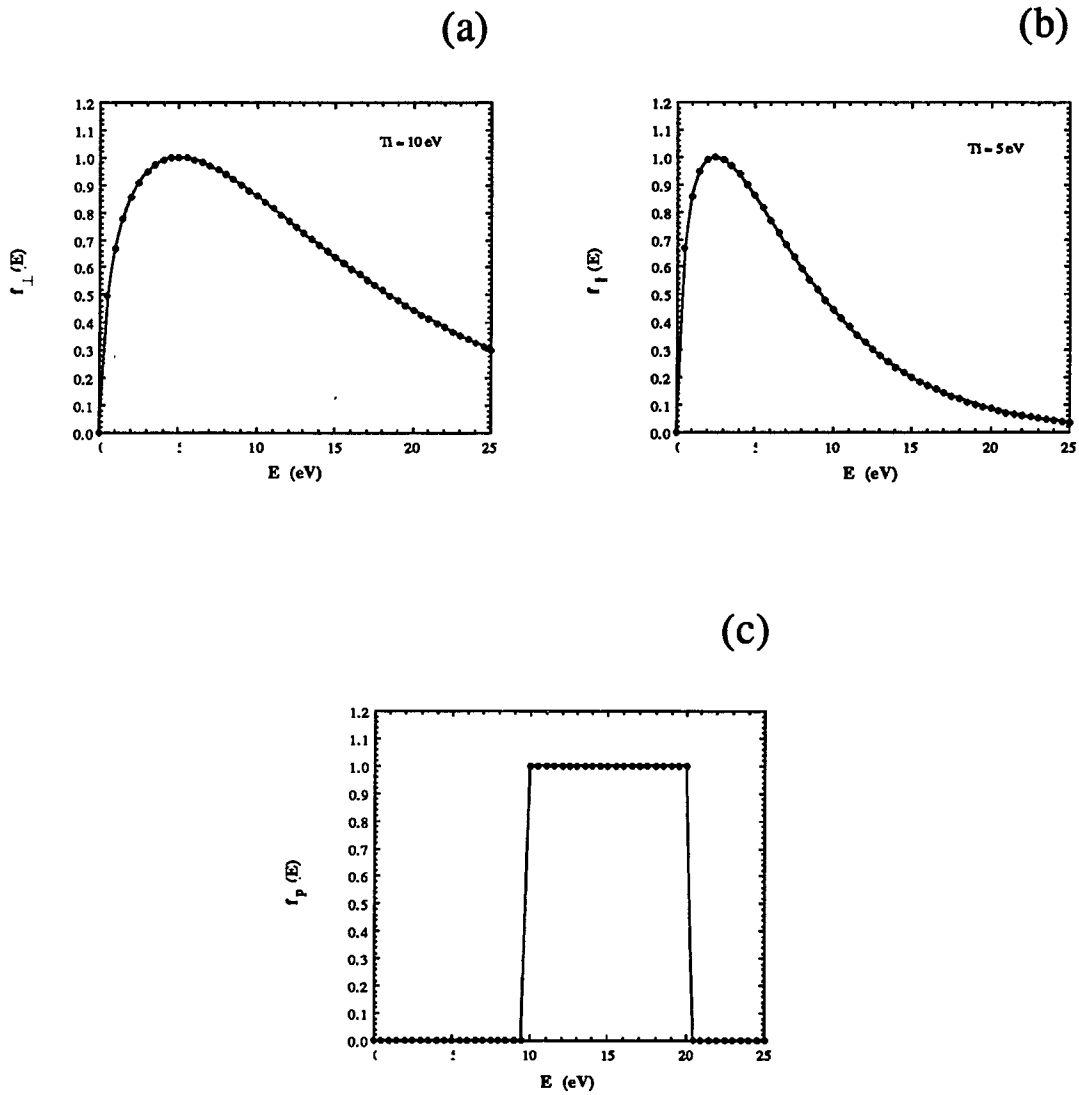
Figure 5.4.   Ion endloss energy distributions. (a) Perpendicular Maxwellian distribution for $T_\perp = 10. \ eV$, (b) parallel Maxwellian distribution for $T_{//} = 5. \ eV$, (c) distribution due to plasma potential spread. The total ion distribution is composed of a superposition of all distributions.

will receive a given energy from one of the distributions is dependent on the form of the

PDF. The PDF's for each of the distribution functions take the form:

$$f_\perp(E) = \frac{2}{\sqrt{\pi}} \frac{1}{(kT_{i_\perp})^{3/2}} E^{1/2} e^{-E/kT_{i_\perp}} , \qquad (5.30)$$

$$f_{//}(E) = \frac{2}{\sqrt{\pi}} \frac{1}{(kT_{i_{//}})^{3/2}} E^{1/2} e^{-E/kT_{i_{//}}} ,$$

$$f_p(E) = \frac{1}{E_2 - E_1} \qquad \text{(for a linear plasma potential profile).}$$

Define a cumulative distribution function (CDF):

$$F(E) = \int_0^E f(E) \, dE . \qquad (5.31)$$

For the distributions of Eqns. 5.30, the CDF takes the form:

$$F_\perp(E) = \frac{2}{\sqrt{\pi}} \gamma(\frac{E}{kT_{i_\perp}}) , \qquad (5.32)$$

$$F_{//}(E) = \frac{2}{\sqrt{\pi}} \gamma(\frac{E}{kT_{i_{//}}}) ,$$

$$F_p(E) = \frac{E - E_1}{E_2 - E_1} ,$$

where $$\gamma(x) = \int_0^x x^{1/2} e^{-x} \, dx .$$

The CDF represents the probability of finding a particle in the distribution at energy less than E. The CDF for a Maxwellian is shown in Fig. 5.5. Referring to Fig. 5.5 (b), if a value, R, of $F(E)$ ($0 \leq F(E) \leq 1$ for properly normalized distributions), is chosen at random, the probability that R will correspond to a given energy, E_R, is proportional to the slope of $F(E)$ at $E = E_R$. Correspondingly, this is proportional to the height of $f(E)$ at energy E_R. This is illustrated in Fig. 5.5 (b) by considering the ranges of $F(E)$, dF_i and dF_j, which correspond to the same increment, dE, along the energy axis. The largest dF for a given dE is found at the energy corresponding to maximum $f(E)$. Therefore, if many such points, R, are chosen, a plot of the frequency of the corresponding values E_R, will approximate the original distribution, $f(E)$.

This is the method by which any given ion is assigned the value of the energy it takes from each of the distributions of Fig. 5.4. The process, then, by which the distributions are "folded" together proceeds as follows:

1. Choose random value, R_1, for $F_\perp(E)$.

2. Determine corresponding energy, E_1, from distribution $F_\perp(E)$ by solving $R_1 = F_\perp(E_1)$. This is usually the most difficult step.

3. Repeat steps 1 and 2 for remaining two distributions, $F_\parallel(E)$ and $F_p(E)$, to determine energies E_2 and E_3 (from $F_\parallel(E)$ and $F_p(E)$ respectively).

4. Determine total ion energy ($E_{tot} = E_1 + E_2 + E_3$).

5. Divide total energy range of interest into energy intervals $\{E_i\}$ and determine into which interval, E_i, that E_{tot} falls.

6. Record one history falling into the energy range of E_i.

7. Repeat steps 1-6 for many ion histories (~5000 histories/energy bin).
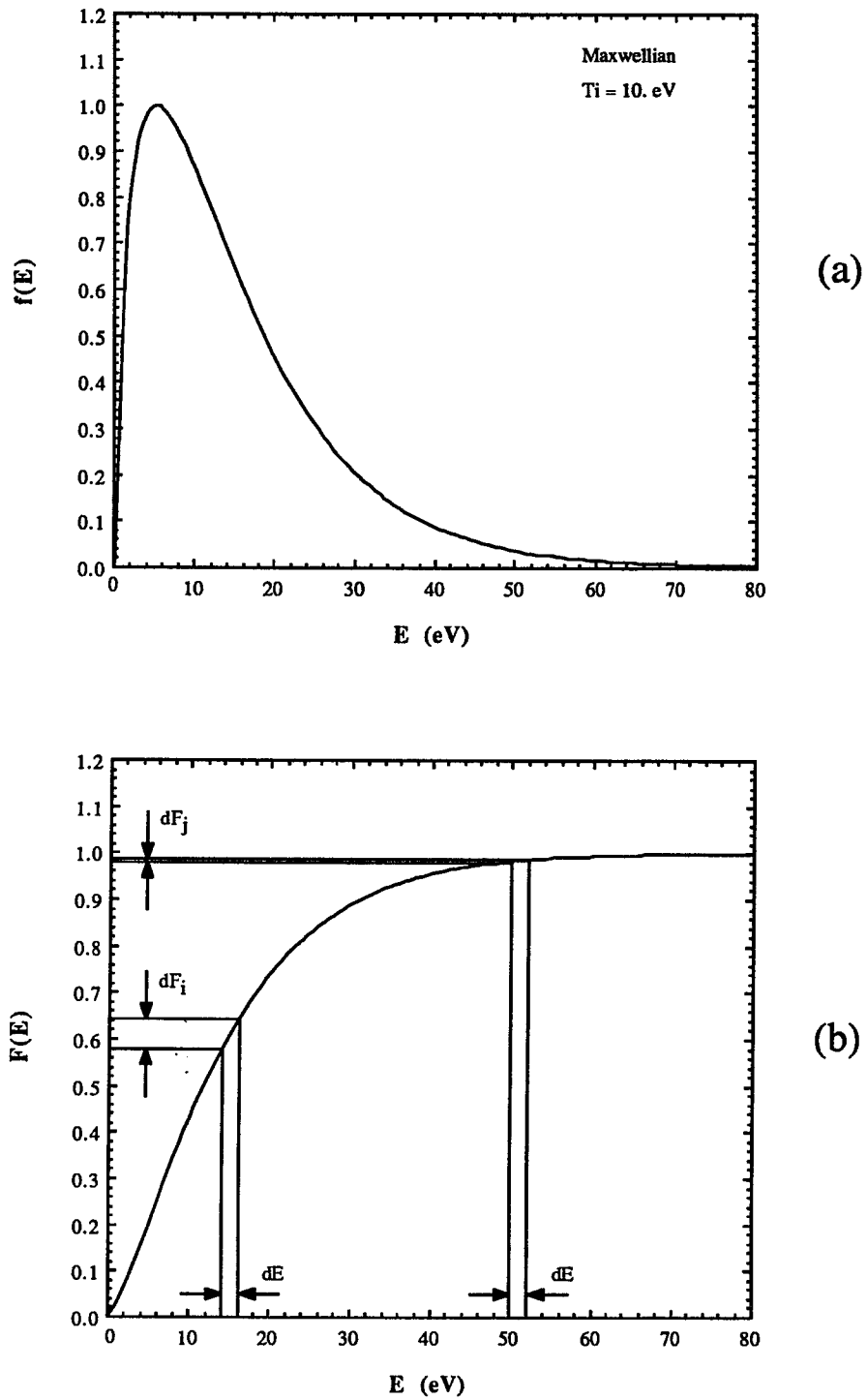
Figure 5.5. (a) PDF and (b) CDF for a *10 eV* Maxwellian distribution. The CDF shows that the range of *F(E)* that corresponds to a given energy increment is large for energies corresponding to large *f(E)*.

8. A plot of the frequency of histories resulting in energy E_i, as a function of E_i, will approximate the actual folded distribution.

Once $f(E)$ has been determined (using the above method), it must be transformed into a form which can be compared to experimental data. As is discussed in chapter 6, measurements of the energy distribution function are of the form:

$$g (E) = \int_{E}^{\infty} f (E) \, dE \ . \tag{5.33}$$

To compare to measurement, therefore, the computed $f(E)$ is transformed by performing, numerically, the integration of Eqn. 5.33. This result, $g(E)$, is the ultimate desired result.

Some sample results are shown in Figs. 5.6 - 5.8. Since the MIMI plasma is sufficiently collisional, it cannot support a large parallel-perpendicular temperature difference. For this reason, all Monte Carlo runs have been performed assuming $T_\perp = T_{//} = T_i$. Fig. 5.6 shows a comparison between the code results for the simple case of $\Delta\phi_p = 0$ and an analytical Maxwellian. As is evident, the results are accurate. The integrated distribution $g(E)$, defined by Eqn. 5.33, must be derived from plots similar to that of Fig. 5.6 since it is the integrated distribution that is generated by the time-of-flight spectrometer.

Figures 5.7 (a) - (d) shows results for two intuitive cases -- $T_i / \Delta\phi_p$ large and $T_i / \Delta\phi_p$ small. In each case the original distributions are plotted next to the folded and integrated distributions. In all cases peak values are normalized to one. The distributions of Fig. 5.7 (a) assume a $10 \ eV$ ion Maxwellian and a plasma potential of essentially a
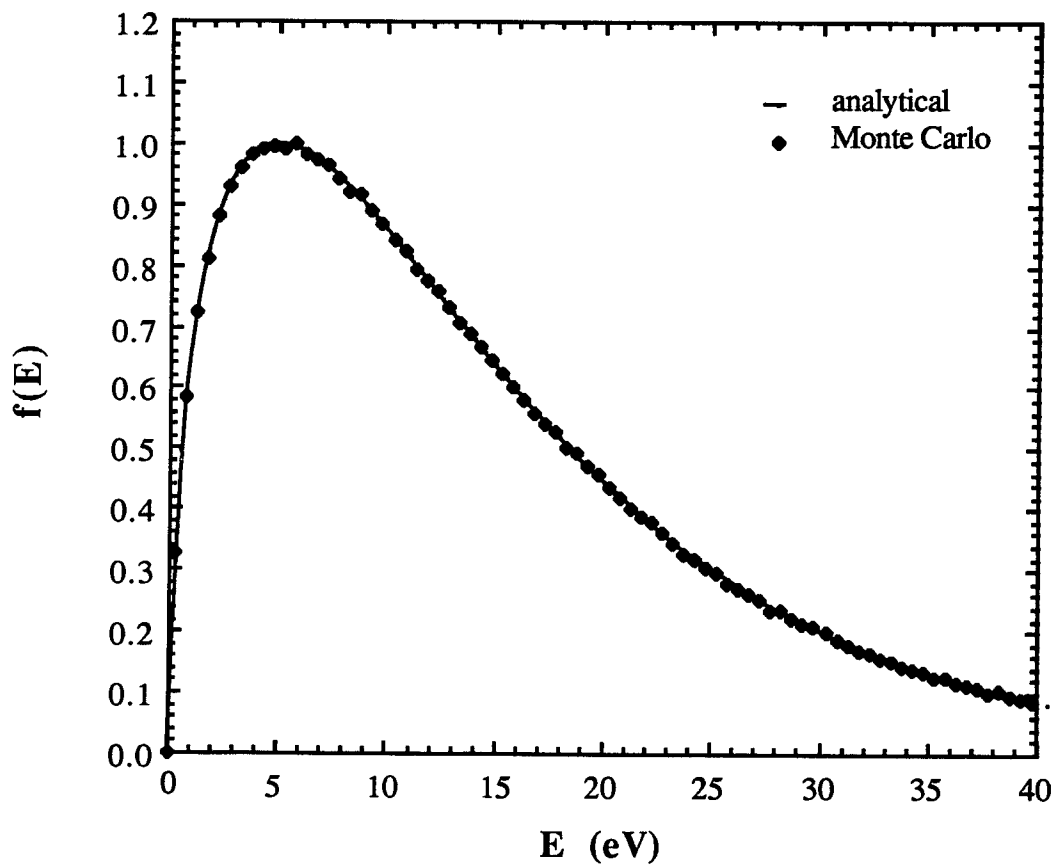
Figure 5.6. Comparison between Monte Carlo solution for *10. eV* Maxwellian and exact solution. The simulation requires *2,000,000* histories.
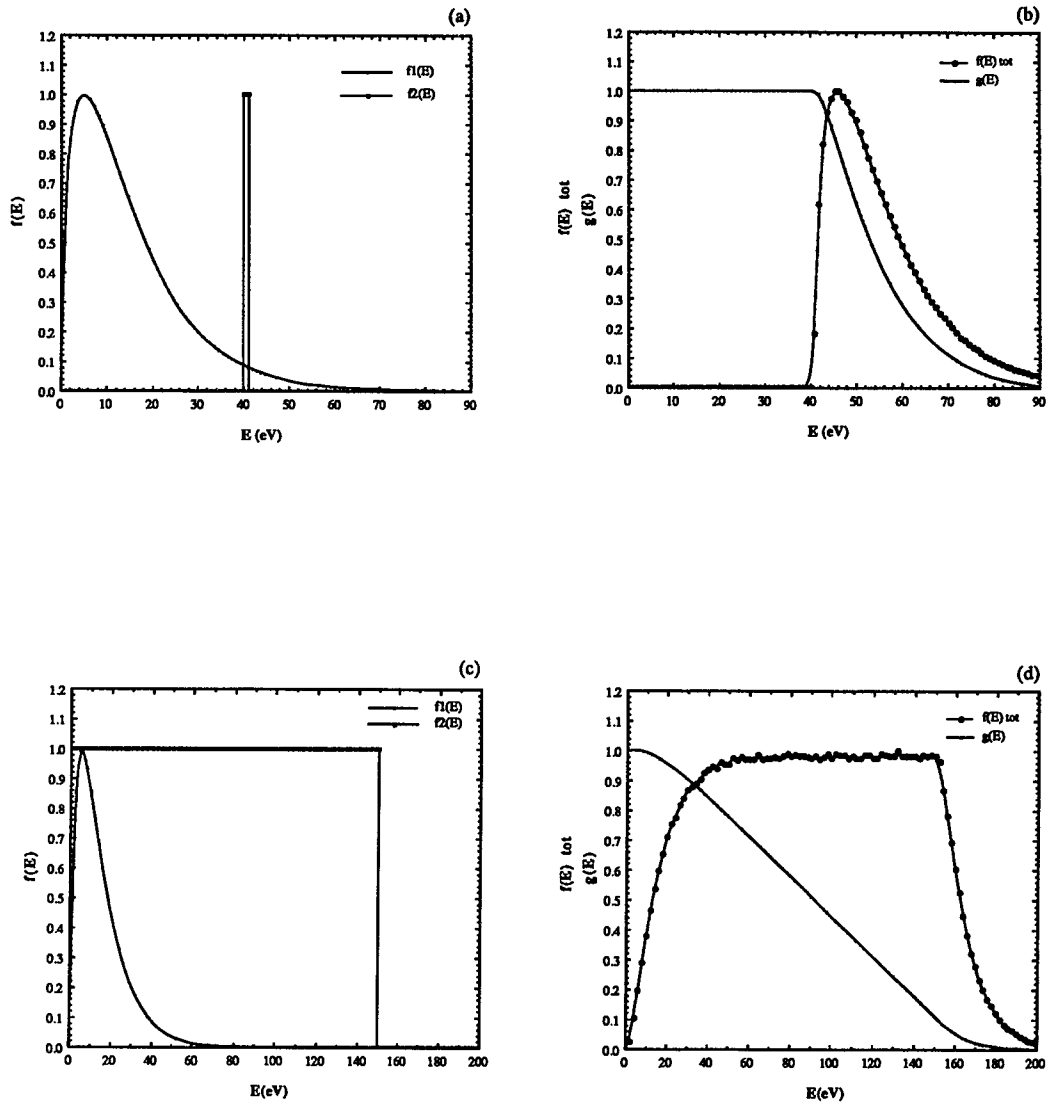
Figure 5.7. Sample superimposed ion energy distributions. Case 1 - $T_i/\Delta\phi_p$ large, (a) $T_i = 10\ eV, 40 < \phi_p < 41\ V$, (b) folded and integrated distributions of (a). Case 2 - $T_i/\Delta\phi_p$ small, (c) $T_i = 10\ eV, 0 < \phi_p < 150\ V$, (d) folded and integrated distributions of (c).
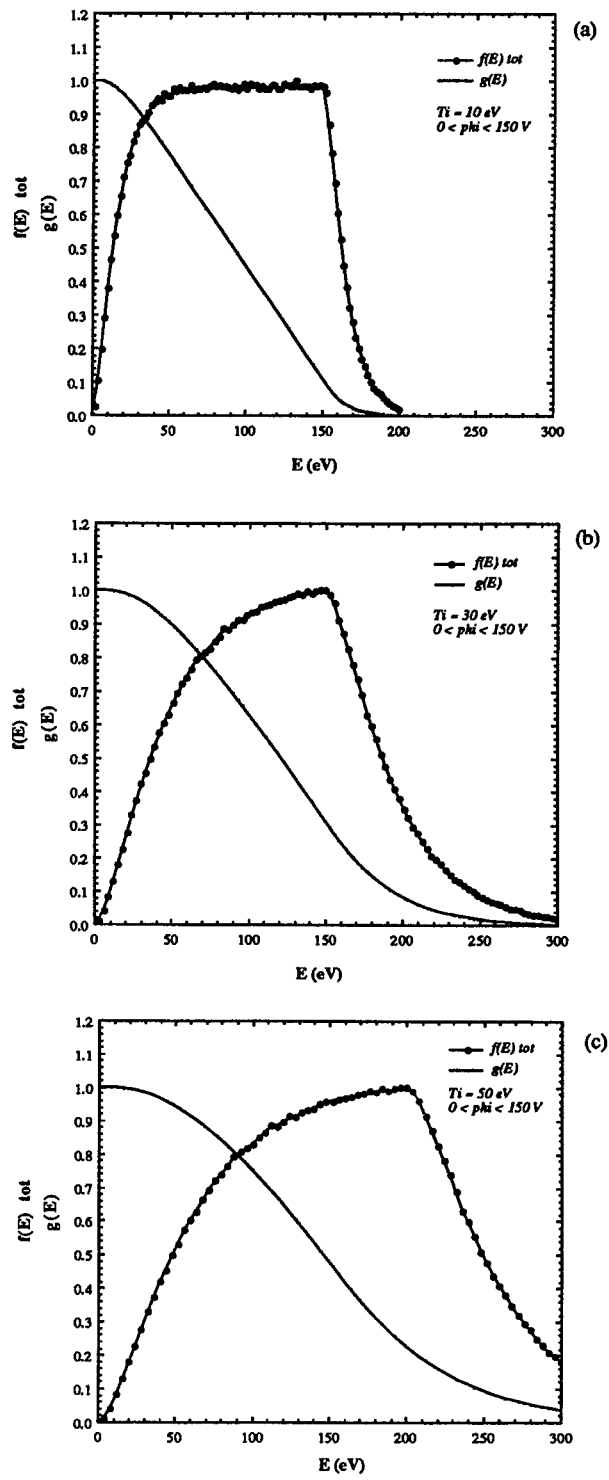
Figure 5.8. Computed folded ion energy distributions for increasing ion temperature.
(a) $T_i = 10$ eV, $0 < \phi_p < 150$ eV, (b) $T_i = 30$ eV, $0 < \phi_p < 150$ eV,
(c) $T_i = 50$ eV, $0 < \phi_p < 150$ eV.

constant *40 V*. Every ion in the distribution will gain exactly *40 eV* from the plasma potential distribution. One would expect, therefore, that the total ion energy distribution function will be identical to the original Maxwellian but shifted by *40 eV*. This is indeed the result seen in Fig. 5.7 (b). Again, the integrated distribution, *g(E)*, is also shown. The distributions of Fig. 5.7 (c) show a case of a large plasma potential spread with a low ion temperature. The folded distribution of Fig. 5.7 (d) is essentially a reproduction of the square plasma potential distribution. The ion temperature, however, has the effect of "rounding" the edges of the distribution at the lower and upper bounds. For this case, *g(E)* appears essentially linear. There is a slight curvature at the lower and upper bounds due to the effect of the non-zero temperature.

Figures 5.8 (a) - (c) show the effect of increasing the ion temperature while maintaining a constant plasma potential profile. With low temperatures, the folded distribution remains square and the integrated distribution linear. As the temperature increases, the folded distribution spreads to much higher energies and becomes markedly convex on the rising portion and concave on the falling portion. The integrated distribution loses its linearity and also has non-negligible values at much higher energies. Plots such as 5.8 (a) - (c) are used in chapter 6 to determine the effect of ion cyclotron resonant heating on ion temperature. Measurements with the time-of-flight spectrometer produce integrated distributions which can be matched to the output of this Monte Carlo code. In this way, ICRH effects can be deduced.

CHAPTER 6

EXPERIMENTAL RESULTS

This chapter contains the important experimental results obtained from the MIMI ECR ion source experiment. Typical signals from the diagnostics described in Sec. 3.3 are shown, which are used to monitor plasma conditions during time-of-flight data acquisition. The method for reduction of raw TOF data is described as is the analysis of the errors involved with the method. A method has also been developed to measure charge-state-specific ion energy distributions and is used to determine ICRH effects on the ion charge state distributions of several gases. The Monte Carlo approach described in Sec. 5.3 is used to determine ion temperature increases resulting directly from the imposed ion cyclotron heating. Measured, steady-state, charge-state distributions for several gases are also presented as are changes in these distributions with ICR heating power and consequently ion temperature. These changes are compared to predicted changes expected from the ICSD steady-state, equilibrium code described in Sec. 5.2. Discrepancies between expected and observed charge state distributions are discussed. Finally, consideration of ICRH confinement time effects, from both a theoretical and experimental standpoint, are shown to have a marked detrimental impact on the achievable ion distributions.

6.1. Presentation of Data

Several diagnostics are used to monitor the plasma during MIMI experimental runs. These diagnostics are described in Secs. 3.3 and 3.4. Figure 6.1 shows a set of typical signals for the standard diagnostics. The pulse width is variable from *.1* to *100 ms* with a standard pulse width being *~50 ms*. These diagnostics allow for measurement of electron density, electron temperature, plasma potential, and ion temperature changes. In addition to the diagnostics of Fig. 6.1, a time-of-flight spectrometer is capable of recording a measurement of the charge-state distribution at any time during the plasma pulse. It requires *1.25 ms* of real time to record the spectrum. Its sample location within the plasma pulse is determined by the triggering CAMAC controller (see Fig. 3.28).

The majority of the information of interest is derived from the processed spectra of the TOF spectrometer, similar to that shown in Fig. 3.27. As described in chapter 3, this spectrum is derived from the average of *~130* individual spectra. This averaging process is required to reduce to near zero, random signal fluctuations caused by amplifier noise, secondary electron and x-ray bombardment of the electron multiplier, plasma fluctuations, and statistical spreads. The effect of this averaging process is now considered.

If several independent measurements, h_i, are made of the same physical quantity, each with an associated error σ_i, the error associated with the average of these measurements is:

$$\sigma_{tot} = \frac{\sqrt{\sum_{i=1}^{N} \sigma_i^2}}{N} ,$$

(6.1)

where   *N = total number of measurements.*
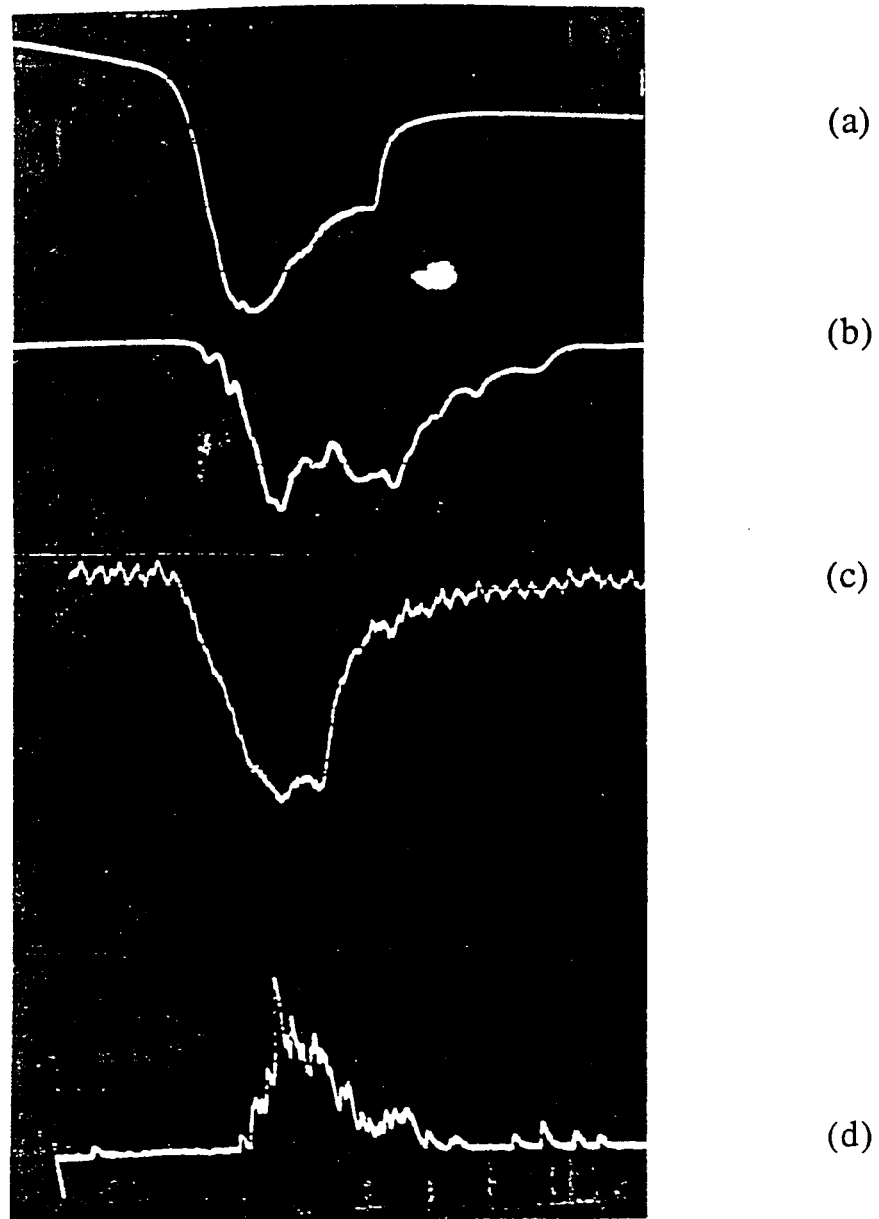
Figure 6.1.   Set of typical MIMI diagnostic signals with a .5 ms wide microwave
pulse. (a) diamagnetic loop measures plasma nkT_e (b) radial Langmuir
probe measures floating potential (c) microwave interferometer measures
line-integrated electron density (d) x-ray detector measures plasma x-ray
emission.

If the error associated with each measurement is identical, then Eqn. 6.1 reduces to

$$\sigma_{tot} = \sigma_i \, / \sqrt{N} \quad .$$

Each individual TOF spectrum (one of the 130 recorded spectra) is subject to the random fluctuations described earlier and therefore, has associated with it, an error which estimates its deviation from the average of an infinite number of such spectra. The averaging of many spectra reduce this associated error in accordance with Eqn. 6.1. In referring to the "error" associated with a spectrum, the actual measured error relates to individual peak heights, each of which possesses the same random fluctuation. Figure 6.2 shows the peak height distribution for an Ar^{2+} peak over the 112 spectra recorded in the single shot. The peak heights have a large spread, from 25 mV to 475 mV, with an average of 194 mV. A standard deviation of 100 mV, shown in the figure, can be found by determining the width of the distribution about the mean which contains ~ 68 % of the total number of data points. Immediately, the necessity of the averaging process becomes apparent. For any of the given pulse heights, the fractional error is very large, exceeding 100% in some cases. An error of this magnitude is unacceptable. If, however, the measured pulse heights of Fig. 6.2 are averaged, assuming each possesses an error of 100 mV, the error in the average will be reduced to $\sigma_{tot} = 100 \, / \sqrt{112} = 9.4 \, mV$. The fractional error thus becomes:

$$\frac{\sigma_{tot}}{h_{ave}} = \frac{9.4 \, mV}{194 \, mV} = \sim 5 \% \quad . \tag{6.2}$$

This is an acceptable experimental error. For the plots presented in this chapter, wherever possible a scatter of data points taken for the same plasma conditions will be used to
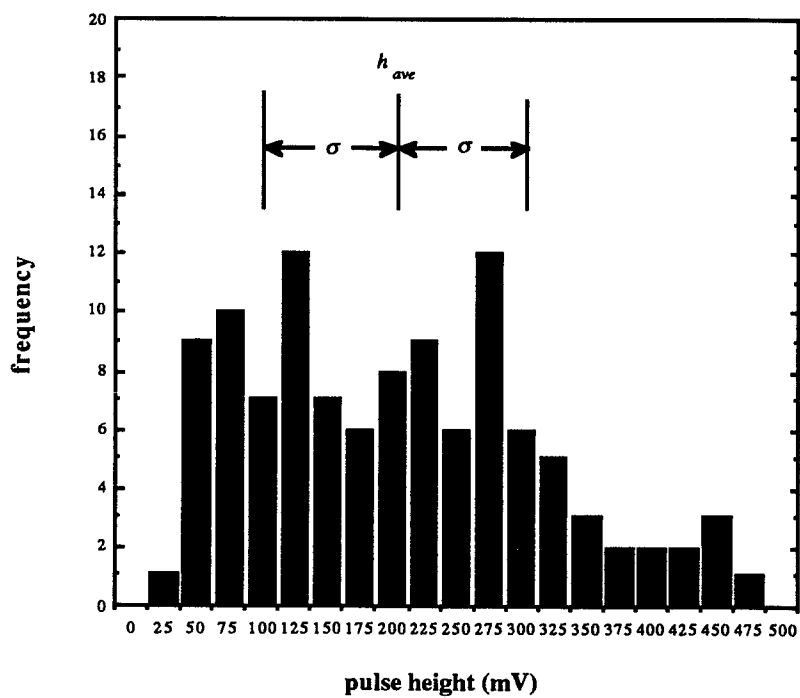
Figure 6.2. Pulse height distribution for the Ar^{2+} peak in a series of 112 TOF spectra taken during one plasma shot. The distribution shows an excessively large standard deviation in the data associated with any one given measurement, necessitating the averaging method described in Sec. 3.4.

indicate confidence in the measured quantity. If, however, only one data point was taken, Eqn. 6.2 will define the error in the measurement.

To increase the accuracy of interpretation of the reduced data taken from these processed spectra, instead of using the peak height of a specific peak as an indication of endloss current density, peak area is computed and used. This will compensate for wide peaks which appear smaller but actually indicate a larger current densities. The high m/q species exhibit this behavior. A FORTRAN program is used to integrate over each peak appearing in a spectrum. The program moves through the spectrum from time $t=0$ and finds each peak in turn. Once a peak is found, it brackets the peak and sums the amplitude of the individual data points which define it. Fortunately, the *100 MHz* digitizer allows for at least twenty data points over each of the peaks which makes the above method accurate without interpolation between data points. It is these integrated values which are used as a measure of endloss current density for each m/q species. The error previously calculated for peak heights is assumed to apply for peak areas as well.

The measurement of charge-state-specific ion endloss currents is now possible. The question then arises how the measured charge state distributions relate to the charge state distributions which actually exists in the plasma. There are many effects which cause the signals recorded by the time-of-flight spectrometer to be m/q dependent. These effects include:

- strong Z_i dependence on confinement times,

- magnetic field focusing and defocusing,

- charge exchange in flight path,

- m/q dependence of radial-to-axial loss ratio,

- TOF m/q gating-grid pulse-width discrimination.

The degree of collisionality of an ion in a plasma is strongly dependent on the charge of the ion. The type of confinement governing the ion's "diffusion" out of the plasma is dependent on its collisionality and therefore its charge. The relevant confinement regimes are discussed in chapter 5 and summarized by Eqns. 5.18 - 5.20. Typically, the lower charge states of an ECR ion source plasma fall into the flow or Pastukhov regimes and since $V_{coll} \propto Z_i^2$, the upper charge states become almost exclusively collisionally confined. The transition between the two regimes occurs usually at an intermediate charge state. Referring to the expressions for the confinement times for each of these regimes (Eqns. 5.18 - 5.20), it is evident that these confinement times are strongly charge dependent. Therefore, the efficiency with which the spectrometer measures the charge spectrum varies from charge state to charge state.

The existence of a strong magnetic field between the plasma region and the spectrometer entrance aperture also affects the relative efficiency with which the spectrometer measures a given charge state distribution. More highly-charged ions will more closely follow the magnetic field lines than the less highly-charged ions. If the spectrometer entrance aperture lies on a field line which maps to the center of the plasma, one might expect the spectrometer to be more sensitive to the higher charge states. Charge exchange during the flight path of an ion is also charge dependent. Equation 5.9 can be modified to show that the mean free path for charge exchange in argon varies as $Z_i^{-1.17}$. Mean free paths for low-charge-state ions are much longer than the distance travelled between the plasma and the spectrometer but become comparable to the flight distance for high-charge-state ions. This effect will increase the spectrometer sensitivity to low charge states.

High-Z particles in an ECRIS plasma are almost exclusively collisionally confined. In this regime, they are effectively demagnetized and therefore feel little effect from the magnetic field. Their diffusion, then will cause them to be lost in the direction of steepest density gradient which, in MIMI's case, is radial. In the opposite extreme, low-Z, uncollisional particles will be strongly confined in the radial direction and will most likely be lost axially, due to velocity space diffusion into the loss cone. This effect will increase spectrometer sensitivity of the less highly-charged ions.

The last effect which significantly affects the charge sensitivity of the spectrometer is TOF gating-grid, pulse-width discrimination. As discussed in chapter 3, ions are allowed to enter the spectrometer in short bursts. The time available for the ions to pass into the acceleration region behind the gating grid is determined by the width of the gating-grid pulse. If the transit time of an ion between the entrance aperture and the gating grid (see Fig. 3.22) is comparable to the pulse width, the signal for that ion species will be partially attenuated. Since low m/q ions have acquired much larger velocities from the ambipolar plasma potential, if the pulse width is sufficiently small, the high m/q ion signal will be preferentially attenuated. This effect is evident in Fig. 6.3 which shows that for identical plasma conditions, the ratios Ne^{2+}/Ne^{1+} and Ne^{3+}/Ne^{1+} increase as the gating-grid pulse width decreases. The Ne^{1+} signal is being preferentially attenuated, as described above, as the pulse width approaches the Ne^{1+} transit time through the entrance-gating grid gap. As shown in the figure, this effect becomes most marked when comparing the singly-ionized ion signal to a high-charge-state signal, since these high charge states are least affected by this attenuation. Under many conditions, it is necessary to use this effect to make certain that the large, low-charge-state signals do not saturate the signal detector, making impossible the measurement of the smaller high-charge-state
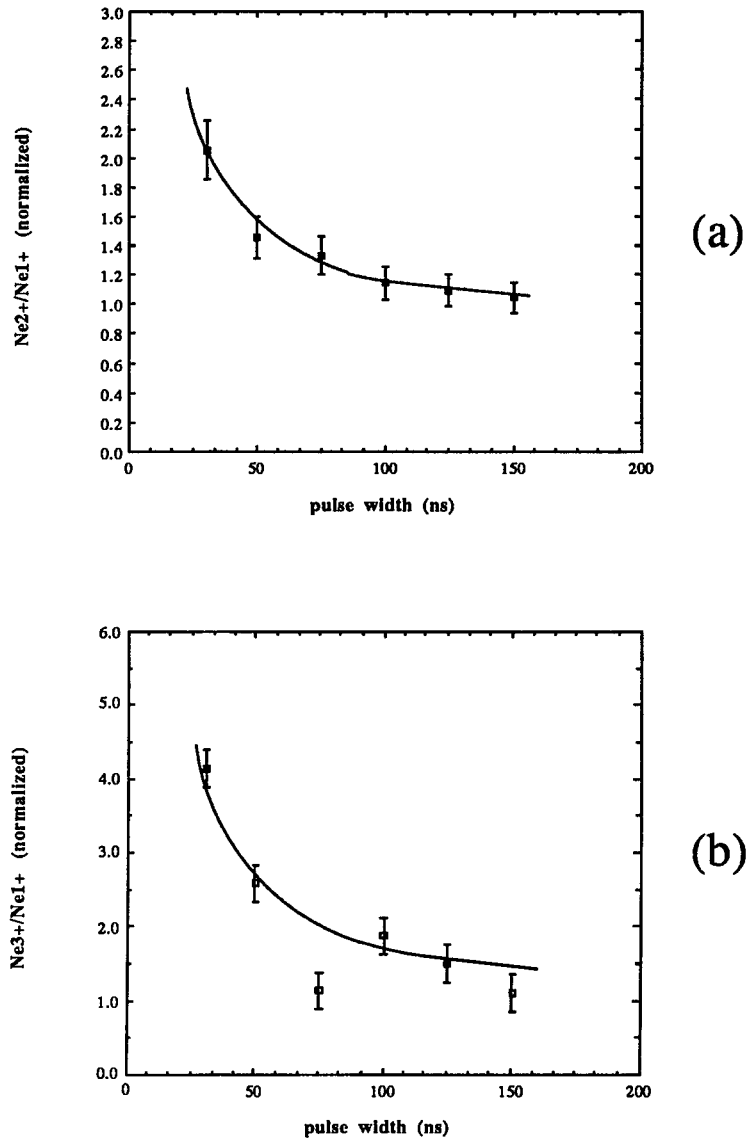
Figure 6.3. TOF signal ratios vs. gating-grid pulse width. The preferential attenuation of the large m/q ions is apparent for small pulse widths.

signals.

Several effects have been described which quite strongly impact the TOF spectrometer's ability to measure ion endloss comprised of varied m/q species. Some of the effects reduce sensitivity at the lower end of the distribution while others increase sensitivity in the same region. Any attempt to correct the measured signals for all of these effects would involve more approximations and more hand-waving than this author cares to do. All is not lost however. The important information to be gathered from such a diagnostic is the degree to which variations in system parameters affect the measured charge state distributions. As long as the "m/q-filtering" effects previously described are not altered by the changing parameters, an observed change in the measured endloss reflects a true change in the plasma confined density. For example, increasing the microwave heating power and consequently electron temperature does not affect the charge exchange rates of the ions traveling between the plasma and TOF entrance aperture. It also does not change the magnetic field focusing, ion confinement, etc. The observed changes in the recorded spectra due to this increased heating would reflect actual changes in the confined plasma charge state distribution. For this reason, the majority of data presented is presented in normalized form since the significance lies in changes in the signals and not magnitudes. Where variations in system parameters affect these m/q-filtering effects, correction for these variations must be included in the analysis. These situations will be discussed individually as they arise.

6.2. Temporal Measurements

This investigation involves study of steady-state, ion charge state distributions and their response to direct ion heating. It does not include time-resolved studies of the components of the distributions though certain knowledge of their temporal evolution is helpful if not necessary. This information allows the operator to choose a location in time, relative to the ECRH turn-on time, where the plasma ion distribution and all comprising components are in a steady state.

Figure 6.4 supplies this information. The figure plots the relative signal amplitudes of multiply-charged ions for argon and krypton as functions of time. Argon and krypton are chosen for these plots because they are the most massive of MIMI's noble, working gases. The highest charge states are expected from these gases and, consequently, the longest build-up times. Both plots show steady state is reached within 15 ms of the ECRH turn-on time. It is therefore assumed that this is the limiting time for all MIMI working gases, after which ion charge state distributions can be assumed to be in steady state. Typically, charge state distributions are measured *30 ms* after ECRH turn-on time to be certain of a steady-state situation.

The data for Fig. 6.4 was taken before the final modifications to the spectrometer were effected. In this configuration, the aperture-to-gating-grid distance was quite large and very strongly attenuated the high m/q signals. (This effect is discussed in Secs. 3.4.2 and 6.1.) For this reason, Kr^{1+} and Kr^{2+} do not appear in Fig 6.4 (b) and the Kr^{3+} and Kr^{4+} signals are quite small. But again, this effect does not alter the interpretation of the data. Also, as seen in the typical spectrum shown in Fig. 3.27, impurities can become a large part of the total collected current. These impurities are primarily due to ion bombardment of contaminated vacuum-vessel walls. They become a
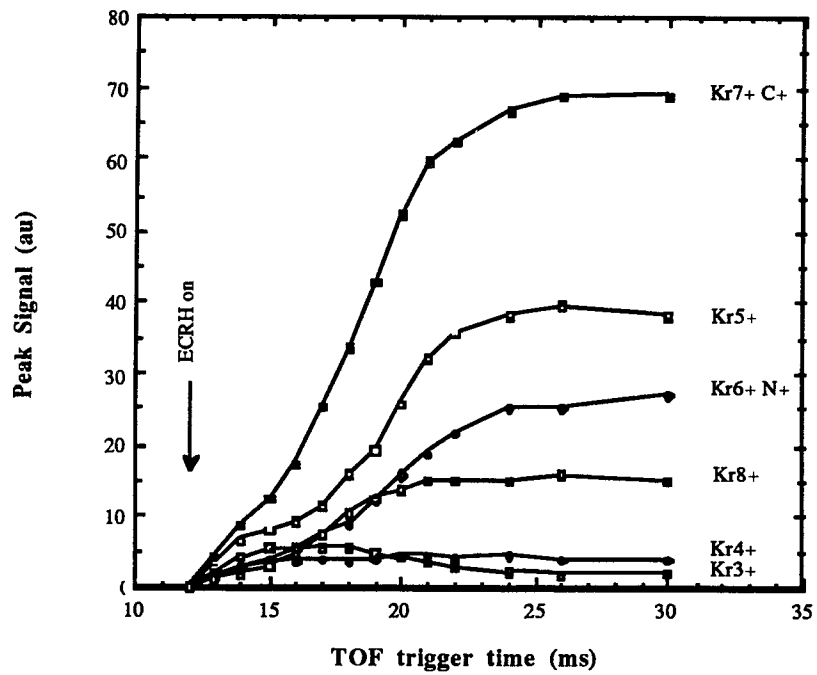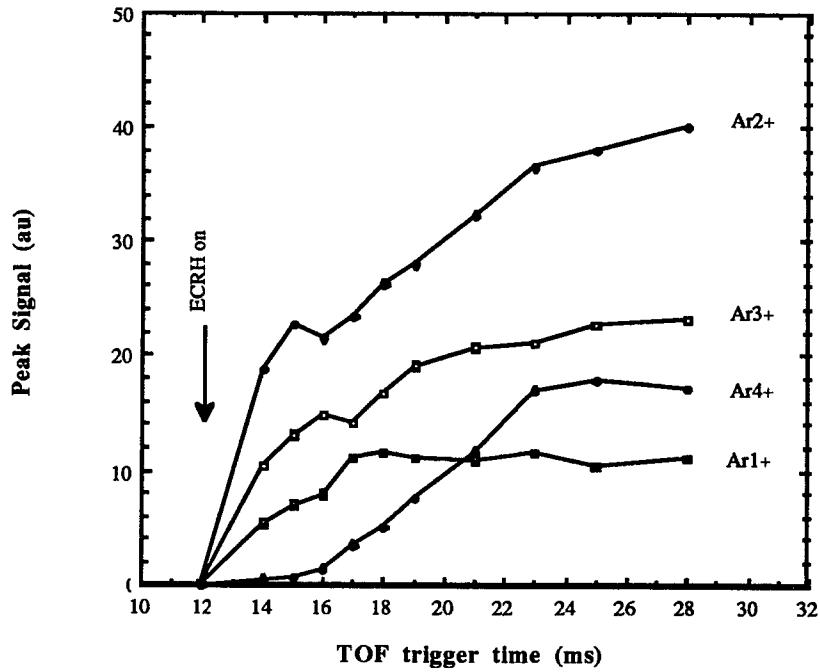
Figure 6.4. Temporal evolution of (a) argon and (b) krypton charge state distributions. Problems involving degeneracies with impurities is evident in the Kr^{6+} and Kr^{7+} signals. Error bars have been omitted for clarity.

problem if a low-charged impurity is degenerate with a higher-charged working gas ion (possesses the same m/q). If this occurs, the TOF peak corresponding to that particular m/q species is non-interpretable. This problem is evident in Fig 4.6 (b) for the Kr^{6+} and Kr^{7+} species which are degenerate with N^{1+} and C^{1+}, respectively. The signal levels are artificially raised due to the impurities and are included only for completeness. Error bars have been removed from Fig. 6.4 for clarity.

6.3. Ion Energy Distribution Measurements

Ion cyclotron heating is employed in the MIMI experiments to directly impart energy to the plasma ions. The ion heating mechanism and ICRH design considerations are discussed in chapter 4. It is important to be able to measure the effect of this ion heating on the ion distribution. Ion temperature measurements with electrostatic probes are perturbing and yield only Z-averaged information. Doppler-shift spectroscopy measurements are non-perturbing and charge-state specific but require use of expensive and as yet unavailable spectroscopy equipment. The gridded nature of the time-of-flight spectrometer, however, allows for measurement of charge-state-specific ion endloss energy distributions. The midplane Maxwellian energy distribution can be determined from the endloss energy distributions using the Monte Carlo method described in Sec. 5.3.

Briefly, the energy distribution measured at the spectrometer entrance is the superposition of three separate and distinct energy distributions. Examples are shown in Fig. 5.4. Ions gain energy from the plasma potential as they fall to system ground from the ionizing region of positive potential. They also carry their Maxwellian parallel energy component. The Maxwellian perpendicular component is transformed to the parallel

direction as the ions move through the region of decreasing magnetic field. When the ions reach the grounded entrance aperture of the spectrometer, they carry wholly parallel energy which is comprised of the sum of the energies imparted to the ions by each of the three separate distributions. The individual contributions to the total energy can be difficult to determine. The Monte Carlo approach described in Sec. 5.3 allows for determination of the individual components of the ion energy distribution and therefore ion cyclotron heating effects can be monitored.

The method for measuring these endloss energy distributions will now be described. Figure 6.5 shows the potential on the spectrometer axis as seen by an endloss ion. As an ion with energy E_i impinges on the entrance aperture of the spectrometer and enters the entrance region (from the left of Fig. 6.5), it will be repelled if:

$$E_i < qV_g \qquad (6.3)$$

where $q = ion\ charge$
         $V_g = gating\text{-}grid\ voltage.$

V_g is always increased to a voltage where Eqn. 6.3 holds true for all ions. Normally, V_g is then pulsed down to ground so that every ion entering the entrance region will pass through the gating grid unimpeded for the duration of the gating-grid pulse. If instead, the gating-grid is pulsed to some intermediate voltage, V_t, only ions with $E_i > qV_t$ will pass into the spectrometer flight tube and be measured. The remainder of the distribution will be repelled. The measured signal for a given charge state, $I_i(qV_t)$, as a function of the intermediate voltage, is then related to the energy distribution as:
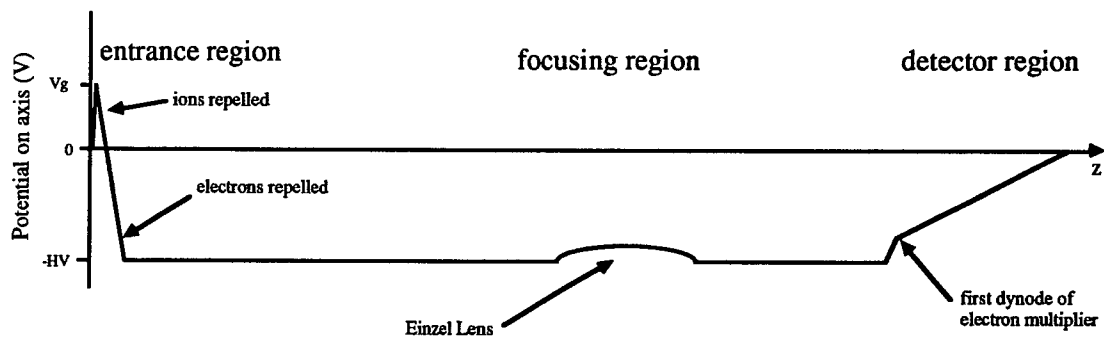
Figure 6.5. Potential profile on axis of spectrometer as seen by endloss ions. Ions are admitted to the spectrometer when the gating-grid voltage is pulsed from V_g to ground.

$$I_i(\,qV_t\,) = \eta \int_{qV_t}^{\infty} f_i(\,E\,)\,dE \tag{6.4}$$

where
$\eta = proportionality\ constant$

$q = ion\ charge$

$V_t = pulsing\ voltage.$

Consequently, the charge-state-specific ion energy distribution, $f_i(E)$, can be found as:

$$f_i(\,E\,) = f_i(\,qV_t\,) = -\frac{dI_i(\,qV_t\,)}{dV_t}\ . \tag{6.5}$$

An example of such a determination is shown in Fig. 6.6. Figure 6.6 (a) plots the data taken during an argon experimental run. As the gating-grid voltage is initially increased from zero, no attenuation of the signal occurs. This is evidence that no particles in the distribution possess these low energies. At $V_g \sim 70\ V$, the signal begins to attenuate, indicating the presence of particles in the distribution with reduced energies $E_i/q \sim 70\ eV$. The signal decreases linearly from $V_g \sim 70\ V$ to $V_g \sim 130V$ indicating a flat-topped distribution for $70\ eV < E_i/q < 130\ eV$. The signal is completely attenuated at $V_g \sim 130\ V$ which indicates that $f_{Ar2+}(E) = 0$ for $E_i/q > 130\ eV$. The derived energy distribution just described is shown in Fig. 6.6 (b). Note the change in scale of the horizontal axis due to the ion charge.

Figure 6.6 is merely an example of the method by which $f_i(E)$ can be determined from raw TOF data. This particular example is chosen because interpretation of the data is straightforward and intuitively satisfying. However, when ion temperatures begin to
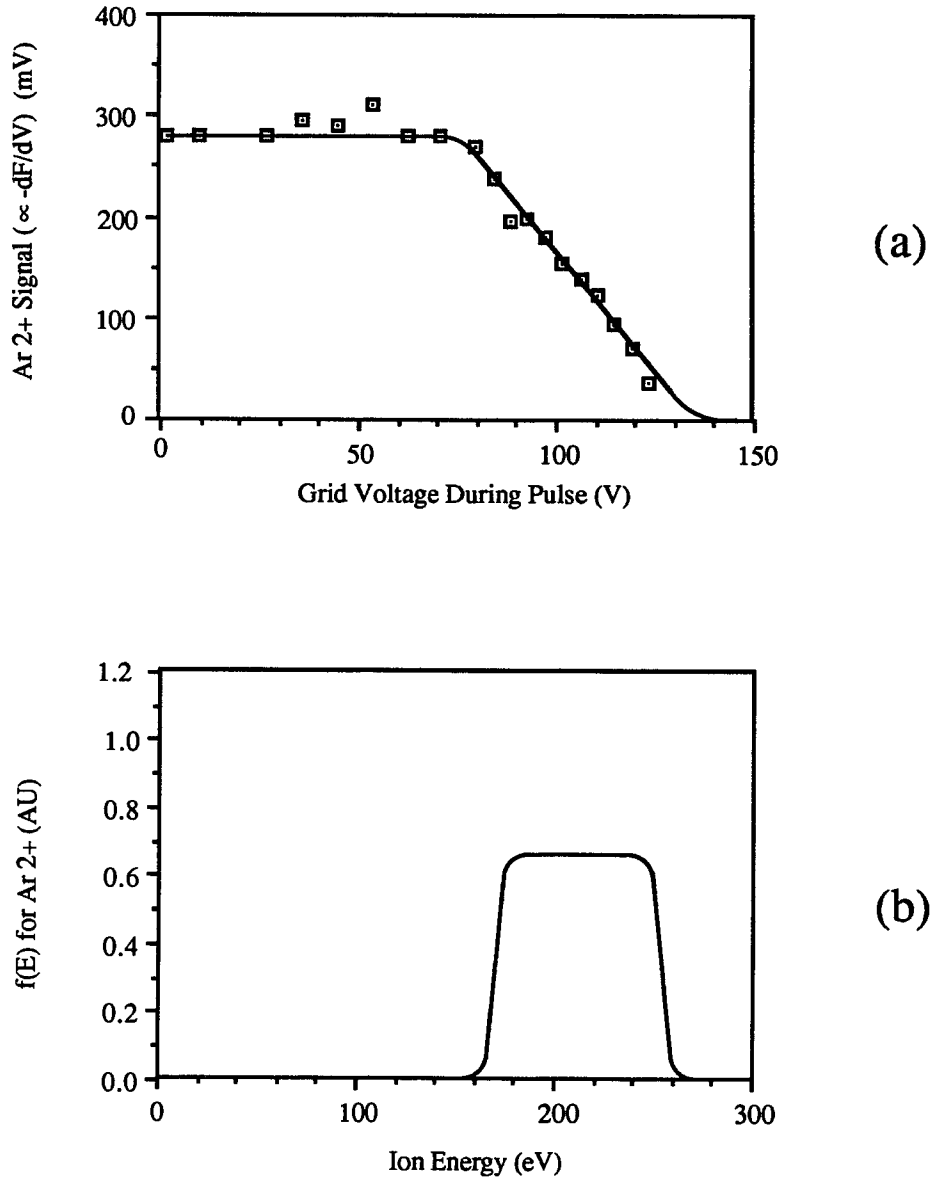
Figure 6.6. Determination of ion energy distribution from raw TOF data. (a) Ar^{2+} signal vs. gating-grid voltage at time of pulse. This is a measure of the ion population at or above energy $E_{ion} = qV_g$ (b) derived Ar^{2+} energy distribution. The shape of the distribution is due primarily to the spread in plasma potential in the ionizing region of the plasma.

affect the shape of the raw data curves and the transition period loses its linearity, simple interpretation and derivation of plots of $f_i(E)$ become much more difficult. For this reason, the plots of $f_i(E)$ generated by the Monte Carlo code, described in Sec. 5.3, for fitting to experimental data, are transformed numerically for direct comparison to the data. This transformation takes the form:

$$g_i(E) = \int_E^\infty f_i(E)\, dE \ . \tag{6.6}$$

This function, $g_i(E)$, is matched to $I_i(qV_t)$, to determine the individual contributions, from each of the distributions described earlier, to the total ion energy distribution. The best fit to the data determines the contribution of the midplane Maxwellian ion temperature distribution. In this way, midplane ion temperatures and ICRH effects, can be deduced.

The properties of three gases are investigated in this study. These gases, oxygen, neon and argon, are chosen for several reasons. First, neon and argon are noble gases and do not form compounds with system impurities. Second, in a TOF spectrum the first four charge states of each of these gases is non-degenerate with impurities. Degenerate peaks are non-interpretable. And third, atomic data for neon and argon ionization processes have been experimentally determined and published. This data is used in this work for theoretical studies of charge-state distribution equilibrium. Oxygen produces the most well-resolved spectrum peaks of all gases tested. The ion cyclotron heating parameters for each of these gases is listed in Table 6.1 below.

Figure 6.7 illustrates the effect of ion cyclotron heating on the measured distributions of O^{2+}. The heating frequency chosen is that which corresponds to the cyclotron frequency of the third charge state at $B=2700\ G$, the magnetic field at the ECR

Table 6.1. Conditions for ICRH in MIMI

working gas	resonant charge state	heating frequency	resonant magnetic field	maximum rf current
oxygen	O^{3+}	750 kHz	2700 G	200 Ap-p
neon	Ne^{3+}	620 kHz	2700 G	200 Ap-p
argon	Ar^{3+}	310 kHz	2700 G	150 Ap-p

resonance zones. Since the plasma is sufficiently collisional, it cannot support a large perpendicular-to-parallel temperature difference and it is therefore assumed $T_{\perp} = T_{//} = T_i$. It is also assumed that the energy distribution from the plasma potential spread has the form shown in Fig. 5.3 (e) with a minimum energy of zero. The effect of the ICRH is determined from plots such as those of Fig. 6.7 as follows. Endloss ion charge state distributions are measured with the TOF spectrometer with and without ICRH as a function of gating-grid voltage. This will generate the data points shown in Fig. 6.7. For the case without ICRH, the midplane ion temperature is assumed to be small (*10 eV*) relative to the energy gained from the ambipolar potential. A best fit of the Monte Carlo code output, $g_i(E)$, determines the midplane plasma potential spread. This is illustrated in Fig. 6.7 (a). This spread is assumed to remain constant with the application of ICRH. The change in the shape of the peak-area-vs.-V_{pulse} curve is assumed to be a direct result of increased ion temperature. The best fit to this data then, determines the increase in T_i

(a)

(b)
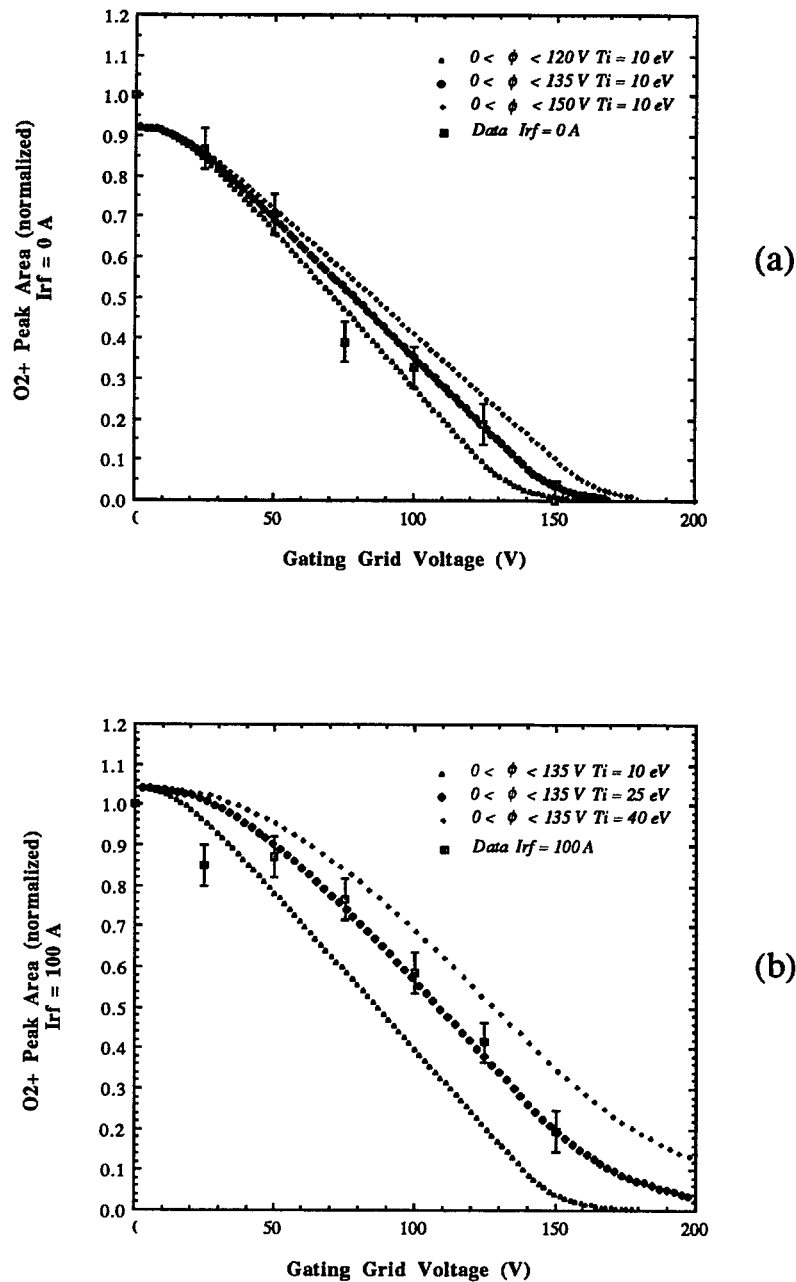
Figure 6.7. Determination of plasma potential spread and ICRH ion temperature increase of O^{2+} using Monte Carlo fit to TOF data. (a) O^{2+} peak area vs. gating-grid voltage for $I_{rf} = 0\,A$ and Monte Carlo fits for $T_i = 10\,eV$ and $0 < \phi < 120V$, $0 < \phi < 135V$, $0 < \phi < 150V$. The fits show a sensitivity of $< 15\,eV$ (b) O^{2+} peak area vs. gating-grid voltage for $I_{rf} = 100\,A$ and Monte Carlo fits for $0 < \phi < 135$ and $T_i = 10\,eV$, $T_i = 25\,eV$, $T_i = 40\,eV$. This fit assumes no change in the plasma potential profile with ICRH.

with ICRH. Fig. 6.7 (a) shows three fits to the data for $0 < \phi < 120\ V$, $0 < \phi < 135\ V$, and $0 < \phi < 150\ V$. The best fit is obviously the center one in the figure showing that this method has a resolution of $< 15\ eV$ for determining the plasma potential spread. Now, assuming $\phi_{p\ max} = 135\ V$, T_i is increased in Fig. 6.7 (b) until a good match to the data is achieved. Again, three cases are shown for $T_i = 10\ eV$, $T_i = 25\ eV$, and $T_i = 40\ eV$. Clearly, the $T_i = 25\ eV$ case is the best fit to the data which shows a $15\ eV$ increase in the O^{2+} ion temperature with ICRH. Figure 6.7 (b) also shows the sensitivity of this measurement to be $< 10\text{-}15\ eV$.

Figure 6.8 shows the same fits to the O^{3+} ion for the same shots of Fig. 6.7. The fit for the case of $I_{rf} = 0\ A$ must be the same as for the O^{2+} ion since the plasma potential profile affects both distributions in the same manner. They are indeed identical. The fit for the case of $I_{rf} = 100\ A$, though, shows an ion temperature of $40\ eV$. This is $15\ eV$ higher than the O^{2+} case. This is consistent with the concept of heating the $3+$ charge state and transferring, through collisions, the absorbed energy to the reminder of the distribution. Calculations shown later in this chapter show ion energy exchange times small compared to typical diffusion times. Also, the possibility of direct heating of nearby charge states exists as the resonance zones of high charge states often overlap.

Figures 6.9 and 6.10 show the same ICRH effect measured with neon. Without ICRH, the plasma potential spread is determined to be $140\ V$ with an ion temperature of $10\ eV$. When ICRH is turned on, the $2+$ charge state increases in temperature to $25\ eV$ and the $3+$ charge state increases to $40\ eV$. This is again consistent with the direct heating of the $3+$ ion and subsequent collisional energy transfer to the remainder of the distribution.

The effect of ion heating for argon is shown in Fig. 6.11. These data were taken
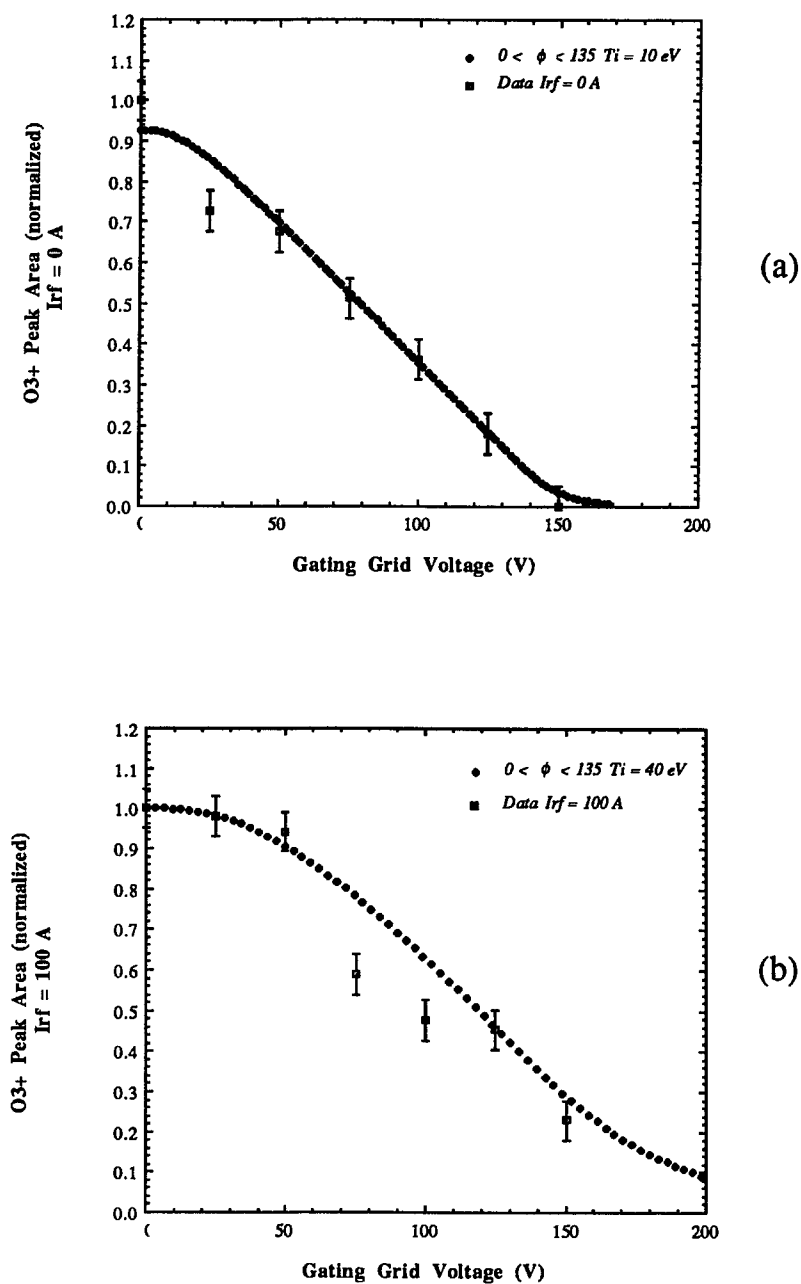
Figure 6.8. Determination of plasma potential spread and ICRH ion temperature increase of O^{3+} using Monte Carlo fit to TOF data. (a) O^{3+} peak area vs. gating-grid voltage for $I_{rf} = 0$ A and Monte Carlo fit for $T_i = 10$ eV and $0 < \phi < 135V$ (b) O^{3+} peak area vs. gating-grid voltage for $I_{rf} = 100$ A and Monte Carlo fit for $0 < \phi < 135$ and $T_i = 40$ eV. The resonant O^{3+} ions have gained 15 eV more than the non-resonant O^{2+} ions of Fig. 6.7.
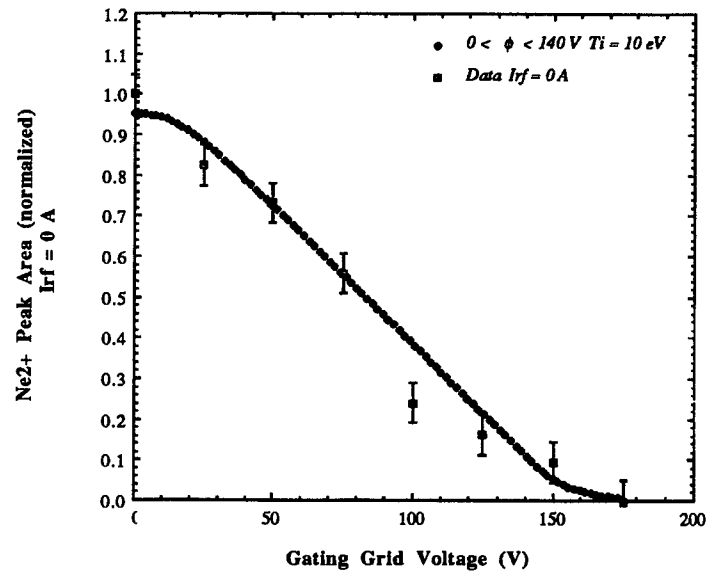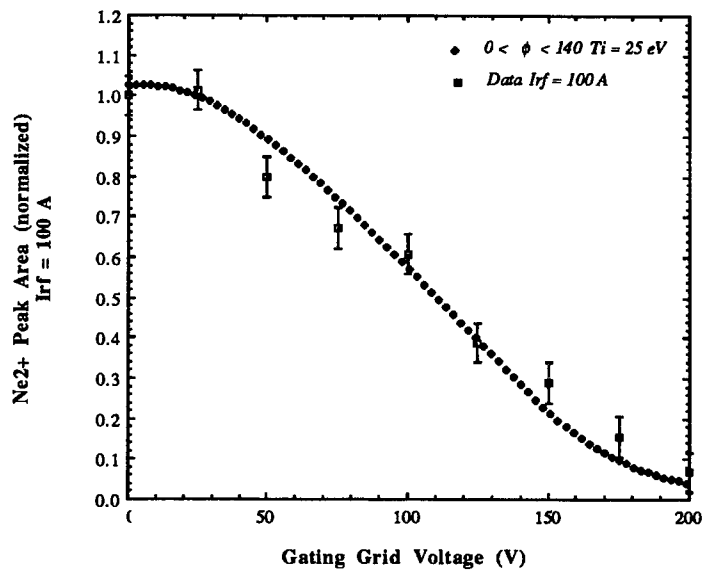
Figure 6.9. Determination of plasma potential spread and ICRH ion temperature increase of Ne^{2+} using Monte Carlo fit to TOF data. (a) Ne^{2+} peak area vs. gating-grid voltage for $I_{rf} = 0\ A$ and Monte Carlo fit for $T_i = 10\ eV$ and $0 < \phi < 140V$ (b) Ne^{2+} peak area vs. gating-grid voltage for $I_{rf} = 100\ A$ and Monte Carlo fit for $0 < \phi < 140$ and $T_i = 25\ eV$.
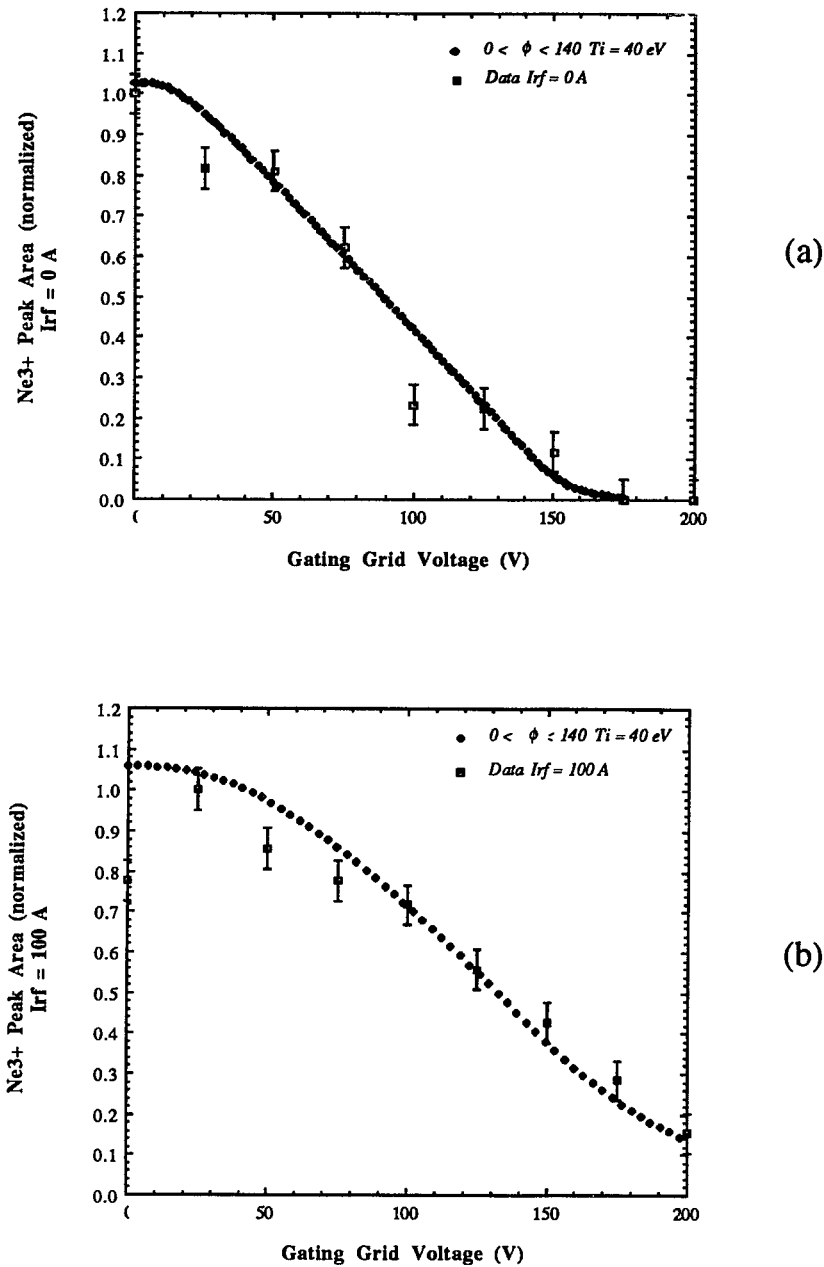
Figure 6.10. Determination of plasma potential spread and ICRH ion temperature increase of Ne^{3+} using Monte Carlo fit to TOF data. (a) Ne^{3+} peak area vs. gating-grid voltage for $I_{rf} = 0$ A and Monte Carlo fit for $T_i = 10$ eV and $0 < \phi < 140V$ (b) Ne^{3+} peak area vs. gating-grid voltage for $I_{rf} = 100$ A and Monte Carlo fit for $0 < \phi < 140$ and $T_i = 40$ eV. The resonant Ne^{3+} ion has gained 15 eV more than the non-resonant Ne^{2+} ion of Fig. 6.9.

with low rf currents (*60 A* peak-to-peak compared to *100 A* for oxygen and neon) and since $P \propto I_{rf}^2$, the measured effect is small. The $I_{rf} = 0\ A$ and $I_{rf} = 60\ A$ cases are plotted together for the *2+* and *3+* ions for comparison. The Monte Carlo fits have been removed for clarity. These fits show ~ *5-10 eV* increase in the ion temperature with the application of ICRH. The effect for higher rf currents is assumed to be similar to that measured for oxygen and neon. This is important information used for the modeling of Sec. 6.4.

An order-of-magnitude ion energy increase estimate can be determined from the ICRH coupling computations presented in chapter 4. The stored energy in the MIMI plasma, calculated from DML measurements, is typically:

$$E_{stored} \sim 0.1\ J\ .$$

(6.7)

Assuming that the plasma is comprised wholly of one species and that the ion confinement time is equal to the electron confinement time ($\tau_{e\ part} \sim \tau_{e\ energy}$ given small cyclotron and bremsstrahlung losses), then

$$\tau_i = \tau_e = \frac{E_{stored}}{P_{ECR}} \sim 10^{-4}\ s\ .$$

(6.8)

The average energy increase per ion as a function of ICRH coupled power then becomes:

$$\frac{\Delta T_i}{N} = \frac{P_{ICRH}\ \tau_i}{e\ n_i V_{plasma}}$$

$$= \frac{P_{ICRH}\ E_{stored}\ Q_i}{e\ P_{ECR}\ n_e V_p}\ .$$

(6.9)

This becomes $\dfrac{\Delta T_i}{N} \sim 0.5\ Q_i\ P_{ICRH}\ (W\ )\ eV/ion$ for the running parameters of
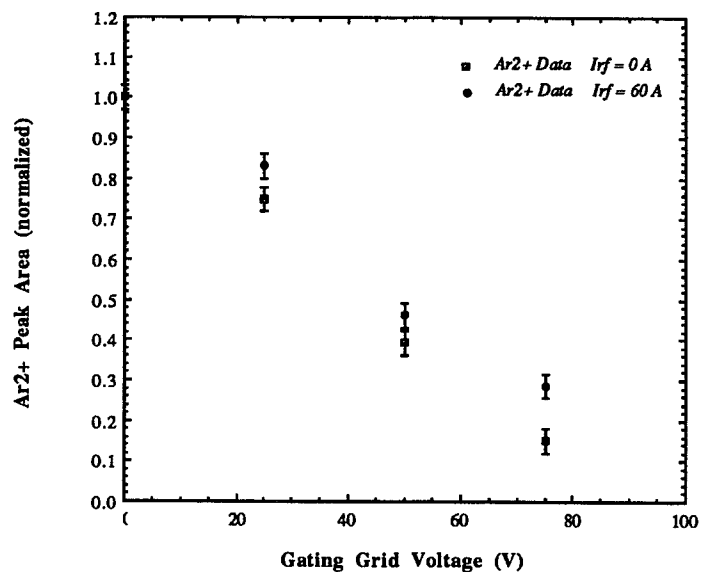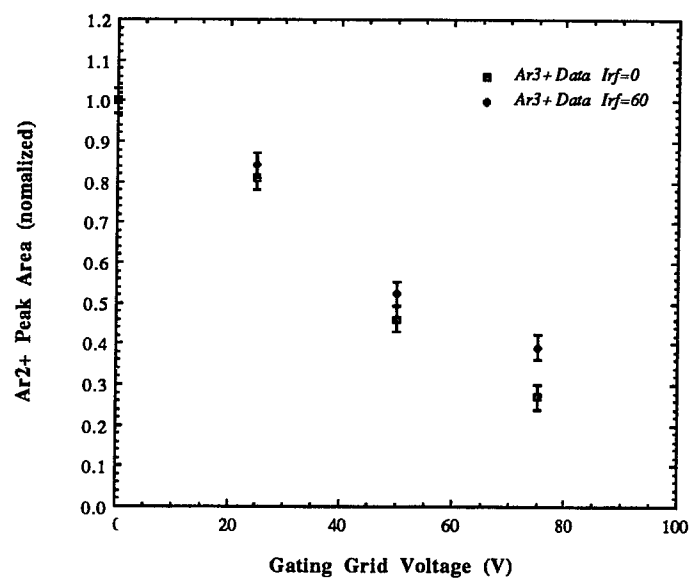
Figure 6.11. Effect of ICR heating on (a) Ar^{2+} and (b) Ar^{3+}. Low rf currents are used for this data. Monte Carlo fits have been removed but show a temperature increase in both charge states of 5-10 eV.

Figs. 6.7 - 6.10. Assuming the plasma consists of wholly Ne^{3+} ions, Fig. 4.4 predicts an antenna loading of $Z_{ant} \sim 0.2m\Omega$. Since the ICRH current for neon is $100\ A$ peak, the coupled power becomes $P = \frac{1}{2}\ I^2\ Z = 10\ W$. The energy increase per ion is then:

$$\frac{\Delta T}{N} \sim 15\ \frac{eV}{ion}\ . \tag{6.10}$$

This is similar to the heating experimentally determined. Again, this is only an order-of-magnitude estimate. However, this calculation does demonstrate consistency between antenna loading computations and experimentally measured loading effects.

Langmuir probe measurements also indicate increased ion temperature with ICR heating. The ion saturation current is found to increase $\sim 1.4x$ with the application of ICRH. If an orbital-limited model is assumed, the ion saturation can be expressed as:[62]

$$I_{sat} = \{\ 4\sqrt{2}\ e\ r_p^2\ (\ 1 - \frac{eV_p}{kT_e}\ )^{1/2}\ \}\ Zn_i\ (\ kT_i\ )^{1/2}\ . \tag{6.11}$$

Electron density is monitored during ICRH and found to be unaffected. This indicates that Zn_i remains unchanged and an increased T_i is responsible for the changing ion saturation current. Unfortunately, the assumption of orbital-limited motion is only marginally valid, and thus the scaling of T_i with I_{sat} is not expressly quadratic. However, the increase in I_{sat} does indicate an increased ion temperature.

One last remark is included in this section regarding the energy transfer from the heated species of the distribution to the remainder of the distribution. An estimate of "energy relaxation" time, or the time required for a particle to share its energy with the

equilibrium distribution that surrounds it, is assumed to be the Spitzer 90° scattering time. This scattering time, discussed in chapter 5, takes the form:

$$\frac{1}{\tau_{ii}} = \frac{0.174 \, Z_i^2}{M_i^{1/2} T_i^{3/2}} \sum_j N_j \, Z_j^2 \quad \mu s^{-1}$$

(6.12)

where

i denotes scattered particle quantities

j denotes scattering particle quantities

T_i in eV

$q_i = Z_i e$

$m_i = M_i m_p$

$n_j = N_j \, x \, 10^{11} \, cm^{-3}$.

For a typical neon charge state distribution computed by the ICSD code and listed in Table 6.2, the scattering times have been computed and included in the table. Table 6.2 assumes a total electron density of $n_e = 2 \, x \, 10^{11} \, cm^{-3}$. Since the scattering times listed in the table are much smaller than typical diffusion times, each ion species will equilibrate with the rest of the distribution before being lost. Therefore, direct ion heating will preferentially raise the temperature of the resonant charge state, however the added ion energy resulting from this direct heating will quickly spread to the other charge states via collisions. This effect is evident in the ICRH temperature increases determined from Figs. 6.8 - 6.11. For these cases, the resonant species have been elevated ~30 eV while the non-resonant species have gained ~10-15 eV through collisions with the hotter, resonant portion of the distribution. Some non-resonant heating of the plasma may also contribute to the bulk ion heating.

Table 6.2. Typical Neon Charge State Distribution and Associated Scattering Times

species	density	90° scattering time
Ne^{1+}	$1.4 \times 10^{10} \, cm^{-3}$	$147 \, \mu s$
Ne^{2+}	$3.8 \times 10^{10} \, cm^{-3}$	$36 \, \mu s$
Ne^{3+}	$2.2 \times 10^{10} \, cm^{-3}$	$16 \, \mu s$
Ne^{4+}	$0.86 \times 10^{10} \, cm^{-3}$	$9 \, \mu s$
Ne^{5+}	$0.22 \times 10^{10} \, cm^{-3}$	$6 \, \mu s$

6.4. ICRH Effects on Ion Charge State Distributions

Ion cyclotron resonance heating has been implemented on MIMI to effect direct energy transfer to the plasma ions. This section deals with the effect of this energy transfer on the steady-state ion charge state distributions. Measured effects are reported for oxygen, neon, and argon, as are correlations with the modeling code ICSD discussed in Sec. 5.2. Time-of-flight-spectrometer, confinement-time sensitivity to ion temperature is accounted for and a "mapping" is performed to relate the measured endloss charge state distribution changes to the actual changes occurring in the confined midplane plasma. Discrepancies between code predictions and measured ion signals are also discussed.

Data for the measured ion signals of neon as a function of rf current are shown in Fig. 6.12. A scatter of data points taken for identical plasma conditions is used instead of error bars to illustrate confidence in the measured quantities. The data are normalized for reasons discussed in Sec. 6.1. It is quite evident from the scaling of the high charge state current densities with rf current that the ICRH is producing a detrimental and undesired effect on the overall charge state distribution. The current densities of the highest charge states drop precipitously with rf current while the current densities of the lowest charge states remain constant and even increase with the highest rf currents. For neon, it appears that the overall effect of the ion heating is therefore to decrease the average Z of the extracted ions.

The results of Sec. 6.3 show that with the rf currents of Fig. 6.12, ion temperatures are markedly affected. This increase in ion temperature will affect the ion confinement times in the plasma after Eqns. 5.21 - 5.22. These equations show:
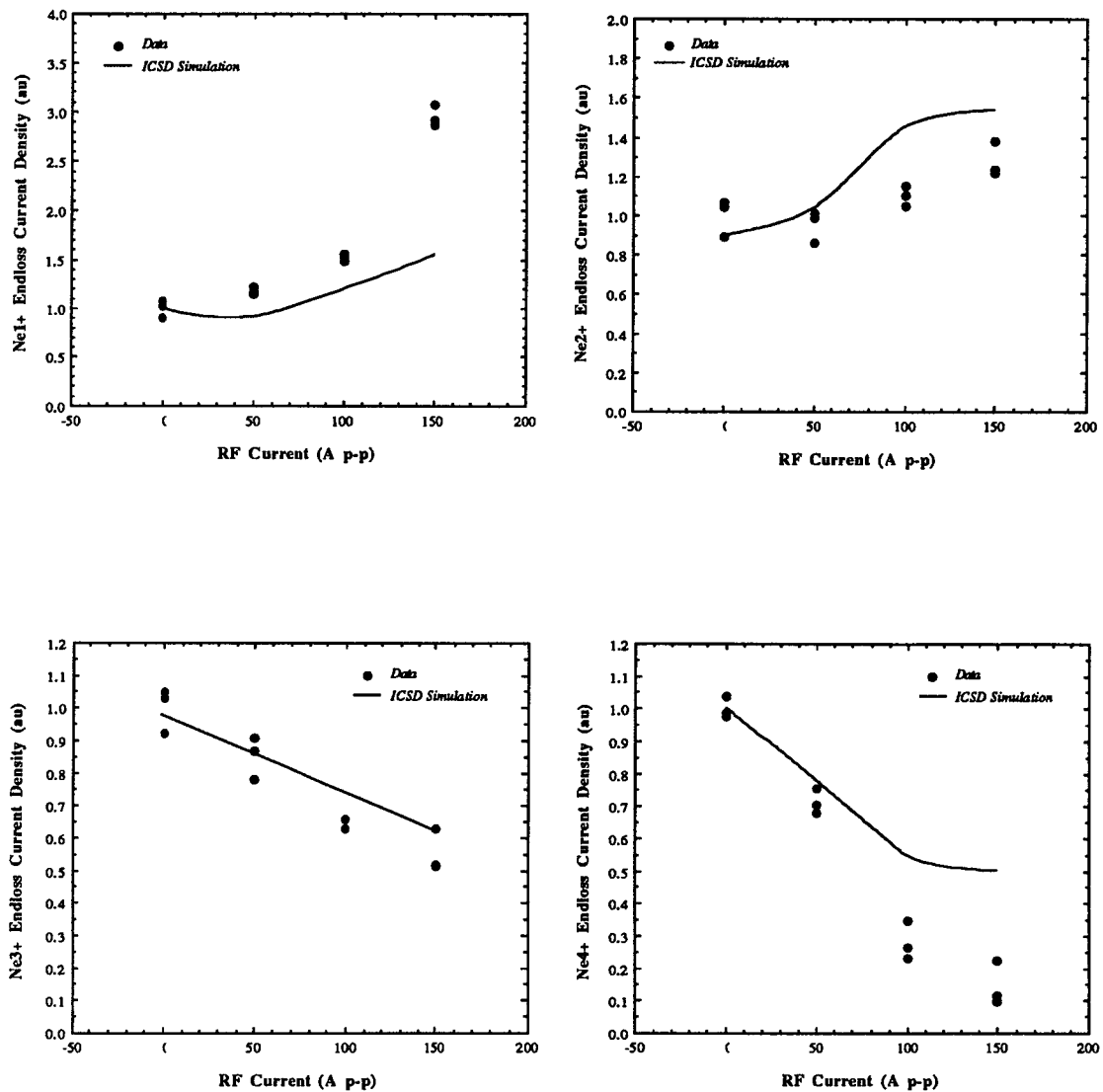
Figure 6.12. Measured and computed neon ion endloss charge state distribution changes with ion temperature. Values are plotted as a funcition of I_{rf} which are related to ion temperature after Eqn. 6.14. The parameters for the simulation are $\phi = 15$ V, $T_i = 5$, 7.7, 16.1, 30 eV. The input to the ICSD code for each run has been corrected for slight measured changes in the electron density with I_{rf}.

- for flow or Pastukhov confinement, $\eta_{coll} \leq 1$,

$$\tau_{fp} \propto (1 + \beta T_i)\, e^{\frac{Z_i q \phi}{kT_i}} \qquad (6.13)$$

- for collisional confinement, $\eta_{coll} >> 1$,

$$\tau_{coll} \propto \frac{1}{T_i^{3/2}}$$

where $T_i = $ *ion temperature*
       $\phi = $ *potential dip*
       $\beta = $ *constant - not function of* T_i.

Since the spectrometer measures endloss, it is sensitive to changes in ion confinement so that a decrease in a given measured signal does not necessarily imply a decrease in the steady-state confined density for that charge state. This is the parameter-sensitive m/q-filtering effect described in Sec. 6.1 and will affect the interpretation of Fig. 6.12.

This ion confinement change with temperature can be accounted for using the ICSD code. By matching the predicted loss rates from the code to the measured loss rates and then imposing the conditions required for the match on the system, the confined densities of each of the charge states can be computed. The ICSD code computes confinement times and densities of each of the charge states present in the mirror. The loss rates of a given charge state i, varies as n_i/τ_i. Since $\tau_i \propto f(T_i)$, the change in τ_i with rf heating must be included in the match to the measured data, even when the data are

presented in normalized form. The ion temperature is assumed to vary with the rf antenna current as:

$$T_{ion} = T_o + \eta I_{rf}^2 .$$ (6.14)

The ion temperature increase with the rf is held consistent with the temperature increases found using the Monte Carlo fits to the time-of-flight plots of Figs. 6.7 - 6.11. T_o, the initial ion temperature and $\Delta\phi$, the confining potential dip, is adjusted to yield the best fit to the data. These best fit values, though, are consistent with values expected from other independent measurements.

The best ICSD loss-rate fit to the measured data is also shown on Fig. 6.12. Code parameters are included in the figure. The electron density is monitored during the runs of Fig. 6.12 and the code inputs are corrected for these slightly varying densities. For these runs, the neutral background is considered to be 99% ionized. The code predicts the general measured trends of each of the charge states with increasing ion temperature. Again the computed signal of the high-charge-state endloss is seen to decrease with temperature, though not as quickly as measured by the TOF. Both the Ne^{1+} and Ne^{2+} endloss is predicted to increase with ion temperature, as it must to maintain charge neutrality. The confinement times for each of the computed points of Fig. 6.12 is plotted in Fig. 6.13. The TOF is effectively measuring n_i/τ_i so if confinement times vary strongly with ion temperature, the measured signals can be markedly affected even if the confined density remains relatively unchanged. Figure 6.13 shows that this is indeed the case. The confinement time for singly-ionized neon is seen to rise with ion temperature, consistent with the flow confinement model of Eqn. 6.13.
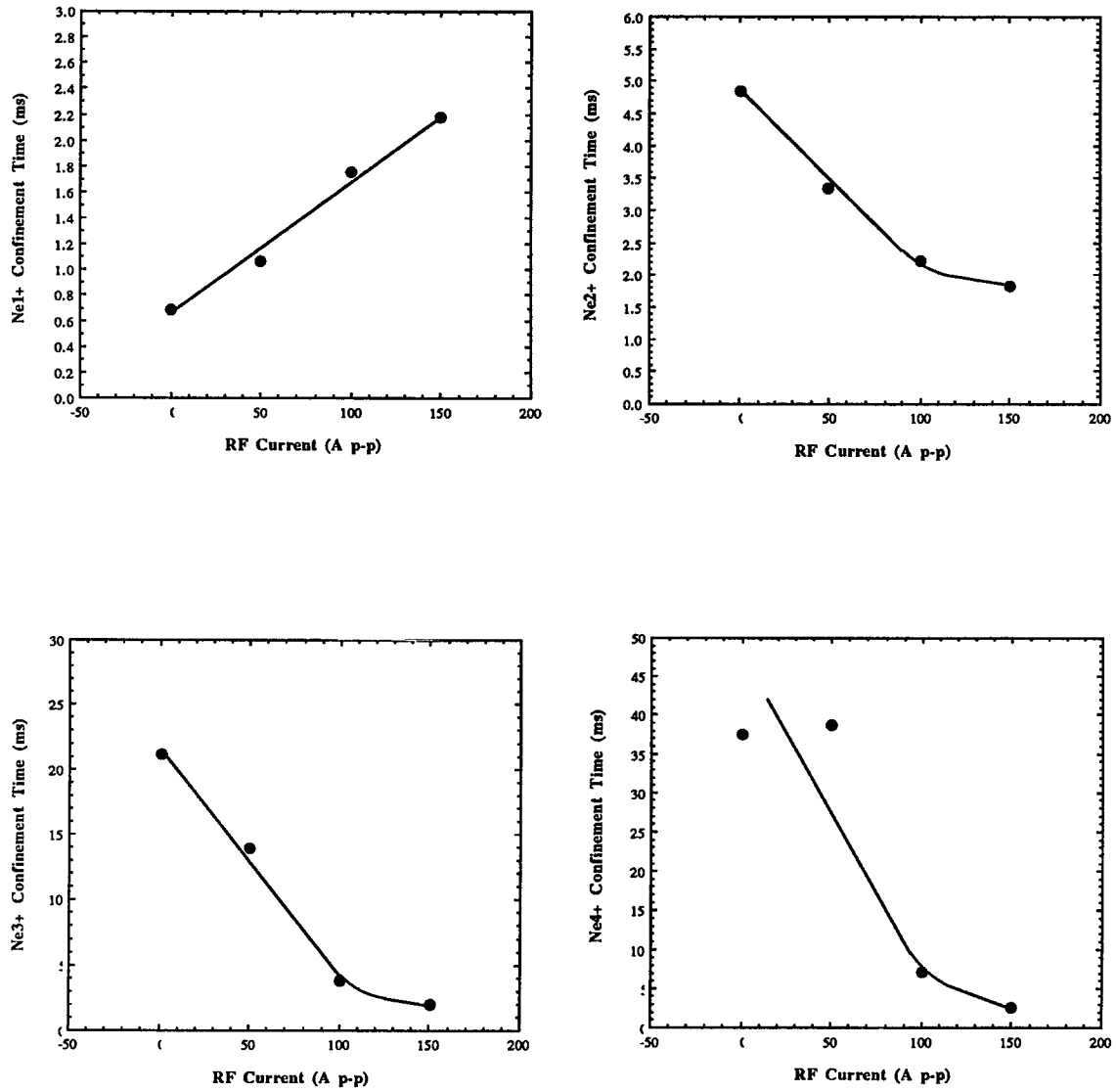
Figure 6.13. Computed neon ion confinement times for conditions of Fig. 6.12.

As the ion charge increases, the confinement times are seen to fall quickly with temperature. This is a result of the fact that the ions become more collisional with increased Z_i and move into the collisional confinement regime where $\tau_{conf} \propto \dfrac{1}{T_i^{3/2}}$.

Also, for those ions that do remain flow confined, with increasing Z_i, the magnitude of the $e^{\frac{Z_i q\phi}{kT_i}}$ term of Eqn. 6.13 becomes a strong function of T_i, decreasing rapidly with T_i. This sharp decrease in τ_{conf} has the effect of increasing the measured signals above that which would be expected from mere confined densities alone. Alternatively, the increasing confinement time of the singly-ionized state of Fig. 6.13, decreases the measured signal of Ne^{1+}.

The trends in the computed charge state distributions with ion temperature modeled by the ICSD code match well with the measured results. However, some discrepancies do exist. Several possibilities exist for the cause of the discrepancies. First, the ICSD code only allows for equal temperatures for all ions in a distribution. The measured ICRH ion temperature changes of Sec. 6.3 show that the resonant species typically gains *15 eV* more than the non-resonant species. Only a "bulk" ion energy increase can be accounted for by the ICSD code. Also, for the very high m/q ions, gating-grid pulse-width attenuation described in Sec. 6.1 is temperature dependent. As the ion temperature increases, the effect will become less pronounced and the measured signal for low charge states will increase above that which would be computed. One last effect which can cause discrepancies in the computed and measured signals is the inherent assumption in the flow and Pastukhov expressions for τ_{conf} of *100%* axial losses. In the Pastukhov case, ions are lost from the system as they diffuse into the loss cone. These ions are then lost axially, which is a valid assumption for collisionless particles. Seldom, though, do ions in an ECR ion source fall into this confinement regime. In the flow

confinement case, τ_{flow} is derived assuming that only particles within one mean free path of the system ends are subject to loss through collisional scattering into the loss cone. For interior particles, the distribution is assumed Maxwellian and loss cone particles are retained. Again the only losses are assumed axial. In the flow confinement regime, this is not strictly valid since collisions do allow particles to diffuse radially across magnetic field lines and be lost to the walls without entering the endloss. The form for the flow confinement time then, overestimates the fraction of lost particles in the endloss and consequently the magnitude of the computed endloss signal changes due to changes in ion confinement time with ion temperature. This effect is indeed apparent in Figs. 6.12 and 6.13. The rapid, confinement-time decrease with ion temperature for the high charge states artificially boosts the computed n_i/τ_i values to levels higher than would be expected.

The conditions are now determined for the best fit between the measured and computed endloss signals. The confined charge state distributions may now be computed. Results for these confined densities for the conditions of Figs. 6.12 and 6.13 are shown in Fig. 6.14 for the first four charge states of neon. As with the endloss densities, the confined densities of the high charge states decrease rapidly with ion temperature. This is a consequence of the rapid decrease in confinement with temperature prescribed by Eqns. 6.13. Charge neutrality must still be maintained, though, which accounts for the increase in the confined densities of the low charge states whose confinement is not negatively affected by temperature changes.

Figures 6.12 - 6.14 illustrate the negative effect which ICRH has on the neon charge state distributions attained in MIMI. With increased ICRH, a marked shift to lower charge states occurs due to the decreasing confinement times of high charge states
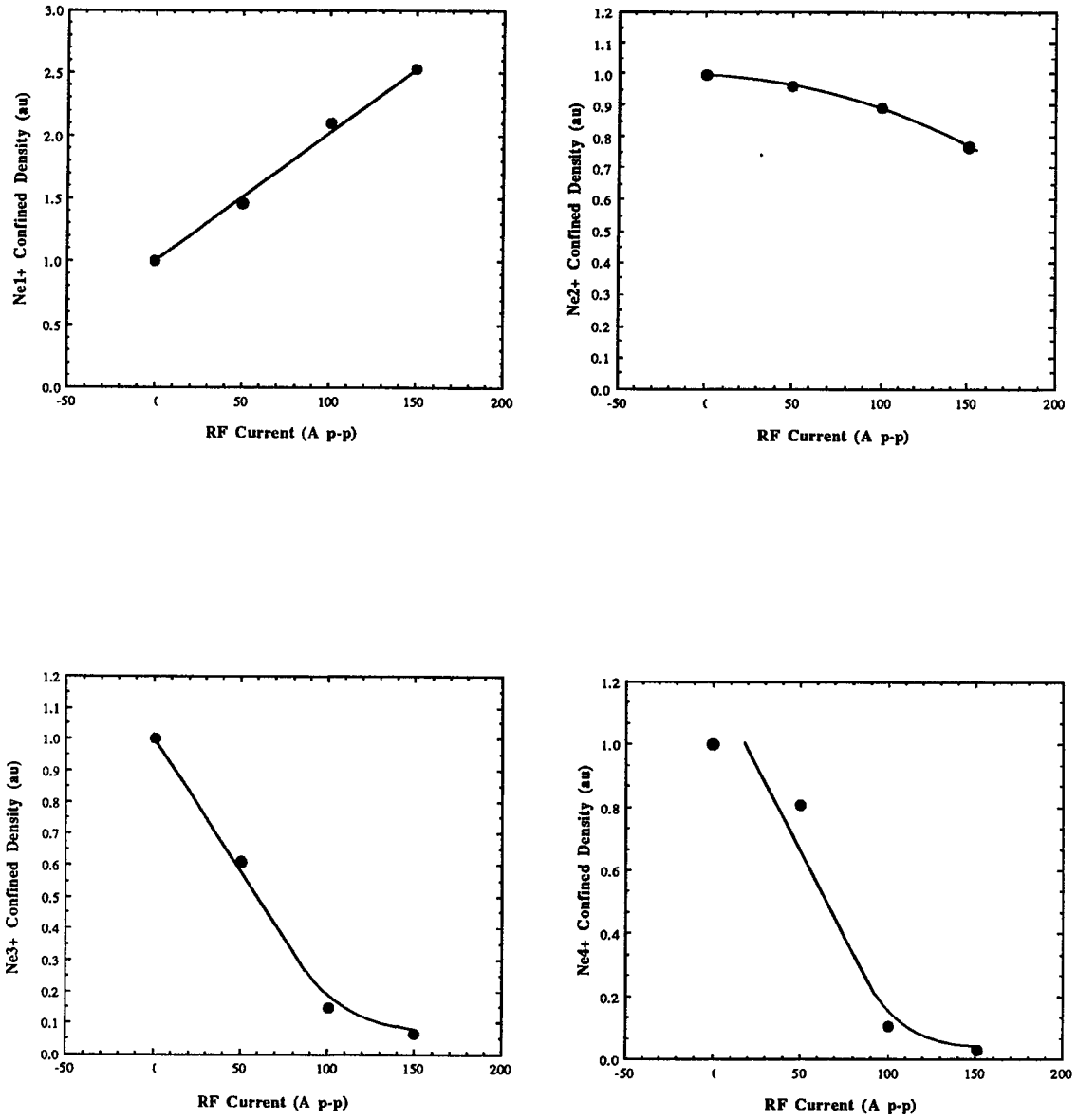
Figure 6.14. Computed neon confined densities for conditions of Fig. 6.12.

with temperature. At large rf powers, results of both measurement and modeling show almost complete loss of all charge states above the first three.

Results similar to that presented for neon in Figs. 6.12 - 6.14 are shown for argon in Figs. 6.15 - 5.17. The same type of behavior is evident for the measurable charge states of argon. The match of the ICSD code is quite good but it again overestimates the predicted endloss current densities for high charge states for reasons discussed earlier. The electron density measured during this run varied significantly with the ICRH current. This accounts for the decreasing current density of the lowest charge state with ion temperature. In this case, charge neutrality is not enforced. Again, the effect of ion heating via ICRH has a marked detrimental effect on the charge state distributions of argon. A predicted and measurable shift to low charge states is observed with increasing ion temperature.

The ICSD simulations shown in Figs. 4.12 - 4.17 require knowledge of single and multiple-step collisional ionization cross sections. These cross sections are not well known and experimental data has been published for only the noble gases. Simulations, therefore, for the third gas, oxygen, studied in this investigation have not been performed. Experimental results are shown for oxygen in Fig. 6.18 and are included for completeness. The trends of oxygen endloss charge state distributions exhibit the same behavior as observed for neon and argon. Therefore, it is expected that the confined oxygen distributions computed from an ICSD simulation would yield similar results - a rapid loss of high charge state densities with increasing ion temperature due to decreasing ion confinement and an increase in the low charge state densities required to maintain charge neutrality.
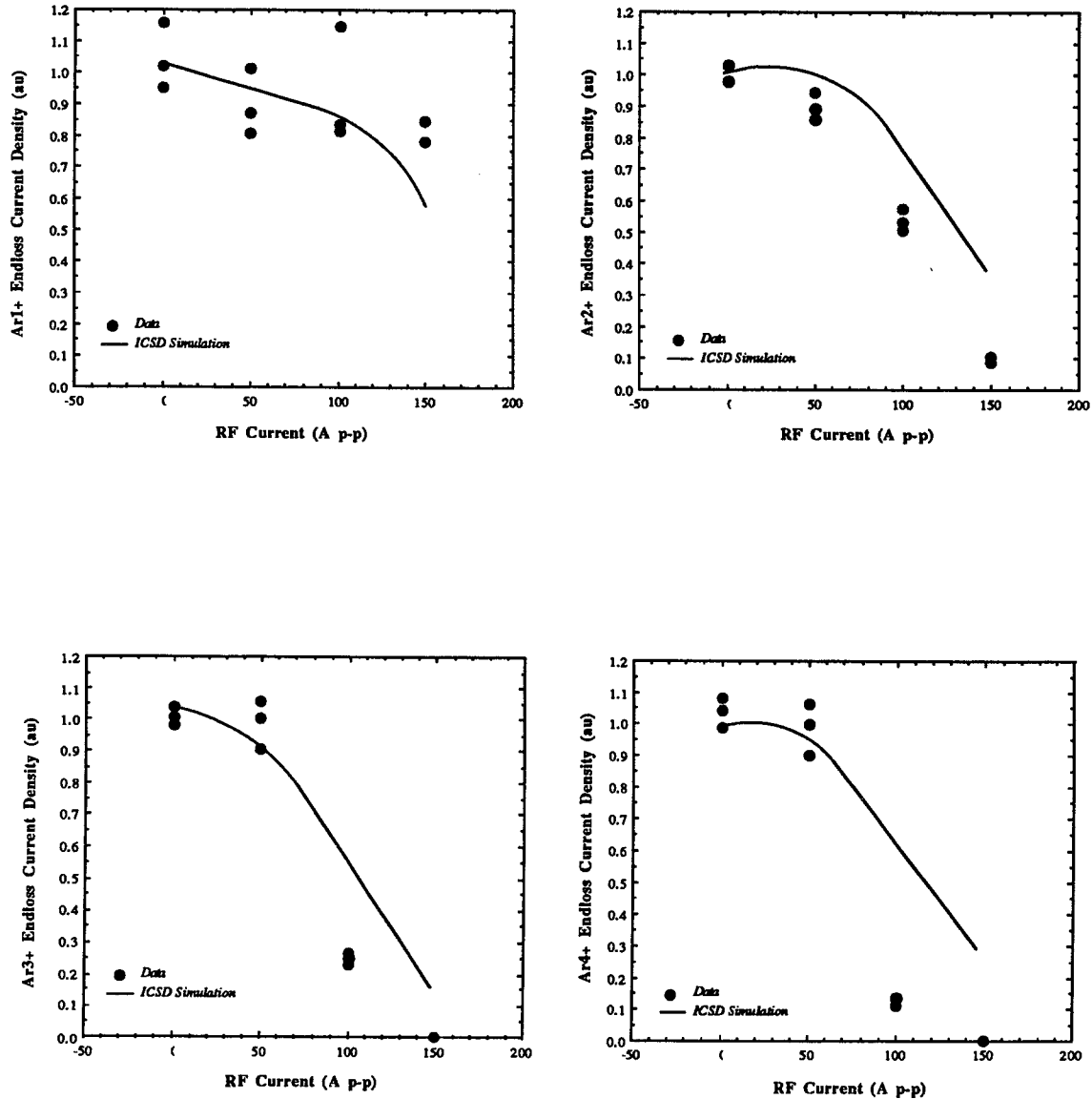
Figure 6.15. Measured and computed argon ion endloss charge state distribution changes with ion temperature. Values are plotted as a funcition of I_{rf} which are related to ion temperature after Eqn. 6.14. The parameters for the simulation are $\phi = 10$ V, $T_i = 25, 27.7, 36.1, 50$ eV. The input to the ICSD code for each run has been corrected for measured changes in the electron density with I_{rf}.
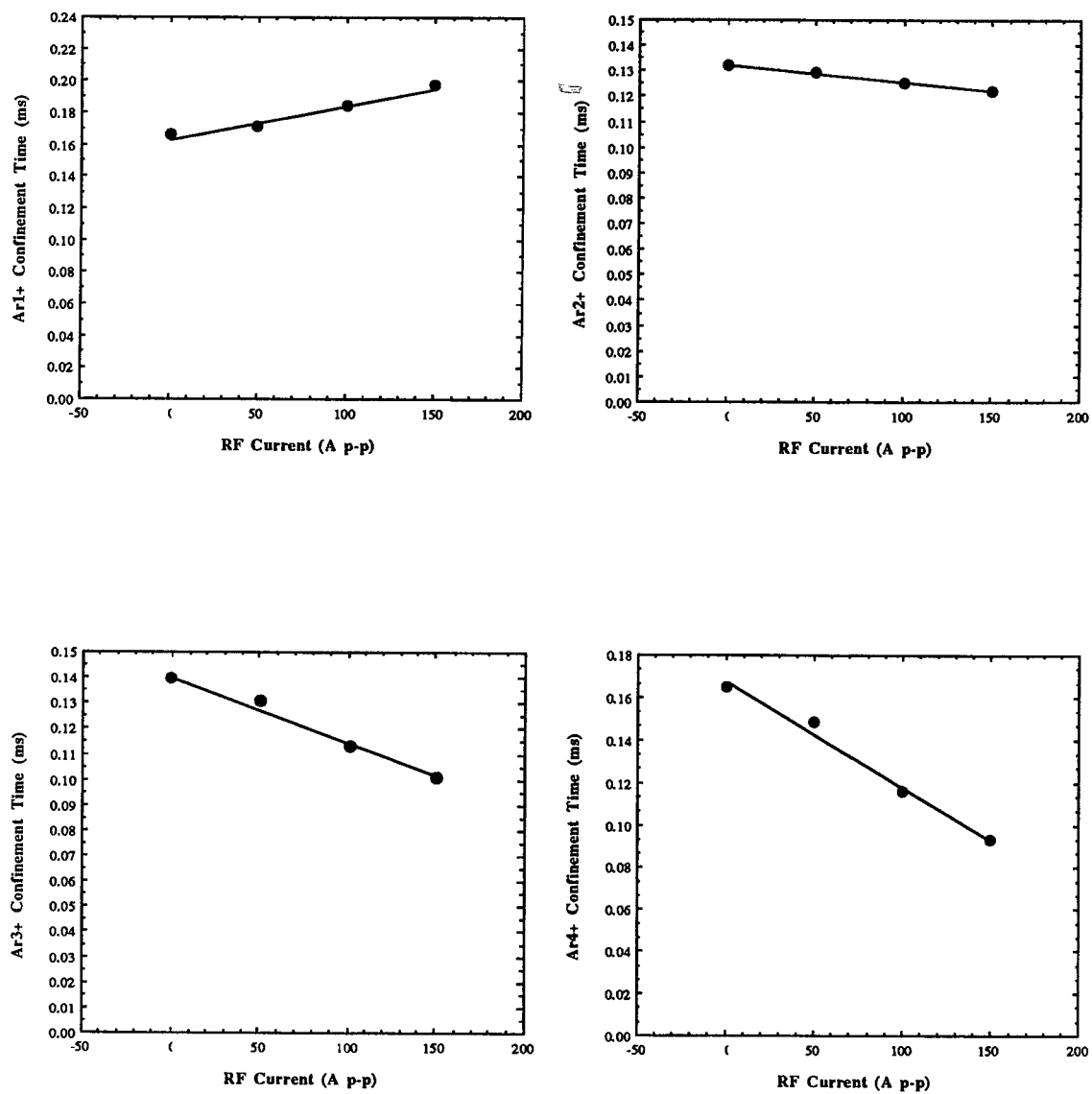
Figure 6.16. Computed argon confinement times for the conditions of Fig. 6.15.
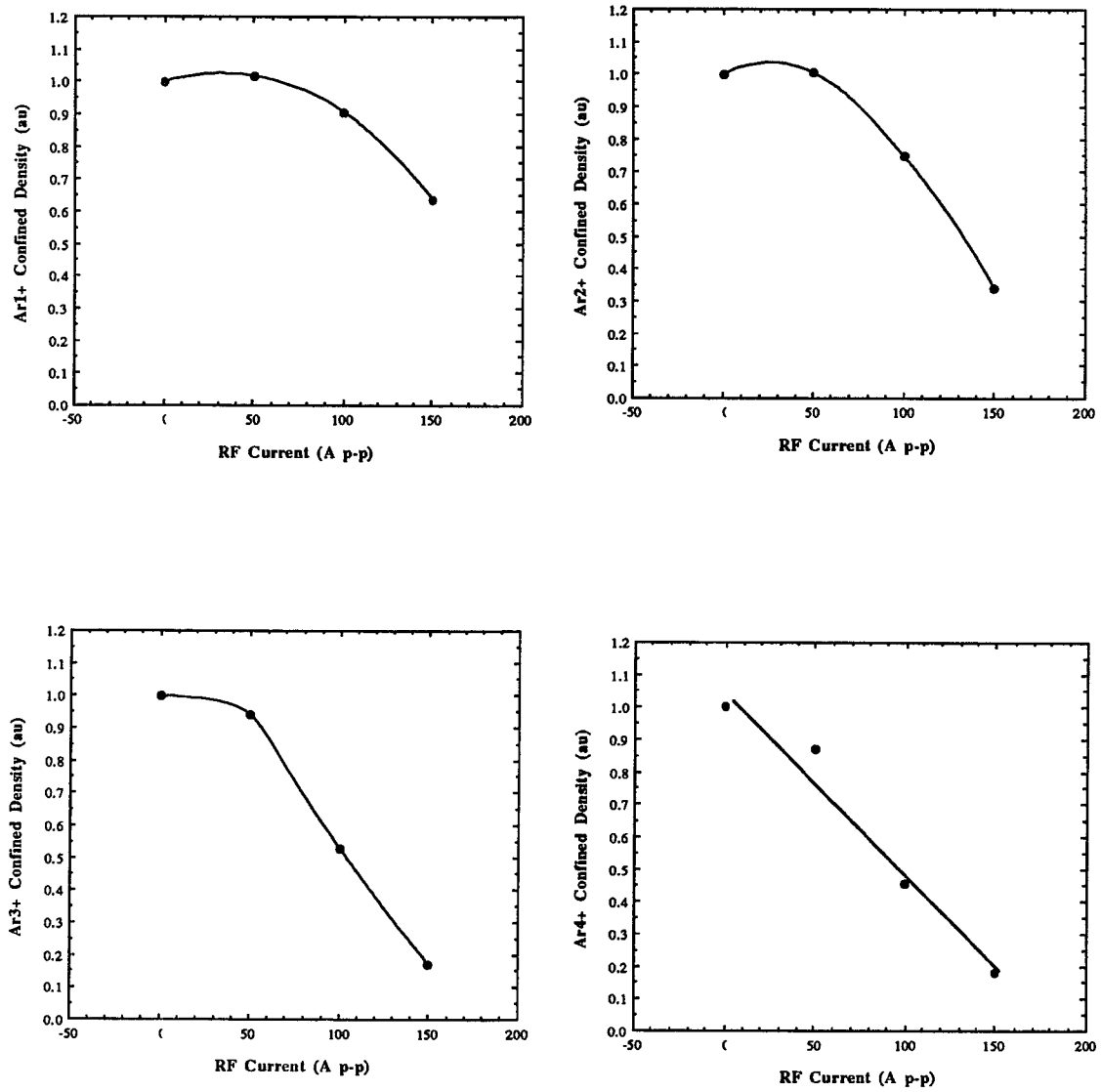
Figure 6.17. Computed argon confined densities for conditions of Fig. 6.15.
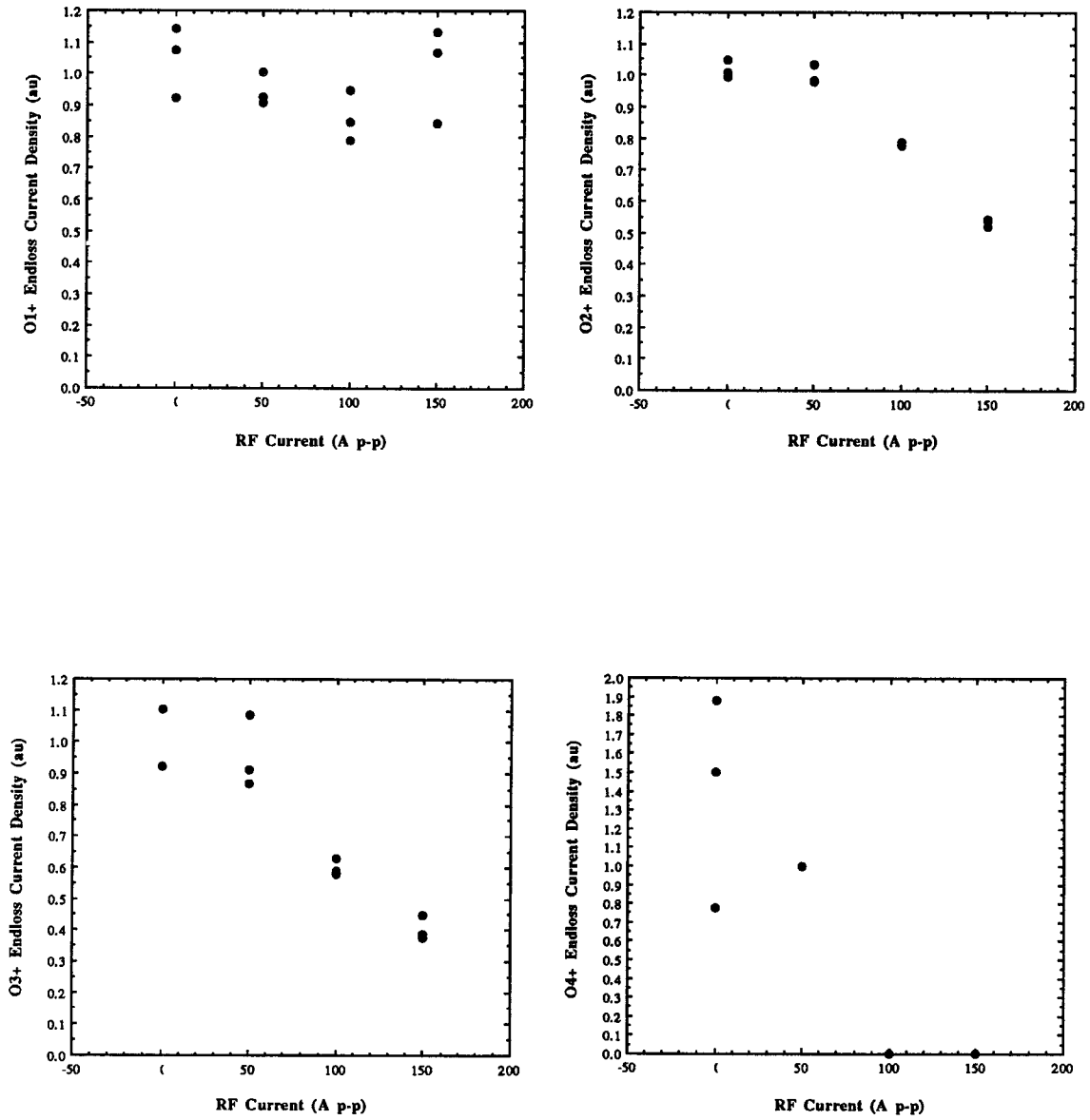
Figure 6.18. Measured oxygen ion endloss charge state distribution changes with ion temperature. Values are plotted as a funcition of I_{rf} which are related to ion temperature after Eqn. 6.14.

The experimental results presented in this section suggest the direct heating of ions in an ECR ion source has a detrimental effect on the ion charge state distribution. An overall shift toward lower average-Z is observed in the endloss and this measured shift is corroborated by simulations which also predict the same shift in the confined ion densities. Since long confinement times are required for production of highly-charged ions, very cold ions appear to be best suited for this purpose since these ions are most strongly collisionally confined through interaction with other ions in the distribution, and electrostatically confined by the potential well created at the ECR resonance zones.

CHAPTER 7

CONCLUSIONS

Electron cyclotron resonance heated ion sources have become the prominent electron-stripping device used to produce multiply-charged ions. These ions are required for many applications ranging from atomic physics research to cyclotron injection. Unfortunately, many of these sources are designed, built and operated based on empirical knowledge acquired from past or existing machines. Much research remains to be performed before a solid understanding of the physical processes governing these sources can be gained. The work presented here attempts to partially bridge the gap between application and understanding.

A time-of-flight spectrometer diagnostic system was implemented on MIMI to measure the endloss current density for specific charge states flowing from the mirror. This diagnostic is central to this investigation as it monitors charge state distribution changes with system parameters. The method of acquiring many spectra in a given shot over a relatively short span of real time, and averaging them to produce one averaged spectrum has proven quite effective in reducing, to near zero, random signal fluctuations caused by amplifier noise, secondary electron and x-ray bombardment of the electron multiplier, plasma fluctuations and statistical spreads. Using this method, quantitative measurements of very low current density signals can be obtained. Also, shot-to-shot reproducibility becomes possible with this method - a difficult and most welcome result.

Ion cyclotron heating has been shown to increase ion temperatures tens of eV. The resonant species typically experiences the greatest temperature increase but transfers much of its energy to the remainder of the distribution via collisions. These temperature increases are consistent with those expected from antenna loading computations.

Modeling of the important physical processes occurring in the plasma yields results consistent with those measured with the time-of-flight spectrometer. The endloss charge state distributions generally possess an overall low average Z. Measurements show ion cyclotron heating has a detrimental effect on the endloss charge state distributions - decreasing the confinement of high-Z ions and causing a shift to low charge states to maintain charge neutrality. These same ICRH effects are predicted by the system modeling. The model is then used to determine the confined steady-state densities and ICRH effects on the confined charge state distributions. These distributions exhibit the same general trends as the endloss, modified somewhat by the changing confinement with ICRH. Steady-state charge state distributions and ICRH effects have been investigated for oxygen, neon, and argon.

Future work might include spectroscopic measurements of midplane Doppler-shifted lines which should prove consistent with results presented in this work. It would provide an easier and possibly more reliable measurement of confined charge state distribution effects. Investigations using heavier gases might provide results significantly different from the light gases used here. The effect of gas mixing is a relatively unexplored topic as is magnetic field shaping, and area easily investigated utilizing MIMI's variable current electromagnetic field coils. Certainly, many possibilities exist for research in unexplored parameter regimes of these highly-used and little-understood ion sources.

APPENDICES

APPENDIX A

SPECTRUM AVERAGING PROGRAM

The following program processes the raw data from the time-of-flight analyser.

The data consists of a large array of points output by the LeCroy TR8188A Transient

Digitizer which digitizes the output of the TOF electron multiplier/ion detector.

Description of the code may be found in Sec. 3.4.4.

```
      PROGRAM SPECTRUM_AVERAGER
C
      INTEGER*2 SDFILE, LENGTH, TYPE, START, BLKCNT
      INTEGER*2 BLOCK, DATBUF(65536), HEADER(17)
      INTEGER*2 BLKCHN, CHNLST, PTR, TEMP, TEMP1
      INTEGER*4 LEN,FINLEN,I,J,IPOS,THP,TBSPEC,TSP,MSPS
      INTEGER*4 TRIG, PERIOD, AMPL
      INTEGER*2 OUT(131072), NPTS, NBP, MSBP
      CHARACTER*1 TEXT(161), AGAIN
      CHARACTER*14 FIN, FOUT
          REAL*4 SUMSPEC(2500), TRAN(1001)
C
C   ARRAY 'OUT' HOLDS DIGITIZED VALUES OF TOF TRACES
C
      WRITE(*,'(1X)')
      WRITE(*,'(A\)') ' Enter number of microseconds to back up: '
          READ(*,*)MSBP
      WRITE(*,'(A\)') ' Enter number of microseconds per spectrum: '
          READ(*,*)MSPS
      MSPS=MSPS*1000
C
   5 CONTINUE
C
      WRITE(*,'(1X)')
      WRITE(*,'(A\)') ' Enter name of binary file: '
      READ(*,'(A)') FIN
C
      OPEN(5, FILE=FIN, STATUS='OLD', FORM='UNFORMATTED')
      READ(5) (HEADER(I),I=1,17)
      READ(5) (TEXT(I),I=1,161)
      LENGTH = HEADER(1)
      WIDTH = HEADER(2)
```

```
        PERIOD = HEADER(4) * 65536
        PERIOD = PERIOD + HEADER(3)
        OFFSET = HEADER(5)
        TRIG = HEADER(7) * 65536
        TRIG = TRIG + HEADER(6)
        AMPL = HEADER(9) * 65536
        AMPL = AMPL + HEADER(8)
        START = HEADER(10)
        BLKCNT = HEADER(11)
        TYPE = HEADER(12)
        BLKCHN = HEADER(13)
        CHNLST = HEADER(14)
        NBP=(10000/HEADER(3))*MSBP
C
C READ IN 16-BIT INTEGERS - 8 BITS/POINT
C
        WRITE(*,'(A\)') ' Enter last block to be read: '
        READ(*,'(I2)') PTR
        LEN = (WIDTH+7)/8
        LEN = (LEN * LENGTH + 1)/2
        DO 15 BLOCK = 1,PTR
        READ(5) (DATBUF(I), I = 1+LEN*(BLOCK-1),LEN*BLOCK)
     15 CONTINUE
C
C EXPAND ARRAY INTO INDIVIDUAL DATA POINTS
C ADJUST TO ZERO CODE LEVEL -- HEADER(5)
C
        LEN=LEN*PTR
        DO 20 J = 1,LEN
                TEMP=DATBUF(J)
                IF(DATBUF(J).LT.0)TEMP1=(TEMP+32768)/256+128
                IF(DATBUF(J).GE.0)TEMP1=TEMP/256
                TEMP1=TEMP1-HEADER(5)
                OUT(J*2)=TEMP1
                TEMP1 = TEMP - (TEMP/256)*256
                IF (TEMP1.LT.0) TEMP1=TEMP1+256
                TEMP1=TEMP1-HEADER(5)
                OUT(J*2-1)=TEMP1
     20 CONTINUE
C
        FINLEN = LEN*2
C
C ADJUST TO AMPLITUDE IN mV -- HEADER(8) AND INVERT SPECTRA
C
        DO 30 J=1,FINLEN
                OUT(J)=-1*OUT(J)*(HEADER(8)/1000)
     30 CONTINUE
C
C    OPEN(7,FILE='OUT2')
C           DO 31 IJK = 1,1000
C           TRAN(IJK)=FLOAT(OUT(IJK+4686))
C 31 CONTINUE
C           WRITE(7,'(8F10.0)')(TRAN(IJK),IJK=1,1000)
C
C NOW SUM SPECTRA
C
        WRITE(*,'(A\)') ' Enter approx. time of first H1+ peak in ns:'
        READ(*,*)THP
```

```
        WRITE(*,'(A\)')' Enter approx. time of second H1+ peak in ns:'
        READ(*,*)TSP
                WRITE(*,'(A\)')' Discr. value is 15mV.  Enter new value or 0:'
                READ(*,*)IDISCR
                IF (IDISCR.EQ.0)IDISCR=15
                TBSPEC=TSP-THP
C
C CONVERT THP AND TBSPEC TO POINTS IN FILE AND INITIALIZE SUMSPEC
C
        THP = (THP/(HEADER(3)/10))+2
        TBSPEC = TBSPEC/(HEADER(3)/10)
        DO 35 I=1,2500
          SUMSPEC(I) = 0.
   35 CONTINUE
        NPTS=MSPS/(HEADER(3)/10)
        IPOS = THP
                INUM=0
   40 IF (IPOS .GE. (FINLEN-NPTS)) GOTO 50
        CALL FINDPEAK(OUT,IPOS,NPTS,TBSPEC,IDISCR)
                WRITE(*,'(4I10)')IPOS,OUT(IPOS-1),OUT(IPOS),OUT(IPOS+1)
        IF (OUT(IPOS) .LE. IDISCR)GOTO 45
        CALL SUMPEAK(SUMSPEC,OUT,IPOS,NPTS,NBP)
                INUM=INUM+1
   45 IPOS = IPOS + TBSPEC
        GOTO 40
   50 CONTINUE
C
C AVERAGE FINAL SPECTRUM
C
        DO 55 I=1,NPTS
                SUMSPEC(I)=SUMSPEC(I)/FLOAT(INUM)
   55 CONTINUE
C
C WRITE TO OUTPUT FILE
C
   60 WRITE(*,'(A\)') ' Enter output file: '
                READ(*,'(A)')FOUT
                OPEN(6,FILE=FOUT,STATUS='NEW')
                WRITE(6,*)(HEADER(I), I=1,17)
                WRITE(6,*)NPTS
                WRITE(6,'(8F10.3)')(SUMSPEC(I),I=1,NPTS)
                CLOSE (5)
                CLOSE (6)
C               CLOSE (7)
        WRITE(*,'(A\)') ' SPECTRUM AVERAGING COMPLETE!!  Another?'
                READ(*,'(1A1)')AGAIN
                IF (AGAIN.EQ.'Y'.OR.AGAIN.EQ.'y')GOTO 5
        END
C
        SUBROUTINE FINDPEAK(OUT,IPOS,NPTS,TBSPEC,IDISCR)
C
        INTEGER*2 OUT(131072), IFLAT, NPTS
                INTEGER*4 IPOS, MAX, TBSPEC, IPOSOLD, NSEARCH, III
C
                II1=1
                II2=2
C
        III=1
```

```
            IPOSOLD=IPOS
  101 CONTINUE
C
     NSEARCH=NPTS/100
     MAX=IPOS-NSEARCH
     DO 105 I=1,2*NSEARCH
               IF(OUT(MAX).LT.OUT(IPOS-NSEARCH+I))MAX=IPOS-NSEARCH+I
  105 CONTINUE
     IPOS=MAX
C
  100 CONTINUE
C   WRITE(*,'(3I10)')II1,IPOS,OUT(IPOS)
     IF (OUT(IPOS) .LE. OUT(IPOS-1))THEN
       IPOS = IPOS - 1
       GOTO 100
     ENDIF
     IFLAT=0
  110 CONTINUE
C   WRITE(*,'(3I10)')II2,IPOS,OUT(IPOS)
     IF(OUT(IPOS).EQ.OUT(IPOS+1))IFLAT=IFLAT+1
     IF (OUT(IPOS) .LE. OUT(IPOS+1))THEN
       IPOS = IPOS + 1
       GOTO 110
     ENDIF
            IPOS=IPOS-(IFLAT/2)
C
     IF (IPOS.GT.129000) GOTO 120
     IF(OUT(IPOS).LT.IDISCR)THEN
            IPOS=IPOSOLD+III*TBSPEC
                   III=III+1
                   WRITE(*,'(A)') ' SKIP'
                   WRITE(*,'(4I10.0)')IPOS,OUT(IPOS-1),OUT(IPOS),OUT(IPOS+1)
                   GOTO 101
            ENDIF
C
  120 RETURN
     END
C
     SUBROUTINE SUMPEAK(SUMSPEC,OUT,IPOS,NPTS,NBP)
C
     INTEGER*2 OUT(131072), NPTS, NBP
            INTEGER*4 IPOS, IJ
            REAL*4 SUMSPEC(2500)
C
     DO 200 IJ=1,NPTS
       SUMSPEC(IJ)=SUMSPEC(IJ)+FLOAT(OUT(IPOS-NBP+IJ))
  200 CONTINUE
C
     RETURN
     END
```

APPENDIX B

MIMI OPERATING PROCEDURES

Following are the start-up and shutdown procedures for the Michigan Mirror Machine, operated in the Plasma Experimental Bay in the Naval Architecture and Marine Engineering Building at the University of Michigan.

STARTUP PROCEDURE

1. Turn all power strips "*ON*". These strips include two strips attached to the right side of the instrument rack, one strip attached to the right side of the CAMAC controller rack, and one strip on the floor to the right of the high voltage klystron switch. This will supply *120 VAC* power to all scopes on the instrument rack, the CAMAC controller, Zenith terminal, optical coupler, all pulsers, the *1/90 - 60c* CAMAC trigger, and the klystron high voltage switching circuit.

2. Turn switch next to the Zenith terminal to "Z-29".

3. At Apollo workstation in Rm. 116 NA&ME Bldg., log on to account: GETTY. In subdirectory "*camac_programs*", start the CAMAC controlling program by entering "*camac*". Check to see if program is running by entering "*pst*" and checking if the process "camac_running" appears. If it does not appear, check *RS-232* connections in back of workstation and at the Zenith terminal in the rear of the lab. Also be sure steps *1* and *2* have been completed. If the program has

successfully started, a set point default file will appear on the Zenith terminal screen. Invoke the run_file, on the Zenith terminal, which contains the proper setpoints for the experiment.

4. Turn on water pumps *119* and *121* on the east wall of the lab. Before these pumps are turned on, the bypass valve on the south wall should be opened and the quadrupole and main valves should be closed. When the pumps are turned on, the pressure gauge on the south wall should read between *60* and *100 psi*. Let the water run through the bypass valve for *~15 min.* before opening the quadrupole and main valves to assure any dirt or rust in the pipes has been flushed out.

5. Turn power switch on Hewlett-Packard Model 620A Oscillator to *"ON"* and turn the power switch to the Hewlett-Packard TWT Model 495A microwave amplifier to *"STANDBY"*. These require *~10 min.* to warm up.

6. Turn on power strip near klystron water pump. This supplies AC power to the klystron cooling system water pump, radiator, klystron filament and magnet power supplies. The water pump will automatically start when this strip is energized.

7. Flip switches labeled *"main power (1)"* and *"control power (2)"* on the high voltage power supply to the *"UP"* position. There is a thirty second delay before either the "high voltage" switch can be turned on or the interlock for the klystron will be energized.

8. Turn on *AC* power switches for the klystron filament and magnet. Increase the magnet current until it reaches *6.2 A*. Increase filament current SLOWLY until it reaches *~2.0 A*. As these elements warm up, the current will decrease due to the

increased resistance of the filament with temperature. Continue with the start up procedure but every ~5 min return and increase the current settings to their desired values of 6.2 A for the magnets and 2.53 A for the filament. Never turn up the filament current unless the magnet supply is near 6.2 A. If the power lights on the filament and magnet supplies do not light when the switches are in the "ON" position, check the interlock which requires sufficient water flow through the klystron magnet cooling system and completion of step 7 of this startup sequence.

9.   Pump out gas lines of the gas handling system with the Ultek roughing pump. (Large pump located on floor directly under MIMI midplane.) Let these lines rough for ~10 min. before allowing leak gas into the lines. When sufficient roughing time has elapsed, close the roughing pump valve nearest the system and open valve connected to bottle of leak gas. Be sure precision leak valve is closed and the valve between the precision leak valve and the system is open. Open the precision leak valve until the pressure in the system has reached the desired pressure (~10^{-5} T).

10.   Check timing pulses from the CAMAC controller and Systron-Donner pulsers to assure correct timing for the scopes, DML, TWT amplifier, klystron switch, and TOF.

11.   If sufficient time has elapsed (~15 min.), open the main water valve for the mirror coils. Close the bypass valve and observe the pressure gauge on the low pressure side of the regulator. It should read 10 psi. Now open the quadrupole valve.

12.   Throw the main power switch for the magnet power supply. The fans should start immediately. Press the "START" button for the main mirror coils. The light above the meters should light and remain lighted. If it lights when the "START"

button is pressed and turns off when the "*START*" button is released, the flow switches most likely are not tripped. The quadrupole flow switch, located above the Sargent-Welsh turbo pump, is most likely the culprit. Close the quadrupole valve on the south wall and after a few seconds, open it quickly. If this does not rectify the problem, the setting on the switch will have to be adjusted.

12. Once the power to the magnets is on, turn the current settings to their desired values. The controls to the current supplies are self-explanatory.

13. Once the klystron filament and magnet supplies have held at their correct settings for *5 min.*, the klystron high voltage may be turned to its full value. Listen to the klystron switch to assure that it is pulsing with the CAMAC timing pulse. A distinct "*click-click*" should be heard as the switch closes and opens, once every *1.5 s.*

14. Flip the "*high voltage (3)*" switch on the high voltage klystron supply to the "*UP*" position. A green light should appear on the control panel of the supply. If it does not, a diagnostic light will light, indicating the problem. Press the "*high voltage on*" button. A red light should now appear on the control panel.

15. Increase the klystron voltage while monitoring the high voltage pulse with the high voltage scope probe and scope located behind the magnet and filament supplies near the klystron voltage supply. This voltage should NEVER exceed *10 kV*. A high voltage spike always appears at the very beginning of the pulse. This is the part of the pulse to be careful of. When this is increased to *10 kV*, the steady-state part of the pulse is typically *9 kV*.

16. Once the high voltage is applied to the klystron, the magnet current supplies are turned up, and the leak gas has been admitted to the vacuum vessel, the oscillator

and TWT amplifier can be turned on. Turn the power switch on the TWT amplifier to "*ON*". Increase the gain until the needle reaches approximately 1/4 - *1/2* full deflection. There is no advantage to turning the gain higher.

17. Turn the selector control on the oscillator to "*CW*". Be sure full attenuation is in when this is done. Slowly remove attenuation while monitoring forward and reflected power from the forward and reflected power crystal detectors. Adjust attenuation for maximum forward power (*~60mV* signal) being certain that the reflected power signal does not increase above *100mV*. The attenuation of the oscillator must be continually adjusted over the first *15 min.* of operation as it warms up. After this initial warm up period it will require only very minor adjustments.

18. The system is now fully operating.

SHUTDOWN PROCEDURE

1. Turn off *1/90 - 60 c* pulser.

2. Increase attenuation of oscillator to full. Switch selector control to "OFF".

3. Turn gain control of TWT amplifier fully *CCW* and turn power switch to "*STANDBY*".

4. Turn high voltage klystron supply to zero and press "*high voltage off*" button. A green light should appear on the control panel. Flip the "*high voltage (3)*" switch down.

5. Turn down the current of the klystron filament supply and the magnet supply. Be sure always to turn down the filament supply first. Turn the AC power switches off for both supplies.

6. Flip switches "*control power (2)*" and "*main power (1)*" on the klystron high voltage power supply to the DOWN position.

7. Turn down both mirror and quadrupole currents. Press the "*STOP*" buttons for both supplies. Leave the main power breaker on for ~*10 min* after the current has been turned down to provide cooling by the supplies' fans.

8. Close the precision leak valve. Shut off the gas supply from the supply bottle and pump out the gas lines with the Ultek roughing pump.

9. Turn off the power strip near the klystron high voltage switch.

10. If the klystron magnet coils feel cool, turn off the power strip near the klystron water pump. If they are still warm, wait ~*5 min* and try again.

11. Throw the magnet supply breaker off.

12. Open the bypass valve for the magnet cooling system and close the quadrupole and main valves.

13. Turn off water pump controls on east wall.

14. Turn off power strips on instrument rack and CAMAC controller rack.

15. Turn off AC power to both the oscillator and TWT amplifier.

16. The system should now be completely shut down.

APPENDIX C

DERIVATION OF FOURIER-TRANSFORMED ANTENNA CURRENT FOR

FULL-TURN LOOP

The derivation of the Fourier-transformed $J_{ext}(r)$, of Eqn. 4.2, due to antenna currents is shown below for a full-turn loop. The expression for $J_{ext}(r,\phi,z)$ can be determined by examination of Fig. C.1. By inspection, the antenna current can be expressed as:

$$J_{\phi\,ext}\,(\,r\,,\phi\,,z\,) = \frac{I}{w}\,u_z(\,\pm\tfrac{w}{2}\,)\,\delta_r(\,b\,) \qquad\qquad \text{(C.1)}$$

where $\quad \delta_r(r_o) \;=\; Dirac\ delta\ function$

$u_z(\pm L) \;=\; 0\ for\ z\,\leq\,-L$

$1\ for\ -L\,<\,z\,<\,L$

$0\ for\ z\,\geq\,L$

$I \;=\; antenna\ current$

$w \;=\; antenna\ width.$

Transforming Eqn. C.1 after Eqn. 4.4,

$$J_{\phi\,ext}(\,r\,,n\,,k_z\,) = \frac{1}{2\pi}\int_{-\infty}^{\infty}dz\int_{0}^{2\pi}d\phi\,\{\,\frac{I}{w}\,u_z(\,\pm\tfrac{w}{2}\,)\,\delta_r(\,b\,)\,\}\,e^{-in\phi-ik_z z}$$

$$= \frac{I}{2\pi w}\,\delta_r(\,b\,)\int_{-w/2}^{w/2}dz\,e^{-ik_z z}\int_{0}^{2\pi}d\phi\,e^{-in\phi}\,. \qquad\qquad \text{(C.2)}$$
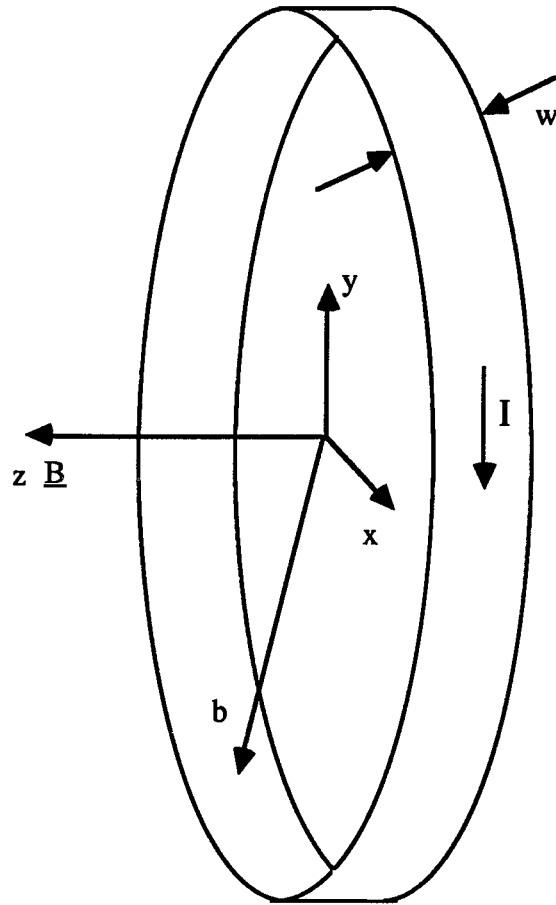
Figure C.1. Full-turn loop antenna.

So finally,

$$J_{\phi\,ext}(\,r\,,n\,=\,0\,,k_z\,)\,=\,I\ \delta_r(\,b\,)\ \frac{sin(\frac{k_z w}{2})}{\frac{k_z w}{2}}\,.\tag{C.4}$$

Note that only the $n = 0$ mode is included since the problem is uniform in ϕ. All coefficients $J_{\phi\,ext}(r,\ n \neq 0, k_z) = 0$ for the full-turn antenna geometry. All other transformed antenna currents can be derived in a similar manner.

APPENDIX D

RUNNING THE ANTENNA-PLASMA COUPLING CODE -- ANTENA

The ANTENA code is run on the e machine CRAY II computer which is part of the National Magnetic Fusion Energy Computing Center (NMFECC). To connect to the system from The University of Michigan, the dialout modem service, available though the Michigan Terminal System, is used. The user must possess an account on the NMFECC system before the logon procedure is initiated. Once this account has been acquired, the following procedure allows the user to access his account and run the ANTENA code. For purposes of illustration, the author's account is used as an example.

From an MTS prompt:

```
Which host? dial1200-aa<RTN>
%H19:NAV113-AK<09>36:H32dial12

AT@SMB1200SPF2
OK
ATDT9,973,7935<RTN><RTN><RTN>

CONNECT
x||x'|xxx<xa   (type this as soon as the first characters appear)
-0307-000-
please log in: mfe<RTN>

password: computing<RTN>
P 7
MFE IS ON LINE
```

e 17107 a 995mca ^zhdfkil<RTN>

REMAINING CPU TIME
LAST LOGON

The user is now logged on to his account on the NMFECC system. The log in line

shown above has the format:

m aaaaaa s dddddd ^zpppppp   where

     m   --   machine designation

     aaaaaa   --   account ID number

     s   --   suffix

     dddddd   --   division

     pppppp   --   password.

The user must have the ANTENA object code stored in his account. To obtain a

copy of this code, contact Gary Smith of LLNL. The execution line is:

'object code filename'   'input filename'

The input file must reside in the users private disk space as must the object code. The

code will generate several output files. The files of interest are named:

    'input filename' + suffix + 2   {data file}   and

    f3 + 'input filename' + 0x   {plot file}.

The data file contains values of the computed quantities specified in the input file and the plotfile contains plots of the quantities listed in the data file. If the user is using a Tektronix graphics terminal, he may review the plots by executing:

<u>netplot 'plot filename' baud=1200</u>.

Once all runs of interest have been completed, to log off the system, execute:

<u>^d</u>

Examples of typical input and output files are shown below. The users manual for the code is an internal report published at Massachusetts Institute of Technology by Brian McVey, listed as Refs. 42 and 43.

Typical ANTENA Code Input File

```
pa ich; echo off
indvar=4; ivarlow=.80; ivarhi=1.1; ivarinc=.05
ibfld=1; iedotj=1; iefld=1; ipabs=1
ifield=2; icoord=0
ispectr=0; ifast=1; islow=1
integkz=2; kmincm=1.e-5; kmaxcm=10; kstepcm=1.e-7; eps=1.e-4
nmax=20
acm=5.08; ccm=7.35; lengcm=150.; rhocm=5.0; phideg=0.; zcm=0.0
wnor=1.0; freq=1.33e6; nazim=-1
ncoils=1; icoil=3; imutual=0; nstep=10
cur=100.
bcm=5.72
widcm=1.91
lngcm=30.5
angdeg=19.2
phi0deg=0.
ikij=1; bfld=3500; ntot=.5e12; npart=2
```

mass=[4.,5.46e-4]; charge=[1,-1]; conc=[100,100]
tpar=[30.,30.]; tper=[30.,30.]; colfreq=[3.9e4,8.9e8]
iprof=3; nstrat=10; wdencm=20.5; wtempcm=[29.,29.]
ilabel=1; label="n= 6"; iparam=1
run
end

Typical ANTENA Code Output File

Package ich: icrh heating output file

Merth...Version 3.1
Code created on 09/19/85 at 13:17:26
Run at 17:59:34 on 02/05/89 on the e machine, suffix d

the output control parameters are,

icoord= 0   ibfld= 1   iefld= 1

ipabs= 1   iedotj= 1

the scan parameters are,

indvar= 4   w/wc(1)   ipart= 1

ivarlow= 8.00e-01   ivarhi= 1.10e+00   ivarinc= 5.00e-02

the spectrum parameter is,   ispectr= 0

the field parameter is,   ifield= 2

plasma fields me.ne.0 stratified profile

the fast and slow mode multipliers are,

ifast= 1   islow= 1

the kz integration parameter is,   integkz= 2

variable step integrator

kmin(cm-1)= 1.000e-05   kmax(cm-1)= 1.000e+01

kstep(cm-1)= 1.000e-07   eps= 1.000e-04   mf= 10

the number of azimuthal modes summed is,   nmax= 20

the plasma-vacuum chamber geometry

   a(cm)= 5.08e+00   c(cm)= 7.35e+00   leng(cm)= 1.50e+02

the nominal field position,

   rho(cm)= 5.00e+00   phi(deg)= 0.   z(cm)= 0.

the frequency and wave number parameters are,

   w/wc(1)= 1.000e+00   freq(hz)= 1.330e+06

   kz(cm-1)= 1.000e-02   nazim=   -1

the antenna array parameters are,

   iantcon= 0   iseries= 0   iparall= 0

   imutual= 0   nstep=10

the number of coils in the array is,   ncoils= 1

   coil 1   nagoya type iii

   current= 1.000e+02, 0.
   b(cm)= 5.72e+00   phi0(deg)= 0.   z0(cm)= 0.
   wid(cm)= 1.91e+00   lng(cm)= 3.05e+01   ang(deg)= 1.92e+01

the dielectric parameter is,

   ikij= 1   maxwellian velocity distribution

the plasma parameters are,

   bfld(g)= 3.500e+03   ntot(cm-3)= 5.000e+11

   m   z   conc   tpar(ev) tper(ev)   vc

   4.00e+00 1.00e+00 1.00e+02 3.00e+01 3.00e+01 3.90e+04
   5.45e-04 -1.00e+00 1.00e+02 3.00e+01 3.00e+01 8.90e+08

the characteristic frequencies and velocities are,

   wp   wc   vz(m/s)   vx(m/s)   vc

1   4.67e+08 8.38e+06 3.78e+04 3.78e+04 3.90e+04
2   3.99e+10 -6.16e+10 3.25e+06 3.25e+06 8.90e+08

the profile parameters are,

iprof= 3   gaussian   nstrat= 10

wden(cm)= 2.050e+01

wtempcm(i)= 2.90e+01, 2.90e+01,

rs	fden	fbfld	ftemp1	ftemp2	ftemp3	ftemp4
5.080e-03	1.000e+00	1.000e+00	1.000e+00	1.000e+00		
1.016e-02	9.994e-01	1.000e+00	9.997e-01	9.997e-01		
1.524e-02	9.975e-01	1.000e+00	9.988e-01	9.988e-01		
2.032e-02	9.945e-01	1.000e+00	9.972e-01	9.972e-01		
2.540e-02	9.902e-01	1.000e+00	9.951e-01	9.951e-01		
3.048e-02	9.848e-01	1.000e+00	9.924e-01	9.924e-01		
3.556e-02	9.781e-01	1.000e+00	9.890e-01	9.890e-01		
4.064e-02	9.704e-01	1.000e+00	9.851e-01	9.851e-01		
4.572e-02	9.615e-01	1.000e+00	9.806e-01	9.806e-01		
5.080e-02	9.515e-01	1.000e+00	9.755e-01	9.755e-01		

the field format is

f = mod(fx) phase(fx), mod(fy) phase(fy), mod(fz) phase(fz)

w/wc(1) = 8.000e-01
b(g,deg)= 1.403e+00-1.789e+02, 1.394e+00 8.740e+01, 9.888e-04 9.287e+01

e(v/cm,deg)= 1.201e-03-3.038e+01, 1.475e-03 6.355e+01, 4.246e-01-1.576e+01

elft(v/cm,deg)= 1.447e-04 1.700e+02   erht(v/cm,deg)= 1.337e-03-2.822e+01
pabst(w/cm2)= 3.97e-01
pabsi(w/cm2),i=1,ns= 1.62e-04, 3.97e-01,
power(w)= 1.527e+01

the source impedances are,

coil 1 p(w)= 1.594e+01 2.451e+03 r(ohms)= 3.188e-03 x(ohms)= 4.902e-01 l(uh)= 7.310e-2

w/wc(1) = 8.500e-01
b(g,deg)= 1.403e+00-1.787e+02, 1.395e+00 8.692e+01, 1.010e-03 9.362e+01

e(v/cm,deg)= 1.148e-03-1.882e+01, 1.366e-03 7.630e+01, 4.828e-01-1.360e+01

elft(v/cm,deg)= 1.225e-04-1.690e+02   erht(v/cm,deg)= 1.256e-03-1.604e+01
pabst(w/cm2)= 4.95e-01
pabsi(w/cm2),i=1,ns= 1.72e-04, 4.94e-01,
power(w)= 1.923e+01

the source impedances are,

coil 1 p(w)= 2.011e+01 2.605e+03 r(ohms)= 4.021e-03 x(ohms)= 5.209e-01 l(uh)= 7.311e-2

w/wc(1) = 9.000e-01
 b(g,deg)= 1.401e+00-1.785e+02, 1.400e+00 8.634e+01, 9.381e-04 9.539e+01

 e(v/cm,deg)= 9.518e-04 2.557e+00, 1.121e-03 9.853e+01, 5.513e-01-9.376e+00

 elft(v/cm,deg)= 1.002e-04-1.419e+02   erht(v/cm,deg)= 1.035e-03 5.783e+00
 pabst(w/cm2)= 6.10e-01
 pabsi(w/cm2),i=1,ns= 1.83e-04, 6.10e-01,
 power(w)= 2.419e+01

the source impedances are,

coil 1 p(w)= 2.539e+01 2.756e+03 r(ohms)= 5.078e-03 x(ohms)= 5.511e-01 l(uh)= 7.305e-2

w/wc(1) = 9.500e-01
 b(g,deg)= 1.397e+00-1.783e+02, 1.414e+00 8.598e+01, 9.484e-04 9.582e+01

 e(v/cm,deg)= 5.590e-04 3.523e+01, 6.806e-04 1.275e+02, 5.956e-01-3.253e+00

 elft(v/cm,deg)= 6.197e-05-1.325e+02   erht(v/cm,deg)= 6.197e-04 3.645e+01
 pabst(w/cm2)= 6.99e-01
 pabsi(w/cm2),i=1,ns= 2.25e-04, 6.99e-01,
 power(w)= 2.838e+01

the source impedances are,

coil 1 p(w)= 3.004e+01 2.905e+03 r(ohms)= 6.009e-03 x(ohms)= 5.811e-01 l(uh)= 7.297e-2

w/wc(1) = 1.000e+00
 b(g,deg)= 1.393e+00-1.782e+02, 1.426e+00 8.581e+01, 9.221e-04 9.551e+01

 e(v/cm,deg)= 3.523e-04 8.124e+01, 4.330e-04 1.694e+02, 6.234e-01 1.027e+00

 elft(v/cm,deg)= 4.083e-05-1.085e+02   erht(v/cm,deg)= 3.926e-04 8.023e+01
 pabst(w/cm2)= 7.68e-01
 pabsi(w/cm2),i=1,ns= 3.82e-04, 7.68e-01,
 power(w)= 3.149e+01

the source impedances are,

coil 1 p(w)= 3.340e+01 3.055e+03 r(ohms)= 6.681e-03 x(ohms)= 6.110e-01 l(uh)= 7.289e-2

w/wc(1) = 1.050e+00
 b(g,deg)= 1.391e+00-1.781e+02, 1.440e+00 8.557e+01, 9.387e-04 9.621e+01

 e(v/cm,deg)= 5.856e-04 1.358e+02, 6.539e-04-1.424e+02, 6.630e-01 4.979e+00

 elft(v/cm,deg)= 5.590e-05-1.007e+02   erht(v/cm,deg)= 6.182e-04 1.315e+02
 pabst(w/cm2)= 8.66e-01
 pabsi(w/cm2),i=1,ns= 3.51e-04, 8.66e-01,
 power(w)= 3.512e+01

the source impedances are,

coil 1 p(w)= 3.690e+01 3.203e+03 r(ohms)= 7.380e-03 x(ohms)= 6.407e-01 l(uh)= 7.279e-2

w/wc(1) = 1.100e+00
 b(g,deg)= 1.386e+00-1.781e+02, 1.454e+00 8.560e+01, 9.207e-04 9.641e+01

 e(v/cm,deg)= 1.161e-03 1.695e+02, 1.098e-03-1.097e+02, 6.834e-01 9.961e+00

 elft(v/cm,deg)= 9.588e-05-1.243e+02   erht(v/cm,deg)= 1.126e-03 1.651e+02
 pabst(w/cm2)= 9.35e-01
 pabsi(w/cm2),i=1,ns= 2.66e-04, 9.35e-01,
 power(w)= 3.708e+01

the source impedances are,

coil 1 p(w)= 3.861e+01 3.352e+03 r(ohms)= 7.723e-03 x(ohms)= 6.704e-01 l(uh)= 7.270e-2

APPENDIX E

ION CHARGE STATE DISTRIBUTION EQUILIBRIUM CODE

Following are the input and output decks for the ICSD computer code. The first code, SIGV, calculates the $<\sigma v>$'s for the ionization proceses, described in chapter 5, for input to the main ICSD code which solves Eqns. 5.5. The output file of the SIGV code is the input for the ICSD code. The order of listings presented in this appendix is:

- Input file for the SIGV program. This file contains all cross section data and some necessary plasma parameters.

- Source program SIGV. This program sets up the input deck for the ICSD code. The user must modify the output file before running the ICSD code. Necessary parameters which must be added are T_i, n_e, n_o, L_{mirror}, R_{mirror}, and ϕ.

- Output of SIGV program and input of ICSD program. The file shown has been modified by adding the parameters mentioned in the step above.

- Source listing for ICSD program. This solves the steady-state equilibrium rate equations described in chapter 5 and outputs normalized densities and confinement times for each charge state.

All data shown is for an example case of an argon plasma.

SIGV INPUT FILE

Zmax	Mion	Te	Ez(eV)
18	40	5000.	15.76

I	Ea(I)	Eb(I)	sigma*0	sigma*1
1	15.76	27.63	1.134e-19	1.76e-20
2	124.	40.74	1.545e-21	8.76e-21
3	239.	59.81	1.903e-22	3.54e-21
4	313.	75.02	3.670e-23	8.63e-22
5	478.	91.01	4.213e-24	2.04e-22
6	625.	124.3	5.170e-25	5.00e-23
7	920.	143.5	4.077e-26	1.00e-23
8	4121.	422.5	0.	0.
9	4121.	478.7	0.	0.
10	4121.	539.0	0.	0.
11	4121.	618.3	0.	0.
12	4121.	686.1	0.	0.
13	9999.	755.8	0.	0.
14	9999.	854.8	0.	0.
15	9999.	918.0	0.	0.
16	9999.	4121.	0.	0.
17	9999.	4426.	0.	0.
18	9999.	0.	0.	0.

SIGV SOURCE LISTING

```
      PROGRAM SIGV
C
C
C This version of the sigv code uses the Schram and Van der Weil
C formulation to calculate <sig*v>.
C
C
      IMPLICIT REAL*8 (A-H,O-Z)
      DIMENSION BETA(99,2), SIGMAZ(99), SIGMA1(99), EA(99), EB(99)
C
      OPEN(8,FILE='*Input file: ')
      OPEN(7,FILE='*Output file: ')
C
      READ(8,'(/)')
      READ(8,*)IZMAX,MION,TE,EZ
      READ(8,'(/,/,/)')
      READ(8,*)(JJ,EA(I),EB(I),SIGMAZ(I),SIGMA1(I),I=1,IZMAX)
C
      DO 10 I=1,IZMAX
        IF(EA(I).EQ.9999.)EA(I)=100000.D0
        IF(EB(I).EQ.9999.)EB(I)=100000.D0
   10 CONTINUE
C
C$$     WRITE(*,*)(EA(I),EB(I),SIGMAZ(I),SIGMA1(I),I=1,IZMAX)
C
      EZ=EA(1)
C
      CALL SIGMAV(BETA,SIGMAZ,SIGMA1,EA,EB,EZ,IZMAX,TE)
C
```

```
      WRITE(7,'("  Place plasma and mirror parameters directly under va
     &riable name.",/)')
      WRITE(7,'(/,"  Zmax  Mion(amu)  Te(eV)  Tion(eV)  Ne(cm-3)
     &  No(cm-3)")')
       WRITE(7,'(4X,1I2,7X,1I2,8X,1F6.0)')IZMAX,MION,TE
       WRITE(7,'(/,/,/,9X,"Lmirror(cm)  Rmirror  Phi(eV)  Tc/Tmirr di
     &v.
     &")')
       WRITE(7,'(/,/,/,/,10X,"              <sigma*v>",/)')
       WRITE(7,'(10X,2E20.10)')(BETA(I,1),BETA(I,2),I=1,IZMAX)
C
      STOP
      END
C
C
C
C
      SUBROUTINE SIGMAV(BETA,SIGMAZ,SIGMA1,EA,EB,EZ,IZMAX,TE)
C
C This subroutine subprogram computes the <sigma*v>'s for single and
C multiple step ionizations.  The <sigma*v>'s are stored in matrix
C BETA with BETA(i,1) the column for single-event multiple-ionizations
C from neutral to ionization state i by Auger processes, and BETA(i,2)
C the column for multiple-step single-event ionizations from charge
C state i to charge state i+1.
C
C Units for I/O are:
C
C BETA    M**3/S
C SIGMAZ  M**2
C SIGMA1  M**2
C EA,EB   eV
C IZMAX   esu
C AMION   amu
C TE      eV
C EZ      eV

      IMPLICIT REAL*8 (A-H,O-Z)
      DIMENSION BETA(99,2), SIGMAZ(99), SIGMA1(99), EA(99), EB(99)
      EVJ=1.602D-19
      PI=3.1415927D0
      EMASS=9.1095D-31
      TEMKS=TE*EVJ
      CONST=DSQRT(8.D0/(PI*EMASS*TEMKS))
      DO 40 I=1,IZMAX
        WRITE(*,'("Averaging sigma*v1 over Maxwellian -- I = ",I2)')I
        CALL WASTE
        BETA(I,1)=SIGMAZ(I)*CONST*(EA(I)*EVJ)*AINTEG(EA(I)/TE)
        WRITE(*,'("Averaging sigma*v2 over Maxwellian -- I = ",I2)')I
        CALL WASTE
        IF(I.NE.IZMAX) THEN
          BETA(I,2)=SIGMA1(I)*CONST*(EZ/EB(I))**2*
     &         EB(I)*EVJ*AINTEG(EB(I)/TE)
        ENDIF
   40 CONTINUE
      CLOSE(6)
      RETURN
      END
C
C
C
C     REAL*8 FUNCTION AINTEG(A,B)
C
C This function subprogram calculates the value of the integral
```

```
C (exp(-x))/x evaluated between a and b needed for the evaluation of
C the <sigma*v>'s.  It writes the relative error of the last step to
C the screen.
C
C     IMPLICIT REAL*8 (A-H,O-Z)
C     DIMENSION R(15)
C     F(X) = (DEXP(-1.*X))/X
C     H=B-A
C     R(15)=H*(F(B)+F(A))/2.D0
C     DO 20 N=2,15
C     H=H/2.D0
C     X=0.D0
C       DO 30 M=1,17000,2
C     IF ((A+M*H) .GT. B) GO TO 25
C     X=X+F(A+M*H)
C     GO TO 30
C  25 I=16999
C 30 CONTINUE
C     L=16-N
C     J=17-N
C     R(L)=R(J)/2.D0+H*X
C     Q=1.D0
C     DO 10 K=2,N
C     Q=Q*4
C     ALPHA=Q/(Q-1.D0)
C     BETA=-1./(Q-1.D0)
C     JJ=15-N+K
C     KK=JJ-1
C     R(JJ)=ALPHA*R(KK)+BETA*R(JJ)
C 10 CONTINUE
C     IF(L.EQ.2) RSEC=R(15)
C     IF(L.EQ.1) THEN
C     RLAST=R(15)
C     EPS=((DABS(RLAST-RSEC))/RLAST)*100.D0
C     WRITE(*,'("epsilon = ",1E15.5," %")')EPS
C     ENDIF
C 20 CONTINUE
C$$   20 WRITE(6,'(6F20.15)') (R(I),I=L,15)
C$$      WRITE(*,*)RLAST
C     AINTEG=RLAST
C     RETURN
C     END


      REAL*8 FUNCTION AINTEG(X)

      IMPLICIT REAL*8 (A-H,O-Z)

C
C This function subprogram calculates the value of the integral
C (exp(-x))/x evaluated between a and +inf. needed for the evaluation
C of the <sigma*v>'s.  The expansion comes from Abromowitz and Stegun.
C
      A0=-.57721566D0
      A1=.99999193D0
      A2=-.24991055D0
      A3=.05519968D0
      A4=-.00976004D0
      A5=.00107857D0
      C1=2.334733D0
      C2=.250621D0
      B1=3.330657D0
      B2=1.681534D0
```

```
      IF (X .GT. 1.0D0) GO TO 10
      E=-DLOG(X)+A0+A1*X+A2*X**2+A3*X**3+A4*X**4+A5*X**5
      EX=DEXP(X)*E
      GO TO 20
10 CONTINUE
      EX=(1.D0/X)*(X**2+C1*X+C2)/(X**2+B1*X+B2)
20 AINTEG=EX/DEXP(X)
      RETURN
      END
```

ICSD INPUT FILE

Place plasma and mirror parameters directly under variable name.

Zmax	Mion(amu)	Te(eV)	Tion(eV)	Ne(cm-3)	No(cm-3)
18	40	5000.	5.	2.e11	.1e11

Lmirror(cm)	Rmirror	Phi(eV)	Tc/Tmirr div.
20.	2.	2.	10.

Zhot	Ti hot(eV)
8	5.

$\leq$sigma*v$\geq$

0.8770787505E-13	0.6927413007E-14
0.5700906590E-14	0.2143475735E-14
0.1080693331E-14	0.5371260637E-15
0.2451869354E-15	0.9835000467E-16
0.3551914701E-16	0.1816247947E-16
0.4964344626E-17	0.2970840674E-17
0.4584275324E-18	0.4917617523E-18
0.0000000000E+00	0.0000000000E+00
0.0000000000E+00	0.0000000000E+00

ICSD SOURCE LISTING

```
      PROGRAM ICSD
C
C This program computes the steady state charge distribution of
```

```fortran
C a plasma confined in a potential well.  It includes single-event
C multiple ionization processes as well as multiple-event single
C ionization processes.  It allows for either flow confinement
C or spatial diffusion, specific to each charge state.  As of now
C this program assumes that diffusion is the dominant loss process
C which is a good assumption for low background gas pressures (low
C charge exchange rates) and low charge states (low radiative
C recombination rates).
C
      IMPLICIT REAL*8 (A-H,O-Z)
      DIMENSION G(99), BETA(99,2), TAU(99), SIG(99), R(99), GEXP(99)
C
C Call subroutine to read in the plasma and mirror parameters.  This
C file should be the modified outpput file of "sigv.ftn".
C
      CALL INOUT(IZMAX,AMION,TION,TE,ANE,ANZ,ALMIRR,RMIRR,V,CONFDIV,
     &BETA,IHOT,TIHOT)
C$$   IHOT=3
C$$   TIHOT=50.
C
C$$   WRITE(*,*)IZMAX,AMION,TION,TE,ANE,ANZ,ALMIRR,RMIRR,V,CONFDIV

C$$   DO 2 I=1,IZMAX
C$$      WRITE(*,*)BETA(I,1),BETA(I,2)
C$$   2 CONTINUE
C
C
C   IZMAX=10
      DO 5 I=1,IZMAX
C      BETA(I,1)=2.D-15
C      BETA(I,2)=3.D-15
       G(I)=.01D0
    5 CONTINUE
C    ANE=1.D17
C    ANZ=2.D17
C    AMION=40.D0
C    TION=5.D0
C    RMIRR=2.D0
C    ALMIRR=.2D0
C    V=2.D0
C    CONFDIV=10.D0
      WRITE(*,'(/)')
C
C Call subroutine to determine the division between collisional
C confinement and flow confinement, ZC, for initial charge state
C distribution.
C
      CALL ZCONF(AMION,TION,IZMAX,G,ANE,CONFDIV,ZC)
C
C Call subroutine to solve system of coupled, non-linear equations
C to determine confinement times and charge state distribution for
C given ZC.
C
   10 WRITE(*,'(" Solving . . . Zc = ",1F4.1)')ZC
C
      CALL SOLVE(IZMAX,BETA,G,ANE,ANZ,ALMIRR,RMIRR,AMION,TION,
     &ZC,V,ALPHAZ,TAU,SIG,R,ZAVE,IHOT,TIHOT)
C
C Update ZC and check to see if it is consistant with calculated
C charge state distribution.
C
      ZCOLD=ZC
C
C$$   WRITE(*,'(" Updating . . . Zc = ",1F4.1)')ZC
```

```
C
      CALL ZCONF(AMION,TION,IZMAX,G,ANE,CONFDIV,ZC)
C
C If ZC has changed with the calculated CSD, recalculate confinement
C times and CSD to create a self-consistant model.
C
      IF(ZC.NE.ZCOLD) GO TO 10
C
C Add mass discrimination effect of spectrometer.
C
      GEXP(1)=G(1)*.067D0
      GEXP(2)=G(2)*.34D0
      GEXP(3)=G(3)*.461D0
      GEXP(4)=G(4)*.533D0
      GEXP(5)=G(5)*.582D0
C
      DO 99 I=6,IZMAX
      GEXP(I)=0.D0
   99 CONTINUE
C
      S=0.D0
      DO 100 I=1,IZMAX
      S=S+GEXP(I)
  100 CONTINUE
C
      DO 110 I=1,IZMAX
      GEXP(I)=GEXP(I)/S
  110 CONTINUE
C
C Write output when convergence is acheived.
C
      WRITE(*,'(/," alphaz      = ",1E11.4)')ALPHAZ
      WRITE(*,'("        <Z>     = ",1F5.2)')ZAVE
      WRITE(*,'(/," g(I)   ni/ne   = ",20E10.3)')(G(I),I=1,IZMAX)
      WRITE(*,'(" r(I) normalized g = ",20F8.5)')(R(I),I=1,IZMAX)
      WRITE(*,'("gexp(I)  m/q effect = ",20F8.5)')(GEXP(I),I=1,IZMAX)
      WRITE(*,'("sig(I)  g(I)/tau(I) = ",20F8.5)')(SIG(I),I=1,IZMAX)
      WRITE(*,'("tau(I)   millisec  = ",20F8.2)')(TAU(K),K=1,IZMAX)
      WRITE(*,'(/)')
C
      STOP
      END


**********************************************************************


      SUBROUTINE SOLVE(IZMAX,BETA,G,ANE,ANZ,ALMIRR,RMIRR,AMION,TION,
     &ZC,V,ALPHAZ,TAU,SIG,R,ZAVE,IHOT,TIHOT)
C
C This subroutine subprogram calculates steady state distributions
C of charge states governed by equations on pages 3-4 of notes. The
C output is given for a specific ZC (= (1/2)*(Zcoll min + Z flow max))
C and iterations must be made to determine the actual ZC. Confinement
C times and charge state distributions are found in arrays TAU and G
C just before STOP.
C
      IMPLICIT REAL*8 (A-H,O-Z)
      DIMENSION G(99), GNEW(99), BETA(99,2), C(3,99), ANU(99), TAU(99)
      DIMENSION SIG(99), R(99)
C
C Set maximum number of iterations, initial alpha, convergence
C criterion.
C
```

```
      NMAX1=10000
      ALPHAOLD=1.D-5
      EPS=1.D-10
C
C Call subroutine to calculate new alpha for given g(I).  This
C subroutine used an iterative scheme to solve f(alpha)=0.
C
    8 CALL ALPHA(G,BETA,ALPHAOLD,NMAX1,IZMAX,AMION,TION,ZC,
     &RMIRR,ALMIRR,V,ANZ,ANE,EPS,C,ALPHAZ,IHOT,TIHOT)
C
C Calculate new values of g(I) for new value of alpha.
C
      GNEW(1)=ANZ*BETA(1,1)/(ALPHAZ*C(2,1)+ANE*BETA(1,2))
      GNEW(IZMAX)=(ANZ*BETA(IZMAX,1)+ANE*G(IZMAX-1)*BETA(IZMAX-1,2))
     &      /(ALPHAZ*C(2,IZMAX))
C
      DO 30 I=2,IZMAX-1
       GNEW(I)=(ANZ*BETA(I,1)+ANE*G(I-1)*BETA(I-1,2))
     &      /(ALPHAZ*C(2,I)+ANE*BETA(I,2))
   30 CONTINUE
C$$     WRITE(*,*)(GNEW(KK),KK=1,IZMAX)
C
C Check for convergence of the g(I)'s.  If the g(I)'s have not
C converged, recalculate a new alpha for the new set of g(I)'s
C and the calculate the next set of g(I)'s until convergence
C is achieved.
C
C     WRITE(*,'("HERE5")')
      DO 10 I=1,IZMAX
C$$     write(*,*)(GNEW(JJ),JJ=1,IZMAX)
      IF((GNEW(I).GE.1.D-8).AND.(G(I).GE.1.D-8)) THEN
      IF(DABS((GNEW(I)-G(I))/GNEW(I)).GE.1.D-6)THEN
C$$       WRITE(*,*)I
       DO 20 J=1,IZMAX
        G(J)=GNEW(J)
   20   CONTINUE
       GO TO 8
       ELSE
        DO 50 K=1,IZMAX
        G(K)=GNEW(K)
   50   CONTINUE
       ENDIF
       ENDIF
   10 CONTINUE
C
C Calculate confinement times after g(I)'s have converged.
C
      ASUM=0.D0
      DO 40 I=1,IZMAX
       AI=I
       ANU(I)=ALPHAZ*C(2,I)
       TAU(I)=1.D3/ANU(I)
       ASUM=ASUM+G(I)*AI
   40 CONTINUE
C
      RSUM=0.D0
      DO 60 I=1,IZMAX
       RSUM=RSUM+G(I)
   60 CONTINUE
C
      DO 70 I=1,IZMAX
       R(I)=G(I)/RSUM
       SIG(I)=G(I)/TAU(I)
   70 CONTINUE
```

```
C
      SSUM=0.D0
      DO 80 I=1,IZMAX
      SSUM=SSUM+SIG(I)
   80 CONTINUE
C
      DO 90 I=1,IZMAX
      SIG(I)=SIG(I)/SSUM
   90 CONTINUE
C
      SUMC=0.D0
      SUMD=0.D0
      DO 100 I=1,IZMAX
      AI=I
      SUMC=SUMC+AI*G(I)
      SUMD=SUMD+G(I)
  100 CONTINUE
      ZAVE=SUMC/SUMD
C
      RETURN
      END


*******************************************************************


      SUBROUTINE ALPHA(G,BETA,AZOLD,NMAX1,IZMAX,AMION,TION,ZC,
     &RMIRR,ALMIRR,V,ANZ,ANE,EPS,C,ALPHAZ,IHOT,TIHOT)
C
C This subroutine subprogram sets up the constants for the equation
C f(alpha)=0 and solves for alpha using an iterative Newton method.
C
      IMPLICIT REAL*8 (A-H,O-Z)
      DIMENSION G(99), BETA(99,2), C(3,99), TSCAT(99)
C
C Assign constants for equation for f(alpha)=0.  See notes for
C explicit form of this equation.
C
      C(1,1)=ANZ*BETA(1,1)
      C(2,1)=CHI(1,TION,AMION,IZMAX,RMIRR,ALMIRR,V,ZC,G,ANE)
      C(3,1)=ANE*BETA(1,2)
      C(1,IZMAX)=ANZ*BETA(IZMAX,1)+ANE*G(IZMAX-1)*BETA(IZMAX-1,2)
      C(2,IZMAX)=CHI(IZMAX,TION,AMION,IZMAX,RMIRR,ALMIRR,V,ZC,G,ANE)
      C(3,IZMAX)=0.D0
C
      DO 10 I=2,IZMAX-1
      C(1,I)=ANZ*BETA(I,1)+ANE*G(I-1)*BETA(I-1,2)
      C(2,I)=CHI(I,TION,AMION,IZMAX,RMIRR,ALMIRR,V,ZC,G,ANE)
      C(3,I)=ANE*BETA(I,2)
   10 CONTINUE
C
C     Correct chi for hot ion species dependent on its confinement
C     regime.
C
      CALL TSCATTER(AMION,TIHOT,IZMAX,G,ANE,TSCAT)
      ZIHOT=IHOT
      IF(ZIHOT.GT.ZC)THEN
      C(2,IHOT)=C(2,IHOT)*((TIHOT/TION)**2.5)
      ELSE
      C(2,IHOT)=C(2,IHOT)
     &     *(H(TSCAT(IHOT),RMIRR,ALMIRR,TION,AMION,V,ZIHOT)
     &     /H(TSCAT(IHOT),RMIRR,ALMIRR,TIHOT,AMION,V,ZIHOT))
     &     *DEXP((ZC-ZIHOT)*V*((1.D0/TIHOT)-(1.D0/TION)))
     &     *DSQRT(TIHOT/TION)
```

```fortran
      ENDIF
C
C Use Newton's method to solve for root and check for convergence.  If
C the method does not converge in NMAX1 iterations, report failure.
C
C$$    WRITE(*,'("Enter ALPHAmin, ALPHAmax")')
C$$    READ(*,*)ALPHAMIN,ALPHAMAX
C
C$$    H=(ALPHAMAX-ALPHAMIN)/100.D0
C$$    DO 100 JJ=1,100
C$$      AJJ=JJ-1
C$$      ALZ=ALPHAMIN+H*AJJ
C$$      WRITE(*,*)ALZ,F1(ALZ,C,IZMAX),F2(ALZ,C,IZMAX)
C$$ 100 CONTINUE
C
C$$    WRITE(*,*)A,B
      A=AZOLD
      B=AZOLD+1.D15
      IF((F1(A,C,IZMAX).LT.0.D0).OR.(F1(B,C,IZMAX).GT.0.D0))THEN
        WRITE(*,'("ALPHA brackets incorrect")')
        STOP
      ENDIF


      DO 20 I=1,NMAX1
      XNEW=.5D0*(A+B)
C$$      WRITE(*,*)A,B
      IF(F1(XNEW,C,IZMAX).GT.0.D0)THEN
        A=XNEW
      ELSE
        B=XNEW
      ENDIF
      IF(((B-A)/B).GT.EPS)THEN
C$$      WRITE(*,*) A,B
        GO TO 20
      ELSE
        GO TO 40
      END IF
  20 CONTINUE
C
      WRITE(*,'("Convergence failed")')
C
      STOP
C
  40 ALPHAZ=A


C$$    DO 20 I=1,NMAX1
C$$      AZNEW=AZOLD-F1(AZOLD,C,IZMAX)/F2(AZOLD,C,IZMAX)
C$$      DIFF=DABS((AZNEW-AZOLD)/AZNEW)
C$$      IF(DIFF.LE.EPS)GOTO 30
C$$      WRITE(*,*)AZOLD,F1(AZOLD,C,IZMAX),F2(AZOLD,C,IZMAX),
C$$    &       F1(AZOLD,C,IZMAX)/F2(AZOLD,C,IZMAX)
C$$      AZOLD=AZNEW
C$$ 20 CONTINUE
C
C$$    WRITE(*,'("Convergence failed")')
C
C$$    STOP
C
C Assign root to ALPHAZ to pass back to preceeding subroutine.
C
C$$ 30 ALPHAZ=AZNEW
C
      RETURN
```

```
      END


*********************************************************************


      REAL*8 FUNCTION F1(AZOLD,C,IZMAX)
C
C This function subprogram evaluates the function of the form
C f(x)=0 for solution of ALPHAZ in the Newton-Raphson method.
C
      IMPLICIT REAL*8 (A-H,O-Z)
      DIMENSION C(3,99), X(99)
C
      DO 10 I=1,IZMAX
      AI=I
      X(I)=AI*C(1,I)/(C(2,I)*AZOLD+C(3,I))
   10 CONTINUE
C
      F=0.D0
C
      DO 20 I=1,IZMAX
      F=F+X(I)
   20 CONTINUE
C
      F=F-1.D0
C
      F1=F
C
      RETURN
      END


*********************************************************************


      REAL*8 FUNCTION F2(AZOLD,C,IZMAX)
C
C This function subprogram evaluates the derivative of the
C function, F1, above for solution of ALPHAZ in the Newton-Raphson
C method.
C
      IMPLICIT REAL*8 (A-H,O-Z)
      DIMENSION C(3,99), X(99)
C
      DO 10 I=1,IZMAX
      AI=I
      X(I)=-1.D0*AI*C(1,I)*C(2,I)/((C(2,I)*AZOLD+C(3,I))**2)
   10 CONTINUE
C
      F=0.D0
C
      DO 20 I=1,IZMAX
      F=F+X(I)
   20 CONTINUE
C
      F2=F
C
      RETURN
      END


*********************************************************************
```

```
      REAL*8 FUNCTION CHI(IZI,TION,AMION,IZMAX,RMIRR,ALMIRR,V,ZC,G,ANE)
C
C This function subprogram evaluates chi (see notes).
C
      IMPLICIT REAL*8 (A-H,O-Z)
      DIMENSION TSCAT(99), G(99)
C
      N=ZC*2.D0
      N=N/2
C
      CALL TSCATTER(AMION,TION,IZMAX,G,ANE,TSCAT)
      TSCATZC=TSCAT(N)*((ZC-.5D0)/ZC)**2
C
      ZI=IZI
      IF(ZI.GT.ZC)THEN
        CHI=TSCAT(IZI)
      ELSE
        CHI=TSCATZC*(H(TSCATZC,RMIRR,ALMIRR,TION,AMION,V,ZC)
     &  /H(TSCAT(IZI),RMIRR,ALMIRR,TION,AMION,V,ZI))
     &  *DEXP((ZC-ZI)*V/TION)
      ENDIF
C
      RETURN
      END



***************************************************************


      REAL*8 FUNCTION H(TSCAT,R,ALMIRR,TION,AMION,V,ZI)
C
C This function subprogram evaluates H.  See notes for explicit form.
C
      IMPLICIT REAL*8 (A-H,O-Z)
C
      GG(X)=((X+1)/X)*DLOG(2.D0*X+2.D0)
C
      Q=1.602D-19
      AMP=1.6726D-27
C
      H=TSCAT*(GG(R)/R)*(1.D0/ALMIRR)*(ZI*V/TION)
     &*DSQRT(TION*Q/(AMION*AMP))
C
      H=H+1.D0
C
      RETURN
      END



***************************************************************


      SUBROUTINE TSCATTER(AMION,TION,IZMAX,G,ANE,TSCAT)
C
C This subroutine subprogram calculates the 90 degree scattering
C times for the entire distribution. The scattering times are
C located in the array TSCAT and passed back to the preceeding
C subroutine.
C
      IMPLICIT REAL*8 (A-H,O-Z)
      DIMENSION G(99), ANNOR(99), TSCAT(99), TRATIO(99)
C
      DO 10 I=1,IZMAX
```

```
      ANNOR(I)=G(I)*ANE/1.D17
   10 CONTINUE
C
      SUM=0.D0
      DO 20 I=1,IZMAX
      AI=I
      SUM=SUM+ANNOR(I)*AI*AI
   20 CONTINUE
C
C Using equation from '87 APS conference for scattering times.
C
      DO 30 I=1,IZMAX
      AI=I
      TSCAT(I)=5.746D-6*(TION**1.5D0)*(AMION**.5D0)/(AI*AI*SUM)
   30 CONTINUE
C
      RETURN
      END
```

```
      ****************************************************************
```

```
      SUBROUTINE ZCONF(AMION,TION,IZMAX,G,ANE,CONFDIV,ZC)
C
C This subroutine calculates the confinement regimes for all multiply
C charged ions based on the ratio of their bounce times to their
C 90 degree scatter times.  A parabolic profile for the mirror is
C assumed.
C
      IMPLICIT REAL*8 (A-H,O-Z)
      DIMENSION G(99), TSCAT(99), TRATIO(99)
C
C
C    Calculate Spitzer scatter times.
C
      CALL TSCATTER(AMION,TION,IZMAX,G,ANE,TSCAT)

C$$   WRITE(*,*)(TSCAT(I),I=1,IZMAX)
C
C    Calculate mirror time.
C
      CALL TMIRROR(AMION,TION,TMIRR)
C
C$$   WRITE(*,*)TMIRR


      DO 10 I=1,IZMAX
      TRATIO(I)=TMIRR/TSCAT(I)
   10 CONTINUE


C$$   WRITE(*,*)(TRATIO(I),I=1,IZMAX)


C
      ZC=0.D0
C
      DO 20 I=1,IZMAX-1
      IF(TRATIO(1).GT.CONFDIV) THEN
        ZC=.5D0
        GO TO 30
      ENDIF
```

```
      IF((TRATIO(I).LT.CONFDIV).AND.TRATIO(I+1).GT.CONFDIV) THEN
      ZC=FLOAT(I)+.5D0
      GO TO 30
      ENDIF
20 CONTINUE
30 CONTINUE
      IF(ZC.EQ.0.D0)ZC=FLOAT(IZMAX)+.5D0
C
      RETURN
      END




*****************************************************************


      SUBROUTINE TMIRROR(AMION,TION,TMIRR)
C
C This subroutine subprogram calculates the bounce times for ions of
C mass AMION temperature TION.  The mirror time is passed back in
C the variable TMIRR.  See notes for derivation of mirror time.
C
      IMPLICIT REAL*8 (A-H,O-Z)
C
      BMOBZ=.74D0
      ALMIRR=.178D0
      B=DSQRT(BMOBZ)/ALMIRR
      Q=1.602D-19
      AMP=1.6726D-27
      VPERPZ=DSQRT(2.D0*TION*Q/(AMION*AMP))
      PI=2.D0*DASIN(1.D0)
C
      TMIRR=PI/(VPERPZ*B)
C
      RETURN
      END




*****************************************************************


      SUBROUTINE INOUT(IZMAX,AMION,TION,TE,ANE,ANZ,ALMIRR,RMIRR,V,
     &    CONFDIV,BETA,IHOT,TIHOT)

      IMPLICIT REAL*8 (A-H,O-Z)
      DIMENSION BETA(99,2)

      OPEN(7,FILE='*Enter input file : ')

      READ(7,'(/,/,/)')
      READ(7,*)IZMAX,MION,TE,TION,ANE,ANZ
C$$   WRITE(*,*)IZMAX,MION,TION,TE,ANE,ANZ
      READ(7,'(/,/,/)')
      READ(7,*)ALMIRR,RMIRR,V,CONFDIV
C$$   WRITE(*,*)ALMIRR,RMIRR,V,CONFDIV
      READ(7,'(/,/,/)')
      READ(7,*)IHOT,TIHOT
      READ(7,'(/,/,/,/,/)')
      READ(7,*)(BETA(I,1),BETA(I,2),I=1,IZMAX)
C$$   WRITE(*,*)(BETA(I,1),BETA(I,2),I=1,IZMAX)


      AMION=MION
      ANE=ANE*1.D6
      ANZ=ANZ*1.D6
```

```
ALMIRR=ALMIRR*1.D-2

RETURN
END
```

REFERENCES

REFERENCES

1. R. Geller, B. Jacquot, and M. Pontonnier, Rev. Sci. Instrum. **56**, 1505 (1985).

2. J. Bol, Y. Jongen, M. Lacroix, F. Mathy, and G. Rychewaert, IEEE Trans. on Nuc. Sci. **NS-32** (5) 1817 (1985).

3. C. Lyneis and D. Clark, IEEE Trans. on Nuc. Sci. **NS-32** (5) 1745 (1985).

4. Y. Jongen, Proceedings from Tenth International Conference on Cyclotrons and Their Applications 322 (1984).

5. G. Ryckewaert, Proceedings from Tenth International Conference on Cyclotrons and Their Applications 226 (1984).

6. J. Loiseaux and M. Fruneau, Proceedings from Tenth International Conference on Cyclotrons and Their Applications 188 (1984).

7. T. Antaya, H. Blosser, and R. Burleigh, Proceedings from Tenth International Conference on Cyclotrons and Their Applications 184 (1984).

8. V. Bechtold, L. Friedrich, and F. Schulz, Proceedings from Tenth International Conference on Cyclotrons and Their Applications 118 (1984).

9. Y. Jongen and G. Ryckewaert, IEEE Trans. on Nuc. Sci. **NS-30** (4) 2685 (1983).

10. R. Geller and B. Jacquot, Physica Scripta Vol. T3, 19 (1983).

11. H. Winter, Institut fur Allgemeine Physik internal report, 455 (1982).

12. L Yarris, Lawrence Berkeley Laboratory Research Review Vol. 10, No. 3 (1985).

13. J Arianer and R. Geller, Ann. Rev. Nuc. Part. Sci. **31**, 19 (1981).

14. R. Geller, Association Euratom-CEA internal report, 114 (1977).

15. S. Bliman, R. Geller, W. Hess, B. Jacquot, and C. Jacquot, IEEE Trans. on Nuc. Sci. **NS-19**, 200 (1972).

16. C. Lyneis, Proceedings from International Conference on ECR Ion Sources and Their Applications, NSCL Report #MSUCP-47, 42 (1987).

17. R. Geller, Appl. Phys. Lett. **16**, 401 (1970).

18. R. Geller, Rapport CEA. R. 2998, 1965, Center d'Etudes Nucleaires de Saclay.

19. D. Bohm, Characteristics of Electrical Discharges in Magnetic Fields (McGraw-Hill, New York).

20. A. van der Woude, IEEE Trans. on Nuc. Sci. **NS-19** 187 (1972).

21. H. Tamagawa, I. Alexeff, C. Jones, and P. Miller, IEEE Trans. on Nuc. Sci. **NS-23** (2) 994 (1976).

22. Y. Gott, M.Ioffe, and Telkovsky, Nuc. Fusion, Suppl. Part 3, 1045 (1962).

23. R. Geller, IEEE Trans. on Nuc. Sci. **NS-23** (2) 904 (1976).

24. Y. Jongen, C. Pirart, and G. Ryckewaert, IEEE Trans. on Nuc. Sci. **NS-28** (3) 2696 (1981).

25. V. Bechtold, N. Chan-Tung, S. Dousson, R. Geller, B. Jacquot, and Y. Jongen, Nuc. Instrum. and Meth. 178, 305 (1980).

26. J. Booske, W. Getty, R. Gilgenbach, and R. Jong, Phys. Fluids **28**, 3116 (1985).

27. J. Booske, F. Aldabe, R. Ellis, and W. Getty, J. Appl. Phys. **64**, 1055 (1988).

28. R. Huddlestone and S. Leonard editors, *Plasma Diagnostic Techniques*, (Academic Press, New York, 1965).

29. J. Booske, doctoral dissertation, Dept. Nuc. Eng., U. Michigan (1985).

30. T. Goodman, doctoral dissertation, Dept. Nuc. Eng., U. Michigan (1989).

31. F. Chen, *Plasma Diagnostic Techniques*, R. Huddlestone and S. Leonard editors, (Academic Press, New York, 1965).

32. B. Polychronopulos, Plasma Phys. **15**, 37 (1973).

33. M. Krishnan and J. Hirshfield, Rev. Sci. Instrum. **51**, 911 (1980).

34. N. Alinovskii, *Recent Advances in Plasma Diagnostics*, edited by V. Tolok, translated by Consultants Bureau (1971), Vol. 3, p. 30.

35. J. Pinkston, M. Rabb, J. Watson, and J. Allison, Rev. Sci. Instrum. **57**, 583 (1986).

36. C. Petty, D. Smith, and D. Smatlak, Rev. Sci. Instrum. **59**, 601 (1988).

37. I. Brown, J. Galvin, R. MacGill, and R. Wright, Rev. Sci. Instrum. **58**, 1589 (1987).

38. J. Osher, Inst. Phys. Conf. Ser. No 38 (5) 201 (1978).

39. P. Grivet, M. Bernard, F. Bertein, R. Castaing, M. Gauzit, and A. Septier, *Electron Optics*, (Permagon, Oxford, 1965).

40. W. Herrmannsfeldt, SLAC Electron Optics Program, Stanford Lin. Acc. Cen. (1981).

41. D. Whaley, T. Goodman, and W. Getty, Rev. Sci. Instrum. **60**, 358 (1989).

42. B. McVey, Mass. Inst. Tech., internal report PFC/RR-84-12 (1984).

43. B. McVey, Mass. Inst. Tech., internal report PFC/RR-84-13 (1984).

44. N. Krall and A. Trivelpiece, *Principles of Plasma Physics*, (McGraw Hill, New York, 1973).

45. T. Stix, *Theory of Plasma Waves*, (McGraw Hill, New York, 1962).

46. D. Smith, doctoral dissertation, Dept. Elec. Eng., U. Wisconsin (1980).

47. J. Howard, Plasma Phys. **23**, 197 (1981).

48. T. Carlson and M. Krause, Phys. Rev. A **140**, 1057 (1965).

49. H. Bethe, Ann. Physik **5**, 325 (1930).

50. B. Schram, A. Boerboom, and J. Kistemacker, Physica **32**, 185 (1966).

51. B. Schram, Physica **32**, 197 (1966).

52. M. Van der Weil, T. El-Sherbini, and L. Vriens, Physica **42**, 411 (1969).

53. G. Fuchs, IEEE Trans. on Nuc. Sci. **NS-19** 160 (1972).

54. W. Lotz, Z. Phys. **216**, 241 (1968).

55. W. Lotz, Z. Phys. **220**, 466 (1969).

56. D. Post, R. Jensen, C. Tarter, W. Grasberger, and W. Lokke, Atom. Data and Nuc. Data Tables **20**, 397 (1977).

57. A. Mueller and E. Salzborn, Phys. Lett. **62A**, 391 (1977).

58. L. Spitzer, *Physics of Fully Ionized Gases,* (Interscience, New York, 1962).

59. V. Pastukhov, Nuc. Fusion **14**, 3 (1974).

60. D. Smith and C. Petty, Bull. Am. Phys. Soc. **31**, 1511 (1986), Paper 5P29.

61. T. Rognlien and T. Cutler, Nuc. Fusion **20**, 1003 (1980).

62. F. Chen, C. Etievant and D. Mosher, Phys. Fluids **11**, 811 (1968).